

University of Southampton Research Repository ePrints Soton

Copyright © and Moral Rights for this thesis are retained by the author and/or other copyright owners. A copy can be downloaded for personal non-commercial research or study, without prior permission or charge. This thesis cannot be reproduced or quoted extensively from without first obtaining permission in writing from the copyright holder/s. The content must not be changed in any way or sold commercially in any format or medium without the formal permission of the copyright holders.

When referring to this work, full bibliographic details including the author, title, awarding institution and date of the thesis must be given e.g.

AUTHOR (year of submission) "Full thesis title", University of Southampton, name of the University School or Department, PhD Thesis, pagination

UNIVERSITY OF SOUTHAMPTON

FACULTY OF ENGINEERING, SCIENCE AND MATHEMATICS

School of Chemistry

**DEVELOPMENT OF RESONANT INELASTIC X-RAY SCATTERING
SPECTROSCOPY**

By

Sarah Hobbs

Thesis for Degree of Doctor of Philosophy

October 2012

UNIVERSITY OF SOUTHAMPTON

ABSTRACT

FACULTY OF ENGINEERING, SCIENCE AND MATHEMATICS

School of Chemistry

Doctor of Philosophy

DEVELOPMENT OF RESONANT INELASTIC X-RAY SCATTERING
SPECTROSCOPY

By Sarah Hobbs

This research focuses on the development of Resonant Inelastic X-ray Scattering spectroscopy (RIXS) as a tool in homogeneous catalysis by looking at 3d transition metal compounds and specifically Cr(salen) epoxidation catalysts. Previous studies have demonstrated the sensitivity of transition metal K-edge X-ray absorption pre-edge and edge features to their chemical environment, but the exact origins are unassigned. The aim of this study is to bring together a collection of complementary, and some novel, X-ray techniques to assign these features and obtain more detailed structural and electronic information on the systems under investigation.

Novel high energy resolution data on transition metal complexes have been obtained and the pre-edge region has been simulated with the FEFF9 multiple scattering code. The increase in spectral structure compared to normal XANES allows for a more detailed analysis and as such, provides detailed insights in the electronic properties. L-edge XAS data obtained using soft X-rays enabled the determination of crystal field parameters, which were compared with other X-ray (RIXS) and optical absorption techniques. The novel RIXS experiments provide L and K-edge spectra unaffected by lifetime broadening or background from the main absorption edge. 2D images of X-ray emission as a function of absorption are obtained, revealing the relationship between them and providing direct and detailed information on the presence and position of molecular orbitals. These 1s2p RIXS experiments make use of hard X-rays enabling *in-situ* experiments, which are important in the field of catalysis, making it a promising tool to monitor the changing electronics of the metal centre as well as ligand coordination during the catalytic process. Whereas the electronic differences on the Cr metal as a function of salen ligand are not revealed by the current RIXS experiments, which is likely due to resolution issues, new preliminary insights in the different catalytic Cr intermediates of the epoxidation reaction have been obtained.

Table of Contents

Chapter 1: Introduction.....	1
1.1 Thesis Overview.....	2
1.2 Catalysis.....	3
1.2.1 Isomerism.....	4
1.2.2 Asymmetric epoxidation.....	7
1.2.3 Salen catalysts.....	8
1.2.4 Other Uses for Salen Materials.....	16
1.3 Spectroscopy.....	18
1.4 Aim of project.....	23
1.5 References.....	24
Chapter Two: Theory of X-ray Absorption Spectroscopy.....	28
2.1 Introduction to XAS.....	28
2.1.1 X-ray Absorption Near Edge Structure.....	30
2.1.2 Extended X-ray Absorption Fine Structure.....	34
2.2 Synchrotrons.....	36
2.2.1 Soft and hard X-rays.....	40
2.2.2 Detection methods.....	41
2.3 K-edge X-ray Absorption Spectroscopy.....	45
2.3.1 K-edge XAS Background.....	45
2.3.2 K-edge XAS Analysis.....	47
2.4 L-edge X-ray Absorption Spectroscopy.....	48
2.4.1 L-edge XAS Background.....	48
2.4.2 L-edge XAS Analysis.....	50
2.5 X-ray Emission Spectroscopy.....	53
2.5.1 XES Background.....	53
2.5.2 XES Analysis.....	57
2.6 Resonant Inelastic X-ray Scattering Spectroscopy.....	57
2.6.1 RIXS Background.....	57
2.6.2 RIXS Analysis.....	63
2.7 Aims of Spectroscopic Development.....	63
2.8 References.....	65
3 Chapter Three – Experimental.....	69
3.1 Introduction.....	69
3.2 Preparation of symmetric salen materials.....	70
3.2.1 Preparation of salen ligands.....	70
3.2.2 Preparation of Pyrrolidine (salen) CrIII-Cl complexes.....	71
3.3 Characterisation.....	72
3.3.1 Characterisation of salen ligand 1.....	72
3.3.2 Characterisation of salen ligand 3.....	72
3.3.3 Characterisation of salen ligand 4.....	73
3.3.4 Characterisation of salen complex 1.....	73
3.3.5 Characterisation of salen complex 3.....	73
3.3.6 Characterisation of salen complex 4.....	73
3.4 Preparation of Iodosobenzene.....	73
3.5 Epoxidation of trans- β -methylstyrene by the Cr(V)=O salen catalysts.....	74
3.6 Spectroscopic Techniques.....	74

3.6.1	Cr K-edge XANES FEFF9 calculations.....	75
3.6.2	Cr L-edge XANES CTM calculations.....	78
3.6.3	Cr RIXS RGAss calculations.....	80
3.7	References.....	81

Chapter Four: Systematic spectroscopic study of reference chromium materials..... 82

4.1	Introduction.....	82
4.2	Theory	83
4.3	Results and Discussion.....	86
4.3.1	Cr K-edge.....	86
4.3.2	Cr L-edge absorption studies.....	102
4.3.3	Cr 1s2p RIXS emission studies.....	112
4.3.4	Cr K β Emission Studies.....	122
4.4	Conclusions.....	138
4.5	References.....	140

Chapter Five: Systematic spectroscopic study of Cr(salen) materials..... 143

5.1	Introduction.....	143
5.2	Salen Catalysts.....	145
5.3	Results and Discussion.....	147
5.3.1	Cr K-edge.....	147
5.3.2	Cr L-edge absorption studies.....	153
5.3.3	Cr K β emission studies.....	157
5.3.4	Cr 1s2p RIXS emission studies.....	161
5.4	Conclusions.....	166
5.5	References.....	168

Chapter Six: Catalysis..... 117

6.1	Introduction.....	171
6.2	Mechanistic studies.....	172
6.3	Catalytic studies on Cr(salen) systems (activity and (enantio)selectivity as a function of ligand).....	174
6.4	In-situ characterisation XAS and RIXS.....	178
6.4	Conclusions.....	189
6.5	References.....	191

Chapter Seven: Conclusions and Future Recommendations..... 193

7.1	Introduction.....	193
7.2	Experiment versus Theory.....	193
7.2.1	K-edge XAS.....	193
7.2.2	The Benefits of High Energy Resolution (HERFD).....	195
7.2.3	L-edge XAS.....	195
7.2.4	K β XES.....	197
7.2.5	1s2p RIXS.....	198
7.3	Catalysis.....	200
7.4	Recommendations and Further Work.....	201
7.5	References.....	204

DECLARATION OF AUTHORSHIP

I, **Sarah Hobbs** declare that the thesis entitled:

The Development of Resonant Inelastic X-ray Scattering Spectroscopy

and the work presented in it are my own. I confirm that:

- This work was done wholly or mainly while in candidature for a research degree at this University;
- Where any part of this thesis has previously been submitted for a degree or any other qualification at this University or any other institution, this has been clearly stated;
- Where I have consulted the published work of others, this is always clearly attributed;
- Where I have quoted from the work of others, the source is always given. With the exception of such quotations, this thesis is entirely my own work;
- I have acknowledged all main sources of help;
- Where the thesis is based on work done by myself jointly with others, I have made clear exactly what was done by others and what I have contributed myself;

Signed: _____

Date: October 2012

Acknowledgements

There are a number of people that have provided me with a great deal of support throughout the course of my time at Southampton, so I would like to take this opportunity to thank all who have influenced and helped me over the last 7 years. Firstly, I would like to thank my supervisor Professor Moniek Tromp for all her helpful advice, support, and encouragement that she has provided for me throughout the course of my PhD. Not only have you been a great supervisor but also a good friend. I would also like to thank my Advisor Professor Gill Reid for all the advice and feedback over the years. Thank you also to Professor John Evans for your supervision during my bachelor's degree and continued support during my PhD.

There are a number of collaborators to the project without whom I would not have been able to even attempt to analyse my data; Frank de Groot, Pieter Glatzel, John Rehr and Josh Kas. For all their help at the ESRF, I would like to thank Peter Glatzel, Janine Grattage and all the other ID26 staff past and present. I would also like to thank Sarnjeet Dhesi from the IO6 beamline at Diamond Light Source for all his assistance on beam times.

I would like to take this opportunity to thank the members of the Tromp/Evans group who I have worked with throughout my PhD. Specifically I would like to thank Rowena Thomas who was not only a huge support throughout in terms of daily discussions about RIXS and simulations but also for being an extremely helpful beamtime companion! Aside from that you were also a fantastic housemate and friend and made the difficult times far easier. Another member of the group who deserves a specific mention is Peter Wells, Pete's wise words and experience have got me through many a difficult time during my PhD both in and out of working life and I really appreciate all the help you have given me (and all the coffees you have bought me). Generally for being you and making working on level 2 so much fun I would like to thank Stuart (Twiglet) Bartlett and my other half, Paolo Farina. I would also like to thank Michal, Ewa, Ania, Sergio and Jamie, thanks to all for making my time here a really enjoyable experience. I would also like to thank my colleagues at the RSC for their continued encouragement during the writing and especially to Fiona McMillan for the supportive phone calls in the last few days before submission.

Glossary of Terms

Techniques

XAS	X-ray Absorption Spectroscopy
XES	X-ray Emission Spectroscopy
XAFS	X-ray Absorption Fine Structure
EXAFS	Extended X-ray Absorption Fine Structure
XANES	X-ray Absorption Near Edge Structure
RIXS	Resonant Inelastic X-ray Scattering
DFT	Density Functional Theory
LDOS	Local Density of States
DOS	Density of States
MS	Multiple Scattering
MO	Molecular Orbital
ES+	Positive Ion Electrospray
NMR	Nuclear Magnetic Resonance
UV/Vis	Ultra Violet / Visible Spectroscopy

Complexes and Catalysis

M	Metal
L	Donor ligand
ee	Enantiomeric excess

General

ν	Vibrational Frequency
λ	Wavelength
ν	Wavelength
m/z	Mass to Charge Ratio

Hz	Hertz
{ ¹ H}	Proton Decoupled
δ	Chemical Shift
ppm	Parts per Million
s	Singlet
d	Doublet
t	Triplet
m	Multiplet
fac	Facial
mer	Meridional
Me	Methyl
Ph	Phenyl
o-	Ortho-
p-	Para-
m-	Meta-

Chapter 1: Introduction

Primarily this research project is about the development of a relatively new X-ray spectroscopy technique called Resonant Inelastic X-ray Scattering Spectroscopy (RIXS). The RIXS technique itself is new and not very well known, but it builds upon the existing processes of X-ray absorption spectroscopy (XAS) and X-ray emission spectroscopy (XES). As the combination of XAS and XES via the scattering approach in RIXS is new, it requires huge developments in theory. The instrumentation, however, is recent and is now more or less there but may require further developments in the way of resolution.

As chromium is the metal of choice throughout this investigation, we start by performing a detailed study of reference chromium materials of known oxidation state and structure. This involves X-ray absorption and emission experiments using these references with the aim of gaining complementary information that will help in analysing and interpreting the data obtained from the RIXS technique. These findings will be used in the next step when the same techniques are applied to the solid Cr(salen) catalyst materials.

The last part of the project is to look into the catalytic applications of the RIXS technique by studying the well-established, but mechanistically still debated, epoxidation reaction with Cr(salen) catalysts (analogous to Jacobsen's Mn(salen) catalyst). We hope to gain information about the active species in the reaction mechanism that is, so far, unexplored. This will enable future research to predict, and therefore tailor, catalytic activity and the design of catalysts. The RIXS technique can then be used as a tool in catalysis to obtain electronic information on the catalytic intermediates *in-situ*.

As the topic of X-ray absorption and X-ray emission spectroscopy will be used throughout this thesis, there will be a whole chapter dedicated to the background and theory behind these techniques (chapter 2). We will start this introduction chapter by covering some fundamentals of catalysis, highlighting the importance of this area of study. Then we will move on to look at the epoxidation reaction in more detail; which is the catalytic reaction employed in this research project. Finally we will briefly explain how different X-ray absorption and emission techniques can help in developing the catalysis (understanding and performance) before finishing the chapter with the overall aims of this research investigation and what we hope to achieve.

1.1 Thesis Overview

Chapter 1 contains an overview of the research project. It then moves on to look at some of the main subject areas in detail; catalysis, salen materials as catalysts and their other uses, and finally a brief introduction to X-ray spectroscopy and its application in this project.

Chapter 2 then moves on to take a detailed look at all the different types of X-ray spectroscopy employed throughout this research both in terms of experiment and theory. This includes all X-ray absorption techniques, X-ray emission techniques and the combination of the two - Resonant Inelastic X-ray Scattering (RIXS) spectroscopy.

Chapter 3 covers the synthetic side of the project; this includes synthesis of the salen ligands and the associated complexation reactions including the characterisation data. This chapter also includes the parameters used in the theoretical simulations of the X-ray absorption and emission spectra.

Chapter 4 contains the reference studies; this is a large part of the project and is the initial step in the study. The reference study consisted of carrying out a range of X-ray absorption experiments on Cr reference materials of known structure (mainly and chlorides). The data were then theoretically calculated to try to identify what we can learn about the electronic structure and geometry of the compounds from these techniques.

Chapter 5 builds on the data obtained in chapter 4, this is the next step of the project and looks at the same series of experiments but this time the subjects are the Cr(salen) materials. These spectra are then also calculated using theoretical programs to see if we can make any electronic or geometry assignments based on chapter 4 and the calculations.

Chapter 6 is the final experimental phase of the project and this time it is the catalytic process involving the Cr(salen) materials that is under investigation. This is the epoxidation of alkenes. The reactions are monitored *in-situ* to see if any advances can be made in the identification of the active species and the reaction pathway occurring.

Chapter 7 contains the final conclusions and recommendations for further work to support and develop the research.

1.2 Catalysis

In the process known as catalysis, a relatively small amount of catalyst material augments the rate of a chemical reaction. Unlike other reagents that participate in the chemical reaction, a catalyst is not consumed by the reaction itself¹. It may change considerably during the course of the reaction, but at the end it returns back to its starting composition and is available to repeat the cycle¹. The catalyst speeds up the rate of a reaction by reducing the activation energy required¹, this is the minimum amount of energy required to allow the chemical reaction to proceed. It does this by providing a new pathway in which the transition state has a lower Gibbs energy of activation. The catalyst does not change the Gibbs Free energy of the overall reaction, so reactions that are thermodynamically unfavourable are not made favourable by a catalyst¹. Catalysts are also able to speed up the rate of reaction in a selective manner² i.e. changing the obtained product selectivity; this is an extremely desirable quality. This is again achieved by reducing the energy of the transition state, in this case the one that leads to the desired product. Because of this ability to speed up some reactions and not others, a catalyst enables a chemical process to work more efficiently and often with less waste. Hence, catalysts are important in the industrial chemistry^{1,3}.

Catalysts can be divided into two main types; heterogeneous and homogeneous. In a heterogeneous reaction, the catalyst is in a different phase from the reactants and in a homogeneous reaction, the catalyst is in the same phase as the reactants¹. Homogeneous catalysis is often considered to be more open to analysis, this is due to the fact that species in solution are easier to characterise as there are no surface effects¹. The downside is the need to separate the catalyst from the reaction solution at the end. In industry heterogeneous catalysts have a much greater economic impact; in this case there is no need for time consuming extraction processes and the catalysts are robust at high temperatures¹.

Fundamentally both types of catalysts are similar; generally in the catalytic process one or more of the reactants associates with the catalyst species at active sites¹. There is then an interaction between the catalyst and the reactant molecules which makes them more reactive. This might involve an actual reaction with the surface, or some weakening of the bonds in the attached molecules. Then the reaction happens, at this stage both of the reactant molecules might be attached to the catalyst, or one might be attached and hit by the other one moving freely in the gas or liquid. The product molecules are dissociated and this leaves the active site available for new molecules to attach to and react with. A

good catalyst needs to bind the reactant molecules strongly enough for them to react, but not so strongly that the product molecules involve the catalysts species. Substances that slow a catalyst's effect in a chemical reaction are called inhibitors. Substances that increase the activity of catalysts are called promoters, and substances that deactivate catalysts are called catalytic poisons ¹. Mechanisms of catalysis have a certain amount of uncertainty associated with them and developments are continually accepted in the light of new experimental evidence. The uncertainty is often caused by the fact that many catalytic intermediates are highly reactive and often present in concentrations too low to be detected spectroscopically ¹.

In this study we will be focusing on homogeneous catalysts with all species in solution, but the principle and possibilities of the analogous heterogeneous systems are covered, including an example of a research group who have tried developing this opportunity of anchoring homogenous catalysts onto a surface.

1.2.1 Isomerism

Isomers are compounds with the same molecular formula but different structural formulas ⁴. Isomers do not necessarily share similar chemical properties, but in some cases where they also share the same functional groups, similar properties may be observed. There are two main forms of isomerism: structural isomerism and stereoisomerism (spatial isomerism). In structural isomers the complexes have the same number and type of atoms, but the atoms and functional groups are joined together in different ways ⁴. Structural isomers have different IUPAC names and may or may not belong to the same functional group ⁵. This group includes chain isomerism whereby hydrocarbon chains have variable amounts of branching; position isomerism which deals with the position of a functional group on a chain; and functional group isomerism in which one functional group is split up into different ones ⁴. In stereoisomers the bond structure is the same, but the geometrical positioning of atoms and functional groups in space is different. This class of isomers includes enantiomers where different isomers are non-superimposable mirror-images of each other, and diastereomers when they are not ⁶. That covers the different classes of isomers; stereoisomers, enantiomers and geometrical isomers.

Diastereo-isomerism is again subdivided into *cis* and *trans* isomers, which have restricted rotation within the molecule (typically isomers containing a double bond) and "conformational isomers" (conformers), which can rotate about one or more single bonds

within the molecule ⁶. In our case we will be looking at the epoxidation of *trans* alkenes, but there is much debate as to the effectiveness of using *cis* vs. *trans* alkenes. For compounds with more than two substituents E/Z notation is used instead of *cis* and *trans*.

In octahedral coordination compounds, facial and meridional isomerism occurs. The isomers can be fac- (with facial ligands) or mer- (with meridional ligands) ⁶. Although conformers can be referred to as stereoisomers, they are not stable isomers, since bonds in conformers can easily rotate thus converting one conformer to another which can be either diastereomeric or enantiomeric to the original one ⁶. While structural isomers typically have different chemical properties, stereoisomers behave identically in most chemical reactions, except in their reaction with other stereoisomers ⁶. Some stereoisomers also differ in the way they rotate polarized light.

One of the main goals for the types of catalysts studied here (Cr(salen) epoxidation catalysts) is to produce a pure enantiomer. Enantiomers are two isomers that are mirror images of each other; a mixture of both of these enantiomers is a racemic mixture ⁶. In synthetic chemistry and the pharmaceutical industry it can be imperative to obtain products that are pure and of the desired isomer ⁷, the 'enantiomeric excess' (ee) of a substance is a measure of how pure it is. In this case, the impurity is the undesired enantiomer (the "opposite-handed" mirror image of a chiral compound). These isomers are chiral, meaning that they possess a non-super imposable mirror image. Chirality is often caused by the presence of an asymmetric carbon atom (a carbon atom with four different groups attached) ⁶. Chirality is a mathematical approach to the concept of "handedness". Molecular chirality is of interest because of its application to stereochemistry in inorganic chemistry, organic chemistry, physical chemistry, biochemistry, and supramolecular chemistry. The importance of stereochemistry in drug action is gaining greater attention in medical practice. Many of the drugs currently used in psychiatric practice are mixtures of enantiomers ⁸. For some therapeutics, single-enantiomer formulations can provide greater selectivities for their biological targets, and improved therapeutic indices than a mixture of enantiomers⁸. We will be looking at catalysts that have the potential to produce optically pure isomers (or at least favouring one isomer) and for which it is key to understand its function in detail in order to improve catalysts efficiency and produce targeted catalysts.

Optimisation of catalytic systems requires a fundamental and detailed understanding of the processes taking place at the catalyst. This means the determination of the structures of the catalytically active sites and species ⁹. We hope to use a combination of techniques

in this study to bring us closer to achieving this aim. Some of the techniques commonly used to characterise catalyst species are: UV-vis spectroscopy; this technique involves photons in the UV-visible region and is commonly used in the quantitative analysis of solutions containing transition metals and highly conjugated organic compounds. The absorption of ultraviolet/visible radiation by a molecule leads to transitions among the electronic levels, for this reason this technique is also referred to as electronic spectroscopy ¹⁰.

Infrared (IR) spectroscopy is an extremely powerful tool for analytical purposes, although IR is useful for both qualitative and quantitative analysis it is best used in conjunction with complementary techniques. When looking at IR spectra it is possible to identify characteristic bands that correspond to certain functional groups, this is because the absorption of infrared radiation for particular functional groups occurs over definite, and easily recognisable, frequency intervals ¹¹. The positions of these characteristic group frequencies can be affected by their environment, for example the electronegativity of neighbouring groups and the spatial geometry of the molecule (steric effects) can affect the bond angles ¹¹. The absorption bands seen in the spectra can arise from both functional groups and the skeletal back bone of the molecule. The intensity of a band due to a particular functional group also depends on how many times that functional group occurs in the sample, the solvent used and also on the neighbouring atoms ¹¹. With so many factors influencing the spectra it is important that you either know which bands you are looking for (which is ok with reference samples) or you need to use a combination of techniques.

With XAS/ XES we are able to obtain information that is similar to that obtained in the standard characterisation techniques with the added advantage of element specificity. Combining XAS/ XES data with techniques like UV-vis will yield a wealth of valuable information about the electronic structure of unknown species.

1.2.2 Asymmetric epoxidation

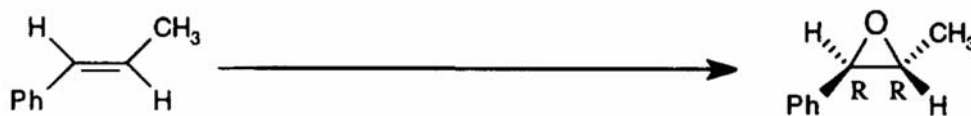


Figure 1 A simplification of the epoxidation reaction, showing the alkene starting material and the epoxide product.

The Sharpless epoxidation¹² reaction is an enantioselective chemical reaction to prepare 2,3-epoxyalcohols from primary and secondary allylic alcohols. The catalytic asymmetric epoxidation of isolated alkenes has been an important goal of synthetic chemistry since the work of Sharpless^{12a, 13}. This is because of the synthetic uses of the products, producing enantiomerically pure products is of importance, especially in drug synthesis^{7, 14}. For this reason the use of catalysts effective in asymmetric synthesis is on the increase. Currently this is an increasingly popular application for the salen family of materials, they have shown to be effective for this purpose. The first use of chiral metal-salen complexes for catalytic asymmetric epoxidation seems to have been the vanadium catalysed oxidation of sulphides reported by Fujita¹⁵. Later the use of cobalt-based catalysts for styrene oxidation was reported by Nishinaga¹⁶. But it was not until Jacobsen¹⁷ and subsequently Katsuki¹⁸ reported the chiral manganese-salen catalysts that significant success was achieved in catalytic asymmetric alkene epoxidation.

The asymmetric epoxidation is an important reaction in organic synthesis and therefore of great interest to the pharmaceutical industry¹⁹. Epoxides are valuable intermediates for the stereo-controlled synthesis of complex organic compounds, and their utility has expanded dramatically with the advent of practical asymmetric catalytic methods for their synthesis¹³. If we can identify the structural, geometric and electronic causes behind the differences in rate and selectivity, this opens up the possibility of tailoring catalysts for specific applications. Most of the work carried out in the area of asymmetric epoxidation of alkenes has been based on either metal-porphyrin or metal-salen complexes^{17a, b}. After the initial reports by Jacobsen¹⁷ and subsequently Katsuki¹⁸ there was a lot of development work carried out by Jacobsen^{17b}; who has shown that the epoxidation of certain *cis*-disubstituted alkenes can be achieved with high ee in a system with bleach as the oxygen source. He has also shown that *trans*-epoxides can be generated with high ee starting with the *cis*-alkenes²⁰. Stereoselective synthesis, which aims to control configurations of the products, has been a remarkable success story²¹.

1.2.3 Salen catalysts

The study of these metal(salen)-mediated epoxidation reactions is becoming increasingly popular ²² both in terms of determining the mechanistic pathways ²³ as well as the practical improvements ²⁴. The biological activity of many pharmaceutical compounds and agrochemicals and the nature of many fragrances and flavours are associated with their absolute configuration ^{7, 14}. The demand on the pharmaceutical industry to make chiral drugs in their enantiomerically pure form is growing. This is because of the varying effects of one enantiomer over the other in certain compounds; it is often desirable if not crucial that one form is produced over the other ^{7, 25}. In this context chemical industries are increasingly more engaged in 'Chirotechnology' ²⁶. Asymmetric catalysis is an economical way to introduce asymmetry, and most asymmetric catalysts consist of metal complexes with chiral ligands ²⁷. Discovering new asymmetric catalysts is a challenge that combines organic, inorganic, organometallic and bio-mimetic chemistry ²⁷. In order to develop efficient transition metal catalysts, there are a number of things that need to be considered, such as; design and synthesis of chiral ligands, matching of ligands with the right metal or suitable substrate and searching for the appropriate reaction conditions ²⁷. The ability to carry out such work represents a critical aspect for developing highly efficient chiral catalysts. The family of chiral salen ligands are, in the opinion of some scientists, the most powerful chiral ligands currently utilised ²⁷. This is due to the fact that they are easy to synthesise and modify by small substitutions on the framework itself. This opens up a wealth of opportunity in terms of steric and electronic tuning of the compounds.

As well as salen materials, similar studies have been carried out using Schiff bases. These are compounds with a functional group that contains a carbon-nitrogen double bond with the nitrogen atom connected to an aryl or alkyl group, not hydrogen ²⁸. Schiff bases are popular due to the fact that, like the salen family, they are appealing frameworks for a tailored catalyst design ²⁹. Chiral Schiff bases are sterically well defined and kinetically non-labile. The synthesis of a large variety of Schiff bases is relatively easy, and when coordinated to a metal the introduction of stereogenic centres near the metal makes the transmission of the stereochemical information more feasible ³⁰.

We will focus on the use of salen materials as asymmetric catalysts in this study. The use of metal complexes with chiral salen ligands in asymmetric synthesis has been wide spread over the past decade or so^{29b}, but the general scientific interest in the metallo-salen complexes has been apparent for more than 80 years. There have been numerous studies

with different transition metals at the catalyst centre, these include; ruthenium, zinc, titanium, vanadium, cobalt, aluminium, chromium, manganese. The choice of metal often depends on the desired application; for example Mn-catalyzed asymmetric epoxidation and Co-catalysed hydrolytic kinetic resolution processes are currently practiced on industrial scale ³¹; whereas Co(salen) catalysts are effective in epoxide ring opening reactions ³¹. Most of the previous work referenced in this study is based on the mechanistic work on manganese and chromium based catalysts. For this study we will also be focusing on chromium systems and the comparison to its manganese analogues.

Perhaps the most prominent of all reactions studied has been the manganese-salen-catalysed asymmetric epoxidation of conjugated α -alkenes; these have been studied extensively by Jacobsen and Katsuki ³². The pioneering study into these Cr(III)-Schiff base complexes was published in 1970 by Coggon *et al.* More recently Jacobsen *et al* have described an alternative approach to the preparation of chromium-Schiff base species with the aim of obtaining a high level of reproducible catalytic activity in several asymmetric reactions ³³. The first reported application of chromium-salen materials was as the promoting agent in catalytic reactions, which was published by Kochi and co-workers in 1983 ³⁴. Chiral Cr(salen) complexes were considered less effective in performing enantioselective epoxidation reactions until Gilheany and co-workers discovered that the epoxidation of trans-olefins could be efficiently carried out in the presence of stoichiometric and catalytic amounts of stable oxo Cr(salen) complexes and iodosylbenzene as the oxygen source ³⁵. This reaction forms the basis of our research into the catalytic process. There have been numerous mechanistic pathways proposed for this reaction (figure 3), with different pathways proposed to explain different results. To understand these observations we must look to the structural and electronic information from these studies to try to assign a mechanism to the reaction.

The general catalytic effectiveness of salen systems has already been explored with both manganese and chromium as the transition metal centre, and the validity of these materials as efficient catalysts has already been proven. However, in order to find out more about the reaction mechanism itself, we need to look at the chromium series alone. The manganese-based system shows a wider spectrum of reactivity ³⁶ and therefore has generally been found to be more useful practically. On the other hand, the stoichiometric variant of the chromium system is easily studied since the oxo complex is isolable ³⁶, whereas the manganese analogue is only observed as a short-lived intermediate ³⁷. We are also able to study the stoichiometric reaction with the chromium series; this means that we eliminate any catalytic effects.

However, the major difference between the Cr and Mn analogues is in their different substrate selectivity in asymmetric epoxidation. Manganese salen complexes show high enantioselectivities in the epoxidation of *Z* alkenes, but *E* alkenes are poor substrates³⁸. Chromium-salen complexes show the opposite characteristics³⁹, and for this reason we will look at *trans* alkene epoxidation for the Cr series.

When using β -methylstyrenes as substrates, O'Mahony and co-workers produced the first example^{35a} of higher asymmetric induction in the case of the *trans(E)*-alkene over its *cis(Z)*-counterpart using chromium-salen-oxo complexes as the catalyst. Other minor differences between the two metals include the greater effect of O-donor ligand additives in the chromium series; the type of oxidant, which is more variable in the manganese series; and the nature of the substituents on the salen rings: Chromium requires electron withdrawing substituents for reasonable rates, but these need not be bulky, in contrast to the manganese case^{39a}. It has been found that the stereochemistry of Cr-catalysed epoxidation was strongly dependent upon the solvent and the donor ligand used, differing from that of the Mn-catalysed epoxidation⁴⁰. It is known that the stereochemistry of radical reactions is not strongly affected by polarity of the solvent used. The Mn-catalysed epoxidation gives the same enantiomer, regardless of the solvent used⁴⁰. However, the stereochemistry of the ionic reactions is affected by the polarity of the solvent. The stereochemistry of the Cr-salen catalysed epoxidation was found to be highly solvent dependent⁴⁰. To achieve highly enantioselective asymmetric epoxidation further modification of the Cr-salen catalyst and optimisation of the reaction conditions are required⁴⁰.

It has been discussed that the chromium mechanism is in fact different to manganese (electrophilic vs. radical) with rates for *trans*-alkenes greater than *cis* and with better diastereoselectivity. Epoxidation with Mn-salen complexes as a catalyst has been proposed to proceed through metallaoxetane and radical intermediates in tandem^{18b, 41}. In contrast, epoxidation with a Cr-salen complex in acetonitrile has been proposed to proceed via a cationic intermediate⁴². We have used acetonitrile as the solvent but previous catalytic studies have shown that dichloromethane had similar results and did not appear to affect the catalytic results^{35a, 43}. The scheme for the Cr mediated alkene epoxidation is shown below.

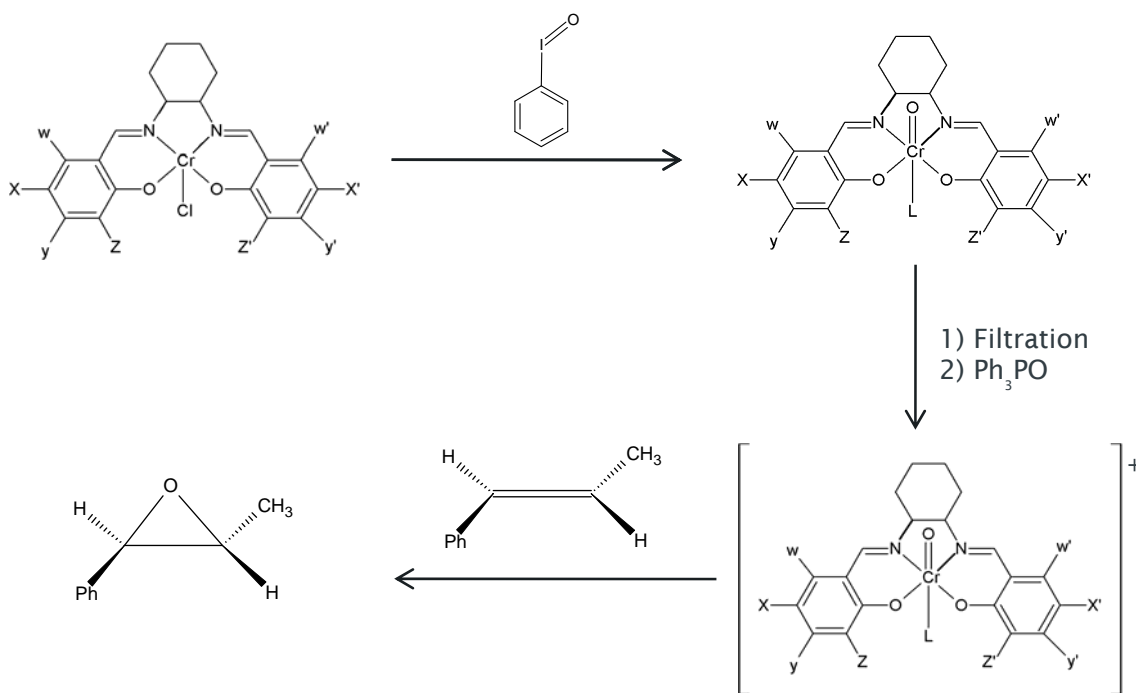


Figure 2 Reaction scheme showing the Cr(salen) mediated alkene epoxidation of *trans*-alkene, proceeding via a cationic intermediate

Figure 2 shows the species involved in the Cr mediated epoxidation, this is the reaction that we will be studying later on in this research project. In the first step the cationic Cr species is formed, we then substitute the Cl atom for a different ligand (Ph_3PO in our case). The alkene is then added for epoxidation. The chromium-salen catalysed epoxidation is of particular interest because i) the stoichiometric variant of the reaction gives a rare opportunity to study stereo-selection in a catalytic process in the absence of factors related to the catalytic cycle; ii) the chromium mechanism is completely different to manganese (electrophilic vs radical) with rates for *trans*-alkenes greater than for *cis* and with better diastereoselectivity^{35a}; iii) additives seem to affect the rates and product mix which leads us to the concept of *ligand accelerated catalysis*⁴⁴ so that if the additives were chiral, better selection might be possible^{35a}. These findings have implications for the mode of stereoselection in epoxidation using metal-salen complexes.

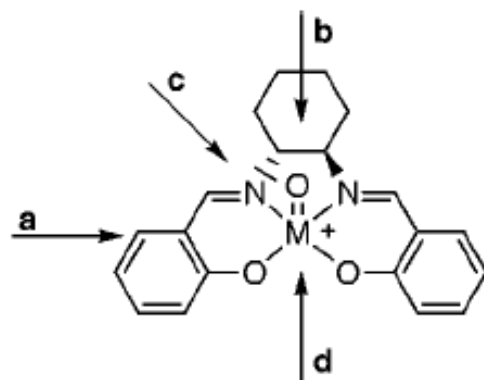


Figure 3 Approach trajectories towards the Cr=O bond⁴³.

From previous studies there are a few approach pathways often considered for the epoxidation of alkenes; one of the more popular ones being the side-on approach model ^{17a, b, 18c, 45}. The other pathways of approach that have been postulated are shown in the diagram in figure 3. Each of these has been proposed at one time or another to explain the different experimental results observed with different substrates.

The side-on approach results in a less hindered approach for the *cis*-alkene, the metal(salen) framework is a rigid, non-labile, structure that happens to be fairly flat (regardless of the metal centre) and so this is the route that is less sterically hindered for the alkene. For this reason the fact that *cis*-alkenes showed the best enantioselectivity in epoxidation was not surprising. This idea was originally proposed by Groves ^{17a, 46} and became a useful working model in the design of transition metal based epoxidation catalysts ^{17b}. If in fact the side-on approach mechanism is taking place then it can be assumed that the epoxidation of *trans*-alkenes with high ee's will always provide a challenging problem. One of the pieces of evidence to support the fact that the mechanisms are different for the Cr and Mn catalysts is the fact that the Cr(salen) catalysts are effective in the epoxidation of *trans*-alkenes, meaning that there must be a method of approach other than side-on ^{35a}.

The work by O'Mahony *et al* called into question the side-on approach model for chromium systems because for chromium, higher asymmetric induction was observed with the *trans*-alkene ⁴³. They therefore proposed another explanation for these Cr systems to explain the fact that Cr(salen) catalysts are effective at epoxidising *trans* alkenes, i.e. that the Cr complex was non-planar with a stepped conformation, allowing for a better steric interaction. This gained some support by other research groups ^{41b, c}

47. It has also been postulated that the mechanism may consist of two molecules of catalyst being involved in the rate determining step⁴⁸. Paddock and Nyugen proposed bi-metallic (di-nuclear) pathways for the production of cyclic carbonates⁴⁹. In the manganese series, and within the side-on approach model, all possible alkene trajectories to the oxo-complex have previously been used as a basis for explaining enantioselectivity³². Jacobsen^{22c}, assuming a flat geometry, considers alkene approach to the metal-oxo bond along either pathway 'a' or 'b' (see figure 3). Which one occurs depends on the nature of the imine bridge and on the presence or absence of large groups at the X-position, pathway 'b' applying to the tetra-*tert*-butyl catalyst (Jacobsens catalyst)⁴³. Early on in the development of this area of study, Katsuki proposed approach 'c' to explain a number of results that were not adequately accommodated by approach 'b'⁵⁰. This theory held when he proposed the non-planar (stepped) geometry of the complex^{41b}. It is more difficult to retain pathway 'b' in a non-planar geometry because the most commonly proposed deviation from planarity is the stepped conformation. Pathway 'b' suffers from some unlikely steric interactions⁴³. Figure 3 also contains an alternative approach; pathway 'd', Houk suggested this approach 'd' for a non-planar complex'⁵¹. In the study by Colm P. O'Mahony *et al* the approach mechanism that is favoured for the chromium system is pathway 'd' with the stepped (non-planar) conformation of the complex³².

A non-planar geometry was postulated, assuming a greater deviation from planarity in the Cr series than in the Mn series, this was to explain the better results for *trans*-alkenes⁴³. Also the fact that the substituents at the Z- position had an affect on the enantioselectivity⁴³ suggested that they had more than a simple blocking role. O'Mahony *et al* proposed that when molecular models are examined there is a natural pathway of approach (based on steric factors) for the *trans*-alkene along 'd', which favours high enantioselection for the observed enantiomer⁴³. It is also thought that approach along 'c', similar to that suggested by Katsuki^{18c, 50} may be in operation at the same time⁴³ as this also gives the correct sense of stereoselection.

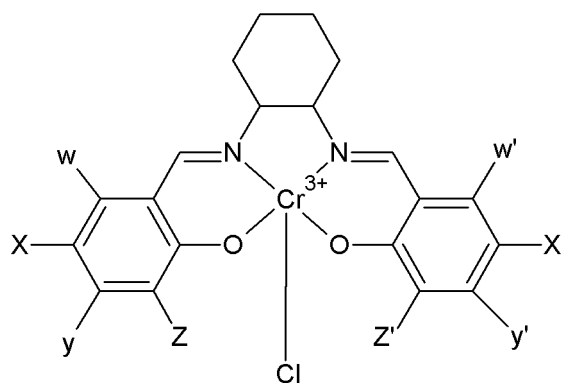


Figure 4 An example of the Cr(salen) complexes that are under investigation in this study. The figure highlights the different locations for substitution on the salen ring.

The first difficulty when examining the Cr series is that the reaction rates are slow with the unsubstituted salen ligand complexes and only alkenes that are electron rich are epoxidised, as the reaction mechanism is thought to be an electrophilic attack of the chromium on the alkene ⁴². This can be avoided by introducing electron withdrawing groups into the structure, essential for reasonable rates in the Cr series ^{35a, 42}. The need for stereoselective reactions to take place close to the stereocontrolling influence limits the distance through which stereocontrol can take place to some four or five bond lengths ³⁰. This should be fine in our case as the changes to the structure are located four bonds from the Cr atom.

The work by O'Mahony *et al* found that in the stoichiometric asymmetric epoxidation of *E*- β -methylstyrene with chromium-salen oxo complexes (with donor ligand L), enantioselectivity is increased by halo-substitution at the 3,3'- (Z) and 6,6' (W)- positions and decreased at the 4,4' (Y)- and 5,5' (X)- positions on the salen rings ⁴³. They also found that by changing the substituent at the 3-3' (Z) positions it is possible to alter the reaction time and the selectivity. It was initially thought that adding bulky alkyl groups in the Z-position lead to high ee whilst the presence of electron withdrawing groups (halogens) was essential for good reaction rates. In contrast to the previous observation it has since been found that any Z- substituent was sufficient to induce high ee, rather than specifically a bulky one ⁴³. The introduction of a chloro substituent in the Y-position has been found to cause either no change or a reduction in selectivity ⁴³. The same study also shows that a halogen in the X-position is either irrelevant or detrimental. It is as yet unclear as to why these effects are observed, this may be something that can be explained by studying the electronic structure and the interaction of the molecular orbitals in these ligand structures.

In the presence of Ph_3PO as the donor ligand (L) attached to the Cr(salen) framework (see figure 2), the larger halogen substituents at the salicylaldehyde portion of the salen framework have an increasingly negative effect on ee⁴³. The work by Ramin *et al* found that the substitution (at the salicylaldehyde part of the salen structure) position seemed to have a stronger influence on the activity than the structure of the side chain itself⁵². What they observed was that substitution in the *ortho* (Z or 3) position of the hydroxyl group on the salen framework hampered the reaction much more than substitution in the *meta* (Y or 4) position. The influence of a group in the *ortho* (Z or 3) position is much bigger than a corresponding substitution in the *para* (X or 5) position, though the double ^tBu substituted catalyst showed no additional decrease in activity compared to the mono-substituted catalyst⁵². Similar results were also achieved by Lu *et al*⁵³. This implies that the impact of substitution could be more related to steric factors than to the solubility or the electronic properties of the different ligands. So far we have seen evidence of both; some studies show that different enantioselectivities are observed with different types of ligands and some are showing that any substituent in a certain position has the same effect.

Reaction conditions have also been found to have an effect on the outcome of the catalytic process. For example O'Mahony *et al* highlighted that the addition of Ph_3PO as the donor ligand (L) significantly increases selection with 3,3'- or 5,5'-substituents but not with 4,4'- or 6,6'- substituents. Also the use of a nitrate counterion was observed to be beneficial in most cases⁴³. The different counterions will have an effect on the axial M=O bond strength, a weaker M=O bond will in theory lead to a faster oxidation rate of the alkene²⁷. So in line with the observations of a beneficial effect of nitrate and Ph_3PO as donor ligands, they probably cause a weakening of the M=O bond. The donor ligand (L) can also have an effect on the enantioselectivity, as well as the substituents at the 3-3' positions on the salen ring. Ph_3PO (L) was found to be the best behaved donor ligand (L) by Colm P. O'Mahony *et al*, being the most consistent in raising the ee⁴³. The increased stereoselection in the system could also be due to the attainment of a conformation that is promoted both by Z-substitution and by the donor ligand, L. In complexes with suitable Z- substituents, the conformation without L reaches an optimum, and the effect of L is thus minimal⁴³. These conformations are caused by the steric influence of the substituents at the salen framework; this can then have an effect on the approach of the alkene. A number of asymmetric catalytic oxidation reactions can be controlled by the presence/absence of coordinating additives. This shows the importance of weak bonding interactions on the effectiveness of salen and [M(salen)] frameworks. Some observations by Imanishi and Katsuki⁴⁰ of the interesting stereochemistries in Cr-catalysed epoxidation

in different solvents of varying polarity led to the following explanations i) Cr-complex gives different active species in toluene and acetonitrile and ii) Cr-catalysed epoxidations in toluene and acetonitrile proceed through different intermediates ⁴⁰. It has already been established that treatment of Cr-salen complexes with iodosylbenzene in acetonitrile gives the corresponding(salen)Cr=O (oxo) species. On the other hand an iron(III)-porphyrin complex has been reported to form a complex with iodosylbenzene (PhIO) in dichloromethane ⁵⁴. This led them to believe that a similar thing may be happening in the case of Cr. Identifying the structure of the intermediate is of high importance. The possibility of studying the stoichiometric reaction for the Cr series and isolating the intermediates makes it possible to gain insights into the reaction mechanism and differentiate between the previously proposed mechanisms ⁴³.

Katsuki and coworkers have introduced a new class of chiral metallo-salen complex in which the salen units are folded ⁵⁵. This folding amplifies the asymmetric induction in the catalytic reactions. The chirality induced by the folding of the salen skeleton is controlled by the stereogenic centres of the ethylenediamine moiety ²⁷.

1.2.4 Other Uses for Salen Materials

Although cationic [Cr(salen)] complexes can be utilised as precursors for the synthesis of chromium-oxo species ⁵⁶, their utility in promoting other asymmetric catalysed reactions has been demonstrated too ^{29b}. For instance, chiral cationic tetradentate [Cr(III)(salen)] complexes are able to catalyse the asymmetric hetero Diels-Alder (HAD) reaction between 1-methoxy-3-[(trimethylsilyl)oxy]buta-1,3-diene and carbonyl compounds in a highly stereocontrolled manner ⁵⁷. Cr(salen) complexes are highly effective catalysts for a number of different synthetic processes, the first of those being for the ring opening of epoxides. Another area in which Cr(salen) materials play an important role is the copolymerisation reaction of carbon dioxide and epoxides ⁵⁸. There has been much emphasis in this area of research due to the economic and environmental benefits of carbon dioxide as a C₁ feedstock. The air-stable, chiral (salen) Cr(III)Cl complex has been shown to be an effective catalyst for the coupling of cyclohexene oxide and carbon dioxide to afford poly(cyclohexenylene carbonate). The work by Darensbourg *et al* suggested the involvement of a concerted attack of epoxide at the axial site of the chromium(III) complex where the growing polymer chain for epoxide ring opening resides ⁵⁸, this is similar to approach pathway 'd' (figure 3). [Cr(salen)Cl] is also effective in promoting the asymmetric ring-opening of meso-epoxides by TMSN₃ ⁵⁹. The supposed asymmetric ring-

opening mechanism involves an activated epoxide coordinated to the [M(salen)] complex. Among all the organometallic systems screened, [Cr(salen)] emerged naturally as the more efficient catalyst even if coordination geometries of the analogous systems are quite similar⁶⁰. Another synthetic application is in the preparation of propylene carbonate dioxide as a building block⁵². Homogeneous chromium-salen complexes were reported as active homogeneous catalysts for carbon dioxide fixation^{49, 58, 61}. A next step can be to develop heterogeneous salen catalysts by exploring the concept of immobilisation. The work by Ramin *et al*⁵² demonstrates the effectiveness of grafting these complexes onto silica supports using different immobilisation techniques. In this work they began by testing a series of homogeneous salen catalysts with different salen ligand structures. The most promising homogeneous complexes were then grafted onto a silica support using different immobilisation methods. Studies were then carried out to test the activity and re-usability of the heterogeneous catalysts. The turn over frequency of the immobilised catalyst turned out to be higher to that of the free catalyst⁵². One suggested reason for this behaviour may be the fact that in the immobilised complexes the active site of the catalysts is isolated, whereas the homogeneous complexes may partly agglomerate during reaction. Homogeneous catalysts with comparable catalytic activity were reported in literature to be more active only in the presence of additional solvents⁴⁹.

Enormous possibilities are still open in this area; the design of particular architectures that constrain the salen units in cooperating actions should enhance the stereochemical communication. In theory a chiral space suitable for any kind of reaction could be created²⁷. The wide range of possible applications of such an area of the enantioselective catalytic redox processes is obvious because the properties of the metallo-salen complexes make the preparation of a large variety of chiral organometallic reagents possible²⁷. The scope of introducing immobilisation for effective heterogeneous complexes has been demonstrated by Ramin *et al*. Their work shows the increase in turnover frequency for the immobilised catalyst in comparison to its free analogue, for propylene carbonate formation. This could be due to the site isolation of the immobilised complex (the homogeneous catalyst may partly agglomerate during the reaction). The study identified that only covalently-bound complexes exhibit reasonable stability under reaction conditions. The ease of catalyst separation from the reaction mixture makes this an attractive possibility even in the case of retaining the already good activity achieved with the homogeneous complexes.

The aim for this research project is to prepare a number of systems containing different salen complexes and/or different donor ligands. Both these variables have been reported

to affect the reaction ⁶². The salen complexes will be varied by substitution at the X- and Z- positions. It has been found that the following scheme; Z=CF₃, L=Ph₃PO, A=NO₃ provides the highest ee of 92% for a trans alkene using a metal based reagent ⁴³, with the Z- substituent of CF₃ combining the effects of both a halogen, F, and a sterically bulky group, of increasing ee. The electron-withdrawing groups are required for reasonable rates in the Cr series; we have used a combination of substituents to observe both these effects.

For this study it will be useful to keep reaction times up to a day or two so that we are able to obtain detailed spectroscopic (XAS) data over the course of the reaction. The presence of a second oxo-containing ligand (donor ligand, L) such as Ph₃PO or pyridine-N-oxides was found to be significant, changing the ee attainable by up to 30% ⁶². Ph₃PO (L) has been reported to be the best behaved ligand being the most consistent with raising the ee, DMSO and DMF show similar effects but the elevation is not as high ⁴³. Ph₃PO (L) has therefore been used as the additional ligand in all reactions.

1.3 Spectroscopy

Most of what we know about the structure of atoms and molecules comes from studying their interaction with light (electromagnetic radiation). Different regions of the electromagnetic spectrum provide different kinds of information as a result of different interactions with the sample. Realising that light may be considered to have both wave-like and particle-like characteristics, it is useful to consider that a given frequency or wavelength of light is associated with a 'quantum of electromagnetic radiation' (a photon). In order to observe intermolecular distances, we must use light having a wavelength smaller than the molecule itself (roughly 1 to 15 Å). This kind of radiation is found in the X-ray region of the spectrum.

Spectroscopy is the study of the interaction between matter and radiated energy ⁶, in this study the absorption and emission of light by matter and the dependence of these processes on the wavelength of the radiation. More recently, the definition has been expanded to include the study of the interactions between particles such as electrons, protons, and ions, as well as their interaction with other particles as a function of their collision energy ⁶³. Historically, spectroscopy originated through the study of visible light dispersed according to its wavelength, e.g., by a prism. Later the concept was expanded to comprise any interaction with radiative energy as a function of its wavelength or frequency. Spectroscopic data is often represented by a spectrum, a plot of the response of intensity

as a function of wavelength or frequency. Spectroscopic techniques have been applied in virtually all fields of science and technology.

An important step towards the understanding and prediction of catalyst behaviour is the determination of the structure of the active species and how this changes during the reaction (reaction intermediates). Information about the electronic properties of the electronically excited species is also of great importance because catalyst-reactant interactions are often enhanced due to the charge re-distribution after the initial electronic excitation⁶⁴. This is important for metal catalysis since the overall reactivity is basically a result of the interactions of the metal d-orbitals with the ligand valence orbitals⁶⁴. X-ray Absorption Near Edge Structure spectroscopy (XANES) is a useful tool for studying the electronic states of metal catalysts (see Chapter 2). Information regarding the electronic properties of the excited system in question (active species) is a key factor in understanding and predicting characteristics in transition-metal chemistry.

The large penetration depth of hard X-rays means that measurements can be performed under, in principle, all conditions (including high temperatures and/or pressures), and it thus also allows for *in-situ or operando* experiments⁶⁵. Recently a lot of effort has been put into *in-situ* experimentation and set-ups have been developed to allow a combination of techniques to be used at the same time. This is useful as XAS gives a combination of different types of information and other techniques are able to provide complementary information to help interpret the results. It is therefore possible to perform *in-situ* experiments in combination with complementary techniques such as; infrared⁶⁶, Raman⁶⁷, UV-vis spectroscopy⁶⁸, and X-ray diffraction⁶⁹. The ability to carry out these types of detailed investigations will enable XAS to contribute significantly in the determination of complex structure and its relation to function of materials.

Time-resolved and *in-situ* measurements are important for providing a method of following reactions and measuring changing structures and species present during the reaction as it proceeds. Such experiments are important in the field of catalysis where often the aim is to investigate the structure of the catalytically active site, as well as to obtain kinetic data from the reaction. With the possibility of such fast experiments and data acquisition it is also possible to take measurements (determining electronic and geometric structures) for relatively short lived reaction intermediates, this is what we have tried to achieve later in this study.

Specially-designed cells combined with XANES may provide insight into reaction dynamics and changes in electronic configuration and oxidation state. Performing the reaction under different temperatures and conditions will give insight into dynamics. With the development of fast, continuous-scanning ⁷⁰ beamlines with the capability to scan an entire edge in less than a minute, time-resolved studies are now possible as well. A quick-scanning monochromator continuously cycles through a small energy region while the absorption spectrum is measured. This technique is based on a continuously moving monochromator which allows the user to obtain spectra with a time resolution down to the millisecond. Third generation synchrotron sources are best used for quick-EXAFS since they provide a high photon flux, which is essential for fast measurements to get satisfactory photon statistics ^{70c}. D.

Lutzenkirchen-Hecht *et al* showed the possibility of investigating solid-solid transformations using time dependent X-ray absorption spectroscopy (QEXAFS) on a second scale ^{70a}. This type of measurement allows very small changes of the edge position to be observed with a high degree of accuracy. A number of solid-solid transformations such as decomposition reactions or redox processes of heterogeneous catalysts occur relatively fast (within less than a minute) ^{70a}. In such cases time resolved investigations are necessary in order to gain insight into the mechanisms of these transformations (e.g. during changes of temperature or gas atmosphere).

Ultrafast X-ray absorption spectroscopy (XAS) in combination with short laser and X-ray pulses in a pump/probe scheme has evolved into a powerful and versatile technique to get electronic and structural information about short-lived excited states of molecules in solution [86]. This approach has so far mainly been used for photochemical reactions but is also promising for the detection and characterisation of short lived catalytic reaction intermediates. This set up is increasingly popular with transition metal complexes with various organic ligands [92-95] because you can synchronise the laser and X-rays so you get the spectrum for the tiny amount of time that the molecule is in its excited state. The laser is used to excite the molecule/reaction, and precisely time the XAS to probe this excited state, which is usually very short lived. X-ray absorption spectroscopy using energy dispersive optics has been widely used to study chemical processes as well as very small samples in restrictive environments ⁷¹. One of the advantages of this technique is that the stability of the optics means that the noise level is dramatically reduced ⁷¹. This method has been applied successfully in the fields of biophysics, chemistry and materials science to track rapid changes in the local and electronic structure of absorber atoms in disordered systems ⁷².

Due to experimental advances new developments continue to be made in the field of XAS, providing new and exciting opportunities. The availability of smaller and smaller beams, faster data acquisition and high fluxes at third generation synchrotron light sources allow more sophisticated X-ray experiments to be performed. Advances in theoretical understanding and the development of such approaches in the form of computer software have led to an increased understanding of pre-edge and near-edge regions, although a lot of work has yet to be done and the theory, compared to the experiments, is in its infancy. Many theoretical approaches to XANES spectral analyses have been developed. They can be mainly classified into three groups; those based on the molecular orbital (MO) ⁷³ methods, density functional theory (DFT) ⁷⁴, and multiple-scattering (MS) methods ⁷⁵. Among them, the MS method is the most popular. It has also been applied to the analysis of the spectra in the Extended X-ray Absorption Fine Structure (EXAFS) region ⁷⁶. For example the work by Nakanishi and Ohta shows the use of the FEFF program in simulating the K-edge spectra of the third row transition metals ⁷⁶. The 2p XAS or L-edge spectra are simulated with calculations performed using charge transfer multiplet theory ⁷⁷, this will be discussed more in chapter 2.

While rapid experimental improvements broaden the range of systems and processes that can be studied by time-resolved XAS, continued developments on the data analysis and theory side are necessary to be able to extract precise quantitative chemical information from XAS spectra. In contrast to the Extended X-ray Absorption Fine Structure (EXAFS) region, for which accurate and quantitative results are generally routine, both the calculation and interpretation of X-ray Absorption Near Edge Structure (XANES) have remained challenging tasks. The complications are caused by the relatively low kinetic energy of the photoelectron in this region, resulting in large scattering amplitudes ⁶⁴. The XANES region is also very susceptible to inaccuracies. The lifetime broadening and the applied experimental resolution yield an overall broadening to the spectra; this causes a blurring of the potential fine structure at the pre-edge, making it difficult to analyse. The pre-edge features are also difficult to analyse because they involve both band structure effects and multiplet effects, currently there is not one theoretical approach that includes all effects.

In X-ray Absorption Spectroscopy we are looking at the $1s \rightarrow 4p$ transition, this correlates to the binding energy of a core electron to the nucleus. This is different for every element and is what gives the technique its element specificity. By looking at the XAS we are also able to obtain information on the empty density of states (unoccupied orbitals) above the

Fermi level. In X-ray Emission Spectroscopy we are probing the $2p \rightarrow 1s$ transition. XES follows the initial absorption of a photon and the core hole, which was created in the initial absorption process, is filled by an electron from a higher orbital. The emission spectrum reflects the occupied density of states (below the Fermi level). XAS and XES are directly related to each other and provide common as well as complimentary information on the local structure of materials.

In this study we use a combination of XAS and XES studies in order to unravel the electronic structure at the metal centre, both the XAS and XES processes are element specific (more detail in chapter 2). Because the energies and relative intensities of X-ray emission lines are almost identical for a given element, X-ray Fluorescence (emitted X-ray radiation after the excitation process) is used routinely as an analytical tool for elemental analysis and particle characterisation⁷⁸. Chemical effects on X-ray Fluorescence have been known for many years and often used as a probe of chemical bonding⁷⁹. The largest chemical effects involve valence-core X-ray transitions, which carry information about the occupancy and symmetry of the orbitals involved in chemical bonding (see chapter 2). For transition metal complexes, the $1s$ orbital is tightly localised on the metal centre, and a common assumption is that the fluorescence intensity reflects the amount of metal p -character in a particular orbital⁸⁰.

In order to obtain the structural and electronic information necessary to gain a better understanding of the structure-function relationships of our catalysts, we need to perform a number of detailed X-ray spectroscopy experiments. Such studies can give us information regarding specific electronic transitions within our systems. For example; at the K-edge we will be probing the $1s \rightarrow 4p$ electronic transition, at the L-edge the $2p \rightarrow 3d$ transition and in the RIXS process we will be looking at an overall transition of $2p \rightarrow 3d$ (similar to the L-edge) but in this case it is a two step process consisting of a $1s \rightarrow 3d$ excitation and a $2p \rightarrow 1s$ decay. This will provide complementary information to that of the L-edge XANES experiments. The RIXS experiments produce 2D information; this means that we are able to see the dependencies of different absorption and emission features which will help in understanding the XANES spectra. Chromium possesses a wide range of oxidation states (from -2 to +6), because of this chromium forms chemical bonds with atoms with very different electronegativity values, resulting in large effects on the local electronic structure involving the Cr atoms. Compounds of the first row transition metals are especially interesting from an electronic structure standpoint as they possess remarkably varied physical and chemical properties⁸¹. Spectroscopic methods provide the most direct means for experimentally obtaining information on the resulting electronic

structure. Synchrotron radiation-based inner-shell spectroscopies are element specific techniques that are sensitive to changes in the electronic structure and the local coordination environment of a selected element⁸². This makes X-ray spectroscopy an ideal technique for the study of these catalytic materials.

1.4 Aim of project

Transition metal elements play a crucial role in coordination chemistry (catalysis) and therefore the factors determining the relevant characteristics, such as; coordination number, oxidation state and spin state, are of great importance. In this project we will employ a number of different techniques in order to obtain detailed structural and electronic information for the transition metal in question.

Initially we will carry out a reference study of well defined chromium oxides and chlorides with a range of oxidation states and geometries. We will start by exploring fairly well established techniques (XANES) where surprisingly little is known about the theoretical analysis of the complicated pre-edge region of the XANES spectra, then we will move on to look at relatively new X-ray techniques (RIXS). In the case of the RIXS technique we will be exploring new territory, where in fact the experimental capabilities far outweigh the current position of the theoretical explanation of the data. One of the aims of this project is to obtain and use this information to design catalysts for a specific function, or tailor existing catalysts to improve efficiency.

The final step of the project is to look at the catalytic applications of the salen complexes and to see if we can monitor the subtle electronic effects using XAFS (X-ray Absorption Fine Structure) and RIXS (Resonant Inelastic X-ray Scattering) spectroscopy. The aim of this step of the project is to monitor the catalysis using XAFS and RIXS to see if we can explain, in terms of electronic structure, the catalytic differences observed.

In summary this project has two key themes; i) the first, and primary, task is the development and advancement of the RIXS technique in terms of the information obtained and analysis; ii) the second being the application to catalysis and how we can then maximise efficiencies in existing synthetic processes.

1.5 References

1. Atkins, P.; Overton, T.; Rourke, J.; Weller, M.; Armstrong, F., *Inorganic Chemistry*. 4th Edition ed.; Oxford University Press: New York, 2006; p 680.
2. (a) Adam, W.; Stegmann, V. R.; Saha-Möllner, C. R., *J. Am. Chem. Soc.* **1999**, *121*, 1879; (b) Sheldon, R. A.; Kochi, J. K., *Metal-Catalyzed Oxidations of Organic Compounds*. Academic Press: New York, 1981; (c) Du, X.-D.; Yu, X.-D., *J. Mol. Catal. A: Chem.* **1997**, *126*, 109.
3. (a) Lordi, V.; Yao, N.; Wei, J., *Chem. Mater.* **2001**, *13*, 733; (b) Perego, C.; Ingallina, P., *Catal. Today* **2002**, *73*, 3; (c) Katsuki, T., *J. Mol. Catal. A: Chem.* **1996**, *113*, 87.
4. Atkins, P.; Overton, T.; Rourke, J.; Weller, M.; Armstrong, F., *Inorganic Chemistry*. 4th Edition ed.; Oxford University Press: New York, 2006; p 219.
5. Clayden, J.; Greeves, N.; Warren, S.; Wothers, P., *Organic Chemistry*. Oxford University Press: New York, 2001; p 19.
6. Clayden, J.; Greeves, N.; Warren, S.; Wothers, P., *Organic Chemistry*. Oxford University Press: New York, 2001; p 381.
7. *Chemical Engineering News* **2000**, *78*, 59.
8. McConathy, J.; Owens, M. J., *J. Clin. Psychiatry* **2003**, *5*, 70.
9. Safonova, O. V.; Tromp, M.; van Bokhoven, J. A.; de Groot, F. M. F.; Evans, J.; Glatzel, P., *J. Phys. Chem. B* **2006**, *110*, 16162.
10. Kemp, W., *Organic Spectroscopy*. third ed.; Macmillan Education LTD: 1991.
11. Socrates, G., *Infrared and Raman Characteristic Group Frequencies*. John Wiley & Sons, LTD: London, 2001.
12. (a) Katsuki, T.; Sharpless, K. B., *J. Am. Chem. Soc.* **1980**, *102*, 5974; (b) J. G. Hill, K. B. S., C. M. Exon, and R. Regenye *Organic Syntheses* **1990**, *7*, 461.
13. Johnson, R. A.; Sharpless, K. B., In *Catalytic Asymmetric Synthesis*, 2nd Edition ed.; Ojima, I., Ed. Wiley VCH: New York, 1993; pp 103.
14. Patel, R. N., *Curr. Opin. Biotechnol.* **2001**, *12*, 587.
15. Nakajima, K.; Kojima, M.; Fujita, J., *Chem. Lett.* **1986**, *15*, 1483.
16. Nishinaga, A.; Yamato, H.; Abe, T.; Maruyama, K.; Matsuura, T., *Tetrahedron Lett.* **1988**, *29*, 6309.
17. (a) Collman, J.; Zhang, X.; Lee, V.; Uffelman, E.; Brauman, J., *Science* **1993**, *261*, 1404; (b) Jacobsen, E. N., In *Catalytic Asymmetric synthesis*, Ojima, I., Ed. Wiley: New York, 1993; pp 159; (c) Zhang, W.; Loebach, J. L.; Wilson, S. R.; Jacobsen, E. N., *J. Am. Chem. Soc.* **1990**, *112*, 2801; (d) Jacobsen, E. N.; Zhang, W.; Muci, A. R.; Ecker, J. R.; Deng, L., *J. Am. Chem. Soc.* **1991**, *113*, 7063.
18. (a) Irie, R. I., Y.; Katsuki, T., *Synlett* **1991**, 265; (b) Irie, R.; Noda, K.; Ito, Y.; Matsumoto, N.; Katsuki, T., *Tetrahedron Lett.* **1990**, *31*, 7345; (c) Hamada, T.; Irie, R.; Katsuki, T., *Synlett* **1994**, 479.
19. Pu, L., *Tetrahedron* **2003**, *59*, 9873.
20. Martinez, L. E.; Leighton, J. L.; Carsten, D. H.; Jacobsen, E. N., *J. Am. Chem. Soc.* **1995**, *117*, 5897.
21. Eliel, E. L.; Wilen, S. H., *Stereochemistry of Organic Compounds*. Wiley, New York: 1994.
22. (a) Katsuki, T., *Synlett* **2003**, 281; (b) Katsuki, T., In *Catalytic Asymmetric Synthesis*, 2nd ed.; Ojima, I., Ed. Wiley-VCH: New York, 2000; pp 287; (c) Jacobsen, E. N., Pfaltz, A., Yamamoto, H., In *Comprehensive Asymmetric Catalysis*, Springer-Verlag: Berlin, 1999; pp 649.
23. (a) Abashkin, Y. G.; Burt, S. K., *Org. Lett.* **2003**, *6*, 59; (b) Cavallo, L.; Jacobsen, H., *J. Org. Chem.* **2003**, *68*, 6202; (c) Cavallo, L.; Jacobsen, H., *Eur. J. Inorg. Chem.* **2003**, 892; (d) Ivanic, J., *J. Chem. Phys.* **2003**, *119*, 9377; (e) Khavrutskii, I. V.; Musaev, D. G.; Morokuma, K., *Inorg. Chem.* **2003**, *42*, 2606; (f) Feth, M. P.; Bolm, C.; Hildebrand, J. P.; Köhler, M.; Beckmann, O.; Bauer, M.; Ramamonjisoa,

- R.; Bertagnolli, H., *Chem. Eur. J.* **2003**, *9*, 1348; (g) Bryliakov, K. P.; Talsi, E. P., *Inorg. Chem.* **2003**, *42*, 7258.
24. (a) Kureshy, R. I.; Khan, N. H.; Abdi, S. H. R.; Ahmad, I.; Singh, S.; Jasra, R. V., *J. Catal.* **2004**, *221*, 234; (b) Kureshy, R. I.; Khan, N. H.; Abdi, S. H. R.; Ahmed, I.; Singh, S.; Jasra, R. V., *J. Mol. Catal. A: Chem.* **2003**, *203*, 69; (c) Kureshy, R. I.; Khan, N. H.; Abdi, S. H. R.; Singh, S.; Ahmed, I.; Shukla, R. S.; Jasra, R. V., *J. Catal.* **2003**, *219*, 1; (d) Sellner, H.; Karjalainen, J. K.; Seebach, D., *Chem. Eur. J.* **2001**, *7*, 2873; (e) McNamara, C. A.; Dixon, M. J.; Bradley, M., *Chem. Rev.* **2002**, *102*, 3275; (f) Prasad, J. S.; Vu, T.; Tottleben, M. J.; Crispino, G. A.; Kacsur, D. J.; Swaminathan, S.; Thornton, J. E.; Fritz, A.; Singh, A. K., *Org. Process. Res. Dev.* **2003**, *7*, 821; (g) Lane, B. S.; Burgess, K., *Chem. Rev.* **2003**, *103*, 2457; (h) Bräse, S.; Lauterwasser, F.; Ziegert, R. E., *Adv. Synth. Catal.* **2003**, *345*, 869.
25. FDA'S policy statement for the development of new stereoisomeric drugs. *Chirality* **1992**, *4*, 338.
26. Sheldon, R. A., *J. Chem. Technol. Biotechnol.* **1996**, *67*, 1.
27. Bandini, M.; Cozzi, P. G.; Umani-Ronchi, A., *Chem. Commun.* **2002**, 919.
28. Leigh, G. J.; Favre, H. A.; Metanomski, W. V., *Principles of Chemical Nomenclature*. Blackwell Science: Oxford, 1998.
29. (a) Atwood, D. A.; Harvey, M. J., *Chem. Rev.* **2000**, *101*, 37; (b) Canali, L.; Sherrington, D. C., *Chem. Soc. Rev.* **1999**, *28*, 85.
30. Clayden, J.; Vassiliou, N., *Org. Biomol. Chem.* **2006**, *4*, 2667.
31. Larrow, J. F.; Jacobsen, E. N., In *Organometallics in Process Chemistry*, Springer Berlin / Heidelberg: 2004; Vol. 6, pp 123.
32. Dalton, C.; Ryan, K.; Wall, V.; Bousquet, C.; Gilheany, D., *Top. Catal.* **1998**, *5*, 75.
33. Jacobsen, E. N.; Schaus, S. E.; Dossetter, A. G.; Jamison, T. F. US 6,211,370 2001.
34. (a) Siddall, T. L.; Miyaura, N.; Huffman, J. C.; Kochi, J. K., *J. Chem. Soc., Chem. Commun.* **1983**, 1185; (b) Srinivasan, K.; Kochi, J. K., *Inorg. Chem.* **1985**, *24*, 4671.
35. (a) Bousquet, C.; Gilheany, D. G., *Tetrahedron Lett.* **1995**, *36*, 7739; (b) Daly, A. M.; Cormac, D. T.; Renehan, M. F.; Gilheany, D. G., *Tetrahedron Lett.* **1999**, *40*, 3617.
36. Samsel, E. G.; Srinivasan, K.; Kochi, J. K., *J. Am. Chem. Soc.* **2002**, *107*, 7606.
37. Campbell, K. A.; Lashley, M. R.; Wyatt, J. K.; Nantz, M. H.; Britt, R. D., *J. Am. Chem. Soc.* **2001**, *123*, 5710.
38. (a) Eoin F. Clarke; Eoghan M. McGarrigle; Gilheany, D. G., *ARKIVOC* **2005**, *5*, 30; (b) Dalton, C. T.; Ryan, K. M.; Langan, I. J.; Coyne, E. J.; Gilheany, D. G., *J. Mol. Catal. A: Chem.* **2002**, *187*, 179.
39. (a) Brandt, P.; Norrby, P.-O.; Daly, A. M.; Gilheany, D. G., *Chem. Eur. J.* **2002**, *8*, 4299; (b) Kerrigan, N. J.; Langan, I. J.; Dalton, C. T.; Daly, A. M.; Bousquet, C.; Gilheany, D. G., *Tetrahedron Lett.* **2002**, *43*, 2107.
40. Imanishi, H.; Katsuki, T., *Tetrahedron Lett.* **1997**, *38*, 251.
41. (a) Srinivasan, K.; Michaud, P.; Kochi, J. K., *J. Am. Chem. Soc.* **1986**, *108*, 2309; (b) Hamada, T.; Fukuda, T.; Imanishi, H.; Katsuki, T., *Tetrahedron* **1996**, *52*, 515; (c) Norrby, P.-O.; Linde, C.; Aakermark, B., *J. Am. Chem. Soc.* **1995**, *117*, 11035.
42. Samsel, E. G.; Srinivasan, K.; Kochi, J. K., *J. Am. Chem. Soc.* **1985**, *107*, 7606.
43. O'Mahony, C. P.; McGarrigle, E. M.; Renehan, M. F.; Ryan, K. M.; Kerrigan, N. J.; Bousquet, C.; Gilheany, D. G., *Org. Lett.* **2001**, *3*, 3435.
44. Jacobsen, E. N.; Marko, I.; Mungall, W. S.; Schroeder, G.; Sharpless, K. B., *J. Am. Chem. Soc.* **1988**, *110*, 1968.
45. Chang, S.; Galvin, J. M.; Jacobsen, E. N., *J. Am. Chem. Soc.* **1994**, *116*, 6937.
46. (a) Groves, J. T.; Nemo, T. E.; Myers, R. S., *J. Am. Chem. Soc.* **1979**, *101*, 1032; (b) Groves, J. T.; Myers, R. S., *J. Am. Chem. Soc.* **1983**, *105*, 5791; (c) Groves, J. T.; Han, Y.; Van Engen, D., *J. Chem. Soc., Chem. Commun.* **1990**, 436.
47. (a) Hashihayata, T.; Ito, Y.; Katsuki, T., *Synlett* **1996**, 1079; (b) Hashihayata, T.; Ito, Y.; Katsuki, T., *Tetrahedron* **1997**, *53*, 9541.

48. Hansen, K. B.; Leighton, J. L.; Jacobsen, E. N., *J. Am. Chem. Soc.* **1996**, *118*, 10924.
49. Paddock, R. L.; Nguyen, S. T., *J. Am. Chem. Soc.* **2001**, *123*, 11498.
50. Hosoya, N.; Hatayama, A.; Yanai, K.; Fujii, H.; Irie, R.; Katsuki, T., *Synlett* **1993**, 641.
51. Houk, K. N.; DeMello, N. C.; Condroski, K.; Fennen, J.; Kasuga, T. Electronic Conference on Heterocyclic Chemistry '96, ECHET96, Rzepa, H. S., Snyder, J., and Leach, C. (Eds), Ed. Royal Society of Chemistry: 1996.
52. Ramin, M.; Jutz, F.; Grunwaldt, J.-D.; Baiker, A., *J. Mol. Catal. A: Chem.* **2005**, *242*, 32.
53. Lu, X.-B.; Xiu, J.-H.; He, R.; Jin, K.; Luo, L.-M.; Feng, X.-J., *Appl. Catal., A* **2004**, *275*, 73.
54. Machii, K.; Watanabe, Y.; Morishima, I., *J. Am. Chem. Soc.* **1995**, *117*, 6691.
55. Hashihayata, T.; Punniyamurthy, T.; Irie, R.; Katsuki, T.; Akita, M.; Moro-oka, Y., *Tetrahedron* **1999**, *55*, 14599.
56. Adam, W.; Hajra, S.; Herderich, M.; Saha-Möllner, C. R., *Org. Lett.* **2000**, *2*, 2773.
57. Schaus, S. E.; Branalt, J.; Jacobsen, E. N., *J. Org. Chem.* **1998**, *63*, 403.
58. Darensbourg, D. J.; Yarbrough, J. C., *J. Am. Chem. Soc.* **2002**, *124*, 6335.
59. Jacobsen, E. N., *Acc. Chem. Res.* **2000**, *33*, 421.
60. (a) Sigman, M. S.; Jacobsen, E. N., *J. Am. Chem. Soc.* **1998**, *120*, 5315; (b) North, M.; Orizu, C.; Tararov, V. I.; Ikonnikov, N. S.; Belokon, Y. N.; Hibbs, D. E.; Hursthouse, M. B.; Abdul Malik, K. M., *Chem. Commun.* **1998**, 387; (c) Coggon, P.; McPhail, A. T.; Mabbs, F. E.; Richards, A.; Thornley, A. S., *J. Chem. Soc. A.* **1970**, 3296.
61. Darensbourg, D. J.; Mackiewicz, R. M.; Rodgers, J. L.; Phelps, A. L., *Inorg. Chem.* **2004**, *43*, 1831.
62. Ryan, K. M.; Bousquet, C.; Gilheany, D. G., *Tetrahedron Lett.* **1999**, *40*, 3613.
63. Chu, S.; Graybeal, J. D.; Hurst, G. S.; Stoner, J. O., In *Encyclopædia Britannica*, internet, 2008.
64. van der Veen, R. M.; Kas, J. J.; Milne, C. J.; Pham, V.-T.; Nahhas, A. E.; Lima, F. A.; Vithanage, D. A.; Rehr, J. J.; Abela, R.; Chergui, M., *PCCP* **2010**, *12*, 5551.
65. Bron, M.; Teschner, D.; Knop-Gericke, A.; Scheybal, A.; Steinhauer, B.; Hävecker, M.; Födisch, R.; Hönicke, D.; Schlögl, R.; Claus, P., *Catal. Commun.* **2005**, *6*, 371.
66. Anderson, J. A.; Liu, Z.; García, M. F., *Catal. Today* **2006**, *113*, 25.
67. Choi, H. C.; Jung, Y. M.; Noda, I.; Kim, S. B., *J. Phys. Chem. B* **2003**, *107*, 5806.
68. Mesu, J. G.; van der Eerden, A. M. J.; de Groot, F. M. F.; Weckhuysen, B. M., *J. Phys. Chem. B* **2005**, *109*, 4042.
69. Günter, M. M.; Ressler, T.; Jentoft, R. E.; Bems, B., *J. Catal.* **2001**, *203*, 133.
70. (a) Lützenkirchen-Hecht, D.; Grunwaldt, J. D.; Richwin, M.; Griesebock, B.; Baiker, A.; Frahm, R., *Phys. Scr.* **2005**, 831; (b) Erbil, A.; Cargill III, G. S.; Frahm, R.; Boehme, R. F., *Phys. Rev. B: Condens. Matter* **1988**, *37*, 2450; (c) Stotzel, J.; Lützenkirchen-Hecht, D.; Fonda, E.; De Oliveira, N.; Briois, V.; Frahm, R., *Rev. Sci. Instrum.* **2008**, *79*, 083107.
71. Pascarelli, S.; Neisius, T.; De Panfilis, S.; Bonfim, M.; Pizzini, S.; Mackay, K.; David, S.; Fontaine, A.; San Miguel, A.; Itie, J. P.; Gauthier, M.; Polian, A., *J. Synchrotron Rad.* **1999**, *6*, 146.
72. (a) Matsushita, T.; Oyanagi, H.; Saigo, S.; Kaminaga, U.; Hashimoto, H.; Kihara, H.; Yoshida, N.; Fujimoto, M., *Jpn. J. Appl. Phys.* **1986**, *25*, 523; (b) Tourillon, G.; Dartyge, E.; Fontaine, A.; Jucha, A., *Phys. Rev. Lett.* **1986**, *57*, 603; (c) Yoshida, N.; Matsushita, T.; Saigo, S.; Oyanagi, H.; Hashimoto, H.; Fujimoto, M., *J. Chem. Soc., Chem. Commun.* **1990**, 354.
73. Isao, T.; Hirohiko, A., *J. Phys. D: Appl. Phys.* **1996**, *29*, 1725.
74. Chermette, H., *Coord. Chem. Rev.* **1998**, *178–180*, Part 1, 699.

-
75. (a) Ankudinov, A. L.; Ravel, B.; Rehr, J. J.; Conradson, S. D., *Phys. Rev. B: Condens. Matter* **1998**, *58*, 7565; (b) Rehr, J. J.; Ankudinov, A. L., *Coord. Chem. Rev.* **2005**, *249*, 131.
 76. Nakanishi, K.; Ohta, T., *J. Phys.: Condens. Matter* **2009**, *21*, 104214.
 77. (a) Ikeno, H.; de Groot, F. M. F.; Stavitski, E.; Tanaka, I., *J. Phys.: Condens. Matter* **2009**, *21*, 104208; (b) de Groot, F. M. F.; Fuggle, J. C.; Thole, B. T.; Sawatzky, G. A., *Phys. Rev. B: Condens. Matter* **1990**, *42*, 5459.
 78. Jenkins, R., *X-ray Fluorescence Spectroscopy*. 2nd edition ed.; Wiley Interscience: New York, 1999.
 79. Meisel, A.; Leonhardt, G.; Szargan, R., *X-ray Spectra and Chemical Binding* Springer-Verlag: New York, 1989.
 80. Bergmann, U.; Bendix, J.; Glatzel, P.; Gray, H. B.; Cramer, S. P., *J. Chem. Phys.* **2002**, *116*, 2011.
 81. Adler, D., *Rev. Mod. Phys.* **1968**, *40*, 714.
 82. Alonso Mori, R.; Paris, E.; Giuli, G.; Eeckhout, S. G.; Kavčič, M.; Žitnik, M.; Bučar, K.; Pettersson, L. G. M.; Glatzel, P., *Anal. Chem.* **2009**, *81*, 6516.

Chapter Two: Theory of X-ray Absorption Spectroscopy

2.1 Introduction to XAS

X-ray Absorption Spectroscopy (XAS) is an important characterisation technique allowing us to obtain detailed information on the geometry and local structure as well as the electronic structure of materials (from valence states) ¹. The properties of materials are determined by the characteristics of these valence electron states; they consist of the partially filled conduction bands in solids and the outer d orbitals of transition metal compounds (for first row transition metals this will be 3 d-orbitals), and are extremely important in governing the chemistry of these compounds.

X-ray Absorption Fine Structure (XAFS) can be divided into X-ray Absorption Near Edge Structure (XANES) and Extended X-ray Absorption Fine Structure (EXAFS), for the purposes of this project we will be concentrating on XANES. XAFS is a powerful and versatile technique for studying the structure of materials in chemistry, physics, biology ² and other fields ³. XAS spectroscopy is an extremely useful tool for the study of the local geometric and electronic structure of specific elements within a material. One of the merits of this technique is the fact that as well as being applied to well-ordered systems like crystals, it can also be applied to materials with little or no long-range order ⁴ such as amorphous powders, liquids and solutions. Because X-rays are fairly penetrating in matter, XAFS is not inherently surface-sensitive, though special measurement techniques can be applied to enhance its surface sensitivity ⁵. In many cases, XAFS measurements can be made on dilute elements and even trace abundance, giving a unique and direct measurement of the chemical and physical state of dilute species in a variety of systems ⁶. The versatility of this technique and the high energy and intensity of X-rays generated from synchrotron radiation sources coupled with fast data acquisition has also allowed for time resolved studies of *in-situ* catalytic reactions.

In the XAS process inner (core) electrons are excited by incident X-rays and the valence electron states are detected with the core electron state (core hole) as a probe ⁷. The core hole is defined as the absence of a core electron. We are able to obtain information on the valence state as the excited state consists of an electron that has been excited into a valence orbital, as the symmetry rules allow ($\Delta l \pm 1$ for dipole transitions). This makes core

level spectroscopy a powerful tool in studying the electronic states of materials. There are several types of interactions of X-rays with matter, specifically the ones we are concerned with are; X-ray absorption, elastic scattering, and inelastic scattering. Absorption occurs when an incident photon interacts with electrons associated with the sample and gives up some of its energy ⁸. This causes transitions of electrons from lower energy levels to higher, unoccupied energy levels. After the excitation of core electrons we are left with vacancies (holes) in the lower levels, which are filled a short time later by transitions of electrons from higher levels down to lower ones (a process called core hole filling) ⁷. The energy emitted in this process may be released radiatively, by emitting fluorescence radiation at a lower energy than the incident X-rays, or non-radiatively, by kicking out an electron in an 'Auger process' ⁹.

When looking at different types of emission process we either have elastic or inelastic processes. In inelastic scattering the initial and final states are at different energies and the energy transferred corresponds to the energy of the electronic transition ¹⁰. This also means that the incident and emitted X-ray energies are different as some energy has been transferred to the sample. In elastic scattering the energy of the initial and final states are the same and the incident and emitted energies are also the same ¹¹.

All of the techniques considered here involve the interaction of X-rays with the samples being studied. X-rays are basically a form of short wavelength electromagnetic radiation. The wavelength λ of all particles, including photons and electrons, is related to their momentum p through the De Broglie relationship ¹²;

$$\lambda = h/p$$

Where h is Planck's constant. Similarly, the particle frequency f is related to the energy E by;

$$f = E/h$$

In order to perform different types of X-ray spectroscopy we need to understand the characteristics of X-rays and how we can tune them to fit their intended purpose. It is possible to tune the X-rays and their characteristics to perform a variety of detailed spectroscopic experiments ¹³. This is done by optimising the radiation as it travels along the beamline, this is explained below.

There are various types of core level spectroscopy¹⁴; three of the most important types are; X-ray Photo Emission Spectroscopy (XPS), XAS and XES. The latter two will be the focus of this research, including combined XAS/XES studies. XAS is a first order process that involves the excitation of electron(s), XES is a second order process where a core electron is excited by the incident X-ray and then the excited state undergoes a subsequent radiative decay by emitting photons and filling the initially created core hole. There are two types of X-ray emission; normal and resonant. In normal X-ray emission the core electron is excited to the continuum (the same as in XPS) and in resonant X-ray emission the core electron is excited near to the excitation threshold¹⁴ (the same as in XAS). The excitation threshold is the binding energy of the core level.

2.1.1 X-ray Absorption Near Edge Structure

Firstly we will discuss the absorption process; when any material interacts with X-rays there are various effects. One of these is absorption; where there is an electronic transition and the excited state created can relax by emitting a photon. XAS is a synchrotron based characterisation technique requiring incident photons with energies up to about 30 keV to excite core electrons⁶. In XAS a core electron is excited near the threshold¹⁴ by the incident X-rays through the electric dipole transition, in the experiments that we are looking at the electron is excited near to the threshold so that we can probe the valence states. In EXAFS the electron is excited above the threshold and then it is possible to look at the interaction with neighbouring atoms¹⁴. These are transitions between energy levels in the system and they are governed by different selection rules depending on whether they are dipole ($\Delta l \pm 1$)¹⁵ or quadrupole transitions ($\Delta l \pm 2$)^{8-9, 16}. As the core electron state is well known, and any transitions will depend on the structure of the complex, the absorption spectrum provides important information on the geometry and the electronic properties of the system under investigation¹⁴.

The term XAS is a broad one that encompasses several different techniques including; X-ray Absorption Near Edge Structure (XANES) and Extended X-ray Absorption Fine Structure (EXAFS). The basic physics of these techniques is the same and they can both be achieved from the same experiment but describe different energy regions of the XAS spectrum. The differences come in the analysis where different approximations, techniques, terminology and theoretical approaches are often employed to simulate or analyse the data^{3a}. This is particularly the case in the low-energy (soft X-ray) and high-energy (hard X-ray) regimes, this will be demonstrated in later chapters.

The basic physical quantity that is measured in XAFS is the X-ray absorption coefficient $\mu(E)$ ¹⁷, this describes how strongly X-rays are absorbed as a function of X-ray energy E ⁶. Typically as the X-ray energy increases the absorption coefficient decreases and the X-rays become more penetrating⁶. For XANES, we are concerned with the intensity of μ as a function of energy, near and at energies just above these absorption edges. Every atom has core-level electrons with well-defined binding energies⁶, the binding energy is the amount of energy it takes to promote a core electron to the continuum, a process known as the photoelectric effect (see figure 1). We can select the element to probe by tuning the X-ray energy to an appropriate absorption edge. These absorption edge energies are well-known (usually to within a tenth of percent), and tabulated⁶.

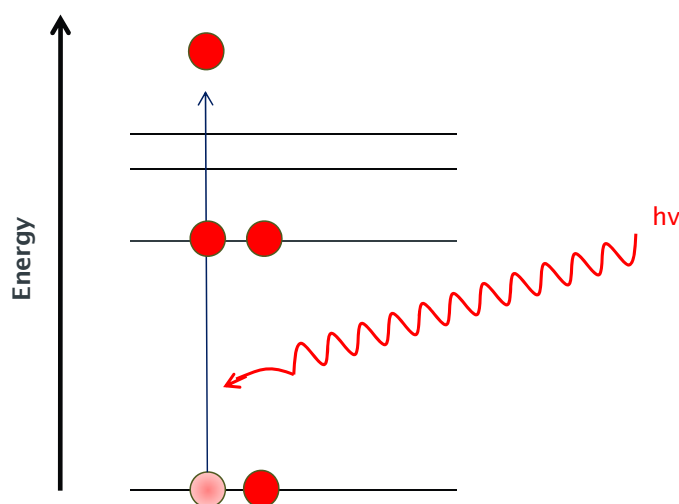


Figure 1 A diagram showing the photoelectric effect – core electron excitation by incoming photons.

Figure 1 shows the excitation of a core electron by the absorption of an X-ray photon, the electron can be promoted to an empty state below the ionization threshold or to an essentially free electron above the ionization threshold; this is known as the photo-electric effect. The photoelectric effect forms the basis of XAS, XPS and XES. In general, the photo-electric effect changes the orbital quantum number l to $l \pm 1$ ^{9,15}. In XANES we are looking at a transition to an empty state below the continuum. After the initial absorption process (photoelectric effect) there is a resulting core hole, an atom with a core hole is extremely unstable and so the core hole lives for approximately 10^{-15} seconds⁹ before it decays.

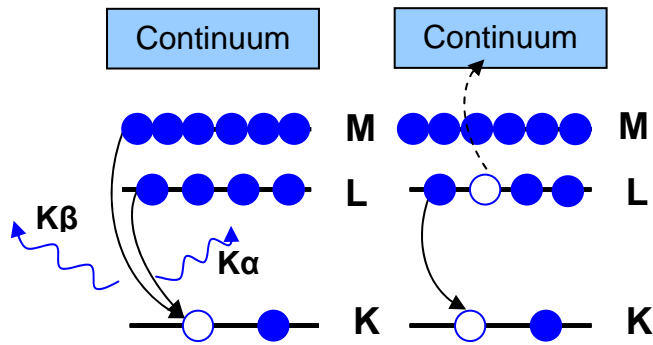


Figure 2 Decay of the excited state: X-ray fluorescence (left) and the Auger effect (right).

There are two major decay processes; fluorescence and Auger, these are both shown in figure 2. In fluorescence ^{9, 14}, on the left hand side, another electron in the atom drops down to fill the core hole. This is either a p or d electron dropping down to fill the 1s core hole in this case. In Auger decay ^{9, 14} an electron from the 2p shell drops to fill the core hole (figure 2, right hand side); the resulting X-ray photon may excite a third electron in the material. When the core hole is filled the energy difference between the two states is released as electromagnetic radiation ⁹.

The resulting X-ray absorption spectrum that is obtained during these experiments is shown below (figure 3).

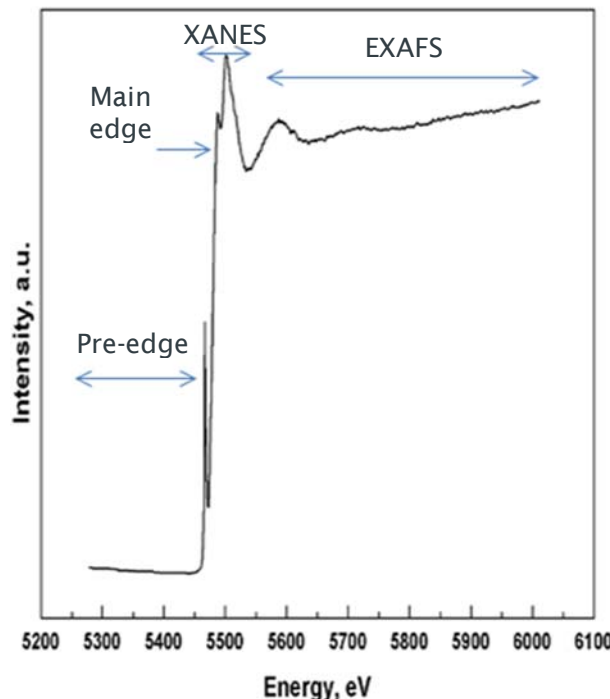


Figure 3 A typical X-ray absorption spectrum showing the different regions studied.

Figure 3 shows a typical XAS spectrum, with the Energy (eV) on the x axis and intensity on the y axis. This figure highlights the different energy regions of the XAS spectrum and what they are called; each region contains different information on the compound. For the purposes of this research we focus on the pre-edge and XANES regions. However, the EXAFS region is currently much better understood. The XANES region is typically found 10-50 eV above the edge, and the EXAFS region is from around 50-1000 eV ⁶ after the edge .

The different absorption edges correspond to transitions from different core states; the K-edge corresponds to an electron excitation from the 1s core state, L_1 corresponds to the 2s and $L_{2,3}$ to 2p core states. By combining the data obtained from both experiments we obtain direct p and d-orbital information.

Both the pre-edge region in the XANES spectra and the EXAFS features are of low intensity, in order to enlarge these features we must increase the concentration of the sample under study. This situation is not ideal for EXAFS as we then start to see self-absorption effects; however for XANES we are then able to enhance the pre-edge region. We have done this in chapter 4, using samples of a high concentration we sacrifice the structure after the edge so that we can focus on the XANES region.

2.1.2 Extended X-ray Absorption Fine Structure

The Extended X-ray Absorption Fine Structure refers to the oscillatory nature of the X-ray absorption coefficient just above the main absorption edge ¹⁷, this energy region is highlighted in figure 3 at about 50-1000 eV above the edge. The K-edges of 3d transition metal compounds contain an Extended X-ray Absorption Fine Structure (EXAFS) region due to scattering of the excited electron by the potential field of the neighbouring atoms ¹⁸. This characteristic of EXAFS can be used to determine bond distances and ligand coordination numbers as well as the type of neighbours (i.e. high Z and low Z). Not only does the EXAFS region provide a fingerprint for any material but it also provides information on the atomic structure and electronic properties ¹⁷.

Many of the current developments towards the understanding of the EXAFS region are complementary to the advances in the understanding of the ground state electronic structure ¹⁷. There were a few steps leading to the understanding of EXAFS but the major breakthrough was from Kronig in 1932 when the oscillations in the EXAFS region were attributed to the influence of neighbouring atoms on the transition matrix element in the golden rule ¹⁹ (a short range order effect). This theory is the most often used today to explain the origins of EXAFS ¹⁷.

The short-range-order theory put forward by Kronig reflects the quantum-mechanical wavelike nature of the final and excited photo-electron state ¹⁷. This means that the EXAFS oscillations are treated as a quantum interference effect between these different waves. The outgoing photoelectron wave spreads through the solid and is reflected back towards the absorber by other surrounding atoms ¹⁷, these outgoing and scattered waves can then interact constructively or destructively (peaks and troughs in the EXAFS region). In this process the outgoing and scattered waves lose energy as they get further away from the absorbing atom, as they get weaker they become too weak to reflect scattered waves and vice versa. This results in the fact that EXAFS can only measure the local atomic structure over a range that is determined by the lifetime of the excited photoelectron ¹⁷ (this is the mean free path).

It was not until the work by Sayers, Stern and Lytle in 1971 that it was widely recognised that information on near-neighbour distances, coordination numbers and fluctuations in bond distances could be obtained ²⁰. Currently the theoretical models available for EXAFS analysis are comparable to experimental reference materials ¹⁷.

The equation below is thought of as the standard EXAFS equation, this quantitative parametrisation of EXAFS has become the standard for much of the work in this area ¹⁷. The validity of the Kronig short-range-order theory was reinforced by Sayers *et al* who developed the EXAFS formula below ²⁰.

$$X(k) = \sum S_o^2 N_R [|f(k)| / k R^2] \sin(2kR + 2\delta_c + \Phi) e^{-2R/\lambda(k)} e^{-2\sigma^2 k^2}$$

This formula contains all of the key elements that a correct theory must have and also provides a convenient method for fitting the local atomic structure around the absorbing atom to the experimental EXAFS data ¹⁷. The dependence of the oscillatory structure on the interatomic distance and energy is included in the $\sin(2kR)$ term. The decay of the photoelectron wave over distance (mean free path) is captured by the exponential term, $e^{-2R/\lambda}$ ¹⁷. This is also the factor that determines the short range in a material that is probed by EXAFS. The strength of the reflected interfering waves depends on the type and number of neighbouring atoms through the backscattering amplitude, $|f(k)|$ ¹⁷. There are also secondary factors; like the spherical-wave factors ($1/kR^2$) and the mean-free-path terms, that are important for a quantitative analysis of the EXAFS amplitude. The phase factor (Φ) reflects the wavelike nature of the backscattering ¹⁷. The phase shift, δ_c , provides a larger contribution to the overall phase ¹⁷. This is because the photoelectron sees the potential created by this atom twice. These phase shift account for the difference between the measured and geometrical interatomic distances. The Debye-Waller factor ($e^{-2\sigma^2 k^2}$) is partly due to thermal effects (causing the atoms to move around), these slight movements cause a dampening of the interference pattern of the rapidly carrying $\sin(2kR)$ term that would be seen if the atoms were un-moving¹⁷. In the same way the effects of structural disorder cause an additive effect on σ^2 . The Debye-Waller factor is essential in EXAFS but often negligible in XANES ¹⁷. The overall amplitude factor S_o^2 is a many-body effect due to the relaxation of the system in response to the creation of the core hole. Although S_o^2 is weakly energy dependant it is often included as a constant ¹⁷.

The essential difference between EXAFS and XANES is in the strength of the scattering, the energy at which the techniques cross-over is at about 30 eV or less past the edge ¹⁷. In EXAFS analysis there are a number of approximations that are needed in order to correctly fit the model to the experimental spectrum; curved-wave corrections are needed at all energies ¹⁷. Spherical approximations for the scattering potentials are needed at high energies (muffin-tin model), and self-consistency is to be ignored ¹⁷. Debye-Waller factors

account for the displacement-displacement correlations and disorder and are very important in order to produce the correct amplitudes ¹⁷.

There are some limitations to this technique; it only allows the user to distinguish between elements that are one row apart in the periodic table ^{2b}. The EXAFS analysis is well understood and agreed upon in terms of a high-order multiple-scattering theory ^{17, 21}. The theoretical interpretation of the XANES region is currently not so well understood, and requires different physical considerations ¹⁷. In the XANES analysis we simulate the experimental spectrum rather than fitting a model to the experiment as in EXAFS analysis.

2.2 Synchrotrons

XAS spectroscopy has developed with the growth of synchrotron radiation research due to the fact that the XAS technique requires a source of finely tuneable energy. Some lab-based experiments are possible but in general most XAS experiments are performed at synchrotron radiation facilities. Such facilities were originally developed for high-energy physics experiments, but subsequently they have been reliably adapted to produce high-energy electromagnetic radiation such as X-rays with desirable spectral characteristics ^{13a}.

At a synchrotron radiation source an electron beam is confined in a storage ring (vacuum tube at UHV – the blue circle in figure 4) by a set of magnets (bending magnets), you can see an example of the placement of one of these magnets in figure 4 (item 3 in the key). When the beam is bent by dipole magnets, this acceleration causes the emission of radiation. The emitted light comes off perpendicular to the direction of acceleration of the electrons and can be seen on the diagram as the beamlines (item 4 on the key). The experimental stations are located at the end of these beamlines after further manipulation of the light has taken place (item 5 in figure 4). The manipulation of the emitted light will be discussed in more detail below. For a synchrotron source the electrons are close to the velocity of light. The light emanating from the particles at relativistic speeds is a ‘characteristic wavelength’ which is determined by the radius of curvature and the energy of the particles ^{13a}.

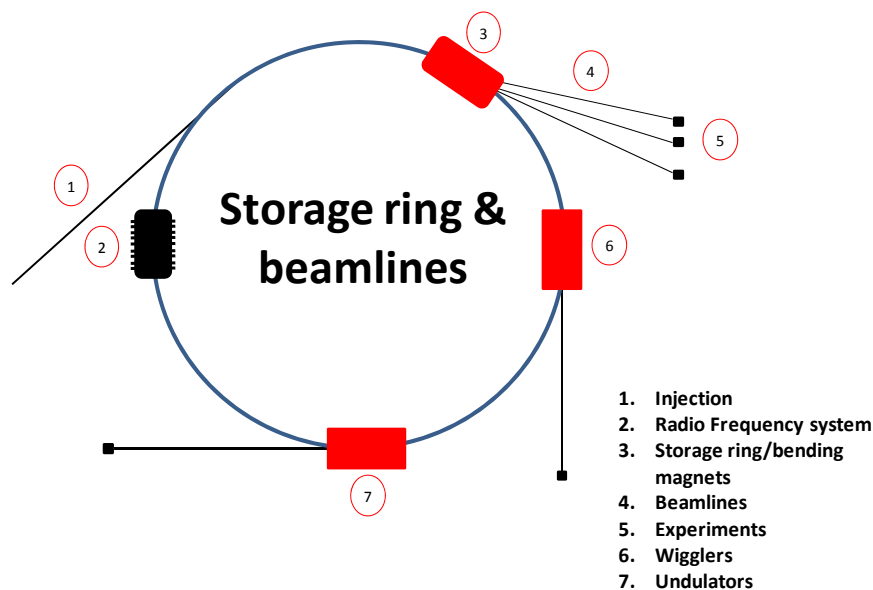


Figure 4 Elements of a synchrotron radiation source.

The light generated at synchrotron radiation sources is usually ‘white’ covering a large part of the electromagnetic spectrum, i.e. a broad range of wavelengths. Synchrotron radiation spans a wide frequency range, from infrared up to the highest-energy X-rays. The characteristic features of this type of radiation are; high intensity, high flux, high collimation (almost parallel rays), broad wavelength range, quasi continuous (or pulsed) and polarised. To ensure a better match between the radiation source and experimental requirements different magnetic devices are necessary to provide different spectral characteristics ^{13a}.

Once the emitted radiation leaves the storage ring it needs to be optimised for use for the desired experiments, this occurs along the beamline (figure 4, number 5). Beamlines are large and complex instruments that include a variety of components such as bending magnets, insertion devices (undulators and wigglers), X-ray monochromators, X-ray mirrors, slits, ultrahigh vacuum pumps, valves and gauges, photon shutters, shielding, safety interlocks, X-ray detectors, UHV chambers, cryostats, reaction cells, magnets, motorized sample stages and data acquisition systems.

All these different components look after three key aspects; controlling the radiation in the storage ring (bending magnets and insertion devices), optimising the radiation that leaves the storage ring along the beamline (optics – explained below), and optimising the sample environment in the experimental hutch (safety interlocks, X-ray detectors, UHV chambers, cryostats, reaction cells, magnets, motorized sample stages and data acquisition systems).

Insertion devices such as ‘wiguers’ and ‘undulators’ are often used to further enhance the characteristics of the emitted radiation, basically these devices change the directions of the electrons continuously in order to produce more radiation than with a bending magnet. The simplest of these is a wavelength shifter (sometimes called a wiggler). Normally a three pole magnet is used to provide a tighter radius of curvature as the electrons pass through a chicane. A magnet lattice which changes its direction many times forces the electron beam on a sinusoidal trajectory, the emission intensity is multiplied by the number of wiggles ^{13b}. This can give rise to an increase in brilliance of a factor of 100. Undulators are another type of insertion device that contain over one hundred magnetic poles lined up in rows above and below the electron beam. The magnets force the electrons into a snake-like path, so that the light from all the curves adds together ²².

The components that make up the optical hutch are necessary to select the required energy of incoming radiation, and to make sure that this energy is highly collimated and focussed down to the optimum beam spot size (normally to the order of mm in height and width).

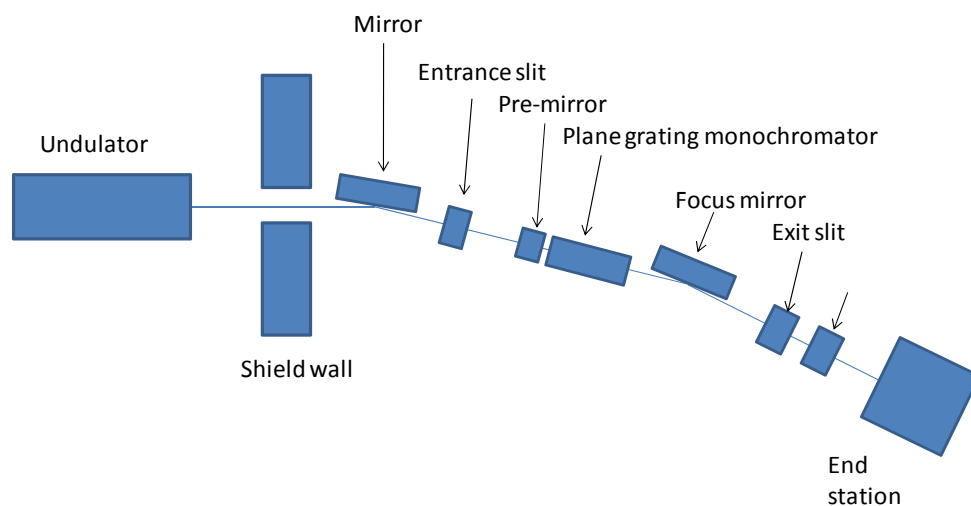


Figure 5 Diagram of the optics for a typical beamline set-up ²³.

Figure 5 shows the layout of the optical hutch on a typical XAS beamline, the beam must go through all these components before it is used to measure a spectrum of the sample in the ‘end station’. Each stage is necessary in order to select the correct wavelength of light (monochromator), reduce the beam size down as small as possible (slits) and focus the

beam (mirrors). The characteristics of synchrotron sources and the experimental station dictate what energy ranges, beam sizes, and intensities are available. Features like safety interlocks, X-ray detectors, motorized sample stages, and data acquisition systems are under remote computer control from outside the optics and experimental hutch, in the office.

An XAS spectrum originates from the fact that the probability of an electron to be ejected from a core level is dependent on the energy of the incoming beam ⁹. For this reason, the energy of the X-rays is varied during the experiment. This requires a monochromatic beam; however the radiation generated by a synchrotron is polychromatic ⁹. The desired wavelength has to be filtered from the polychromatic beam. A monochromator is used for this purpose, and in the case of hard X-rays the monochromator is based on crystal optics. The incoming beam is diffracted on a crystal and the wavelength of the diffracted beam is given by Bragg's law ¹²;

$$n\lambda = 2d \sin \theta$$

By varying the angle, θ , between the X-ray propagation direction and the surface of the crystal, the energy of the X-ray beam can be varied ²⁴. Typically Si crystals are used, for example Si(111) or Si(311) in the case of this research. The diffraction plane determines the distance and as such the angle needed for a particular energy. It also determines the energy resolution and because the life time broadening is usually above 1 eV ¹⁶, these crystals provide sufficient resolution. In principle one crystal is enough to obtain the desired wavelength of the beam. In practice, a double crystal monochromator is used in order to obtain an outgoing beam that is parallel to the incoming beam.

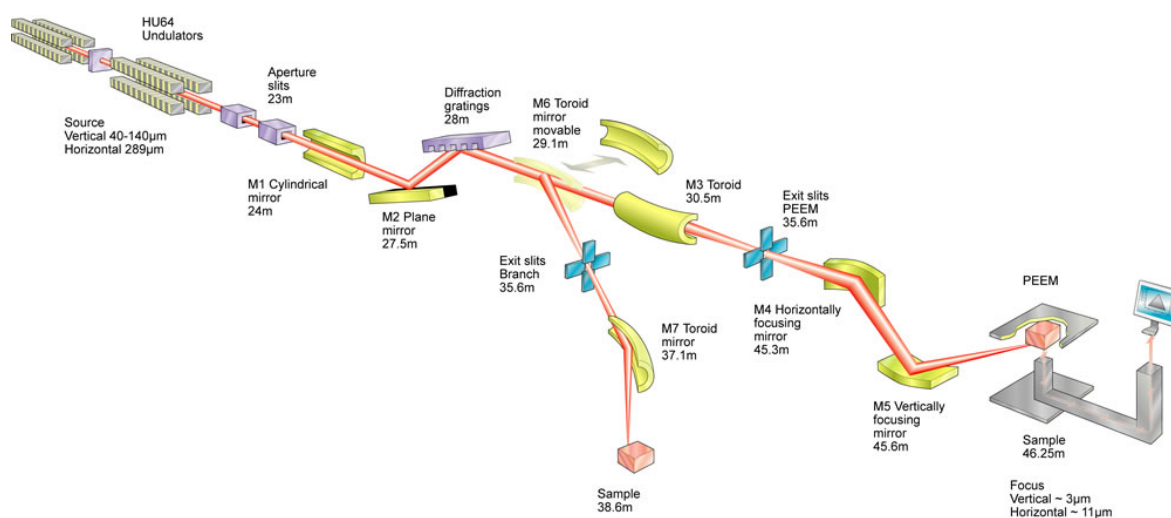


Figure 6 Beamline Design Specifications for IO6 at Diamond Light Source

Figure 6 shows the schematic for IO6 at Diamond Light Source, where the L-edge experiments in this study were performed. The L-edge experiments were carried out on the shorter branchline (not PEEM) and were carried out under ultra high vacuum (UHV) conditions. This is due to the penetrating power of the soft X-rays; soft X-rays have a large absorption cross section with air; from about 530 eV to 1 keV the transmission through 10 cm of air is less than 10 %⁹. This means that it is necessary to perform experiments under ultra high vacuum (UHV). The use of low energy X-rays also means the penetration depth is decreased and in this case limited to the top layers of the sample increasing the risk of beam damage. This is also minimised by performing the experiments under UHV. Figure 6 shows path of the beam and the conditioning steps it must go through before it reaches the sample. The section labelled 'diffraction gratings' is the monochromator which selects X-rays of a specific wavelength for the experiment, the exit slits then cut the beam size down so that small areas can be sampled.

2.2.1 Soft and hard X-rays

The X-ray region consists of soft X-rays up to 2 keV and hard X-rays at higher energies (>3 KeV). Soft X-rays are so called because they do not penetrate air and so are relatively safe to work with; experiments in these different X-ray regions require different instrumentation^{10, 26}. In order to get a tuneable monochromatic X-ray beam, or to analyze the energy of emitted X-rays, different types of devices are used depending on the energy regime²⁶. Soft X-ray experiments use optics based on grating monochromators, whereas hard X-ray experiments are performed with perfect-crystal Bragg monochromators for both excitation and also as X-ray analysers^{10, 26}. Both of these types of optics are based on

the diffraction of X-rays, the reason for the different instrumentation is that the wavelength of hard X-rays is comparable or shorter than the spacing of crystalline planes, which is not true for soft X-rays.

The fact that different optics are required is not the only difference between the two experiments; the experimental conditions are much more strict for soft X-ray experiments. The soft X-rays are more strongly absorbed by matter; for example the attenuation length in air and water for 6.2 keV hard X-rays is 400 mm and 450 μm respectively²⁶. However, the attenuation length for 620 eV soft X-rays is 0.7 mm and 0.73 μm respectively²⁶. It is for this reason that most soft X-ray experiments are carried out under ultra high vacuum (UHV) conditions. The radiation dose (amount of energy deposited/absorbing mass) is also much higher for soft x-ray energies for the same number of photons. This is highlighted from the examples above: for 620 eV soft X-rays, where the photon energy is ten times smaller than for 6.2 keV hard X-rays, the attenuation length is ~60 times larger²⁶. This means that samples are more likely to be ‘damaged’ by soft X-rays than hard X-rays.

2.2.2 Detection methods

2.2.2.1 Transmission Measurements

Photons generally are emitted at X-ray, UV-visible, and infrared wavelengths. These decay processes afford a number of possible detection methods, the most common of which are transmission, fluorescence and electron yield detection. Transmission mode involves passing X-rays through the sample and comparing the incident intensity to the transmitted intensity. Before this type of measurement the sample thickness must be considered, as absorption coefficients vary greatly across the X-ray energy range and among materials. If the samples are too thick the beam may be totally attenuated at the edge (lose X-ray intensity after the sample), while samples that are too thin (dilute) result in a poor signal-to-noise ratio as there is minimal difference between beam intensity before and after the sample. Figure 7 shows a typical transmission setup along the path of the X-ray beam, the intensity of the X-ray beam is measured before (I_0) and after (I_1) passing through the sample using gas ionization chambers or photodiodes. The XAS spectrum will then show the variation of $(\log I_0 / I_1)$ vs. energy (eV). A helpful calibration technique is to place a reference standard (red box in the figure) and detector after the I_1 detector, this way the reference spectrum is measured simultaneously with the sample.

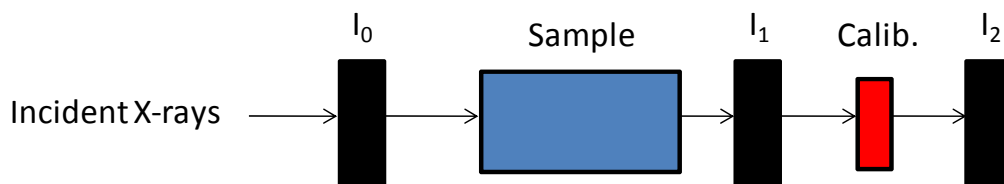


Figure 7 Beamline schematic for a typical X-ray transmission experiment.

Transmission measurements can be performed on any type of sample (gas, liquid, solid) provided the thickness and density is controllable.

2.2.2.2 Total Electron Yield Measurements

The absorption of X-rays results in the emission of electrons from the sample proportional to the absorption coefficient²⁷. The process of collecting all electrons produced is known as Total Electron Yield (TEY). This is measured with electron multipliers which directly monitor the electrical current from the sample²⁸ through a lead (in vacuum), or via gas ionization collected by a grid close to the sample surface (non-vacuum). Alternately, an electron energy analyzer may be used to discriminate between photo and Auger electrons; this method is Partial Electron Yield (PEY). The limitation here is that this method is only sensitive to the first ~10s of nm of the sample surface²⁹ due to electron scattering, and only works for solid samples. Auger electrons and fluorescence are competing processes and the ratio between the two changes depending on the element³⁰. Another limitation is that you cannot discriminate between emission energies and so we are not able to obtain Resonant Inelastic X-ray Scattering (RIXS) information, which is an important aspect of this project.

2.2.2.3 Fluorescence Measurements

The last of the three most commonly utilised techniques is fluorescence mode; this is where instead of measuring the intensity after passing through the sample (transmission) the emitted photons are measured. X-ray fluorescence is similar to electron-yield in that it is proportional to the absorption coefficient²⁷ as valence electrons emit photons to fill the core holes left by absorption. Another common feature is that the fluorescence yield may be measured in total or partial modes, the latter requiring an energy-discriminating detector^{24d}. For partial-yield, solid-state detectors such as germanium and drifted silicon detectors are often used due to their high efficiency and moderate energy resolution (enough to separate emission from different species)^{24d}.

The fluorescence yield mode is especially well-suited for dilute samples due to its selectivity and bulk-sensitivity. However, when used for concentrated samples, we see what is called 'self-absorption'. This can lower the apparent absorption coefficient and cause a dampening of the features in the spectrum. This is partially due to a reduction in the penetration depth as the absorption increases (directly impacting the coefficient due to Beer's law), and re-absorption of the fluorescence photons by the same species before the photons can leave the sample ³¹.

2.2.2.4 Detection Method in RIXS

In the Resonant Inelastic X-ray Scattering (RIXS) process a secondary monochromator (crystal analyzer) with an energy bandwidth in the order of the lifetime broadening is used as a fluorescence detector. In the case of the Cr K-edge this results in the removal of the 1s core hole lifetime broadening and therefore allows the measurement of the K-edge with greater resolution ³², with the removal of the 1s core hole lifetime the Cr K-edge spectrum is now broadened only by the 2p core hole lifetime and the experimental broadening. The longer the lifetime of the core hole the smaller the broadening affecting the spectrum. This means that although the 2p hole has a longer lifetime the resulting broadening on the spectrum is smaller. This is why it is beneficial to look at the 1s lifetime removed spectra, the 1s core hole lifetime is smaller than the 2p but has a larger broadening effect. The uncertainty principle relates the lifetime of an excited state (due to the spontaneous radiative decay or the Auger process) with the uncertainty of its energy.

$$\delta E \approx \hbar / \tau$$

The equation above shows the relationship of the energy to the lifetime (τ) of a system. The nature of the reciprocal relationship of the energy to the lifetime explains why a core hole with a shorter lifetime has a larger broadening and vice versa.

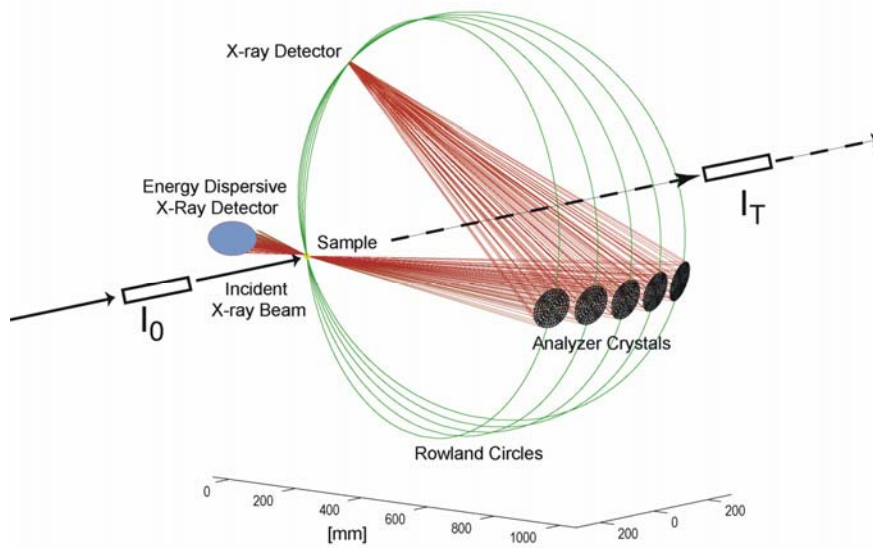


Figure 8 Detailed schematic of the Beamline setup at ID26 for the RIXS measurements ²⁶.

Figure 8 (above) shows the position of the sample in the path of the X-ray beam along with the positions of the ion chambers, analyzer crystals and detectors. In the energy range of the transition metal K-edges these detectors are based on perfect crystal Bragg optics ^{24d}. The common Rowland geometry uses spherically bent crystals with a suitable Bragg reflection at a specific X-ray emission energy and the X-rays are focussed onto a detector ^{24d}. The X-ray emission is measured as the incident X-ray energy is tuned through an absorption edge, the intermediate state probed is determined by the incident energy. The fluorescence light emitted during the decay process can be recorded using a crystal analyzer with an energy bandwidth similar to that of the primary monochromator of the synchrotron beamline ^{24d}. In this way both incident and emitted energies can be selected.

The overall RIXS process can be viewed as an inelastic scattering of the incident photon at the central atom (in our case the 3d transition metal Cr) and is theoretically described by the Kramers-Heisenberg formula ³³.

In the RIXS experiment the incident energy (Ω) as well as the emitted energy (ω) is varied. The recorded intensity is proportional to;

$$F(\Omega, \omega)$$

And is thus plotted versus a 2D grid: the RIXS plane. The Cr K-edge XANES and Resonant Inelastic X-ray Scattering (RIXS) experiments were carried out on beamline ID26 at the European Synchrotron Radiation Facility in Grenoble, France.

2.3 K-edge X-ray Absorption Spectroscopy

2.3.1 K-edge XAS Background

In recent years a large amount of work has been carried out using EXAFS; the origin³⁴, interpretation and analysis^{17,35} of which is well understood⁶. The XANES region, however, is still somewhat ambiguous; the origins of the features appearing here are not fully explained and there are debates as to the origins of the features observed because there is as yet no theoretical approach available which describes all the effects properly.

This region is often just called upon as a finger print region, especially with respect to chromium. Previously the Cr K-edge XANES region of reference compounds has frequently been used as a finger print in terms of analysing less defined systems. In order to use them as a finger print XANES spectra are taken of compounds with well defined geometries and oxidation states and these are then compared to the XANES spectra of unknowns. There are a number of examples where this method has been employed; the XAS study of the Phillips catalyst by E. Groppo *et al*³⁶ where CrO₃ and Cr₂O₃ XANES spectra were measured and compared to that of the Cr catalyst and used to identify the Cr species present. Similarly the work by M. Santhosh Kumar *et al*³⁷ and also by F.G. Requejo *et al*³⁸. The purpose of these types of study is to deduce coordination geometry and oxidation state by inspection of pre-edge features and edge shifts. These studies show that even without a detailed theoretical analysis the pre-edge and edge structures can be used to derive useful electronic and structural information.

In X-ray absorption a core electron is excited to an empty state (photoelectric effect), in this way the absorption process, more specifically the XANES region, probes the unoccupied part of the electronic structure (the unoccupied density of states). This provides essential information on the energy and electronic distribution of the molecular orbitals probed. When the incident energy reaches the binding energy an electron is excited to the lowest unoccupied orbital allowed by the dipole selection rules, this is the main absorption edge (figure 3). The Cr K-edge is produced from the dipole allowed one electron 1s→4p transition and correlates to the 1s core level binding energy. The electromagnetic field of the photon couples the initial and final electronic states giving rise

to selection rules that determine the symmetry of the orbitals that can participate in the transition ²⁶. The K-edge absorption spectra for 3d elements are broadened by the lifetime of the 1s core hole (for normal XANES) which is usually 1.0-1.3 eV ³⁹.

Spectra with higher resolution may be required in order to fully analyse any subtle variations in the XANES spectra during catalysis. We would expect to see changes in the XANES region with any changes in geometry or oxidation state during the reaction. As the pre-edge region is made up of weak transitions, samples of higher concentration and high resolution experiments will be required. These high resolution spectra are also necessary to obtain more insights into the XANES technique itself, rather than using it as a fingerprint. The K-edge XANES studies performed during this investigation can be grouped into two categories; normal XANES and High Energy Resolution Fluorescence Detection XANES (HERFD). The experimental spectra of the normal XANES are broadened because of the finite lifetime of the core hole, resulting in experimental spectra being much broader than the actual density of states (DOS) which is being probed ⁴⁰.

The position of the absorption edge has been shown to be highly sensitive to its ligand surroundings and geometry ^{38,41}. However complexes with formally different oxidation states can also show similar XANES features and positions ⁴². A detailed analysis of the pre-edge opens up a wealth of structural and electronic information. An obvious link can be made between the geometry ^{7,37-38,43}, as well as electronics, of the complex and the intensity of pre-edge features. An effect of coordination geometry on the fine structure in the K-edge region of transition metal complexes which is often observed is that the 'white line' appears only in the XANES spectra for tetrahedrally coordinated compounds ⁴. This is because for complexes of lower symmetry there is a greater degree of hybridisation between p and d or s-orbitals; this mixing of orbitals means that dipole allowed transitions to the p-orbitals contains d character and results in intensity in the pre-edge due to this dipole-quadrupole mixing ⁴⁴. When inversion symmetry is broken the 3d and 4p states mix and form a combined 3d + 4p symmetry states. We can see this effect in the K-edge XANES of Cr₂O₂ and CrCl₃ in chapter 4. This mixing of states means that the dipole and quadrupole transitions reach the same final states, and so their peaks are visible at the same energy. If an octahedral metal site is distorted then, depending on the particular distortion, more p character will be mixed into the 3d band. The result is that a distorted octahedron will show an increased intensity in the pre-edge features ⁴⁵. If the symmetry of the complex decreases, an increased level of hybridisation becomes possible and therefore more features are observed in the pre-edge. A more detailed description of

the differences in pre-edge intensity of octahedral and tetrahedral Cr compounds can be found in chapter 4 when looking at the chromium reference study.

The complexity of the XANES region arises due to the fact that it is formed by numerous effects that mainly reflect the delocalised metal p density of states ⁷, providing information on hybridisation and bonding within the molecule or materials. The intensities or areas and positions of pre-edge peaks can be reliably used to determine oxidation states and coordination chemistry (geometry) ^{38, 41}. The pre-edge features are difficult to analyse because they can involve both band structure effects and multiplet effects ¹⁶. In general there are two main reasons for the obscurity at the pre-edge region;

- 1) The lifetime broadening and the applied experimental resolution yield a broadening of around 1.5 eV; this causes a blurring of the potential fine structure at the pre-edge ¹⁶.
- 2) The combination of both direct quadrupole transitions and dipole transitions to p-character that has hybridised with the 3d band ¹⁶.

2.3.2 K-edge XAS Analysis

It is necessary to use theoretical models in order to correctly analyse the spectra obtained and correctly interpret the spectral shapes and intensities. Two main approximations are; the density-of-states (DOS) approximation and the core hole approximation. In the DOS approximation it is assumed that the calculated ground state DOS can be used. It is also assumed that extra valence electrons have no effect. In the core hole approximation it is assumed that the core hole created does not modify the DOS.

Although the fundamentals of X-ray absorption are well established, numerical simulation of XANES spectra remains far from routine because of the complexity of the processes. The XANES spectral shape reflects a complex relationship between charge screening and orbital hybridisation effects ⁴⁶. There can be added difficulties in the interpretation of XANES spectra; for example self-absorption effects in the XAS measurements (as seen in chapter 4) can cause uncertainties in the spectral intensity. Electronic structure models can be used to calculate the filled density of states, thus identifying part of the orbitals taking part in the transitions forming the pre-edge and edge. The key step is the relation of the absorption cross section to the density of unoccupied electronic states. The real space multiple scattering approach of the FEFF code has been extended to the near edge region by simulating full multiple scattering (FMS) of the photoelectron from atomic sites

⁴⁷, and calculations of XANES have been relatively successful for both metallic and semiconducting materials ⁴⁷⁻⁴⁸, despite neglect of non-spherical contributions to the electrostatic potentials ⁴⁹. 1s absorption spectra of Cr are very well reproduced with single particle methods (FEFF), this is because the 3d metals show no visible multiplet effects for a 1s core level (K-edge) because all core states are filled, meaning that there are no interactions between core holes and valence electrons ⁵⁰.

2.4 L-edge X-ray Absorption Spectroscopy

2.4.1 L-edge XAS Background

The development of high-resolution soft X-ray grating monochromators at synchrotron radiation facilities has enabled the measurement of L_{2,3} edges for a reasonable number of 3d transition metal compounds ⁵¹. It is possible to achieve resolving powers of 1.4×10^{-4} DE/E (with Si[111] crystals) and 0.3×10^{-4} DE/E (with Si[311] crystals) ⁵². In addition to transition metal compounds it is also possible to measure 3d elements present in biological systems ⁵³ or as dilute impurities with large organic multidentate ligands ⁵⁴. The 2p X-ray absorption experiments are different in nature to the 1s absorption experiments. The L-edges are dominated by dipole transitions from the 2p core level to empty 3d states, and because of the large coulomb interaction between these two states, it depends greatly on the electronic structure. This means that an analysis of the L_{2,3} edges may provide information about the oxidation state and symmetry of the transition metal ions ¹⁸. The high resolution of the L-edge data requires a much more advanced description.

The L_{2,3} X-ray absorption spectra relate to the transition of a 2p core state to an empty state on exposure to an incident X-ray beam. The nature of the absorption process is the same as in K-edge XAS but the transitions occur between different energy levels. The transition being probed at the Cr L-edge is the 2p→3d electronic transition (figure 12). The L₁ edge corresponds to the 2s and L_{2,3} to 2p core states. These transitions are located in the soft X-ray region; 400 – 950 eV.

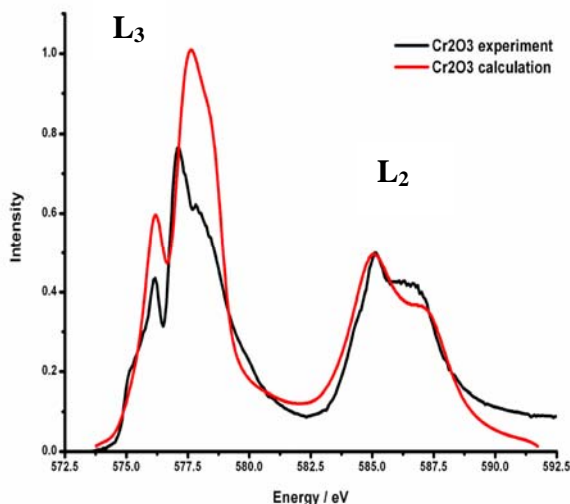


Figure 9 Experimental Cr $L_{2,3}$ spectra for Cr_2O_3 (black line) compared with the theoretical simulation (red line).

Figure 9 shows an example of a Cr $L_{2,3}$ edge spectrum to highlight the level of structure at the edges and the different regions of the spectrum. The L_3 edge is on the left and the L_2 on the right. The L_2 edge is subject to increased lifetime broadening effects due to an additional Auger decay channel and so appears broader than the L_3 part of the spectrum⁵². The L-edge is typically split into an L_3 edge ($2p_{3/2}$) and an L_2 edge ($2p_{1/2}$) by the core hole spin-orbit interaction¹⁸, the L_3 edge is a result of transitions to the $2p_{3/2}$ states and the L_2 from the transitions to $2p_{1/2}$ states. The lifetime broadening that affects the spectra is also small. As with K-edge XANES the resolution of the experimental spectra is governed by the lifetime of the core hole. In the L-edge experiments it is the lifetime of the 2p core hole that broadens the spectra, rather than the 1s as in the K-edge spectra. The 2p core hole has a longer lifetime than that of a 1s core hole, this results in better resolution for L-edge absorption experiments than K-edge absorption (due to the reciprocal relationship of the broadening to the lifetime). Typically the lifetime broadening at the L-edge is ~ 0.4 - 0.5 eV compared to 1.0 - 1.3 eV at the K-edge³⁹.

The origin of the fine structure present at the L-edge is largely due to the appearance of ‘multiplet effects’, i.e. the 2p core hole wave function has a large overlap with the 3d wave functions, which causes the so-called multiplet effect that causes the 2p XAS line shapes¹⁶. The multiplet effects visible in the L-edge spectra are generally 50-100 times stronger than 1s,3d interactions and so do not affect the features in the K pre-edge.

The $L_{2,3}$ edges of the transition metals are sensitive to local ligand coordination, this is reflected in the splittings of the 3d-orbitals involved. In systems of higher symmetry e.g.

octahedral (O_h) systems, the transition metal 3d-orbitals split because of the local symmetry in e_g and t_{2g} orbitals, with an energy difference of $10Dq$. Early studies to assess the dependence of the $L_{2,3}$ edges on the size of the $10Dq$ ligand field splitting in octahedral (O_h) and tetrahedral (T_d) systems were performed on transition metal fluorides, and a clear dependence exists¹⁸. The local symmetry of the metal (Ni) was investigated using systems with O_h , tetragonal and distorted T_d sites. These studies showed that, for these Ni systems, the local ligand environment and symmetry changes the 3d splittings and this in turn changes the $L_{2,3}$ spectra⁵⁵. According to these studies the $L_{2,3}$ spectra are sensitive to local site symmetry but less sensitive to the type of ligand attached. Previous work on Cr systems showing a classic Jahn-Teller distorted system, CrF_2 , reveals that an analysis of the distortion is possible and that a clear 3d-orbital splitting pattern can be determined⁵⁶.

Transition metal 2p XAS has also been shown to be sensitive to charge-transfer effects⁵⁷, i.e. charge transfer from the ligand orbitals to the metal 3d-orbital (the energy difference between the $3d^5$ and $3d^6\bar{L}$ configurations, where \bar{L} refers to the core hole being on the ligand). In other words that is the charge difference between initial and final states⁵⁷. This causes a consistent change in L_3 edge satellite spectral features depending on the electro-negativity of the halide attached⁵⁸.

The transition metal L-edges contain a wealth of information on the electronic structure of the absorbing metal atom due to the fact that direct d-orbital information is obtained, due to the nature of the transition. This information is important for transition metal systems as this governs their chemical behaviour. This makes it an ideal technique with which to study catalysts since during the reaction the catalytic species normally changes oxidation state, which involves a change in the number of d-electrons. There are a number of properties of the transition metals that result from the partially filled d shell, these include; 1) the formation of compounds whose colour is due to d – d electronic transitions 2) the formation of compounds in many oxidation states, due to the relatively low reactivity of unpaired d electrons and 3) the formation of many paramagnetic compounds due to the presence of unpaired d electrons⁵⁹.

2.4.2 L-edge XAS Analysis

There are a number of possible methods currently used to calculate and analyse the $L_{2,3}$ edge spectra. When applying the single electron excitation description (e.g. FEFF) to transition metal oxides, good agreement is found for the oxygen K-edges but for the metal

$L_{2,3}$ edges, the agreement is poor^{8, 60}. The reason for the deviation from the DOS is the presence of many-body effects beyond the single electron excitation. These are mainly divided into the charge-transfer effects (the energy differences between different occupations of the 3d states, causing large reordering effects in the energy positions of configurations because of the core hole potential) and the intra-atomic multiplet coupling effect (large 2p3d two-electron interactions, as mentioned)⁵⁰.

In the case of strongly correlated excited states (or localised states) in XAS, like the transition metal 3d states, the interaction between the electrons, as well as the interactions of electrons with the core hole after the absorption process, has to be taken into account explicitly⁵⁰. In the final state of an X-ray absorption process, a partly filled core state is found (2p⁵). In the case of a system with partly filled 3d levels the final state will also have an incompletely filled 3d band. The 2p hole and the 3d hole have radial wave functions that overlap significantly; this atomic effect can be very large. Experimentally it has been shown that while the direct core hole potential is largely screened, these so-called multiplet effects are hardly screened in the solid state. The reason that multiplet effects need to be considered at the L-edge is that the 1s3d two particle interactions (at the K-edge) have no visible effect on the absorption spectra whereas the 2p3d two particle interactions (at the L-edge) have a large effect on the spectral shape.

Theoretical approaches based on the ligand field atomic multiplet calculations^{18, 61} have been widely used in the analysis of the transition metal $L_{2,3}$ edges. As the multiplet structure depends on the d state occupancy we are therefore able to extract information on the oxidation state by using atomic multiplet calculations to simulate the distinct absorption line shapes produced by the 2p excitation⁵². The experimentally obtained $L_{2,3}$ absorption spectra (2p XAS) and the ligand field atomic multiplet calculations show a 'fingerprint' absorption spectrum consisting of transitions to dipole allowed final states for every 3dⁿ ground state. These spectra, with associated chemical shift values, form the basis of a strong sensitivity of the technique to the transition metal oxidation state^{51a, 62}.

In Charge Transfer Multiplet (CTM) theory the atomic model is considered, where only the interactions within the absorbing atom are taken into account, without any influence of the surrounding atoms. Atomic multiplet theory is the description of the atomic structure with quantum mechanics. Solid state effects are then introduced, the first solid state effect that is included is the effect of the crystal field (this accounts for the symmetry aspects). The second effect is that of bonding, this is described by the charge-transfer effect.

Atomic multiplet theory is able to accurately describe the 3d and 4d X-ray absorption spectra of the rare earths ⁸. However, in case of the 3d metal ions, atomic multiplet theory can not accurately reproduce the XAS spectra accurately because the effects of the neighbours are too large. It is therefore necessary to include both the symmetry effects and the configuration–interaction effects of the neighbours ⁸. Ligand field multiplet theory takes care of all symmetry effects, while charge transfer multiplet theory (CTM4XAS) allows the use of more than one configuration ⁸.

The starting point of the Ligand Field Multiplet (LFM) model is to approximate the transition metal as an isolated atom surrounded by a distribution of charges in a specific symmetry, which mimics the environment around the transition metal ⁵⁰. Only the site symmetry, i.e. point group symmetry, of the central metal atom is taken into account and the nature of the ligands attached is not considered. In this aspect the Ligand Field Multiplet model makes full use of the results of group theory. Group theory also makes possible a close link to atomic multiplet theory. Theoretically speaking the only thing ligand field theory does is translate the results obtained in atomic symmetry to cubic symmetry and further to any lower point groups ⁵⁰.

In the case of 2p XAS of transition metal compounds, the atomic multiplet theory (with crystal field effect, but without charge-transfer effect) serves as a good starting approximation and the charge-transfer effect gives some corrections to this first approximation ^{1a}. The Charge Transfer Multiplet (CTM) theory is an extension of the charge transfer theory, in this case the atomic multiplet coupling effect is taken into account for each configuration. So as well as coupling the $3d^n, 3d^{n+1}\underline{L}$ states through the hybridisation effect (charge-transfer effect between the ligand p and transition metal 3d states) in the CTM theory the atomic multiplet effect is taken into account in each of the $3d^n, 3d^{n+1}\underline{L}$ configurations. In the final state of the transition metal 2p XAS, the $2p^5 3d^{n+1}$, $2p^5 3d^{n+2}\underline{L}$ configurations are coupled through the charge-transfer effect and the atomic multiplet coupling is included in each of the $2p^5 3d^{n+1}$, $2p^5 3d^{n+2}\underline{L}$ configurations⁵⁰. The core hole potential is assumed to act only on the 3d states. This is an approximation and the interactions of the core hole on other valence electrons are neglected.

The many-body charge transfer effects in XAS have been studied for various systems, however in general the charge-transfer effects have much less of an effect in XAS than in XPS. In the case of 2p XAS spectra, the spectral shape is mainly determined by the intra-atomic multiplet coupling effects. The physical reason for the weaker charge-transfer

effects in XAS is the screening of the core hole potential by the photo-excited electron. In the 2p XAS of transition metal compounds the photo-excited electron stays in the 3d states and participates directly with the screening of the core hole potential, thus suppressing a further screening by the charge-transfer effect in going from initial to final states.

2.5 X-ray Emission Spectroscopy

2.5.1 XES Background

XAS and XES are directly related to each other and provide common as well as complementary information on the local structure of materials. XES follows the initial absorption of a photon and is therefore often referred to as a secondary process⁶³. In XES the core hole, which was created in the initial absorption process (photoelectric effect), is filled by an electron from a higher orbital. As explained above, an absorption spectrum reflects the unoccupied density of states (above the Fermi level) while the emission spectrum reflects the occupied density of states (below the Fermi level)⁶⁴.

Similarly to XAS, XES has the advantage that it is sensitive to the composition of the bulk of the material under study rather than its surface. This is due to the increased penetration depth of the hard X-rays compared to other techniques such as X-ray photoelectron spectroscopy (XPS)⁶⁵. It is also a very flexible technique in terms of sample environment as there is no need for high vacuum conditions. This makes it possible to use this technique for experiments under controlled atmospheric conditions, at cryogenic or high temperatures and also for *in-situ* catalysis. The experimental properties of XES are vast and it has been used in many different areas of study such as materials chemistry and environmental soil science⁶⁵. There have also been studies into nanocrystalline and amorphous materials, such as metals and alloys. These groups of materials exhibit certain unusual properties that are of great interest for practical applications; for coatings with enhanced hardness, wear resistance, high corrosion protection characteristics⁶⁵. Valence-to-core XES provides information on the formation of amorphous (nanocrystalline) materials that cannot be accessed using any other technique⁶⁵. Given the problem currently faced with the level of urban soil contamination in some cities understanding the processes of solubility and mobility of metals in soil is a key factor in the correct management of this resource. These are just some of the applications of this powerful technique, in some cases the Cr-containing sample was so complex that information on the Cr local environment was not available using XAS⁶⁵.

In the excitation process if an electron is removed from the 1s orbital the subsequent emission process is K fluorescence, if it is removed from the 2s or 2p orbital it is called L fluorescence (and so on) ²⁶. The fluorescence lines are labelled α , β , γ , etc depending on the intensity of the emission line (α being the most intense) ²⁶. So from this, the most intense K fluorescence line ($K\alpha$) results from the filling of the 1s core hole by an electron from a 2p-orbital, this is the fluorescence line at which the K-edge XANES are measured ²⁶. The $K\alpha$ and $K\beta$ lines are separated by several hundred electron volts with the $K\alpha$ being the lowest in energy. The electromagnetic field of the photon couples the initial and final electronic states giving rise to selection rules that determine the symmetry of the electron orbitals that can participate in the transition; this is the same as in XAS ²⁶. Both XAS and XES are sensitive to the local electronic structure and bonding configuration of the absorbing atom and there are many examples where the information in XES is complementary to that of XANES ²⁶(some XES studies will be shown in chapter 4).

Each of the $K\alpha$ and $K\beta$ emission lines shows a fine structure; this is due to two major effects:

- 1) The interaction of the electron spin with its own orbital momentum. This spin-orbit interaction is strong for the $K\alpha$ lines (~ 10 eV) and weaker for the $K\beta$ (< 1 eV) ²⁶.
- 2) Interactions between electrons, these electron-electron interactions can occur either within the valence shell or between a core electron and a valence electron ²⁶. This makes the $K\alpha$, β lines sensitive to the valence shell electron configuration. The $K\alpha$ lines are dominated by the 2p spin orbit splitting ($K\alpha_1$, $K\alpha_2$) while the $K\beta$ lines show strong interactions between the 3p and 3d orbitals that separate the $K\beta_{1,3}$ and $K\beta'$ spectral features ²⁶.

The role of XES is to measure changes in the K emission spectrum for different chemical environments of the absorbing atom (in this case Cr). Unlike XAS, XES does not necessarily require good tunability or resolution of the incident X-rays ²⁶; however an adequate analyzer is required to measure the emitted X-rays. XES studies on transition metals have been carried out with X-ray tubes long before synchrotron radiation sources were available as shown by Meisel et al. 1989 ⁶³; Tsutsumi 1959 ⁶⁶; Tsutsumi et al. 1976 ⁶⁷.

The particular emission line we are looking at in this study is the $K\beta$ emission line; this is less intense than the $K\alpha$. For the 3d elements the $K\beta$ main line is formed by the 3p \rightarrow 1s transition. The $K\beta$ main line and the $K\beta$ satellite lines are shown in figure 10, as you can see the intensity of the satellite region is much lower than that of the main line.

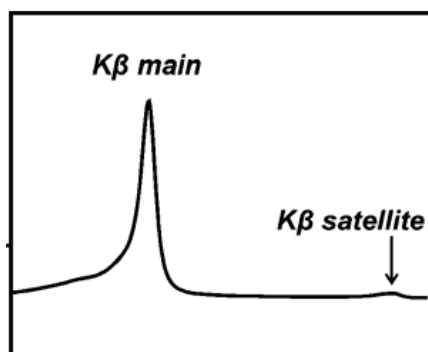


Figure 10 K β main line and satellite line of Cr highlighting the difference in intensities of these regions ⁶⁸.

In the case of 3d elements the K β main lines (K $\beta_{1,3}$ and K β') make up the core-to-core region of the spectrum and result from the 3p \rightarrow 1s transition. Whereas K β satellite lines correspond to the valence-to-core transitions ⁷ (see figure 11). The core-to-core region (main line), shown in figure 10, contains a main K $\beta_{1,3}$ peak, along with a low energy tail (K β'). The shift of the K $\beta_{1,3}$ (main) peak has been used to characterise small changes in oxidation state, where it has been shown that compared to XANES, the shifts are more linearly correlated with the oxidation state and depend less on structure ^{26, 69}. The K β lines show these comparatively weak satellites on their high-energy side that arise from transitions between the valence orbitals and the metal 1s core shell and are called K $\beta_{2,5}$ and K β'' lines ²⁶. This is the region of the spectrum that we will be investigating in more detail in this research project, the K β satellite region. The satellite region lies towards higher energy relative to the main line and is shown in higher resolution in figure 11. This region is also made up of fine structure that we are unable to see in figure 10 due to the intensity of the K β main line.

The K β satellite region of the spectra consists of fine structure that arises due to valence-to-core transitions ⁷. The valence-to-core transitions are chemically sensitive fluorescence lines ⁶⁸. The valence-to-core transitions are made up of the K $\beta_{2,5}$ and K β'' emission lines and directly reflect the configurations of the electron orbitals that participate in the chemical bond, and therefore provide valuable information. None of the K emission lines directly reflect the 3d electron configuration due to symmetry selection rules (as was the case for K edge XAS) ²⁶. However, the interaction between the electron spin in the 2p or 3d shell and in the valence orbitals is very strong ⁷⁰. This so-called *exchange* interaction is the main reason for the chemical sensitivity of the K $\beta_{1,3}$ and K β' lines ²⁶. The K α, β emission lines are therefore sensitive to the total spin in the valence shell which translates to the oxidation state ⁷¹.

XES can also be used to probe the valence shell directly. In this case, the energy of the emission spectrometer is tuned close to the energy difference between the core hole in the intermediate state and the Fermi level of the system under study ⁷². It has been shown that these emission lines are very sensitive to the ligand orbitals of 3d transition metals and thus the type of ligand can be identified ⁷².

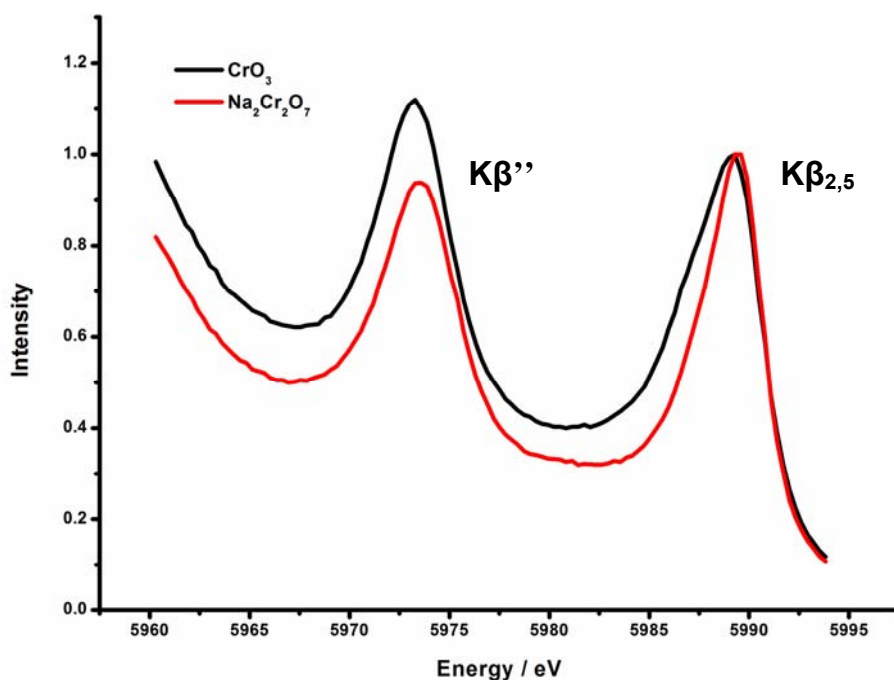


Figure 11 $K\beta$ satellite lines of Cr reference materials, indicating the positions of the cross-over peaks ($K\beta''$) and $K\beta_{2,5}$ peaks.

The strongest valence-to-core features are labelled $K\beta_{2,5}$ lines, this is the peak that appears towards higher energy in figure 11, and they involve the highest energy molecular orbitals with Cr 3d, 4s and 4p character as well as ligand 2s and 2p character. The $K\beta''$ transitions (cross-over peaks) are seen at slightly lower energies than the $K\beta_{2,5}$ lines (around 572.5 eV for Cr in figure 11). These cross-over peaks will be the key area of the spectrum in determining the nature of the different ligands attached to the central Cr atom. This can be determined by the relative positions of the peaks relative to the $K\beta_{2,5}$ lines, this is discussed further in chapter 4 (reference study). In this study the ligands that we will be focussing on are C, N and O as these have already been shown to have characteristic peaks in this region, they are also present in the salen framework.

Studies show that the relative shifts between the cross-over peak energies for C, N and O ligands correspond mainly to the difference in 2s binding energies of the atomic species ⁷³. This is because the cross-over peaks have been assigned as ligand 2s→metal 1s transitions, and so they reflect the ligand 2s binding energies ⁷⁴.

The position of the Kβ'' peak can be used as a fingerprint for the presence of Cr-O, Cr-N or Cr-C bonds in the sample, which is difficult to distinguish by other XAS experiments ⁷³. With XES you can distinguish neighbouring atoms in the periodic table via the position of Kβ'', something which cannot be done with EXAFS ^{2b, 73}.

Transitions from the Kβ'' and Kβ_{2,5} (satellite region) valence levels are the most sensitive to changes in the local structure. These tend to show similar shifts to those observed in XANES, with a shift to higher energy with higher oxidation state ²⁶. In summary, the core-to-core and valence-to-core emission lines that make up the Kβ XES spectrum are governed by the nature of the ligand in the first coordination sphere around the metal atom. This characteristic means that we are able to obtain information on the local environment around the metal for 3d transition metal compounds.

2.5.2 XES Analysis

Non-resonant X-ray Emission Spectra (fluorescence spectra) are treated in the same way as the X-ray absorption process for states below the Fermi level. The fine structures of the valence-to-core XES spectra of the Cr Kβ satellites and the core-to-core XES (main lines) were calculated based on the full multiple scattering theory using the FEFF9 code (see chapter 4).

2.6 Resonant Inelastic X-ray Scattering Spectroscopy

2.6.1 RIXS Background

Broadly speaking there are two main types of resonant scattering processes; elastic and inelastic. Inelastic scattering events differ from elastic scattering events in that the frequency of the emitted photon is not the same as the incident photon; it is generally of lower frequency (lower energy) ¹⁰. The energy difference between the scattered and incident energy in inelastic scattering is transferred to the sample by causing electronic

transitions in the same way as in the absorption process ¹⁰. Elastic scattering occurs when an incident photon interacts with the electrons and a photon of the same frequency but different direction is emitted ¹⁰. Experimentally it is typical that the absorption and emission processes are considered separately, however it is apparent that they are connected. In X-ray absorption spectroscopy the focus is on the energy dependence of the total absorption, without measuring the scattering intensity versus angle, as done in scattering experiments ⁷. However more information can be obtained by including Inelastic X-ray Scattering as will be discussed later in this chapter.

Resonant X-ray Emission Spectroscopy is divided into two categories depending on the electronic levels participating in the transition. The first is when the transition occurs from the valence state to the core state, and there is no core hole left in the final state, for example the 3d to 2p radiative decay following the 2p to 3d excitation ^{1a}. In this case the emission process is regarded as Resonant Inelastic X-ray Scattering (RIXS). Compared with the non-resonant version, RIXS has a larger intensity and depends on each intermediate state, which is convenient to identify the character of electronic excitations ^{1a}.

The second category of emission arises when the decay occurs from one core state to another core state, so that a core hole is left in the final state of the emission process ^{1a}. A typical example is the 3p to 1s decay following the 1s to 4p excitation ^{1a}. In general the lifetime of a shallow core hole is longer than that of a deeper one; so the lifetime broadening is determined by the core hole in the final state, instead of the intermediate state ¹⁰. Taking advantage of these facts it is possible to use these measurements to detect a weak signal of core electron excitations that cannot be detected using conventional XAS measurements because of the large lifetime broadening of a deep core hole ^{1a}.

Intense X-ray sources at third generation storage rings, efficient X-ray emission spectrometers and experimental facilities that offer outstanding user support have greatly facilitated the development and relatively wide spread availability of the technique, even to the non-expert user. This has led to the technique being employed by, not only physicists, but also scientists from other fields such as; catalysis ^{24d} chemistry and environmental science ⁷⁵. The recent advances in the field of RIXS are largely due to the availability of undulator radiation from third-generation synchrotron radiation sources, as well as highly efficient detectors ^{24d}.

The electronic states that lead to the edge of an absorption spectrum are resonantly excited states that subsequently decay. In the case of Cr the decay process with the highest

probability after the initial excitation is the 2p to 1s transition or the $K\alpha$ fluorescence line²⁶. The figure below (figure 12) shows the initial excitation and subsequent radiative decay processes that make up this second order process.

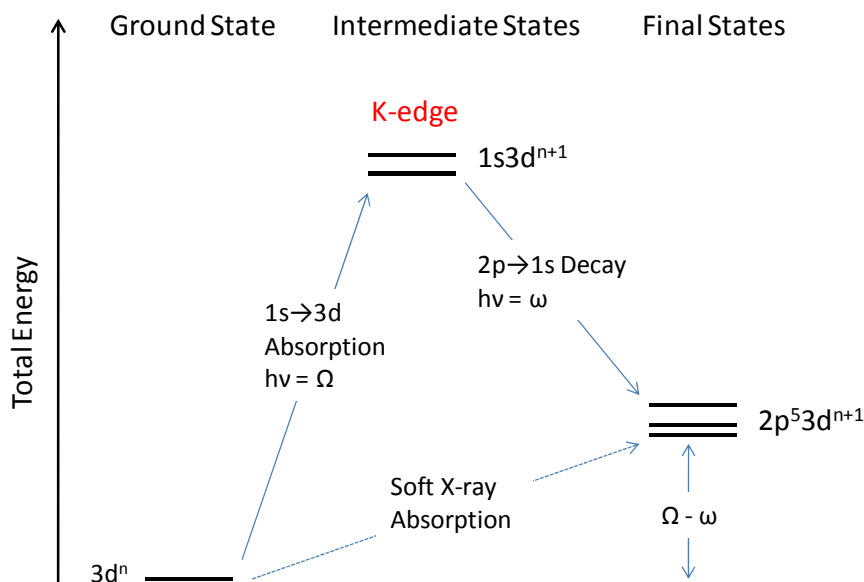


Figure 12 An energy schematic describing the electronic transitions occurring during the 1s2p RIXS technique and the soft X-ray L-edge absorption experiments⁷⁶.

Figure 12 shows the electronic transitions occurring at the K-edge and at the L-edge; the L-edge experiment is marked as 'soft X-ray absorption'. The L-edge has been measured using both soft and hard X-ray techniques (directly and indirectly). In the soft X-ray technique we look at the direct $2p \rightarrow 3d$ absorption (L-edge) to dipole allowed final states, probing the 3d shell directly. The dipole-allowed transitions in 2p XAS are $2p \rightarrow 3d$ and $2p \rightarrow 4s$, but as the transitions to the 3d states dominate and the transitions to 4s-orbitals are not included. From this schematic we can see that the final state reached after measuring the initial absorption process and the subsequent emission experiment (together these make up RIXS) is the same as that reached via soft X-ray L-edge XAS. It is for this reason that we are able to obtain complementary information in a direct approach.

The K-edge type information obtained comes from the High Energy Resolution Fluorescent Detection XANES spectra (HERFD) that are measured during the RIXS process. In the HERFD experiments only one fluorescence line is monitored (in this case the $K\alpha_1$ emission line), with an energy resolution better than the core hole life time broadening, and this results in high energy-resolution fluorescence detection (HERFD)

XANES spectra. To measure a specific energy, a secondary fluorescence detector with an energy resolution that is similar to the core hole lifetime broadening is used so that only one emission line is probed. This is how we ensure that the XAS spectrum is only broadened by the 2p core hole lifetime rather than by the 1s core hole lifetime (the 2p resulting in a reduced broadening compared to the 1s). For Cr this value is 1.08 eV for the K-edge and 0.2 eV for L_3 ³⁹. It also has a sharpening effect on the structures; this is clearly visible when comparing the normal and HERFD spectra (chapter 4). This results in a much better resolved fine structure, compared to normal transmission or total fluorescence spectra [2,3]. The different XAS data (normal and HERFD) were collected during the same experiment for all of the samples in this investigation.

When the incident X-ray beam hits the sample this causes the excitation of a 1s core electron to the valence orbital. In this intermediate state we are left with a 1s core hole after the initial excitation, and a $3d^{n+1}$ state^{57, 76}. The intermediate state is very unstable with the presence of a 1s core hole and so another electron (now from the 2p shell) drops down to fill it. The final state is therefore a $2p^5 3d^{n+1}$ state with a completely filled 1s level. We know the energy of the incident photon in the experiment, the energy of the emitted photon is measured in XES with the secondary spectrometer, and from these measurements we can work out the energy transferred (or the energy of the transition). With this information we are able to compile a 2D contour plot (as shown in figure 13). In this study using a hard X-ray technique in RIXS to probe the lowest unoccupied orbitals, the metal 3d shell, we can obtain a more localised view of the electronic d structure which is important in our field of work; catalysis and material science.

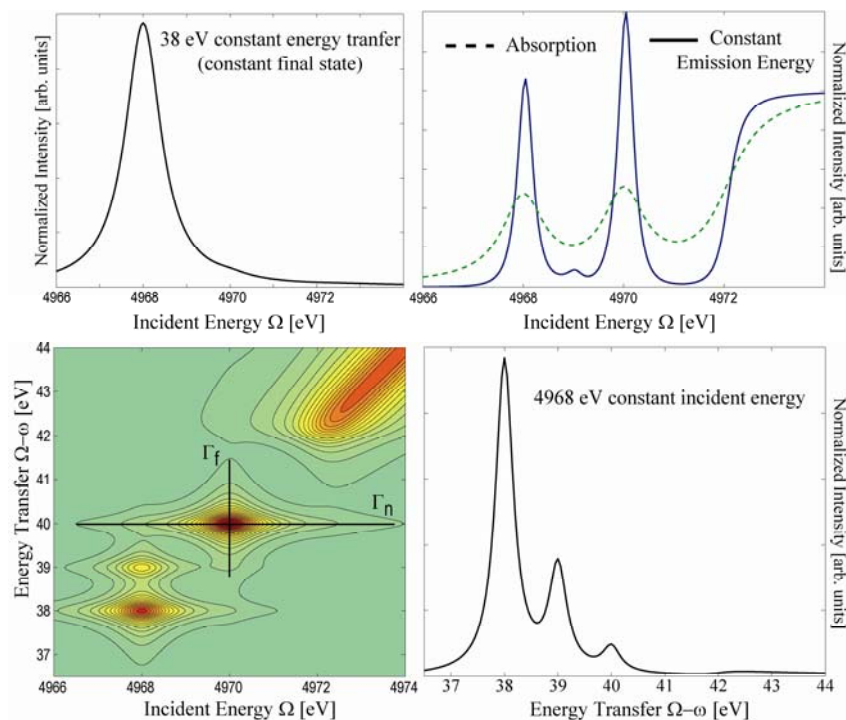


Figure 13 Typical 2D RIXS contour plot with individual line plots 7.

Figure 13 shows a typical 2D contour plot obtained from the RIXS experiment and clearly highlights the advantages of the second energy axis, energy transfer. This allows the removal of the strong background that is present at the main K-edge in the range of the pre-edge structure. This enables the separation of the pre-edge features from the main K-edge along the incident energy axis 7. These effects can be seen when looking at the 1s2p RIXS spectra of the Cr compounds in chapters 4 and 5. RIXS plots are generally displayed as 2D contour plots because this is deemed the most comprehensive method of displaying 1s absorption and 1s2p X-ray emission processes. However, sometimes it is more convenient to compare 1D spectral shapes 7. The three most straightforward cross sections to take from the RIXS plane are shown above in figure 13. These are the Constant Incident Energy (CIE), which is a vertical cross section at fixed excitation energy, this relates to resonant X-ray emission spectra. Constant Energy Transfer spectra (CET), a horizontal cross section at constant transferred energy; this implies that for all excitation energies the same final states are probed. The third is the Constant Emission Energy (CEE) spectra, a diagonal cross section at constant emission energy, this is related to the ‘lifetime removed’ XANES spectra 16. The increased resolution offered by the RIXS technique is shown in figure 13 when comparing the low energy resolution XANES experiment to the line of Constant Emission Energy (CEE) from the RIXS plot (top right hand plot). There is a feature in the CEE plot at 4969 eV that does not appear in the normal absorption spectrum (dotted line in the same figure), the CEE plot shows a sharpened version of the K

pre-edges. There is an argument as to which is the best method of showing the data to obtain the desired electronic information on the system in question. In some cases the more absorption like spectra are considered to be the most appropriate, so the CEE spectra, because they are more direct as they result from transitions from the ground state⁷. The CIE spectra are related to X-ray emission and so yield more indirect information. In this instance potentially more information is contained within it as it is essentially a 2p XAS-like spectrum that is being measured using hard X-rays¹⁶. The lifetime broadenings for the intermediate states and final states apply in the Ω (the incident energy axis) and $\Omega - \omega$ (final state energy) directions respectively.

The RIXS process allows the L-edge to be probed indirectly (2 step process) combined with the advantages of using high energy X-ray absorption and emission (allowing *in-situ* experiments). The K-edge information obtained in K-edge XAS and from the RIXS experiment will be similar as it is the same transitions that are being probed, just at higher resolution (figure 12). For the L-edge although the plots may not exactly coincide they will still contain information on the metal ion electronic structure that is complementary to L-edge absorption⁷⁷. This is a result of the fact that splittings due to crystal field, multiplet and spin-orbit interactions are the same in both techniques⁷. The exact features may differ slightly due to different symmetry operations taking place in the one step vs. the two step process. It is shown later (chapter 4) that although the techniques are complementary, we are able to reproduce general peak shapes but not the exact 2p XAS spectra. This 2D picture is extremely valuable when trying to identify the correlation between the incident and emitted energies.

Spectral intensity in the pre-edge region in both XANES and RIXS arises from dipole and quadrupole transitions. Electron-electron interactions in the valence shell can give a rich multiplet structure and cause multi-electron excitations. Other effects such as crystal field, orbital hybridisation and band structure effects also need to be taken into account in a theoretical analysis of the pre-edge⁷⁸. Another interesting feature observed in RIXS is that orbital hybridisation between two neighbouring metal atoms can occur, causing spectral intensity in the pre-edge and resulting in an excited state with an electron that is delocalised over the neighbouring metal atom⁷⁸. This is referred to as a non-local peak, and could be very beneficial when studying catalytic systems as this is often thought to be the end species / catalyst sink⁷⁹.

Studies have shown that with an increase in the experimental resolution of the monochromator and detector from around 1 eV to 0.3 eV, closer to that obtained with 2p

XAS, a great deal more information would be revealed¹⁶. The level of information obtained from calculations of 1s2p RIXS spectra with this increase in resolution is much better than that from the corresponding 2p XAS experimental data. This shows how powerful the RIXS technique could be¹⁶.

2.6.2 RIXS Analysis

All of the RIXS plots measured in this study are simulated using the RGAss program. RGAss includes the electronic configurations for the ground states, intermediate states and final states in the excitation and emission processes as well as parameters for the local geometry of the central atom, crystal field splitting value and the type of transition probed. Other effects such as charge transfer and d-d interactions are also included.

2.7 Aims of Spectroscopic Development

Throughout the course of this project the aim, in terms of spectroscopic development, is to use what we have learnt from the well established techniques like K-edge and L-edge XAS and combine this in order to develop the applications of the RIXS technique. Each of these experiments provides us with complementary information on the geometry and/ or electronic structure of the materials under investigation. The challenge now is to see if by combining these techniques we can perform a more detailed analysis of these transition metal systems.

The K-edge provides information on the unoccupied density of states of the system. Here we obtain direct p-orbital information, revealing the orbitals taking part in the electronic transition forming the pre-edge and edge. At the L-edge we probe the d-orbitals in the 2p→3d transition. This d-orbital information is extremely valuable when trying to understand and predict transition metal chemistry. The clear advantage of measuring the L_{3,2} edges for the study of 3d transition metals is that they are caused by dipole allowed transitions. This means that besides the energy positions, the intensities into all the individual final states can be accurately calculated, as shown in chapters 4 and 5. This allows a detailed analysis of the features contained within the absorption edge and the transitions that they originate from. The combination of information obtained from K and L-edge XAS experiments with associated theoretical calculations will enable us to assess both p and d-orbital contributions to the bonding characteristics of the chromium

containing compounds. Understanding the electronic behaviour of these materials, and catalytic systems is key in the design and development of future catalysts.

Using a hard X-ray technique such as RIXS to probe the lowest unoccupied orbitals (metal 3d shell) we can obtain a more localised view of the electronic structure. The recent progress in this area has allowed for new techniques, such as RIXS, to provide a more detailed description of the electronic structure of real life catalysts. This in turn enables us to better understand and predict the chemistry occurring, as transition metal chemistry is governed mainly by the d electrons. It will also aid the future design and tailoring of catalysts. RIXS provides information that is complementary to both X-ray absorption and emission processes and provides insight to their correlation to each other. The energies of fluorescence emission are very sensitive to the chemical environment. When different emission lines can be resolved and assigned to specific chemical environments, selective XAFS can be performed ⁸⁰. This allows the characterisation of individual components in chemical mixtures. Several applications have recently been demonstrated, such as spin-selective XAS, valence-selective extended XAFS, and range extended XAFS using detection channels for a certain edge, valence and/or spin-state ^{1a}.

2.8 References

- (a) de Groot, F. M. F.; Kotani, A., In *Core Level Spectroscopy of Solids*, CRC Press: 2008; pp 1; (b) Meitzner, G., In *In-Situ Spectroscopy in Heterogeneous Catalysis*, Wiley-VCH Verlag GmbH & Co. KGaA: 2004; pp 179.
- (a) Cramer, S. P.; Ralston, C. Y.; Wang, H. X.; Bryant, C., *J. Electron. Spectrosc. Relat. Phenom.* **1997**, *86*, 175; (b) Ortega, R., *Metallomics* **2009**, *1*, 137.
- (a) Cabaret, D.; Bordage, A.; Juhin, A.; Arfaoui, M.; Gaudry, E., *PCCP* **2010**, *12*, 5619; (b) Ammundsen, B.; Jones, D. J.; Rozière, J., *J. Solid State Chem.* **1998**, *141*, 294; (c) Ignatov, A. Y.; Ali, N.; Khalid, S., *Phys. Rev. B: Condens. Matter* **2001**, *64*, 014413; (d) Saitoh, T.; Bocquet, A. E.; Mizokawa, T.; Namatame, H.; Fujimori, A.; Abbate, M.; Takeda, Y.; Takano, M., *Phys. Rev. B: Condens. Matter* **1995**, *51*, 13942; (e) Sánchez, M. C.; García, J.; Blasco, J.; Subías, G.; Perez-Cacho, J., *Phys. Rev. B: Condens. Matter* **2002**, *65*, 144409; (f) Grush, M. M.; Chen, J.; Stemmler, T. L.; George, S. J.; Ralston, C. Y.; Stibrany, R. T.; Gelasco, A.; Christou, G.; Gorun, S. M.; Penner-Hahn, J. E.; Cramer, S. P., *J. Am. Chem. Soc.* **1996**, *118*, 65; (g) Bargar, J. R.; Tebo, B. M.; Villinski, J. E., *Geochim. Cosmochim. Acta* **2000**, *64*, 2775.
- Pantelouris, A.; Modrow, H.; Pantelouris, M.; Hormes, J.; Reinen, D., *Chem. Phys.* **2004**, *300*, 13.
- Degroot, F. M. F., *J. Electron. Spectrosc. Relat. Phenom.* **1994**, *67*, 529.
- Bunker, G., *Introduction to XAFS: A Practical Guide to X-ray Absorption Fine Structure Spectroscopy*. 1 ed.; Cambridge University Press: 2010.
- Glatzel, P.; Bergmann, U., *Coord. Chem. Rev.* **2005**, *249*, 65.
- de Groot, F., *Coord. Chem. Rev.* **2005**, *249*, 31.
- de Groot, F. M. F.; Kotani, A., In *Core Level Spectroscopy of Solids*, CRC Press: 2008; pp 11.
- de Groot, F. M. F.; Kotani, A., In *Core Level Spectroscopy of Solids*, CRC Press: 2008; pp 335.
- de Groot, F. M. F.; Kotani, A., In *Core Level Spectroscopy of Solids*, CRC Press: 2008; pp 287.
- Martin, P. J.; Oldaker, B. G.; Miklich, A. H.; Pritchard, D. E., *Phys. Rev. Lett.* **1988**, *60*, 515.
- (a) Evans, J., *PCCP* **2006**, *8*, 3045; (b) Kunz, C., *J. Phys.: Condens. Matter* **2001**, *13*, 7499.
- Nilsson, A., *J. Electron. Spectrosc. Relat. Phenom.* **2002**, *126*, 3.
- Pompa, M.; Li, C.; Bianconi, A.; Congiu Castellano, A.; Della Longa, S.; Flank, A. M.; Lagarde, P.; Udron, D., *Physica C: Superconductivity* **1991**, *184*, 51.
- de Groot, F. M. F.; Glatzel, P.; Bergmann, U.; van Aken, P. A.; Barrea, R. A.; Klemme, S.; Havecker, M.; Knop-Gericke, A.; Heijboer, W. M.; Weckhuysen, B. M., *Phys. Rev. B: Condens. Matter* **2005**, *109*, 20751.
- Rehr, J. J.; Albers, R. C., *Rev. Mod. Phys.* **2000**, *72*, 621.
- van der Laan, G.; Kirkman, I. W., *J. Phys.: Condens. Matter* **1992**, *4*, 4189.
- Kronig, R. d. L., *Zeitschrift für Physik A Hadrons and Nuclei* **1932**, *75*, 468.
- Sayers, D. E.; Stern, E. A.; Lytle, F. W., *Phys. Rev. Lett.* **1971**, *27*, 1204.
- (a) Rehr, J. J.; Albers, R. C.; Zabinsky, S. I., *Phys. Rev. Lett.* **1992**, *69*, 3397; (b) Zabinsky, S. I.; Rehr, J. J.; Ankudinov, A.; Albers, R. C.; Eller, M. J., *Phys. Rev. B: Condens. Matter* **1995**, *52*, 2995; (c) Binsted, N.; Cook, S. L.; Evans, J.; Greaves, G. N.; Price, R. J., *J. Am. Chem. Soc.* **1987**, *109*, 3669; (d) Filipponi, A.; Di Cicco, A.; Natoli, C. R., *Phys. Rev. B: Condens. Matter* **1995**, *52*, 15122; (e) Filipponi, A.; Di Cicco, A., *Phys. Rev. B: Condens. Matter* **1995**, *52*, 15135.
- Farge, Y., *Appl. Opt.* **1980**, *19*, 4021.

23. Young, A. T.; Martynov, V.; Padmore, H. A., *J. Electron. Spectrosc. Relat. Phenom.* **1999**, *101–103*, 885.
24. (a) Hayashi, H.; Kawata, M.; Takeda, R.; Udagawa, Y.; Watanabe, Y.; Takano, T.; Nanao, S.; Kawamura, N., *J. Electron. Spectrosc. Relat. Phenom.* **2004**, *136*, 191; (b) Bergmann, U.; Cramer, S. P., In *Crystal and Multilayer Optics*, San Diego, 1998; pp 198; (c) Verbeni, R.; Kocsis, M.; Huotari, S.; Krisch, M.; Monaco, G.; Sette, F.; Vanko, G., *J. Phys. Chem. Solids* **2005**, *66*, 2299; (d) Glatzel, P.; Sikora, M.; Smolentsev, G.; Fernández-García, M., *Catal. Today* **2009**, *145*, 294.
25. Diamond <http://www.diamond.ac.uk/Home/Beamlines/IO6/specs.html>.
26. Bergmann, U.; Glatzel, P., *Photosynth. Res.* **2009**, *102*, 255.
27. Bunker, G., In *Introduction to XAFS: A Practical Guide to X-ray Absorption Fine Structure Spectroscopy*, 1st Edition ed.; Cambridge University Press: 2010; p 268.
28. Kasrai, M.; Lennard, W. N.; Brunner, R. W.; Bancroft, G. M.; Bardwell, J. A.; Tan, K. H., *Appl. Surf. Sci.* **1996**, *99*, 303.
29. (a) Abbate, M.; Goedkoop, J. B.; de Groot, F. M. F.; Grioni, M.; Fuggle, J. C.; Hofmann, S.; Petersen, H.; Sacchi, M., *Surf. Interface Anal.* **1992**, *18*, 65; (b) Tourillon, G.; Dartyge, E.; Fontaine, A.; Lemonnier, M.; Bartol, F., *Phys. Lett. A* **1987**, *121*, 251.
30. Stöhr, J.; Noguera, C.; Kendelewicz, T., *Phys. Rev. B: Condens. Matter* **1984**, *30*, 5571.
31. Tröger, L.; Arvanitis, D.; Baberschke, K.; Michaelis, H.; Grimm, U.; Zschech, E., *Phys. Rev. B: Condens. Matter* **1992**, *46*, 3283.
32. Hamalainen, K.; Kao, C. C.; Hastings, J. B.; Siddons, D. P.; Berman, L. E.; Stojanoff, V.; Cramer, S. P., *Phys. Rev. B: Condens. Matter* **1992**, *46*, 14274.
33. Glatzel, P.; Yano, J.; Bergmann, U.; Visser, H.; Robblee, J. H.; Gu, W.; de Groot, F. M. F.; Cramer, S. P.; Yachandra, V. K., *J. Phys. Chem. Solids* **2005**, *66*, 2163.
34. Sayers, D. E.; Stern, E. A.; Lytle, F. W., *Phys. Rev. Lett.* **1971**, *27*, 1204.
35. Lee, P. A.; Pendry, J. B., *Phys. Rev. B: Condens. Matter* **1975**, *11*, 2795.
36. Groppo, E.; Prestipino, C.; Cesano, F.; Bonino, F.; Bordiga, S.; Lamberti, C.; Thüne, P. C.; Niemantsverdriet, J. W.; Zecchina, A., *J. Catal.* **2005**, *230*, 98.
37. Santhosh Kumar, M.; Hammer, N.; Rønning, M.; Holmen, A.; Chen, D.; Walmsley, J. C.; Øye, G., *J. Catal.* **2009**, *261*, 116.
38. Requejo, F. G.; Ramallo-López, J. M.; Rosas-Salas, R.; Domínguez, J. M.; Rodríguez, J. A.; Kim, J. Y.; Quijada, R., *Catal. Today* **2005**, *107–108*, 750.
39. Fuggle, J. C.; Inglesfield, J. E., *Topics in Applied Physics*. Springer-Verlag Berlin and Heidelberg GmbH & Co. K: 1992.
40. Tromp, M.; Bokhoven, J. A. v.; Safonova, O. V.; Groot, F. M. F. D.; Evans, J.; Glatzel, P. X-ray Absorption Fine Structure-XAFS13, 2007; pp 651.
41. Wilke, M.; Farges, F.; Petit, P.-E.; Brown Jr, G. E.; Martin, F., *Am. Mineral.* **2001**, *86*, 714.
42. Tromp, M.; Moulin, J.; Reid, G.; Evans, J., In *X-Ray Absorption Fine Structure-XAFS13*, Hedman, B.; Painetta, P., Eds. 2007; Vol. 882, pp 699.
43. Tromp, M.; van Bokhoven, J. A.; van Strijdonck, G. P. F.; van Leeuwen, P. W. N. M.; Koningsberger, D. C.; Ramaker, D. E., *J. Am. Chem. Soc.* **2004**, *127*, 777.
44. (a) Westre, T. E.; Kennepohl, P.; DeWitt, J. G.; Hedman, B.; Hodgson, K. O.; Solomon, E. I., *J. Am. Chem. Soc.* **1997**, *119*, 6297; (b) DeBeer George, S.; Brant, P.; Solomon, E. I., *J. Am. Chem. Soc.* **2004**, *127*, 667.
45. de Groot, F., *Chem. Rev.* **2001**, *101*, 1779.
46. Solomon, E. I.; Hedman, B.; Hodgson, K. O.; Dey, A.; Szilagyi, R. K., *Coord. Chem. Rev.* **2005**, *249*, 97.
47. Ankudinov, A. L.; Ravel, B.; Rehr, J. J.; Conradson, S. D., *Phys. Rev. B: Condens. Matter* **1998**, *58*, 7565.
48. Gilbert, B.; Frazer, B. H.; Zhang, H.; Huang, F.; Banfield, J. F.; Haskel, D.; Lang, J. C.; Srajer, G.; Stasio, G. D., *Phys. Rev. B: Condens. Matter* **2002**, *66*, 245205.

49. Gilbert, B.; Frazer, B. H.; Belz, A.; Conrad, P. G.; Neelson, K. H.; Haskel, D.; Lang, J. C.; Srajer, G.; De Stasio, G., *J. Phys. Chem. A* **2003**, *107*, 2839.
50. de Groot, F. M. F.; Kotani, A., In *Core Level Spectroscopy of Solids*, CRC Press: 2008; pp 93.
51. (a) van der Laan, G.; Thole, B. T.; Sawatzky, G. A.; Verdagner, M., *Phys. Rev. B: Condens. Matter* **1988**, *37*, 6587; (b) de Groot, F. M. F.; Fuggle, J. C.; Thole, B. T.; Sawatzky, G. A., *Phys. Rev. B: Condens. Matter* **1990**, *41*, 928; (c) Chen, C. T.; Sette, F., *Phys. Scr.* **1990**, 119; (d) Cramer, S. P.; de Groot, F. M. F.; Ma, Y.; Chen, C. T.; Sette, F.; Kipke, C. A.; Eichhorn, D. M.; Chan, M. K.; Armstrong, W. H., *J. Am. Chem. Soc.* **1991**, *113*, 7937.
52. de Groot, F. M. F.; Fuggle, J. C.; Thole, B. T.; Sawatzky, G. A., *Phys. Rev. B: Condens. Matter* **1990**, *42*, 5459.
53. (a) George, S. J.; Van Elp, J.; Chen, J.; Ma, Y.; Chen, C. T.; Park, J. B.; Adams, M. W. W.; Searle, B. G.; de Groot, F. M. F., *J. Am. Chem. Soc.* **1992**, *114*, 4426; (b) van Elp, J.; Peng, G.; Zhou, Z. H.; Adams, M. W. W.; Baidya, N.; Mascharak, P. K.; Cramer, S. P., *Inorg. Chem.* **1995**, *34*, 2501; (c) van Elp, J.; Peng, G.; Zhou, Z. H.; Mukund, S.; Adams, M. W. W., *Physical Review B* **1996**, *53*, 2523.
54. Peng, G.; van Elp, J.; Jang, H.; Que, L.; Armstrong, W. H.; Cramer, S. P., *J. Am. Chem. Soc.* **1995**, *117*, 2515.
55. van Elp, J.; Peng, G.; Searle, B. G.; Mitra-Kirtley, S.; Huang, Y. H.; Johnson, M. K.; Zhou, Z. H.; Adams, M. W. W.; Maroney, M. J.; Cramer, S. P., *J. Am. Chem. Soc.* **1994**, *116*, 1918.
56. Theil, C.; van Elp, J.; Folkmann, F., *Phys. Rev. B: Condens. Matter* **1999**, *59*, 7931.
57. Ikeno, H.; de Groot, F. M. F.; Stavitski, E.; Tanaka, I., *J. Phys.: Condens. Matter* **2009**, *21*, 104208.
58. van der Laan, G.; Zaanen, J.; Sawatzky, G. A.; Karnatak, R.; Esteve, J. M., *Phys. Rev. B: Condens. Matter* **1986**, *33*, 4253.
59. Matsumoto, P. S., *J. Chem. Educ.* **2005**, *82*, 1660.
60. de Groot, F. M. F.; Vanko, G.; Glatzel, P., *J. Phys.: Condens. Matter* **2009**, *21*, 104207.
61. Tanaka, A.; Jo, T., *J. Phys. Soc. Jpn.* **1992**, *61*, 2040.
62. Cartier dit Moulin, C.; Rudolf, P.; Flank, A. M.; Chen, C. T., *J. Phys. Chem.* **1992**, *96*, 6196.
63. Meisel, A.; Leonhardt, G.; Szargan, R., *X-ray Spectra and Chemical Binding* Springer-Verlag: New York, 1989.
64. (a) Nilsson, A.; Stöhr, J.; Wiell, T.; Aldén, M.; Bennich, P.; Wassdahl, N.; Samant, M. G.; Parkin, S. S. P.; Mårtensson, N.; Nordgren, J.; Johansson, B.; Skriver, H. L., *Phys. Rev. B: Condens. Matter* **1996**, *54*, 2917; (b) Nakamura, J.; Yamada, N.; Kuroki, K.; Callcott, T. A.; Ederer, D. L.; Denlinger, J. D.; Perera, R. C. C., *Phys. Rev. B: Condens. Matter* **2001**, *64*, 174504.
65. Eeckhout, S. G.; Safonova, O. V.; Smolentsev, G.; Biasioli, M.; Safonov, V. A.; Vykhodtseva, L. N.; Sikora, M.; Glatzel, P., *J. Anal. At. Spectrom.* **2009**, *24*, 215.
66. Tsutsumi, K., *J. Phys. Soc. Jpn.* **1959**, *14*, 1696
67. Tsutsumi, K.; Nakamori, H.; Ichikawa, K., *Phys. Rev. B: Condens. Matter* **1976**, *13*, 929.
68. Safonova, O. V.; Tromp, M.; van Bokhoven, J. A.; de Groot, F. M. F.; Evans, J.; Glatzel, P., *J. Phys. Chem. B* **2006**, *110*, 16162.
69. (a) Pizarro, S. A.; Glatzel, P.; Visser, H.; Robblee, J. H.; Christou, G.; Bergmann, U.; Yachandra, V. K., *PCCP* **2004**, *6*, 4864; (b) Visser, H.; Anxolabéhère-Mallart, E.; Bergmann, U.; Glatzel, P.; Robblee, J. H.; Cramer, S. P.; Girerd, J.-J.; Sauer, K.; Klein, M. P.; Yachandra, V. K., *J. Am. Chem. Soc.* **2001**, *123*, 7031; (c) Gamblin, S. D.; Urch, D. S., *J. Electron. Spectrosc. Relat. Phenom.* **2001**, *113*, 179.
70. Peng, G.; de Groot, F. M. F.; Haemaelaenen, K.; Moore, J. A.; Wang, X.; Grush, M. M.; Hastings, J. B.; Siddons, D. P.; Armstrong, W. H., *J. Am. Chem. Soc.* **1994**, *116*, 2914.

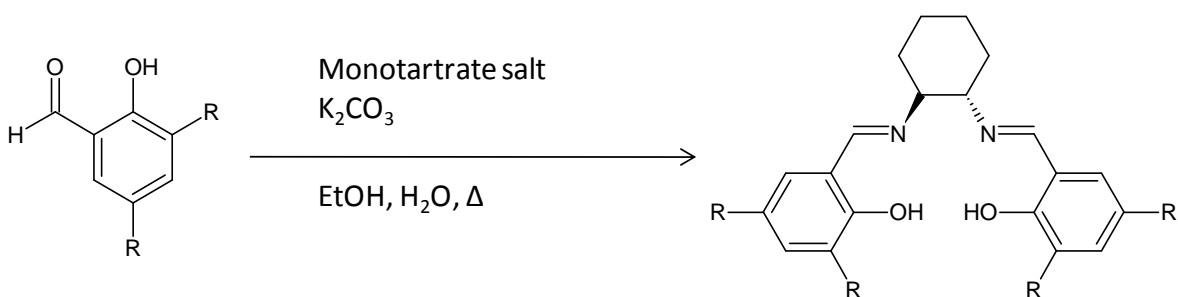
-
71. Messinger, J.; Robblee, J. H.; Bergmann, U.; Fernandez, C.; Glatzel, P.; Visser, H.; Cinco, R. M.; McFarlane, K. L.; Bellacchio, E.; Pizarro, S. A.; Cramer, S. P.; Sauer, K.; Klein, M. P.; Yachandra, V. K., *J. Am. Chem. Soc.* **2001**, *123*, 7804.
 72. Smolentsev, G.; Soldatov, A. V.; Messinger, J.; Merz, K.; Weyhermüller, T.; Bergmann, U.; Pushkar, Y.; Yano, J.; Yachandra, V. K.; Glatzel, P., *J. Am. Chem. Soc.* **2009**, *131*, 13161.
 73. Safonov, V. A.; Vykhodtseva, L. N.; Polukarov, Y. M.; Safonova, O. V.; Smolentsev, G.; Sikora, M.; Eeckhout, S. G.; Glatzel, P., *J. Phys. Chem. B* **2006**, *110*, 23192.
 74. Bergmann, U.; Bendix, J.; Glatzel, P.; Gray, H. B.; Cramer, S. P., *J. Chem. Phys.* **2002**, *116*, 2011.
 75. Yano, J.; Pushkar, Y.; Glatzel, P.; Lewis, A.; Sauer, K.; Messinger, J.; Bergmann, U.; Yachandra, V., *J. Am. Chem. Soc.* **2005**, *127*, 14974.
 76. Glatzel, P.; Bergmann, U.; Yano, J.; Visser, H.; Robblee, J. H.; Gu, W.; de Groot, F. M. F.; Christou, G.; Pecoraro, V. L.; Cramer, S. P.; Yachandra, V. K., *J. Am. Chem. Soc.* **2004**, *126*, 9946.
 77. Caliebe, W. A.; Kao, C. C.; Hastings, J. B.; Taguchi, M.; Kotani, A.; Uozumi, T.; de Groot, F. M. F., *Phys. Rev. B: Condens. Matter* **1998**, *58*, 13452.
 78. Glatzel, P.; Sikora, M.; Fernández-García, M., *Eur. Phys. J. Special Topics* **2009**, *169*, 207.
 79. Daly, A. M.; Renahan, M. F.; Gilheany, D. G., *Org. Lett.* **2001**, *3*, 663.
 80. de Groot, F. M. F., *Top. Catal.* **2000**, *10*, 179.

3 Chapter Three – Experimental

3.1 Introduction

The name salen comes from the precursors salicylaldehyde and ethylenediamine. Salens are among the most widely studied ligands in chemistry¹. They are commonly applied in homogeneous catalysis (see chapter 1). Perhaps the most well known and well studied salen complex is Jacobsen's catalyst (N,N'-bis(3,5-di-tert-butylsalicylidene)-1,2-cyclohexanediaminomanganese(III) chloride)². This coordination complex of manganese and a salen type ligand is used as an asymmetric catalyst in the Jacobsen epoxidation, which is well known for its ability to enantioselectively transform prochiral alkenes into epoxides. Before the development of Jacobsen's catalyst, asymmetric epoxidation catalysts required the substrate to have a directing functional group, for example in Sharpless epoxidation³. Such enantiomerically pure epoxides are important building blocks for complex molecules with specific chirality. Differences in chirality can lead to dramatically different chemical activity in biologically active compounds, therefore the possibility of obtaining specific stereo centres in a molecule is of great importance to the pharmaceutical industry⁴. Jacobsen's catalyst is considered one of the most important in this field and was used to synthesise phenylisoserine, which is a side chain to the famous anti-cancer drug Taxol, in 1992⁵. Salens are also used as ligands for other catalysts that are important for asymmetric synthesis^{1c}.

The salen framework is formed by a double condensation reaction between 2 equivalents of the salicylaldehyde precursor and the (+)-(R,R)-1,2-diammoniumcyclohexane mono-(+)-tartrate salt⁶.



Scheme 1 Condensation reaction for the formation of the salen type ligands.

One of the advantages of these types of ligands is the relatively easy synthetic procedure and the fact that it produces high yields. In theory it also opens up the possibility to introduce steric and electronic tuning of these types of materials. This can be achieved by varying the substituents on the salicylaldehyde precursor. The salen ligands generally appear as bright yellow solids and are soluble in polar organic solvents.

3.2 Preparation of symmetric salen materials

3.2.1 Preparation of salen ligands

3.2.1.1 Preparation of (R,R)-N,N'-Bis(3,5-di-tert-butyl-salicylidene)-1,2-cyclohexanediamine - symmetric salen ligand 1⁶

A three necked round bottomed flask was equipped with a mechanical stirrer, a reflux condenser, and an addition funnel. The flask was charged with monotartrate salt (3.712 g, 14.0 mmol, 1.0 equiv), K₂CO₃ (3.924 g, 28.4 mmol, 2.0 equiv), and distilled water (15 mL). The mixture was stirred until dissolution was achieved, before adding ethanol (30 mL). The resulting cloudy solution was heated to reflux (75-80 °C), and 3,5-di-tert-butyl-2-hydroxybenzaldehyde in ethanol (6.7 g, 28.6 mmol in 30 ml, 2.0 equiv) was added drop wise using an addition funnel. The funnel was rinsed with ethanol, and the yellow slurry was refluxed for 2 h before allowing it to cool to room temperature. Water (6 mL) was added and the mixture was stirred and cooled to <5 °C over 2 h and stirred at that temperature for an additional hour. The yellow product was collected by vacuum filtration and washed with ethanol (2x15 mL). The crude solid was re-dissolved in CH₂Cl₂ and washed with water and NaCl. After drying over Na₂SO₄ the solvent was removed *in vacuo* and the solid was isolated as a yellow powder (7.05 g, 12.8 mmol, 92%).

3.2.1.2 2,2'-((1R,2R)-(-)-1,2-cyclohexanediylbis((E)(nitrilomethylidene))Bis(4-(tert-butyl)-6-4-(4-morpholinylmethyl)phenol) -1,2-cyclohexanediamine – salen ligand 3

Salen ligand 3 was purchased from Sigma Aldrich and used as received.

3.2.1.3 2,2'-[(1R,2R)-1,2-Cyclohexanediylbis[(E)-(nitrilomethylidene)]bis[4-(tert-butyl)-6-(4-piperidinylmethyl)phenol] -1,2-cyclohexanediamine – salen ligand 4

Salen ligand 4 was purchased from Sigma Aldrich and used as received.

3.2.2 Preparation of Pyrrolidine (salen) Cr^{III}-Cl complexes⁷

3.2.2.1 Preparation of ((N,N'-3,5-di-tert-butylsalicylidene)-1,2-cyclohexanediaminato)-chloro-chromium(III) Pyrrolidine (salen) Cr^{III}-Cl complex (1)⁷

All Cr(salen) complexes were synthesised using Schlenk techniques. Dry tetrahydrofuran (THF, 10 mL) was added to a mixture of CrCl₂ (0.184 g, 1.50 mmol, 1.5 equiv) and monomeric ligand (0.546 g, 1.00 mmol, 1 equiv). The mixture was stirred under N₂ for 6 h. and saturated aqueous ammonium chloride was added (10 mL). The mixture was then stirred under air for 6 h before being diluted with tert-butyl-methyl ether (25 mL). The aqueous layer was removed before washing the organic layer with saturated ammonium chloride (25 mL x 4) and brine (25 mL x 2), dried over Na₂SO₄, concentrated under vacuum, and dried by azeotropic distillation with benzene (3 x 5 mL) to give the product as a brown solid (0.557 g, 0.88 mmol, 88%).

3.2.2.2 Preparation of 2,2'-((1R,2R)-(-)-1,2-cyclohexanediylbis)((E)(nitrilomethylidyne))Bis(4-(tert-butyl)-6-(4-morpholinylmethyl)phenol) Cr^{III} Cl complex (3)⁷

All Cr(salen) complexes were synthesised using Schlenk techniques. Dry tetrahydrofuran (THF, 10 mL) was added to a mixture of CrCl₂ (0.058 g, 0.47 mmol, 1.5 equiv) and monomeric ligand (0.200 g, 0.32 mmol, 1 equiv). The mixture was stirred under N₂ for 6 h. and saturated aqueous ammonium chloride was added (10 mL). The mixture was then stirred under air for 6 h before being diluted with tert-butyl-methyl ether (25 mL). The aqueous layer was removed before washing the organic layer with saturated ammonium chloride (25 mL x 4) and brine (25 mL x 2), dried over Na₂SO₄, concentrated under vacuum, and dried by azeotropic distillation with benzene (3 x 5 mL) to give the product as a brown solid (0.040 g, 0.055 mmol, 17 %).

3.2.2.3 Preparation of 2,2'-[(1R,2R)-1,2-Cyclohexanediylbis[(E)-(nitrilomethylidyne)]bis[4-(tert-butyl)-6-(4-piperidinylmethyl)phenol] Cr^{III} Cl complex (4)⁷

All Cr(salen) complexes were synthesised using Schlenk techniques. Dry tetrahydrofuran (THF, 10 mL) was added to a mixture of CrCl₂ (0.058 g, 0.48 mmol, 1.5 equiv) and monomeric ligand (0.200 g, 0.32 mmol, 1 equiv). The mixture was stirred under N₂ for 6

h. and saturated aqueous ammonium chloride was added (10 mL). The mixture was then stirred under air for 6 h before being diluted with tert-butyl-methyl ether (25 mL). The aqueous layer was removed before washing the organic layer with saturated ammonium chloride (25 mL x 4) and brine (25 mL x 2), dried over Na₂SO₄, concentrated under vacuum, and dried by azeotropic distillation with benzene (3 x 5 mL) to give the product as a brown solid (0.105 g, 0.15 mmol, 31%).

3.3 Characterisation

Infrared spectra of complexes were recorded as Nujol mulls between CsI plates over the range 4000–200 cm⁻¹ using Perkin-Elmer 983G. Infrared spectra of ligands were recorded as pure compound solid samples using a Thermo Nicolet 380 FT-IR spectrometer with a Smart Orbit Goldengate attachment. ¹H and ¹³C{¹H} NMR spectra were recorded at ambient temperatures using a Bruker AV300 spectrometer and referenced internally to the solvent resonance. Mass spectra were obtained by positive ion electrospray (ES⁺) in a methanol solution using a VG Biotech platform. Reference UV/Vis spectra were recorded using a Perkin Elmer Lambda 19 spectrometer as solids by diffuse reflectance (DR) using BaSO₄ as a diluent. Solution UV/Vis spectra were obtained using Perkin-Elmer Lambda 2s with a double beam or a Perkin-Elmer Lambda XLS with a single beam. In both cases the samples were dissolved in ethanol and referenced with a blank of the solvent used. The wavelength range measured was 50,000 - 12,500 cm⁻¹ (200-800 nm).

3.3.1 Characterisation of salen ligand 1

ES⁺ (m/z): 635 [C₃₆H₅₄N₂O₂]⁺; UV/Vis frequency (EtOH)/cm⁻¹ (ε/dm³mol⁻¹cm⁻¹) 30300 (9000). IR (nujol mull)/cm⁻¹: 2949 (νCH), 2867 (νCH₂), 1629 (ν imine), 1592 (ν C=C). ¹H NMR (300 MHz, CDCl₃) δ ppm 1.16 (s, 18 H, ^tBu) 1.33 (s, 18 H, ^tBu) 1.51 - 1.93 (m, 8 H, CH₂ methylene) 3.18 - 3.30 (m, 2 H, N-CH) 6.90 (d, J=2.56 Hz, 2 H, CH aromatic) 7.22 (d, J=2.20 Hz, 2 H, CH aromatic) 8.22 (s, 2 H, N=CH) 13.64 (s, 2 H, OH).

3.3.2 Characterisation of salen ligand 3

ES⁺ (m/z): 719 [C₃₈H₅₆N₄O₄]⁺; UV/Vis frequency (EtOH)/cm⁻¹ (ε/dm³mol⁻¹cm⁻¹) 35700 (1410), 29400 (4650), 23500 (380); IR (golden gate) 2951 (νCH), 2848 (νCH₂), 1624 (ν imine), 1596 (ν C=C) cm⁻¹; ¹H NMR (300 MHz, CDCl₃) δ ppm 1.26 (s, 18 H, ^tBu) 1.35 - 1.99 (m, 8 H, CH₂ methylene) 2.46 - 2.57 (m, 8 H, N-CH₂) 3.26 - 3.38 (m, 2 H, N-CH) 3.57 (d, J=14.27 Hz, 4 H, NCH₂ next to aromatic ring) 3.68 - 3.77 (m, 8 H, O-CH₂) 7.09 (s, 2 H, CH

aromatic) 7.33 - 7.40 (m, 2 H, CH aromatic closest to N) 8.30 (s, 2 H, N=CH) 13.41 - 13.52 (m, 2 H, OH).

3.3.3 Characterisation of salen ligand 4

ES⁺ (m/z): 715 [C₄₀H₆₀N₄O₂]⁺; UV/Vis frequency (EtOH)/cm⁻¹ (ε/dm³mol⁻¹cm⁻¹) 35700 (1620), 29400 (4580), 23500 (350); IR (golden gate) 2928 (νCH), 2852 (νCH₂), 1630 (ν imine), 1598 (ν C=C) cm⁻¹; ¹H NMR (300 MHz, CDCl₃) δ ppm 1.17 (s, 18 H, ^tBu) 1.50 (d, *J*=5.49 Hz, 20 H, CH₂ methylene and N ring) 2.35 (br. s., 8 H, N-CH on the N ring) 3.17 - 3.28 (m, 2 H, N-CH) 3.45 (d, *J*=14.27 Hz, 4 H, N-CH₂) 6.95 - 7.02 (m, 2 H, CH aromatic) 7.23 - 7.32 (m, 2 H, CH aromatic closest to N) 8.21 (s, 2 H, N=CH).

3.3.4 Characterisation of salen complex 1

UV/Vis Frequency (EtOH)/cm⁻¹ (ε/dm³mol⁻¹cm⁻¹) 32300 (6730), 23500 (2620), 20400 (950); IR (nujol mull) 2950 (νCH), 2860 (νCH₂), 1620 (ν imine), 1535 (ν C=C), 365 (ν Cr-Cl) cm⁻¹.

3.3.5 Characterisation of salen complex 3

ES⁺ (m/z): 719 [salen complex 3 + H⁺]; UV/Vis frequency (EtOH)/cm⁻¹ (ε/dm³mol⁻¹cm⁻¹) 35700 (7330), 29400 (2160), 23500 (1800), 20000 (180); IR (nujol mull) 2931 (νCH), 2850 (νCH₂), 1620 (ν imine), 1550 (ν C=C), 475 (ν Cr-Cl)cm⁻¹.

3.3.6 Characterisation of salen complex 4

ES⁺ (m/z): 715 [salen complex 4 + H⁺]; UV/Vis frequency (EtOH)/cm⁻¹ (ε/dm³mol⁻¹cm⁻¹) 35700 (7800), 29400 (2940), 25000 (2730); IR (Nujol mull) 2930 (νCH), 2850 (νCH₂), 1631 (ν imine), 1547 (ν C=C), 454 (ν Cr-Cl) cm⁻¹.

3.4 Preparation of Iodosobenzene⁸

Finely ground iodosobenzene diacetate (32.20 g, 0.10 mol) was placed in a beaker; 3M sodium hydroxide was added over a 5 minute period with vigorous stirring. The lumps of solid that form were triturated with a stirring rod for 15 minutes, and the reaction mixture was left to stand for an additional 45 minutes to complete the reaction. Water (100 mL) was added, the mixture was stirred vigorously and the crude solid was collected on a Buchner funnel. The wet solid was returned to the beaker and triturated in 200 mL water. The solid was again collected on the Buchner funnel, washed there with water (15 mL), and dried by maintaining suction. Final purification was achieved by triturating the dried

solid in chloroform (75 mL). The iodosobenzene was separated by filtration and air dried. (20.825 g, 0.95 mol, 95%).

3.5 Epoxidation of trans- β -methylstyrene by the Cr(V)=O salen catalysts⁹

Iodosobenzene (0.0125 g, 0.057 mmol, 1.2 equiv) was added to a stirred solution of the salen complex 1 (0.030 g, 0.047 mmol, 1 equiv) in CH₃CN (5 mL). A deep green/black colour appeared. After stirring for 30 minutes this solution was filtered and the filtrate cooled to 0 °C using an ice/water bath. Ph₃PO (0.0132 g, 0.047 mmol, 1 equiv) was added, after 5 minutes trans- β -methylstyrene (0.006 mL, 0.047 mmol, 1 equiv). The reaction mixture was stirred at 0 °C until the solution was orange-brown indicating the reaction had gone to completion. The solvent was removed *in vacuo* and the residue treated with diethyl ether. The diethyl ether washings were flushed through an alumina plug.

3.6 Spectroscopic Techniques

The HERFD, normal XANES and RIXS spectra were collected at beamline ID26 at the European Synchrotron Radiation Facility (ESRF, Grenoble, France). The storage ring was operated in 16 bunch mode with a beam current of between 60 to 90 mA with an electron energy of 6 GeV. The incident energy was selected with a Si (311) double crystal monochromator, the monochromator was calibrated by using a Cr metal foil. The incoming beam passed a Si-coated collimating mirror, the monochromator, and a Si-coated focusing mirror (rejecting higher harmonics). For the energy resolved measurement of the K α emitted X-rays 5 spherically bent (R = 1 m) Ge (422) crystals in Rowland geometry were used with an avalanche photo diode (APD) as counter. The overall energy resolution of the spectrometer was determined to be 0.6 eV by scanning the elastic peak. HERFD XANES spectra were recorded by setting the spectrometer to the maximum of the Cr K α_1 fluorescence line. The samples were measured as pressed powders, and in some cases as solutions, and were orientated at 45° relative to the incident beam. The K β emission lines were measured using a spherically bent Ge (333) crystal with a 850 mm bending radius. The energy resolution was determined to be 1 eV. To obtain the 2-dimensional 1s2p RIXS planes, scans were recorded as a function of incident energy and the measured fluorescence energy was varied in steps of 0.4 eV.

Quick pre-edge scans were taken before and after the collection of the RIXS planes in order to test for any beam damage experienced by the samples. The RIXS data processing

was done with MATLAB (The MathWorks TM, Inc.) using codes developed by the ID26 staff. The measured intensities were plotted in a 2-dimensional grid of incident energy (Ω) versus energy transfer or final state energy ($\Omega - \omega$, where ω is the emitted energy). The main edge in the Cr spectra does not have any visible effects on the pre-edge region and so was not subtracted.

The L-edge XANES experiments were performed at beamline I06 at Diamond Light Source (Harwell Science and Innovation Park, Didcot, UK). The storage ring was operated in normal mode with a beam current of 250 mA with an electron energy of 3 GeV. The incident energy was selected with a collimated light plane grating monochromator with a 2.250 fixed focus constant. The experiments were measured in total electron yield mode, where the sample is connected to ground through an ammeter and the neutralization current is monitored by a total electron yield detector. The overall energy resolution of the spectrometer was determined to be 0.05 eV. Due to the fact that the soft X-rays are absorbed by air the synchrotron radiation travels from the ring in an evacuated beamline to the end-station where the samples are mounted in a UHV chamber.

3.6.1 Cr K-edge XANES FEFF9 calculations

FEFF is an automated program for performing *ab initio* multiple scattering calculations of X-ray Absorption Fine Structure (XAFS), X-ray Absorption Near-Edge Structure (XANES) and various other spectra for clusters of atoms. The code provides scattering amplitudes and phases used in many modern XAFS analysis codes, as well as various other properties¹⁰.

FEFF9 has a variety of new features and options over that of FEFF8. The improvements include; 1) *ab initio* Debye-Waller factors; 2) improved treatment of inelastic losses; 3) an improved treatment of the core hole interaction; and 4) more accurate treatment of crystalline systems¹¹.

FEFF also allows the simultaneous calculation of excitation spectra and electronic structure of materials. The approach takes into account core hole effects and can include local fields. The possible applications of the program include performing simulations of extended X-ray-Absorption Fine Structure (EXAFS) experiments, full multiple scattering calculations of various X-ray Absorption Spectra (XAS) and projected local densities of states (LDOS) calculations¹⁰. The spectra include X-ray Absorption Near Edge Structure (XANES), non-resonant X-ray Emission Spectra (XES) as shown in this work but other types of spectroscopy can also be simulated especially with the development of FEFF9.

The theoretical frame work behind the FEFF code is based on the real-space Green's function approach for which the explicit calculation of final states is avoided by expressing the Fermi Golden rule in terms of a single-particle Green's function in the presence of an appropriately screened core hole ('final state rule')¹². There are two factors in the development of the FEFF code, which offer the possibility to interpret XANES either in terms of the local electronic structure or within an EXAFS-like scattering picture and these are i) the implementation of full multiple scattering (FMS) cluster calculations of both XAS and the density of states (DOS) and ii) the use of self-consistent field (SCF) potentials¹².

In FEFF the SCF loop calculates the Coulomb potentials, the electron density, the Fermi energy E_f , occupation numbers and the charge transfer q_i between atoms¹². It is the charge transfer that accounts for the chemical properties of the different elements such as oxidation state and electron affinity and therefore is especially important in coordination compounds, for which metal-ligand bonding occurs through charge transfer (dative bonding)¹². The X-ray absorption spectrum based on the SCF scattering potentials contains information on chemical properties such as hybridisation and charge transfer¹², it is because of this that we are able to obtain structural and electronic information on the system.

3.6.1.1 Parameters used in the FEFF9 simulations

Cr₂O₃: Exchange model [ixc]: 2 (ground state + a constant imaginary part); E_0 correction /Fermi level shift [V_r]: -1.17; pure imaginary potential [V_i]: -1.4; ground state potential [ixco]; 2; SCF: 6.0; FMS: 12.0. Three different potential labels were used for the absorbing Cr atom, the non-absorbing Cr atom and the O atom.

The SCF calculations were performed on a cluster with a radius of 6 Å that contains 92 atoms of the molecule and FMS calculations with a radius of 12 Å that contains all 499 atoms of the molecule. The coordinates of the input structure was obtained from X-ray crystal structure database.

CrO₃: Exchange model [ixc]: 2 (ground state + a constant imaginary part); E_0 correction /Fermi level shift [V_r]: -1.17; pure imaginary potential [V_i]: -1.4; ground state potential [ixco]; 2; SCF: 6.0; FMS: 12.0. Three different potential labels were used for the absorbing Cr atom, the non-absorbing Cr atom and the O atom.

The SCF calculations were performed on a cluster with a radius of 6 Å that contains 66 atoms of the molecule and FMS calculations with a radius of 12 Å that contains all 66

atoms of the molecule. The coordinates of the input structure was obtained from X-ray crystal structure database.

CrCl₃: Exchange model [ixc]: 2 (ground state + a constant imaginary part); E₀ correction /Fermi level shift [V_r]: -1.17; pure imaginary potential [V_i]: -1.4; ground state potential [ixco]; 2; SCF: 6.0; FMS: 12.0. Three different potential labels were used for the absorbing Cr atom, the non-absorbing Cr atom and the Cl atom.

The SCF calculations were performed on a cluster with a radius of 6 Å that contains 41 atoms of the molecule and FMS calculations with a radius of 12 Å that contains all 41 atoms of the molecule. The coordinates of the input structure was obtained from X-ray crystal structure database.

K₂CrO₄: Exchange model [ixc]: 2 (ground state + a constant imaginary part); E₀ correction /Fermi level shift [V_r]: -1.17; pure imaginary potential [V_i]: 0; ground state potential [ixco]; 2; SCF: 6.0; FMS: 12.0. Four different potential labels were used for the absorbing Cr atom, the non-absorbing Cr atom, the K atom and the O atom.

The SCF calculations were performed on a cluster with a radius of 6 Å that contains 49 atoms of the molecule and FMS calculations with a radius of 12 Å that contains all 71 atoms of the molecule. The coordinates of the input structure was obtained from X-ray crystal structure database.

K₂Cr₂O₇: Exchange model [ixc]: 2 (ground state + a constant imaginary part); E₀ correction /Fermi level shift [V_r]: -1.17; pure imaginary potential [V_i]: 0; ground state potential [ixco]; 2; SCF: 6.0; FMS: 12.0. Four different potential labels were used for the absorbing Cr atom, the non-absorbing Cr atom, the K atom and the O atom.

The SCF calculations were performed on a cluster with a radius of 6 Å that contains 51 atoms of the molecule and FMS calculations with a radius of 12 Å that contains all 51 atoms of the molecule. The coordinates of the input structure was obtained from X-ray crystal structure database.

Na₂CrO₄: Exchange model [ixc]: 2 (ground state + a constant imaginary part); E₀ correction /Fermi level shift [V_r]: -1.17; pure imaginary potential [V_i]: 0; ground state potential [ixco]; 2; SCF: 6.0; FMS: 12.0. Four different potential labels were used for the absorbing Cr atom, the non-absorbing Cr atom, the Na atom and the O atom.

The SCF calculations were performed on a cluster with a radius of 6 Å that contains 60 atoms of the molecule and FMS calculations with a radius of 12 Å that contains all 93

atoms of the molecule. The coordinates of the input structure was obtained from X-ray crystal structure database.

Na₂Cr₂O₇: Exchange model [ixc]: 2 (ground state + a constant imaginary part); E_o correction /Fermi level shift [V_r]: -1.17; pure imaginary potential [V_i]: 0; ground state potential [ixco]; 2; SCF: 6.0; FMS: 12.0. Four different potential labels were used for the absorbing Cr atom, the non-absorbing Cr atom, the Na atom and the O atom.

The SCF calculations were performed on a cluster with a radius of 6 Å that contains 51 atoms of the molecule and FMS calculations with a radius of 12 Å that contains all 51 atoms of the molecule. The coordinates of the input structure was obtained from X-ray crystal structure database.

Cr(acac)₃: Exchange model [ixc]: 2 (ground state + a constant imaginary part); E_o correction /Fermi level shift [V_r]: -1.17; pure imaginary potential [V_i]: -1.4; ground state potential [ixco]; 2; SCF: 6.0; FMS: 12.0. Three different potential labels were used for the absorbing Cr atom, the C atom and the O atom.

The SCF calculations were performed on a cluster with a radius of 6 Å that contains 42 atoms of the molecule and FMS calculations with a radius of 12 Å that contains all 42 atoms of the molecule. The coordinates of the input structure was obtained from X-ray crystal structure database.

Cr(CO)₆: (no distortion) Exchange model [ixc]: 2 (ground state + a constant imaginary part); E_o correction /Fermi level shift [V_r]: -1.17; pure imaginary potential [V_i]: -1.4; ground state potential [ixco]; 2; SCF: 6.0; FMS: 12.0. Four different potential labels were used for the absorbing Cr atom, the non-absorbing Cr atom, the C atom and the O atom.

The SCF calculations were performed on a cluster with a radius of 6 Å that contains 64 atoms of the molecule and FMS calculations with a radius of 12 Å that contains all 458 atoms of the molecule. The coordinates of the input structure was obtained from X-ray crystal structure database.

3.6.2 Cr L-edge XANES CTM calculations

Theoretical Cr L-edge calculations were performed using the Charge Transfer Multiplet (CTM) program developed by de Groot¹³. The strength of the crystal field (in both the initial and the final state) and a factor with which to reduce the ab initio Hartree-Fock values are needed as inputs for the CTM calculations. The shape, position, and intensity of the peaks (after broadening) appear to be mainly influenced by the crystal field strength

and the 3d-3d Slater- Condon parameters (F2 and F4). The crystal field strength parameters for these XAS calculations are related to those derived from UV/Vis spectra, however as explained in chapter 4 the initial and final state values are different. This may be partly affected by the presence of a core hole. Crystal field parameters ($10Dq$) ranging from 1 eV to 3 eV were employed relatively successfully in the Cr L_{2,3} edge CTM calculations of Cr references.

For our calculations, we assumed perfect octahedral (Oh) or tetrahedral (T_d) symmetry and tried $10Dq$ values between 1 and 3 eV. This is obviously not the correct geometry for all samples but they are the only two options in the code, and therefore is the only thing that can be done. The scaling parameter for the Slater integrals was varied between 40% and 70%. A Lorentzian broadening of 0.1-0.9 eV (HWHM) and a Gaussian broadening of 0.2 eV (σ) was used to convert the discrete electronic transitions into a continuous spectrum. The CTM calculations did not contain an estimate of the absolute energy. The absolute energy scale was therefore adjusted manually to match the experimental data.

3.6.2.1 Parameters used in the CTM calculations

Cr₂O₃: $10Dq = 2$ eV, SK = 70%, $2\Gamma = 0.1$ up to 582eV, then 0.7 after, $\sigma = 0.3$ eV. **CrCl₃**: $10Dq = 1$ eV, SK = 60%, $2\Gamma = 0.1$ up to 585 eV, then 0.4 after, $\sigma = 0.2$ eV. **Cr(acac)₃**: $10Dq = 2$ eV, SK = 75%, $2\Gamma = 0.2$ up to 582eV, then 0.7 after, $\sigma = 0.2$ eV. **Na₂CrO₄**: $10Dq = -1.6$ eV, SK = 40%, $2\Gamma = 0.2$ up to 597 eV, then 0.7 after, $\sigma = 0.2$ eV. **CrO₃**: $10Dq = -3$ eV, SK = 50%, $2\Gamma = 0.4$ up to 597 eV, then 0.9 after, $\sigma = 0.8$ eV, Spin-orbit on, no charge transfer. **Cr(salen₁)**: $10Dq = 2$ eV, SK = 65%, $2\Gamma = 0.1$ up to 586 eV, then 0.6 after, $\sigma = 0.2$ eV, Spin-orbit on, no charge transfer. **Cr(salen₃)**: $10Dq = 2$ eV, SK = 65%, $2\Gamma = 0.1$ up to 584 eV, then 0.6 after, $\sigma = 0.2$ eV, Spin-orbit on, no charge transfer. **Cr(salen₄)**: $10Dq = 2$ eV, SK = 65%, $2\Gamma = 0.1$ up to 586 eV, then 0.6 after, $\sigma = 0.2$ eV, Spin-orbit on, no charge transfer.

The Slater integrals are calculated with the Hartree-Fock approach within the RCN code of Cowan¹⁴, these HF values are reduced by 20% to take into account configuration interaction effects. These 80% of HF values describe the atomic spectra well¹⁴. The 3d spin-orbit interaction is 'switched on'.

3.6.3 Cr RIXS RGAss calculations

The RGAss program used to calculate the 1s2p RIXS experiments is a PC interface to the Atomic Multiplet Code written by R.D.Cowan (LANL) with extensions by B.T.Thole and others. The program consists of different components used to produce the final simulation; RCN/RCN2/RCG - Copyright Los Alamos National Laboratory and U.S. Government, RACER - Copyright 1984-1996 B. T. Thole and TFluor - Copyright B. T. Thole, H. Ogasawara, M. A. van Veenendaal, P. Ferriani, and C. M. Bertoni.

RGAss includes the electronic configurations for the ground states, intermediate states and final states in the excitation and emission processes as well as parameters for the local geometry of the central atom, crystal field splitting value, the type of transition probed (dipole or quadrupole), charge transfer effects, p-d / d-d interactions (U_{pd} and U_{dd} and degree of mixing) and a Gaussian broadening of full width at full maximum (FWFM), this is in contrast to that used in the CTM approach which uses the full width at half maximum (FWHM).

3.6.3.1 Parameters used in the RGAss calculations

Cr₂O₃: charge transfer: on, crystal field value: 2, Slater integral reduction: 70%. **CrO₃**: charge transfer: off, crystal field value: 3, Slater integral reduction: 50%. **CrCl₃**: charge transfer: on, crystal field value: 2, Slater integral reduction: 60%. **K₂CrO₄**: charge transfer: off, crystal field value: 0.7, Slater integral reduction: 40%. **K₂Cr₂O₇**: charge transfer: , crystal field value: , Slater integral reduction: %. **Cr(acac)₃**: charge transfer: on, crystal field value: 2, Slater integral reduction: 75%. **Cr(salen1)**: charge transfer: on, crystal field value: 2, Slater integral reduction: 65%. **Cr(salen3)**: charge transfer: on, crystal field value: 2, Slater integral reduction: 65%. **Cr(salen4)**: charge transfer: on, crystal field value: 2, Slater integral reduction: 65%.

3.7 References

1. (a) Bandini, M.; Cozzi, P. G.; Umani-Ronchi, A., *Chem. Commun.* **2002**, 919; (b) Canali, L.; Sherrington, D. C., *Chem. Soc. Rev.* **1999**, *28*, 85; (c) Holbach, M.; Zheng, X.; Burd, C.; Jones, C. W.; Weck, M., *J. Org. Chem.* **2006**, *71*, 2903; (d) Katsuki, T., *Adv. Synth. Catal.* **2002**, *344*, 131; (e) Larrow, J. F.; Jacobsen, E. N., *Topics. Organomet. Chem.* **2004**, *6*, 123.
2. (a) Jacobsen, E. N.; Zhang, W.; Muci, A. R.; Ecker, J. R.; Deng, L., *J. Am. Chem. Soc.* **1991**, *113*, 7063; (b) Yoon, T. P.; Jacobsen, E. N., *Science* **2003**, *299*, 1691.
3. Crabtree, R. H., Wiley: 2005; p 405.
4. Caputo, C. A.; Jones, N. D., *Dalton Trans.* **2007**, 4627.
5. Deng, L.; Jacobsen, E. N., *J. Org. Chem.* **1992**, *57*, 4320.
6. Larrow, J. F.; Jacobsen, E. N.; Gao, Y.; Hong, Y.; Nie, X.; Zepp, C. M., *J. Org. Chem.* **1994**, *59*, 1939.
7. Konsler, R. G.; Karl, J.; Jacobsen, E. N., *J. Am. Chem. Soc.* **1998**, *120*, 10780.
8. (a) Saltzman, H.; Sharefkin, J. G., *Org. Synth.* **1973**, *5*; (b) Saltzman, H.; Sharefkin, J. G., *Org. Synth.* **1963**, *5*, 60.
9. Kerrigan, N. J.; Müller-Bunz, H.; Gilheany, D. G., *J. Mol. Catal. A: Chem.* **2005**, *227*, 163.
10. Rehr, J. J.; Kas, J. J.; Vila, F. D.; Prange, M. P.; Jorissen, K., *PCCP* **2010**, *12*, 5503.
11. Ankudinov, A. L.; Ravel, B.; Rehr, J. J.; Conradson, S. D., *Phys. Rev. B: Condens. Matter* **1998**, *58*, 7565.
12. van der Veen, R. M.; Kas, J. J.; Milne, C. J.; Pham, V.-T.; Nahhas, A. E.; Lima, F. A.; Vithanage, D. A.; Rehr, J. J.; Abela, R.; Chergui, M., *PCCP* **2010**, *12*, 5551.
13. (a) de Groot, F. M. F.; Kotani, A., In *Core Level Spectroscopy of Solids*, CRC Press: 2008; pp 93; (b) Stavitski, E.; de Groot, F. M. F., *Micron* **2010**, *41*, 687.
14. Ikeno, H.; de Groot, F. M. F.; Stavitski, E.; Tanaka, I., *J. Phys.: Condens. Matter* **2009**, *21*, 104208.

Chapter Four: Systematic spectroscopic study of reference chromium materials

4.1 Introduction

In order to develop a deeper understanding of the RIXS technique, it is important to start this study with a systematic investigation of reference chromium compounds with well defined structures and oxidation states. This chapter begins by looking at the Cr K-edge XANES as well as Cr L-edge absorption spectra along with associated calculations before moving on to emission studies. Later in the chapter $K\beta$ emission studies as well as RIXS spectra for the same compounds are shown. Understanding the information obtained from XES, HERFD and RIXS is still in its initial stages. The underlying theory is not straightforward, with different core holes at different stages of the RIXS process interacting with all other molecular orbitals, and is still very much under development using different theoretical approaches. All will be demonstrated in a step-by-step manner in this chapter.

At the Cr K-edge the $1s \rightarrow 4p$ transition is probed, providing direct information on the unoccupied density of states (DOS) with p-character. The L-edge originates from the $2p \rightarrow 3d$ transition and therefore provides direct information on the metal 3d shell, which is fundamental in determining the chemistry of transition metals. The $1s2p$ RIXS ($1s$ denotes the primary excitation and $2p$ refers to the location of the core hole in the final state) contains information similar to both the Cr K- and L-edges as well as complementary information regarding the electronic structure of the filled density of states¹. The RIXS spectrum provides a clearer picture of the pre-edge features including higher resolution and separation of features due to a reduced lifetime broadening affecting the spectrum^{1d, 2}. This then means that the direct correlation between the absorption and emission features is revealed. As well as the additional information regarding the pre-edges, we also indirectly probe the L-edge due to the fact that the final state in the RIXS process is the same as the final state reached in the direct L-edge experiments^{1d}. The $K\beta$ emission studies provide information on the nature of the ligands surrounding the central Cr atom. Looking at the valence-to-core emission lines gives us detailed information on the first coordination shell of Cr; the $K\beta$ emission spectra of 3d metals are known to show pronounced chemical sensitivity³.

There are two distinct methods of addressing the analysis of the pre-edge region; the finger print approach, using the pre-edge as a comparison with known references, and the calculations to accurately simulate the experiment. Previously the Cr K-edge XANES region of reference compounds has frequently been used as a fingerprint in terms of analysing less defined systems. XANES spectra are taken of compounds with well defined geometries and oxidation states and these are then used to compare to the XANES spectra of unknowns. In the XAS study of the Phillips catalyst by E. Groppo *et al.*⁴ CrO₃ and Cr₂O₃ XANES spectra were measured and compared to that of the Cr catalyst and used to identify the Cr species present. Similarly the work by M. Santhosh Kumar *et al.*⁵ also uses XANES spectra of model compounds to assess the different phases of the Cr active species present in the industrial Cr catalysts for the dehydrogenation of propane. The work by F.G. Requejo *et al.*⁶ uses the XANES spectra of pure Cr(CO)₆, Cr₂O₃ and K₂Cr₂O₇ to compare directly with their supported Cr materials (Cr-MCM-41), the purpose being to deduce coordination geometry and oxidation state by inspection of pre-edge features and edge shifts. Wilke and co-workers determined a correlation between pre-edge intensity and the local site symmetry⁷. So even without a detailed theoretical analysis, the pre-edge and edge structures can be used to derive detailed information on the possible types of species present. Although such approaches to analysing the pre-edge region are interesting, there is a great deal more information that can be extracted by performing detailed calculations⁸.

This chapter focuses on Cr references with known and well defined oxidation states and structures, which help to explore and develop the different X-ray absorption and emission techniques. The following chapter will then investigate homogeneous Cr catalysts in detail. First the Cr reference compounds were characterised with Cr K-edge XAS, both normal and HERFD experiments were performed along with theoretical simulations using FEFF⁹. These were followed with Cr L-edge XAS (both soft X-ray and, indirect, hard X-ray studies) and X-ray emission studies (XES, RIXS).

4.2 Theory

The different theoretical approaches used to calculate the pre-edges are generally considered as belonging to one of three categories; (i) the multi-electronic approach based on the Ligand Field Multiplet theory (LFM)⁹, (ii) the single-particle approach based on Density Functional Theory (DFT)¹⁰, an (iii) the many-body Green's function methods¹¹.

In this work we use the first and third approach. The XAS K-edge XANES are simulated using the FEFF code in order to perform local density of states calculations. FEFF is a real space multiple scattering code based on a single electron excitation¹². The basic

independent particle theory of XAS is already well developed, but ignores many important many-body effects which are important for reliable XANES simulations¹². For this reason more recent theoretical studies are aimed at first principles calculation and the modelling of many-body effects beyond that of the single particle picture¹². The developments are based on the real-space Green's function (RSGF) approach, and include the treatment of many-body effects. The three principles behind the improved calculations from FEFF8.4 to FEFF9 are: i) an extension of the RSGF code for full-spectrum calculations; ii) an efficient many-pole representation of the dielectric function; iii) an efficient Lanczos approach for phonon spectra and Debye-Waller (DW) factors¹². The FEFF9 approach also includes solid state effects (edge shifts, fine structure, and temperature dependent Debye-Waller factors).

The RSGF approach has already been widely used in the analysis of Extended X-ray Absorption Fine Structure (EXAFS) as well as for XANES¹³. An X-ray absorption spectrum is basically a measurement of the 'X-ray absorption coefficient' ($\mu(\omega)$) which characterises the decay in intensity (I) of X-rays passing through a material of a given thickness (d)¹⁴.

$$I(d) = I_0 e^{-\mu(\omega)d} \quad \text{(equation 1)}$$

The FEFF program includes limited input parameters; the type of exchange potential, the ranges of Full Multiple Scattering (FMS) and Self-Consistent Field (SCF) muffin tin potential calculations, the maximum angular quantum number, and the atomic numbers of the central absorbing atom in the sample, and its surrounding neighbours, along with their coordinates^{8a}. These can be generated from ATOMS (one of the cards in the FEFF input file) using crystallographic data. Recent advances in FEFF have seen the development of parameter free approaches for calculations of the spectra that include many-body effects¹².

The Charge Transfer Multiplet approach is not used for the calculations at the K-edge as there is no need to consider any multiplet effects, because the single electron description works well. However it is used when looking at the $L_{2,3}$ edges of Cr. The multiplet calculations describe the transition for a single Cr ion from a $3d^n$ ground state to $\underline{2p}3d^{n+1}$ final state ($\underline{2p}$ denotes the position of the core hole)¹⁵.

All multiplet calculations start with the atomic multiplet calculations and then different effects are included afterwards¹⁶. Cowan's atomic multiplet program is used to calculate

the initial and final state, final state coulomb and exchange interactions, and the 2p and 3d spin orbit interactions ¹⁵.

In CTM theory, in addition we take into account the many-body effects that become important in the case of the Cr L-edges, i.e. the charge transfer and multiplet effects ¹⁷. In this calculation charge transfer effects and covalency are taken into account by a reduction of the *ab initio* Hartree-Fock values of the coulomb and exchange integrals ¹⁵. The local symmetry is described using a crystal field splitting only. Both of these factors are important for the calculation of most XPS and XAS spectra for transition metal systems ¹⁷.

The CTM theory is an extension of the atomic multiplet theory; in this case the atomic multiplet coupling effect is taken into account for each configuration. So as well as coupling the $3d^n, 3d^{n+1}\underline{L}$ states through the hybridisation effect (charge transfer effect between the ligand p and transition metal 3d states), in the CTM theory the atomic multiplet effect is taken into account in each of the $3d^n, 3d^{n+1}\underline{L}$ states ¹⁷. In the final state of the transition metal 2p XAS, the $2p^5 3d^{n+1}$, $2p^5 3d^{n+2}\underline{L}$ configurations are coupled through the charge transfer effect and the atomic multiplet coupling is included in each of these two configurations ¹⁷⁻¹⁸. The CTM calculation has the option to include more configurations, including the next charge transfer state, metal-ligand charge transfer ($3d^{N-1}L$) and adding two charge transfer channels ¹⁸. The core hole potential is assumed to act only on the 3d states. This is an approximation and the interactions of the core hole on other valence electrons are neglected ¹⁹. The inclusion of the crystal field effects have turned out to be very successful. The reason for the success of this model is that the explained properties are mainly determined by symmetry considerations (described with crystal field splitting) ¹⁸.

In short, the calculations of the transition metal 2p XAS consist of 3 main steps. The first part of the calculation produces the energy levels in the initial state $3d^n$ multiplet and the final state $2p^5 3d^{n+1}$ multiplet in spherical ($O(3)$) symmetry. The second step is the calculation of the atomic multiplet spectrum by means of the dipole transition from ground state to all final states. Finally the projection of all spherical multiplets to cubic (O_h) symmetry is determined ^{9b}. The effect of the cubic crystal field is essentially the reduction in symmetry from spherical to cubic. The local symmetry is described using a crystal field splitting. In O_h symmetry, the 3d orbitals are split into e_g and t_{2g} orbitals with an energy difference of $10Dq$ (for T_d they are split into e and t_2 respectively). In lowering the symmetry to D_{4h} , the orbitals are further split by the ligand field parameters D_s and D_t , however only D_s is used as a parameter in the calculation ¹⁵. The program allows

octahedral (O_h), tetrahedral (T_d) and D_{4h} geometries to be calculated; however this refers to the local geometry around the central metal only and therefore further structural (and electronic) information on the materials, in our case the surrounding ligands, cannot be included as an extended structure is not input into the program, the only ligand effects taken into account are the geometry and the crystal field ¹⁸.

The crystal field parameters (also called Ligand Field parameters ¹⁶) and the reduction factor are obtained by comparison of the simulation with the experimental spectra; therefore they are obtained from the calculation. The broadening of the line spectrum is determined by the lifetime of the final states which in turn is determined by Auger decay from this final state ($2pd^{n+1}$) ¹⁵. Individual spectral features and shoulders can therefore have different broadening factors ^{15-16, 18}, however the calculated spectra are broadened as a whole with a Lorentzian of 2Γ eV full width at half maximum and convoluted with a Gaussian of σ eV ¹⁵ which describes the total lifetime and instrumental broadening processes occurring in the experiment ¹⁶.

The 1s2p Resonant Inelastic X-ray Scattering experiments are calculated using a program called RGAss. This program works in a similar way to the CTM approach and also includes multiplet and charge transfer effects as well as a crystal field component. One difference is the Gaussian broadening; in the CTM approach the Gaussian is taken as the full width at half maximum (FWHM) and in the RGAss program it is taken at full maximum. This leads to a difference of a factor of 2.

4.3 Results and Discussion

4.3.1 Cr K-edge

The experimental Cr K-edge XANES, HERFD and associated FEFF9 calculations for a series of reference compounds are shown below, figure 3. From these spectra it is possible to see the merits of the high resolution XANES experiments over the normal XANES. The HERFD experiments provide increased resolution along with more pronounced features compared to those shown in the normal XANES experiments and have proved to be an important development in the determination of spectral details for the K pre-edge region. These additional features resolved in the HERFD also show how well these advanced multiple scattering calculations reproduce the pre-edge. Adding the calculated empty density of states (DOS) plots with the XANES allows us to identify the different orbital contributions to the XANES features, thus revealing the orbitals/transitions probed

during the experiment and therefore gaining insights into the electronic structure of the central Cr atom.

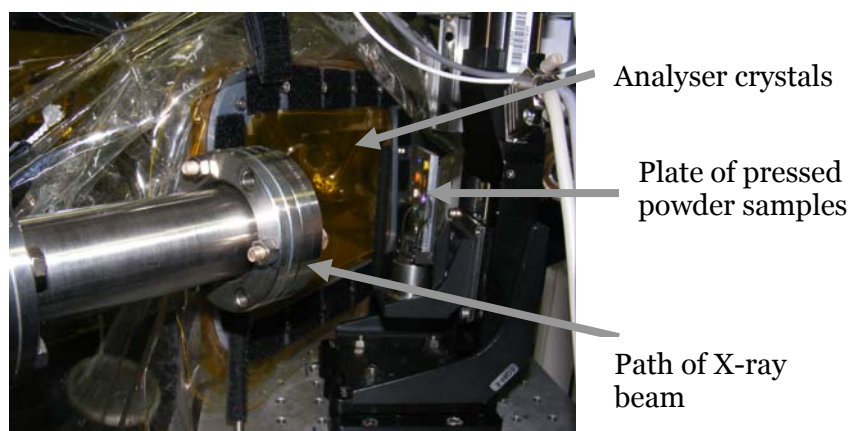


Figure 1 Experimental setup of the Cr reference powder samples for XAS analysis.

Figure 1 shows the position of the plate of Cr reference pressed powder pellets in the path of the X-ray beam and the crystal analysers. All experiments were carried out as pressed powders and at room temperature.

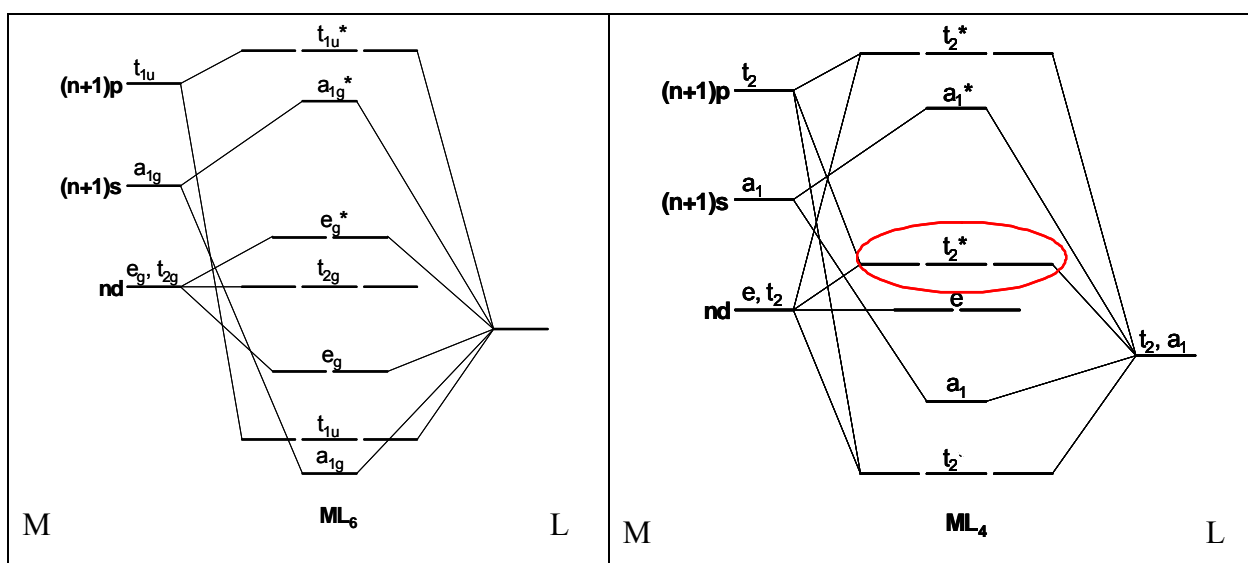
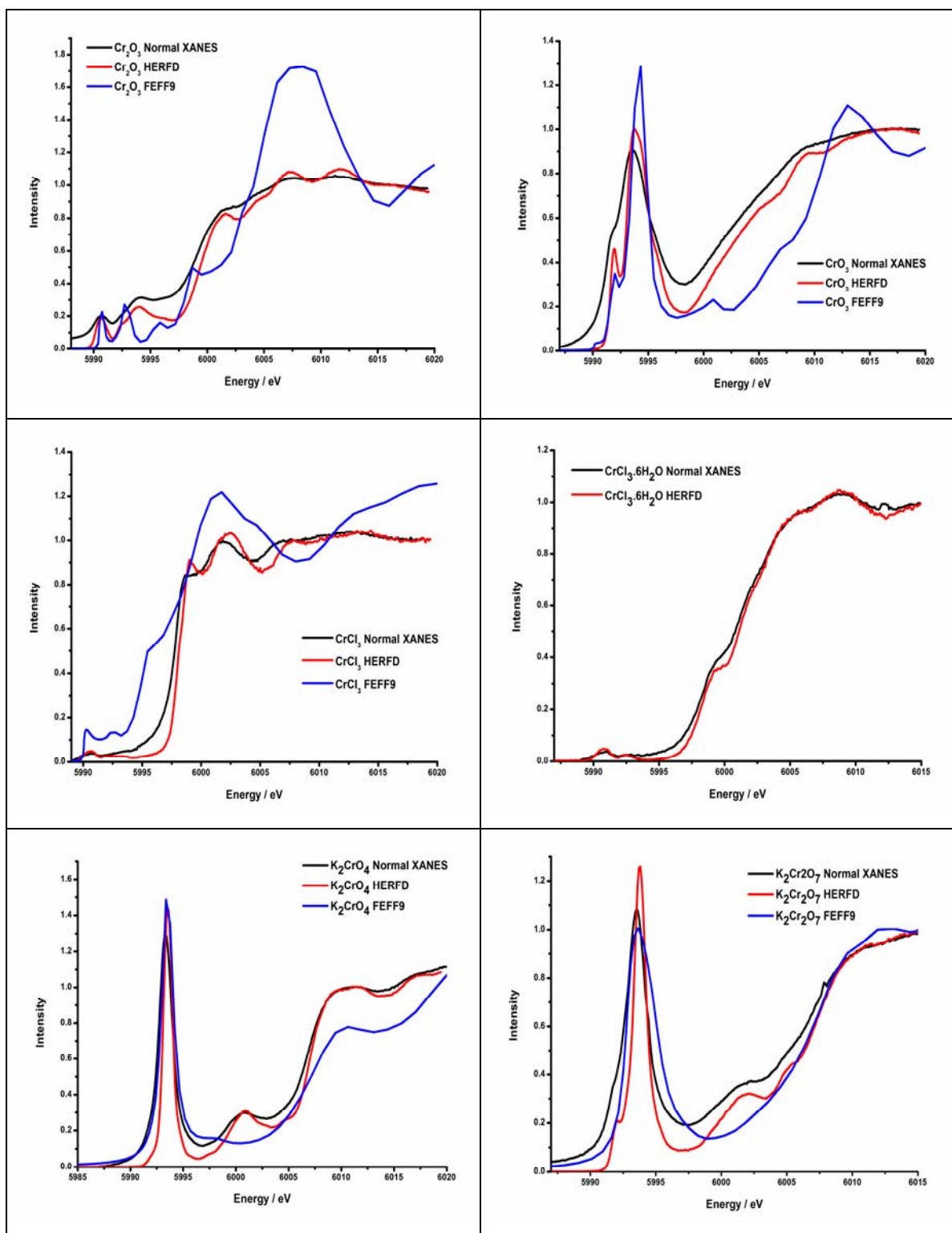


Figure 2 Molecular orbital energy level diagram for ‘perfect’ octahedral (left) and tetrahedral (right) metal complexes. The annotated t_2^* orbital on the right d and p character as described.

Figure 2 shows a molecular orbital energy level diagram for a typical O_h and T_d metal complex. This is useful in explaining the appearance of the pre-edges of the reference materials in terms of the level of orbital hybridisation in each case and will be referred to when describing the XANES and HERFD spectra. In the tetrahedral case (on the right)

the mixing of metal d and p-orbitals is observed, which will be referred to again when describing the calculated density of states at the pre-edge.



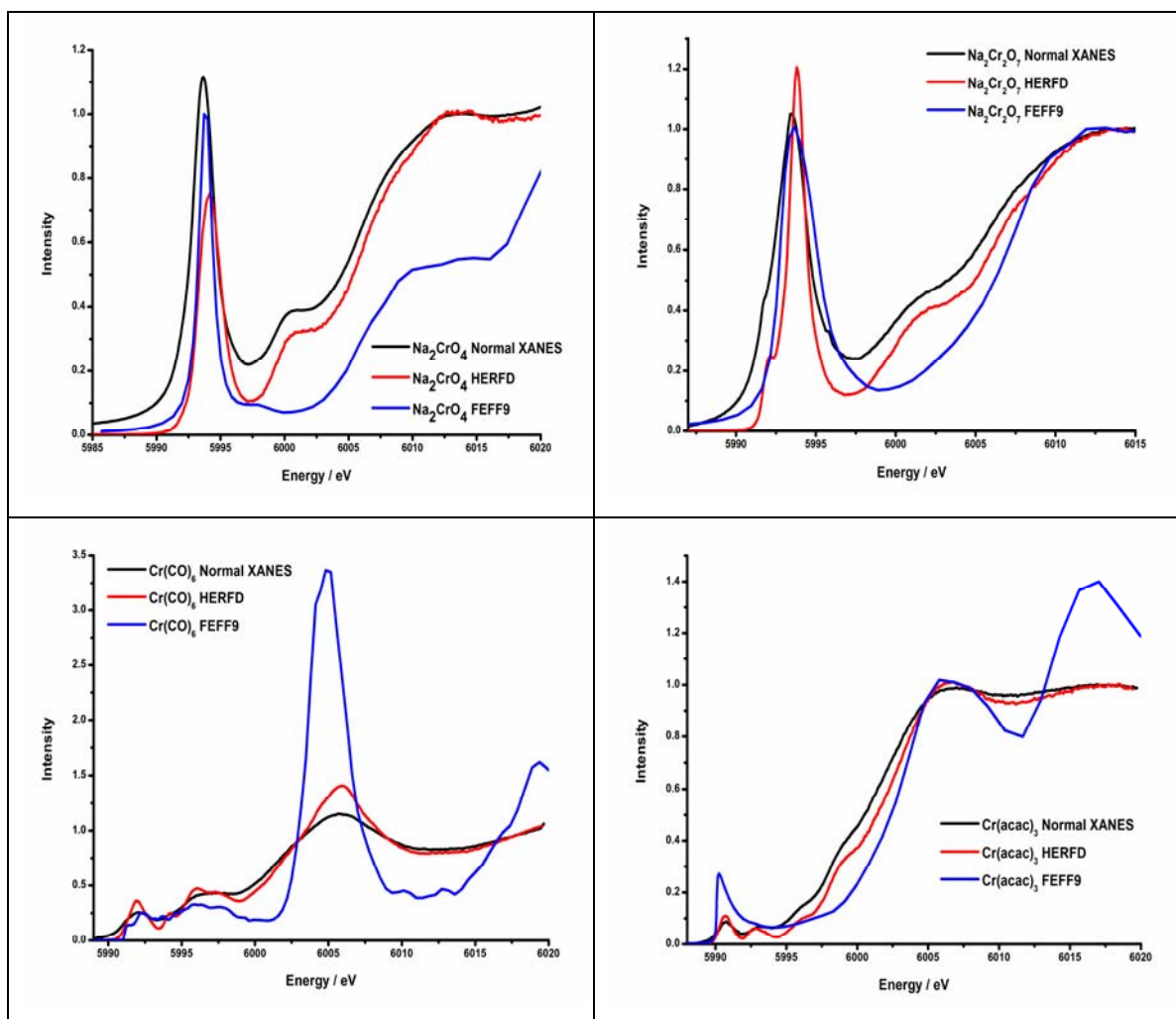


Figure 3 Comparison between XANES spectra calculated using FEFF9 and experimental spectra of normal XANES and High Energy Resolution Fluorescence Detection XANES for a series of Cr compounds.

Figure 3 shows the Cr K-edge XANES with the HERFD XANES and the XANES simulations carried out with FEFF9. A negative broadening was used in the calculations to reproduce the high resolution data. For each compound the additional information available in the high energy resolution spectra is clear, with increased intensity of features and more features visible in the pre-edge XANES region. In the HERFD process we select a specific emission line over which to measure the XANES of the sample (in this case the $K\alpha_1$ emission line). A secondary fluorescence detector with an energy resolution that is similar to the core hole lifetime broadening is used, the advantage of this is that only one emission line is probed; so the XAS spectrum is only broadened by the 2p core hole lifetime rather than of the 1s core hole lifetime (the 2p being larger than the 1s and so having a reduced broadening effect). In this case for Cr this value is 1.08 eV for the K-edge and 0.2 eV for L_3 ²⁰. It has a sharpening effect on the structures visible when comparing the normal and HERFD spectra for Cr_2O_3 in the pre-edge region. The different XAS data

(normal and HERFD) were collected simultaneously during the same experiment for all of the samples shown.

In the spectra for the distorted O_h symmetry Cr_2O_3 it is evident that there is a lot more detail contained within the HERFD. The first pre-edge peak at around 5991 eV is better resolved. Moving onto the second pre-edge feature we can now see that this is made up of three peaks (at 5993, 5994 and 5996 eV), whereas in the normal XANES this appears as one broad feature. Over the edge and up to about 15 eV after the edge we are still able to see more detail in the HERFD compared to the normal XANES, however, after this point both the HERFD and normal XANES appear to flatten off which is due to self-absorption effects (where emitted photons are absorbed by neighbouring Cr atoms in the sample). This takes place because the samples contain a very high percentage of Cr, which was necessary to increase signal to noise and reduce data acquisition times in this pre-edge region, which is the main interest for this study (EXAFS is not investigated here), and is especially helpful for the extended 2D RIXS plots (vide infra). The FEFF9 calculation for Cr_2O_3 reproduces the features at 5991, 5993 eV, although these are not reproduced exactly as they appear in the experiment; however the feature at 5994 eV does not appear in the calculation and we have a peak at 5996 eV instead. This might be due to multiple electron excitations and the approximate treatment of the core hole interaction in FEFF9²¹. The position of the main edge is shifted by approximately 2 eV in the calculated spectrum (with an additional shoulder in the main edge), which is also seen for the $Cr(acac)_3$ calculation (spectra energy aligned on the pre edge features).

The spectra for tetrahedral CrO_3 show a similar trend, the singular pre-edge feature from the normal XANES plot is split into two peaks in the HERFD, appearing at 5992 and 5994 eV. The peak at 5992 eV appears as a shoulder in the normal XANES but is better resolved in the HERFD. At the edge we see greater resolution than for the normal XANES but the flattening off of both lines after the edge is indicative of self absorption. The FEFF9 calculation shows the two features in the pre-edge, with one small peak at 5992 eV and the main peak at 5994 eV. The experimental spectrum shows a small shoulder at 6005 eV and another at 6009 eV, whereas the calculation shows two additional features at slightly lower energies of 6001 eV and 6007 eV. In the case of the 3d transition metal oxides it has been shown by De Vries *et al.* and quantum mechanical analysis that it is not necessarily the valence itself, but more the resulting metal-oxygen distances that determine the edge energy in these cases²². We can see the increase in structure at the pre-edge when moving from the O_h Cr_2O_3 to the CrO_3 which has lower symmetry (T_d).

The CrCl_3 XANES shows much less detail in the pre-edge region for both normal XANES and HERFD, compared to the oxide structures above. We can see one small pre-edge feature appearing at 5991 eV and a small shoulder at 5992-5993 eV, this is expected for a slightly distorted O_h geometry as we start to see more orbital mixing. In the calculation there are two pre-edge features at 5991 eV and 5993 eV, the intensities are not accurately reproduced, but this is not always possible with FEFF^{21b, 23}. There is evidence of a significant shoulder appearing just before the main edge in the calculation; this is not visible in the experimental spectra. Again, a 2 eV edge shift from calculation to experiment is observed, as was observed for Cr_2O_3 , $\text{Cr}(\text{acac})_3$ and is observed for the other distorted O_h Cr(III) example (see below). After the edge the experimental spectra contains much more detailed features with different intensities compared to the calculation, before self absorption effects kick in. Altogether, FEFF9 does not seem to reproduce the experimental spectra for CrCl_3 very well. This may be due to the following reasons; multiple electron excitations and approximate treatment of the core hole interactions (as mentioned before), inaccurate treatment of the charge-transfer effects in this system, or simulation of a slightly different crystal structure from what was measured. Whereas the purple anhydrous CrCl_3 was used as a starting compound, it is possible that some hydrate was formed during the sample preparation and transfer, albeit no significant colour changes were observed after the experiment.

The experimental spectra for $\text{CrCl}_3 \cdot 6\text{H}_2\text{O}$ show two pre-edge features in the XANES region at 5991 eV and 5992.5 eV. There is greater resolution going from the normal XANES spectrum to the HERFD, this is clear in the sharper appearance of the two pre-edge peaks. The main edge-rise starts at 5999 eV and shows a step-like feature at 5999 eV; this feature is present in both the normal XANES and the HERFD but appears broader in the normal XANES spectrum. The structure of the hydrated chromium chloride is unknown; hence no spectra could be simulated. The XANES is similar to the anhydrous form, so possibly indicating Cr-Cl coordinations have the biggest effect on the spectrum, or that the CrCl_3 was in fact hydrated. Although, the CrCl_3 sample appeared bright purple and the hydrated form dark green.

The XANES spectra of T_d K_2CrO_4 show an intense pre-edge feature at 5993 eV for both the normal and HERFD XANES. There is also a second, less intense, peak at 6001 eV in both spectra; whereas only in the HERFD there is an additional small shoulder on the high energy side just before the edge rise. The FEFF9 calculation accurately reproduces the first intense pre-edge feature at 5993 eV. The second pre-edge feature is not present in the calculation and the edge is shifted by approximately 1 eV. The absence of the second

pre-edge feature at 6001 eV in the calculation could be due to the fact that in the experiment distortions occur in atom positions making certain transitions possible that are not predicted by FEFF which is based on a reported crystal structure. We have tried to reproduce the additional features with FEFF9 but have not been successful. Another factor could again be due to the approximate treatment of the core hole^{8b}. The intensity of the pre-edge relative to the main edge is slightly higher than for the experimental XANES, this is to be expected as FEFF9 does not always reproduce the relative intensities correctly^{21b, 23}. The absolute energies in the calculation are based on atomic total energy calculations using the Dirac-Fock-Desclaux atom code. The accuracy of this approximation varies from a few eV at low Z to a few hundred eV for very large Z. This may be why we often see discrepancies in the edge positions²⁴. The muffin-tin approach employed in the FEFF calculation is known not to be fully adequate for these types of complexes²⁵.

The Cr (VI) $K_2Cr_2O_7$ K-edge XANES spectra show a very intense pre-edge feature at 5994 eV, this feature appears in both the normal XANES and HERFD spectra. The normal XANES spectrum shows a small, broad feature on the low energy side on the first pre-edge peak at 5992 eV. This feature is better resolved in the HERFD XANES and is clearly visible as a small feature. There is also a smaller pre-edge feature at 6002 eV; this appears as a broad hump in the normal spectrum, but as a much sharper feature in the HERFD. The added resolution obtained from the HERFD reveals a small feature at 6005 eV that is not visible in the normal XANES spectrum. The main edge occurs at around 6007 eV. The FEFF9 calculation nicely reproduces the main pre-edge peak at 5994 eV and the main edge position at 6007 eV, but the small feature on the low energy side of the main pre-edge peak is not present in the calculation along with the broad feature at 6002 eV.

Similarly to the potassium chromate sample, Na_2CrO_4 also shows an intense pre-edge feature at 5994 eV, this feature is present in both the normal XANES and the HERFD spectra. There is also a second broad feature at 6001 eV, which occurs in both experimental spectra. The main edge occurs at 6007 eV and appears slightly shifted going from the normal XANES spectrum to the HERFD spectrum. The calculation with FEFF9 reproduces the pre-edge feature at 5994 eV well; the broad feature at 6001 eV is also visible in the calculation. There is an additional feature at 6006 eV in the calculation that is not present in the experimental spectra; this appears as a small hump visible on the edge-rise. It is interesting to observe that although the XANES spectra for the two chromates are very similar in number of features and their positions, the intensities are

significantly different between the two. This could be due to slightly different crystal structures as a result of the different sizes of Na and K, with Na being smaller in size.

$\text{Na}_2\text{Cr}_2\text{O}_7$ shows an intense pre-edge feature at 5994 eV with a small peak on the low energy side (5992 eV). This is present in both the normal XANES and HERFD spectra; however the small peak at 5992 eV appears sharper in the HERFD spectra due to the increased resolution. There is a second pre-edge feature at 6002 eV; this appears in the normal XANES spectrum but is better resolved in the HERFD spectrum. The main edge occurs at 6006 eV which is reproduced in the FEFF9 simulation. The simulation also reproduces the first main pre-edge feature in the T_d sample. The broad feature observed experimentally at 6002 eV is not reproduced by theory, similarly to the $\text{K}_2\text{Cr}_2\text{O}_7$.

The calculation for the $\text{Cr}(\text{CO})_6$ XANES spectra appears to reproduce the experimental data surprisingly well, including most of the large number of small pre-edge features present. The normal XANES shows only two broad features at 5991.5 eV and the second at 5997 eV, the HERFD XANES shows a lot more detail especially at the second peak. The first peak at 5991.5 eV is better resolved in the HERFD spectra, appearing much sharper. The second peak is separated into three features in the HERFD; one at 5994 eV, 5996 eV and 5997.5 eV. The calculation shows two peaks under the first pre-edge feature, shown experimentally, with a smaller feature on the low energy side at 5991 eV and the second larger peak at 5992.5 eV. The next peak is at 5993.5 eV but does not coincide exactly with that in the HERFD (5994 eV). There is a broad feature consisting of a few smaller peaks at 5995 eV, 5996 eV and 5997.5 eV, these peaks all coincide with the broad feature in the normal XANES and the two main peaks at 5996 eV and 5997.5 eV match up with those seen in the HERFD XANES. The main edge for the normal and HERFD XANES appears at 6006 eV, however there is a shift of 1 eV for the calculated edge which appears at 6005 eV.

In the XANES spectra for $\text{Cr}(\text{acac})_3$ the first pre-edge feature appears at 5991 eV and is visible in the normal as well as the HERFD XANES, the second feature, also visible in both, is at 5993 eV. Moving from the normal XANES to the HERFD there is slightly better resolution observed in the pre-edge features with the first peak appearing more intense. Again it is observed that the pre-edge region for $\text{Cr}(\text{acac})_3$ is much less intense than in the case of the T_d cases such as K_2CrO_4 due to the fact that the geometry is O_h . The normal XANES shows two shoulders appearing at 5996 eV and 5999 eV; these can also be seen in the HERFD XANES. After the edge, self absorption effects are present and the spectra flatten off after 6006 eV. The FEFF9 calculation reproduces the first pre-edge feature at

5991 eV but after this there are no visible features before the edge. The position and intensity of the edge is well reproduced, however features after the edge are no longer visible in the experiment and so are not directly comparable. It is entirely possible that the FEFF package will not be able to reproduce all the pre-edge features due to reasons mentioned before, but the positions and relative intensities of the first pre-edge feature and the main edge are comparable.

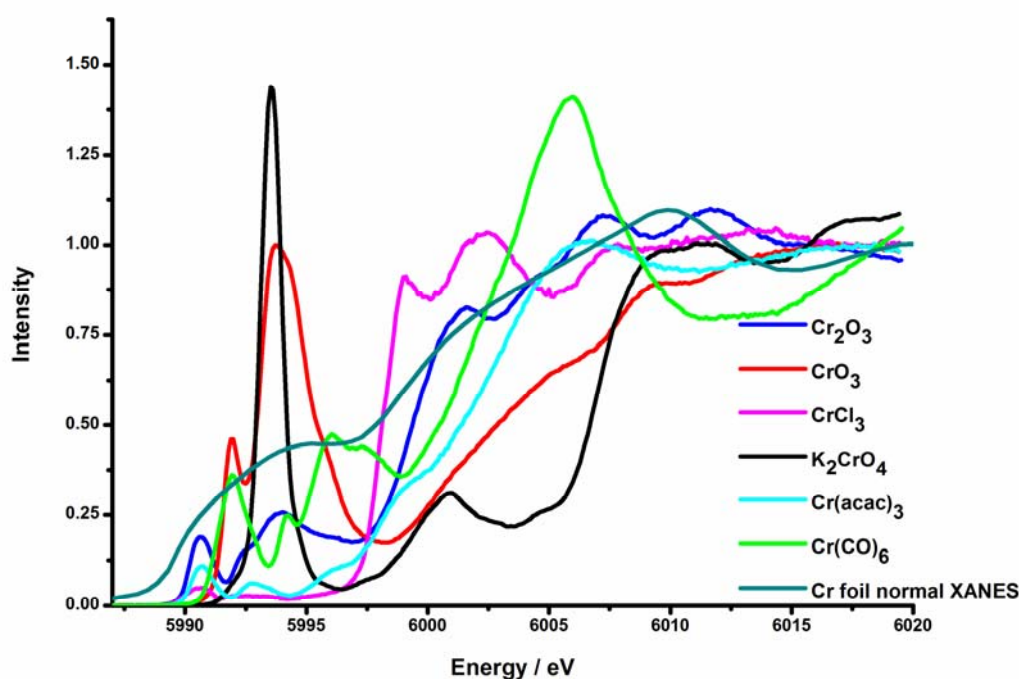


Figure 4 Experimental HERFD XANES for a series of Cr reference compounds compared to the normal XANES of Cr foil.

Comparing the experimental HERFD spectra for all reference samples we see a shift to higher absolute energy of the absorption edge in the order; CrCl_3 , Cr_2O_3 , $\text{Cr}(\text{CO})_6$, $\text{Cr}(\text{acac})_3$, CrO_3 , K_2CrO_4 (figure 4). The edge energy difference can be attributed to many factors; the energy difference between CrCl_3 and Cr_2O_3 (both Cr^{3+}) can be attributed, at least in part, to the electronegativity difference between Cl^- and O^{2-} . With oxygen being more electronegative than Cl, Cr_2O_3 is shifted to higher energy, it also depends on the location of the initial and final states (see below).

The absolute position of the X-ray absorption edge is dependent on the energy difference between the initial state and the final state. The edge position depends on the binding energy of the 1s core electron for the element under study, and so is element specific. The calculation of the K-edge reflects the unoccupied p states of the metal being investigated.

This is because it is the $1s \rightarrow 4p$ transition that is being probed. The general trend, when the initial state is located on the metal and the final state on the ligand, is that the Cr K-edge energy positions shift towards higher energy with an increase in oxidation state ^{5, 25b}. This same trend has also been observed in previous studies involving the use of Cr K-edge XANES spectra of reference materials as fingerprints for analysing and interpreting Cr XANES of unknown Cr species (in the case of supported Cr catalysts) ⁵⁻⁶. The increase in edge shift with an increase in oxidation trend is followed by most transition metal systems, within a similar ligand range, and when the final state is localised on the ligand ^{25b}. Normally the increase in the coulomb potential with an increase in oxidation state is felt mainly by the metal valence orbitals. With the final state focused on the ligand this is no longer the case. This results in the final state remaining relatively un-shifted and so the difference between the initial state and final state is larger as observed in the energy of the absorption edge ^{25b}. This trend is also followed by the reference Cr materials in this study, looking at figure 4 we can see that as the oxidation state of the Cr increases so does the position of the edge.

Another common feature is the low energy shift of chlorine containing compounds, the edge position shifts towards the Fermi level; this can be seen from the CrCl_3 simulation (see above and below). In most previous reference papers only oxidic ligands have been studied ⁵⁻⁶, showing the trends as explained above. In the case of the Cl ligands we can see that these are shifted in the opposite direction and lie to the left of the Cr foil rather than to the right. This is due to the fact that the Cl atoms are less electronegative than the oxidic ligands ^{25a}. An increase in electronegativity of the attached ligand leads to an increased splitting of the orbitals. This results in a shift to higher energy with increasing electronegativity of the neighbouring atoms ^{25a}, which is indeed what we see in the experimental spectra. This effect explains at least partly why the edge position shifts towards higher energy not only with increasing oxidation state of the absorbing atom, but also with increasing electronegativity of the nearest neighbour atoms ^{25a}.

The XANES technique directly probes the empty density of states (for extended structures) or molecular orbitals (for molecules) in that we are looking at the excitation of a $1s$ core electron into the lowest unoccupied molecular orbitals or states. This enables us to obtain a detailed picture of the local electronic structure around the chromium atom. In the Cr systems studied multiple pre-edge features are observed, an obvious link can be made between the geometry ^{1d, 5-6, 25b}, as well as the electronics, of the complex and the intensity of pre-edge features. For complexes of lower symmetry there is a greater degree of hybridisation between p and d or s-orbitals; this mixing of orbitals means that dipole

allowed transitions to the p-orbitals contains d character and results in intensity in the pre-edge due to this dipole-quadrupole mixing²⁶. When inversion symmetry is broken the 3d and 4p states mix and form combined 3d + 4p symmetry states. This means the dipole and quadrupole transitions reach the same final states, and so their peaks are visible at the same energy. We can see this effect when comparing the pre-edges of T_d K_2CrO_4 and O_h $Cr(acac)_3$, with the appearance of an intense peak in the pre-edge region for the K_2CrO_4 .

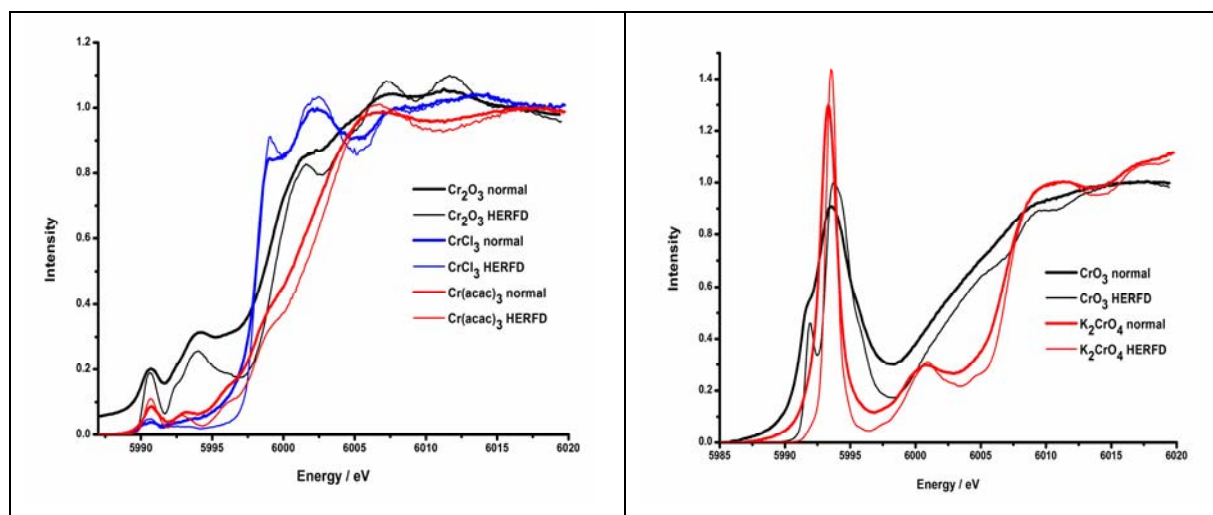


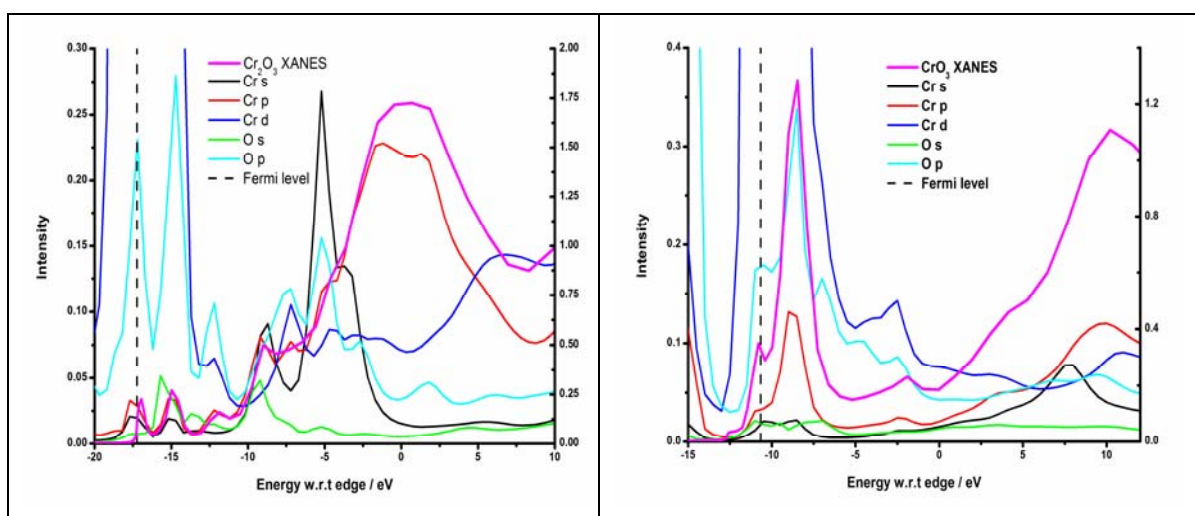
Figure 5 Cr K-edge XANES for a series of complexes grouped by geometry; octahedral (left) and tetrahedral (right).

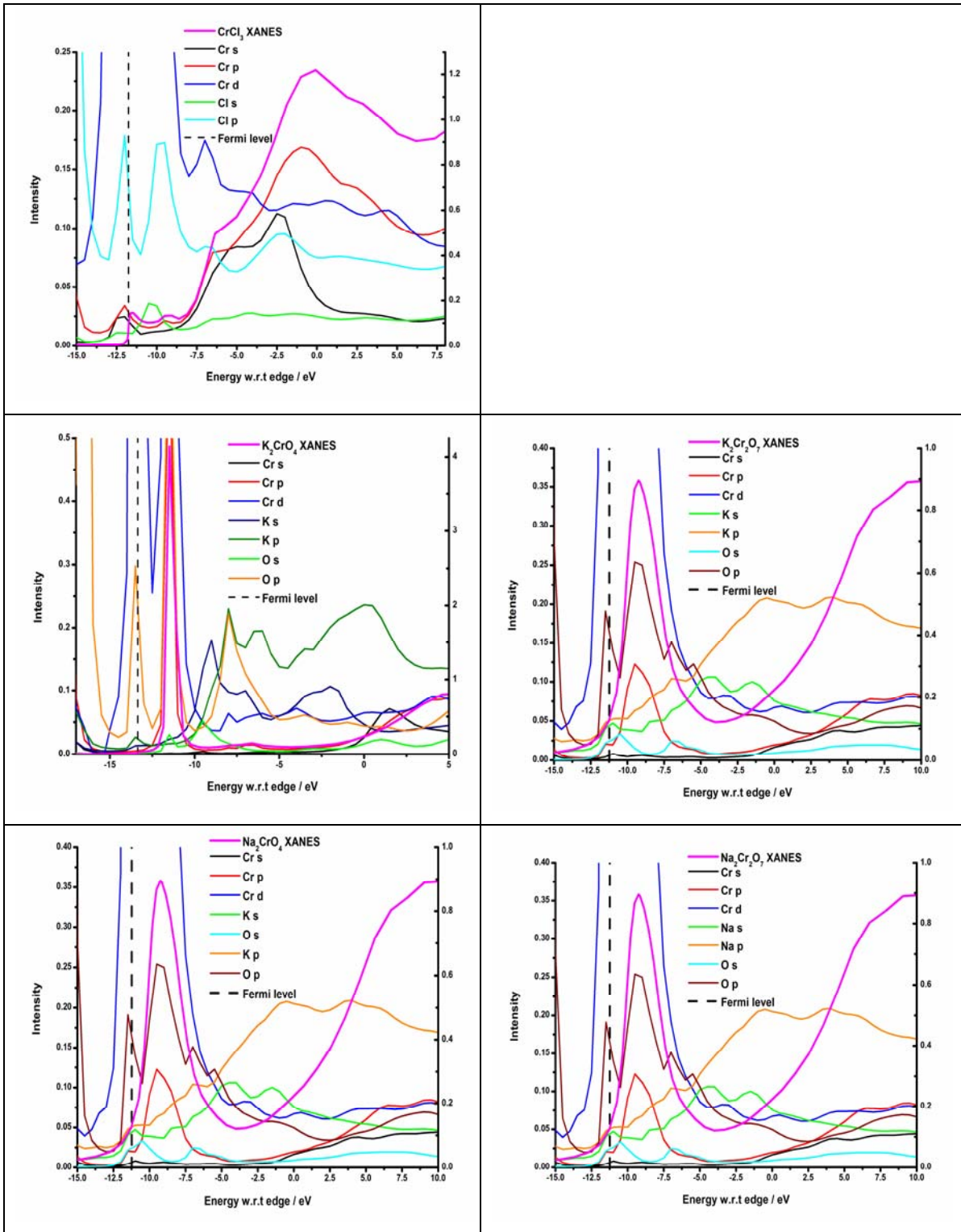
Figure 5 shows clearly the difference at the pre-edge for the different geometries. By comparing O_h (or distorted O_h) and T_d cases we can see that in the T_d compounds (on the right) there is the appearance of intense peaks in this pre-edge region. The pre-edge peaks are caused, in part, by dipole forbidden electron transitions from $1s \rightarrow 3d$ orbitals (quadrupole transitions) these are the transitions behind the pre-edges of O_h complexes. In the T_d case this transition is able to take place due to the lack of an inversion centre at the Cr metal centre; this enables the metal 3d and 4p states to mix, allowing direct dipole transitions to the 4p character of the 3d band. The intense peak at 5993 eV in the K_2CrO_4 spectrum is due to the presence of such a quadrupole ($1s \rightarrow 3d$) transition. Even in the O_h case small pre-edges are visible (from quadrupole transitions) purely because of the high density of states for the 3d band. So even though they have a transition strength of 0.1% of the dipole transitions they are visible as very small peaks, albeit at ~1-3% of the intensity of the dipole transitions²⁷.

From the molecular orbital energy level diagrams in figure 2 it is evident that in the O_h case there is limited mixing of the metal p and d orbitals, therefore in theory only $s \rightarrow p$ (dipole allowed) transitions are visible in the pre-edge region (although it has been

observed that this is not necessarily true for the distorted O_h cases as explained below). This results in a relatively clear pre-edge as shown in figure 5. The T_d complexes however, show mixing of the metal 4p and 3d orbitals. This results in $s \rightarrow p$ transitions having d character. It is the increased probability of these quadrupole transitions in a T_d environment that leads to the intense pre-edge features in complexes such as CrO_3 and K_2CrO_4 . The distorted O_h compounds (Cr_2O_3) also appear to show pre-edge features, it is the distortions in the central atom positions that allow these transitions to occur due to an increased level of orbital mixing compared to a pure O_h system. The changes in the positions of the pre-edge peaks reflects the difference in the energy required for the electronic transition from $1s \rightarrow 3d$ for each of the different Cr samples. So for the Cr_2O_3 sample less energy is needed for the transition in comparison to K_2CrO_4 , whose pre-edge peak sits at higher energy, and so on.

The calculated density of states plots allows the determination of the transitions forming the features of the pre-edge. The three main electronic transitions forming the pre-edge are: i) local electric quadrupole transitions, $1s \rightarrow 3d$; ii) non-local electric dipole transition, $1s \rightarrow p$, where the empty p states of the absorbing atom are hybridised with the empty 3d states of the nearest metal neighbours via the empty p states of the ligands; iii) local electric dipole transition, $1s \rightarrow p$, where the empty p states of the absorbing atom are hybridised with the empty 3d states of the absorbing atom²⁸. The 3d empty states are probed in the pre-edge region either directly through local electric quadrupole transitions or indirectly through either non local electric dipole or local electric dipole transitions^{21a}.





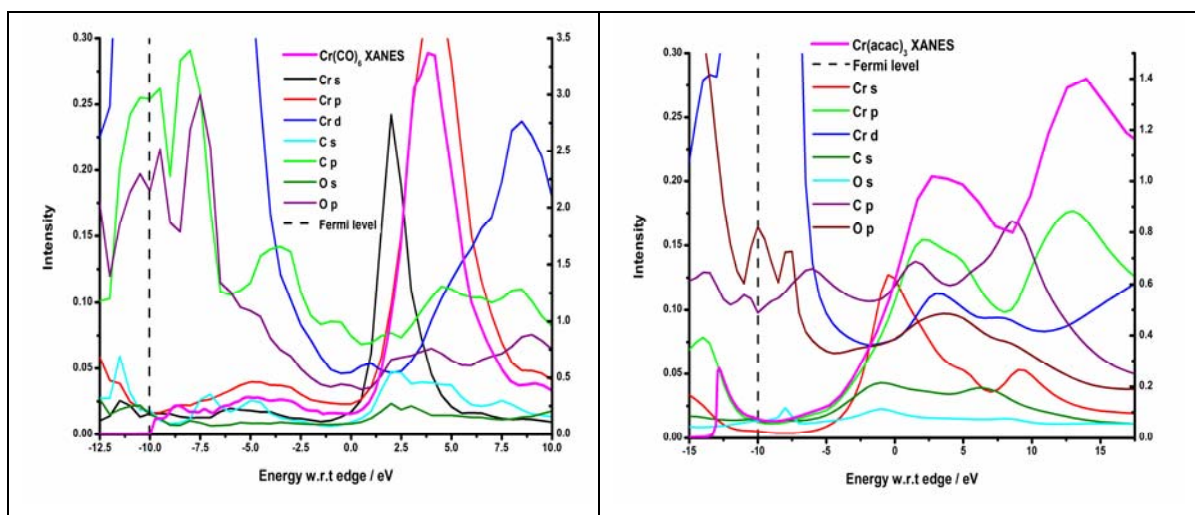


Figure 6 Density of states and associated XANES calculations performed with FEFF9 for a series of Cr reference compounds.

The density of states calculations shown in Figure 6 identify the specific orbitals involved in the transitions producing the features observed in the XANES. In all samples the Cr p-DOS will line up nicely with the XANES, this is because it is the Cr p-DOS that is being probed in this experiment. Any other orbitals that are involved in the transitions will also line up with Cr p allowing the orbitals to overlap; these interactions will be discussed for each sample.

The XANES and associated density of states plots for Cr_2O_3 show Cr p-orbital and Cr s-orbital contributions at both the first two pre-edge features (-17 eV and -15 eV). This is because the transition at the Cr K-edge is from an $s \rightarrow p$ orbital and the Cr s orbital has overlapped with the orbital being probed (Cr p). The intense Cr p and O p-orbital overlap indicates a bonding interaction between Cr and O, this is just above the Fermi level (the point above which all orbitals are empty). Orbitals are more likely to overlap and hybridise when they are a close in size and shape as well as being in the same orientation, therefore this is more likely to occur for two p-orbitals. There is also Cr p overlap with Cr d-orbitals forming the features at -17 eV and -15 eV. There appears to be a certain degree of covalent character in the Cr d and O p-states forming a bonding interaction, more so than for purely O_h systems. The O s-orbital contribution is only present for the second feature at -15 eV, and then again at -9 eV, this then tails off and does not contribute to the main edge. The third pre-edge feature at -12 eV shows Cr p overlap with O p and Cr d-orbitals (evidence of the hybridisation of p and d-orbitals of the different elements). At -9 eV, the fourth pre-edge feature shows contributions from O s, Cr s, Cr p and O p-orbitals. In a first row transition metal oxide in octahedral symmetry, the lowest empty metal p state is the 4p band that is formed from the anti-bonding combinations of the metal 4p-

states with the O 2p-states²⁷. We expect to see contributions from both Cr p and O p-orbitals in this region due to bonding interactions from the overlap of these p-orbitals in space, and because the electronic transitions probed are from a 1s core state to the lowest possible states with p character. Due to the fact that the Cr₂O₃ solid is not a pure symmetry complex there will be other orbitals visible at the edge as well, for example the overlap of Cr p DOS with Cr d.

In the CrO₃ spectra the first pre-edge feature at -11 eV has Cr p overlap with O p and Cr d-orbitals, a smaller contribution is observed for Cr s and O s-orbitals. The same orbital contributions are seen for the second more intense pre-edge feature at -9 eV, the O p-orbital contribution to the pre-edge is visible because of the overlap of the Cr p and O p-orbitals (a bond) and the nature of the transition being probed. The largest Cr d-orbital contribution appears at -9 eV along with a large amount of O p character (due to the bonding interaction with Cr p-orbitals), the huge Cr d-orbital contribution arises due to hybridisation effects with Cr p-orbitals in this geometry. These two (Cr d and O p) atomic orbitals are hybridised to form the anti-bonding molecular orbital (see figure 2).

Transitions from s→d orbitals are forbidden, the d character is visible in the empty density of states plot due to the T_d environment of the chromium. The geometry of the complex allows a degree of mixing between d and p-orbitals; this means an s→p transition shows d character. The feature at -2 eV again shows Cr p-orbital overlap with O p (bonding interaction) and Cr d (due to hybridisation) forming a small pre-edge peak in the XANES. Towards the main edge there is a rise in the Cr p and Cr d density of states, Cr d character is also present. Again this is due to covalency of the Cr d and Cr p-orbitals in the T_d environment.

The density of states calculation for CrCl₃ shows only two small features in the pre-edge region, the pre-edges arise from excitations into the lowest unoccupied states and by looking at the empty DOS it is possible to determine which molecular orbitals they originate from. The first of these two shoulders appears at approximately -11.5 eV and contains Cr p overlap with Cr s, Cl p and Cr d character. This suggests some overlap of these orbitals meaning that the anti-bonding molecular orbital shows character of all three. The Cr p and Cl p are of the same size and shape and so will form a bonding interaction. The small amount of d character present is often observed for octahedral compounds²⁷ and is from quadrupole transitions. The second pre-edge at -9 eV shows Cr p overlap with Cl p and Cr d-orbital contributions, with Cr d and Cl p character appearing at both the pre-edge features it suggests some covalency of these orbitals. The second feature also appears at the tail of a Cl s-orbital peak. The shoulder at -6.5 eV arises from Cr p overlap with Cl p

and Cr d-orbitals. Moving towards the main edge the XANES lines up with the Cr p empty density of states, as expected, but there are features at -2.5 eV in both the Cr s and Cl p density of states where these overlap with the Cr p-orbitals. The absorption spectrum shows mainly p-orbital contribution from the unoccupied orbitals, this is due to the dipole selection rules. We can see from the above XANES and density of states plots that the pre-edge features show strong d-orbital contribution from the chromium; this follows a $1s \rightarrow 3d$ transition which is visible through orbital mixing. The pre-edges usually appear weaker than the main edge as they arise from a quadrupole transition rather than a dipole transition and only become (dipole) allowed in certain geometries.

The first main feature in the theoretical XANES spectra for K_2CrO_4 appears at -12 eV, the empty DOS plot show Cr p overlap with O p-orbitals as well as small O s-orbital contributions and huge Cr d-orbital contributions to this first pre-edge peak. Cr p and O p-orbitals will form a bond if they are in the same orientation in space, as they are of the same size and shape; this means that O p character is visible with Cr p as a probe. Due to the fact that the Cr d-orbital contribution is so large, the resulting huge pre-edge feature is indicative of Cr(VI) and also of the T_d environment. In this case it is clear that there is Cr p and Cr d-orbital overlap causing hybridisation of these orbitals (see figure 1). The calculated XANES spectra for K_2CrO_4 only show the appearance of one pre-edge feature (compared to two in the experimental spectra). FEFF may not reproduce all the features as not all phenomena are included. There are significant K p and O p empty DOS features at -7.5 eV however there is only a small shoulder present in the XANES. This means that the overlap of these orbitals will also form a molecular orbital but since there is not a significant amount of Cr p contribution this orbital will not be directly probed in the K-edge XAS.

The calculated XANES spectrum for the O_h $Cr(acac)_3$ shows a relatively clear pre-edge region, with only one small feature appearing at -12 eV, at this energy there are corresponding peaks in the density of states for the C p, O p and Cr d-orbitals. The XANES region is then clear until the edge, at the edge rise there is overlap of Cr p with C s, C p, Cr s and small O s-orbital contributions. The main contributions to the features at and after the edge are from the Cr d and O p-orbital overlap with Cr p (the probe), these form the feature at 3 eV. The level of covalency in an O_h compound is obviously much less and so a relatively clear pre-edge results.

From the calculated plots in figure 6 it is clear to see that the calculated K-edge is a reflection of the unoccupied p states of the Cr metal, this has to be the case as this is the

orbital directly probed in the experiment (and calculated in the XANES). We then look to see which orbitals overlap with Cr p-DOS to identify the transitions forming the peaks. Good agreement is found when calculating the Cr K-edge over the whole XANES region with the final state calculations, with the inclusion of the core hole potential. This enables us to nicely reproduce the details of the spectral shape. In general the XANES region, more specifically the pre-edge region, of reference Cr compounds have been studied and calculated using multiple scattering methods (in this study FEFF9). We have found that the intensity of the pre-edge region is much larger for materials in which the metal site has T_d site symmetry than for O_h systems. In T_d systems the local mixing of metal 4p and 3d-orbitals is symmetry allowed, whereas for systems with inversion symmetry (O_h systems) it is forbidden. However, it is also shown that even in the O_h case small mixtures of p states into the 3d band are found in the calculations; this is obviously less than for a T_d case. This degree of mixing depends on the disorder of the system, and is therefore higher in the distorted O_h case, as shown with Cr_2O_3 . We have also been able to identify the nature of the orbitals contributing to the XANES features from the projected DOS. However it is clear that a detailed knowledge of the structure of the material is required in order to perform these calculations, this means that unknown materials are not easily characterised. The merits of using the fluorescence detector for the HERFD measurements has been proven by the appearance of better resolved pre-edge features allowing for a more detailed analysis of the electronic structure compared to normal XAS spectra.

4.3.2 Cr L-edge absorption studies

The K-edge XANES region is useful in providing information on the metal oxidation state and coordination environment but arises mainly from the metal p density of states, and in certain geometries from metal d density of states (although indirectly). By directly probing the metal 3d shell (at the L-edge) we get a more detailed view of the electronic structure at the metal site ²⁷, this is extremely useful as the chemistry of the transition metals is governed by the nature of the d band. In this case the 4s-orbitals are considerably lower in energy than the 3d-orbitals and so the near edge structure of the $L_{2,3}$ edge is more closely related to the empty 3d states. The next step in the project is to look at the 2p X-ray Absorption Spectra (2p XAS), these experiments become more complicated to analyse due to the presence of multiplet effects ²⁷, which were less of an issue in the K-edge absorption studies. The multiplet effects visible in the RIXS and L-edge spectra are generally 50-100 times weaker for 1s,3d interactions and so do not affect the features in the K pre-edge ^{1d}. The L-edge has been measured using both soft and hard X-ray techniques (directly and indirectly). In the soft X-ray technique we look at the

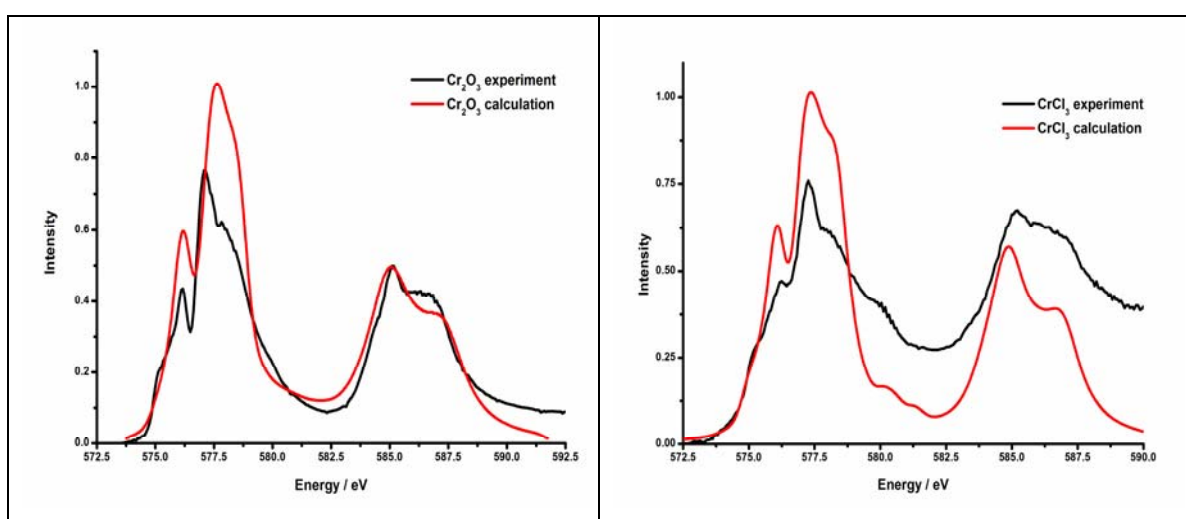
direct $2p \rightarrow 3d$ absorption (L-edge) to dipole allowed final states, probing the 3d shell directly. The dipole-allowed transitions in 2p XAS are $2p \rightarrow 3d$ and $2p \rightarrow 4s$, but as the transitions to the 3d states dominate the transitions to 4s-orbitals are not included^{9b}. The L-edges for the reference materials are shown below (figure 7). The local ligand coordination is evident at the $L_{2,3}$ edges in the energy splittings of the 3d orbitals involved, this corresponds to the crystal field splitting value (Δ or $10Dq$). This value is determined by the type and nature of ligand attached to the metal^{15, 29}. In octahedral (O_h) systems, the transition metal 3d-orbitals split because of the local symmetry into e_g and t_{2g} orbitals with an energy splitting of Δ_{oct} . The d_{xy} , d_{xz} and d_{yz} (t_{2g}) orbitals will be lower in energy than the d_{z^2} and $d_{x^2-y^2}$ (e_g) because they are further from the ligands and therefore experience less repulsion. In a tetrahedral (T_d) crystal field splitting the d-orbitals are again split into two groups, with an energy difference of Δ_{tet} where the lower energy orbitals will be; d_{z^2} and $d_{x^2-y^2}$, and the higher energy orbitals will be; d_{xy} , d_{xz} and d_{yz} , opposite to the O_h case. In addition, as the ligand electrons in T_d symmetry are not oriented directly towards the d-orbitals, the energy splitting will be lower than in the O_h case³⁰.

When looking at the core level spectroscopies of strongly correlated systems, such as transition metal compounds, the single electron excitation picture often breaks down. The many-body effects beyond the single electron excitation are mainly divided into the charge-transfer effect and the intra-atomic multiplet coupling effect¹⁷. Charge transfer effects are the effects of charge redistribution between the initial and final states. The charge transfer effects have been shown to be much weaker in XAS than for spectroscopies such as X-ray Photoelectron Spectroscopy (XPS) however, the multiplet coupling effect is of primary importance when looking at XAS, especially in transition metal 2p XAS^{9b, 15, 18, 31}. With the inclusion of these charge transfer effects, the spectral shapes can be accurately reproduced by theory and therefore can be explained, and the electronic structure understood. The Charge Transfer Multiplet (CTM) theory includes both the charge transfer and multiplet effects, which makes it a very effective theoretical approach that is especially useful in the calculation of most XAS spectra in transition metal systems¹⁷.

These multiplet coupling effects are caused by interactions between the core hole and the 3d valence electrons. In the final state of the X-ray absorption process there is a partly filled core state ($2p^5$). When looking at a system with a partly filled 3d shell the final state will have an incompletely filled 3d band. The 2p hole and the 3d hole have radial wave functions that overlap significantly; this wave function overlap is an atomic effect that can be very large¹⁸. Experimentally it has been shown that while the direct core hole potential is largely screened these multiplet effects are hardly screened in the solid state. This

implies that the atomic multiplet effects are of the same order of magnitude in atoms as in solids¹⁹. In the case of the strongly correlated transition metal 3d excited states (or localised states), the interaction between the electrons (as well as the interactions of electrons with the core hole after the absorption process) has to be taken into account. The main assumption when calculating transition metal 2p XAS is that the 3d-3d and 2p-3d two-particle interactions are the most influential on the spectral shape¹⁸. It is these interactions which define the ground state of the transition metal ion and split the XAS final state into a large number of configurations^{9b}. The solid state effects are taken into account by including a cubic crystal field in the calculation, the effect of the cubic crystal field is the reduction in symmetry. However distortions from this are not considered, only perfect geometry is available in the calculation. Multiplet calculations can also be used to describe transition metal K-edges²⁷, however it is unnecessary as the 1s3d interactions are included in the calculation but have almost no effect on the resulting spectrum when compared to single particle calculations. This is in direct contrast to the L-edge case where the 2p3d interactions have a huge effect on the spectral shape¹⁸.

Soft X-rays have a large absorption cross section with air; from about 530 eV to 1 keV the transmission through 10 cm of air is less than 10 %³². This means that it is necessary to perform experiments under ultra high vacuum (UHV). The use of low energy X-rays also means the penetration depth is decreased and in this case limited to the top layers of the sample therefore increasing the risk of beam damage. This is also minimised by performing the experiments under UHV. Below are shown the 2p XAS of the reference Cr materials, these were carried out in UHV conditions at Io6, Diamond.



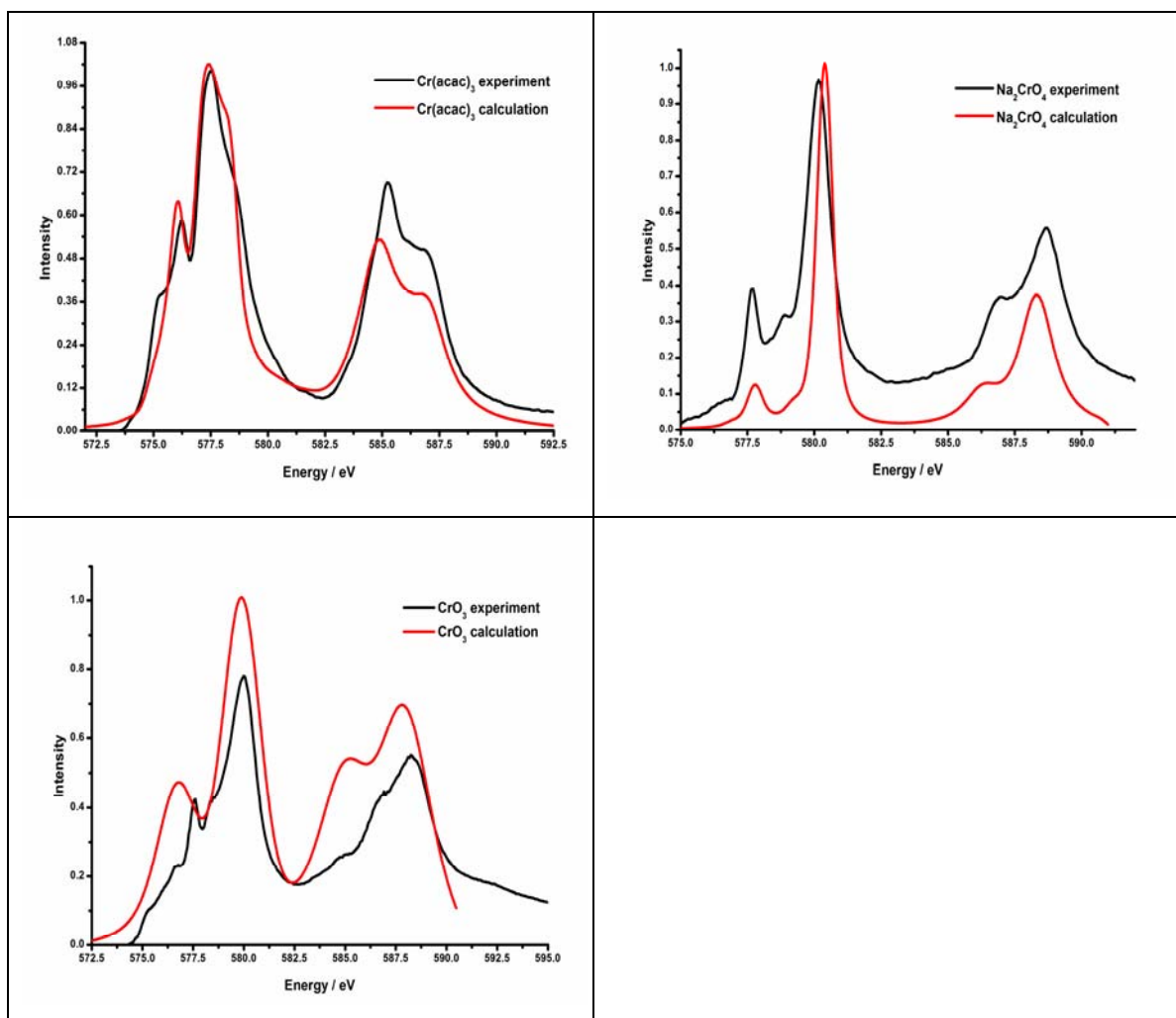


Figure 7 Comparison of calculated $L_{2,3}$ edge XANES with experimental $L_{3,2}$ edge XANES for a series of Cr references.

In the above spectra (figure 7) only effects larger than the lifetime broadening are observed. In the case of the 2p XAS experiment the lifetime broadening is lower in comparison to the K-edge and so additional features are observed in the experiment. The lifetime broadening at the L_2 edge is 1.2 eV and 0.8 eV at the L_3 edge³³. The size of the lifetime broadening is determined by the lifetime of the core hole, as the lifetime of the 2p core hole is more than that of the 1s core hole the result is a reduced level of broadening over the 2p XAS spectrum due to the reciprocal relationship of lifetime to broadening. In figure 7 we can see that the L-edges are split into the L_3 ($2p_{3/2}$) and L_2 ($2p_{1/2}$) edges, this is caused by the spin orbit coupling of the 2p core hole^{9b} and for Cr_2O_3 they are split by 8 eV (this has also been found in previous experimental data¹⁵). In the case of Cr_2O_3 the ratio between the L_3 and L_2 edges is not quite the 2:1 ratio expected from the nature of the configurations forming the peaks. The L_2 peak arises from the $2p_{1/2}$ state and the L_3 peak arises from the $2p_{3/2}$ state. The relative intensities of the L_2 and L_3 are determined by the degeneracy of the states. A $2p_{1/2}$ configuration consists of two states and the $2p_{3/2}$

configuration consists of four states. Therefore the intensity ratio of the $2p_{3/2}$ (L_3) to the $2p_{1/2}$ (L_2) peak should be 2:1^{32, 34}. There has been some previous work looking into the branching ratios of transition metal compounds and how these change across the series³⁵. It was found that the electrostatic interactions between the core hole and valence electrons also has an effect on the branching ratio³⁶. Existing studies have shown that the experimental intensity ratio of the L_3 to L_2 edge is often much lower for the early transition metals³⁷. The Cr_2O_3 spectrum shows a feature on the low energy side of the L_3 edge at about 576 eV, this small shoulder does not appear in the calculated spectrum but does appear for other Cr(III) samples and also appears in published Cr_2O_3 spectra¹⁵. The peak at 5776.5 eV (e_g peak) is well reproduced by theory; however the main peak at 577 eV (t_{2g} peak) is slightly shifted in the calculation by approximately 1 eV. The small peak on the high energy side of the main edge at about 579 eV also appears as a broad shoulder in the calculation. The L_2 edge consists of the main peak at 585 eV and the high energy shoulder at 587 eV; both of these features are well reproduced by theory. The relative intensity of the two peaks forming the L_3 edge is reproduced in the calculation, however the relative intensity between the two edges is not. At the L_2 edge the shoulder on the high energy side is less intense when compared to the main peak in the calculation.

The experimental spectrum for CrCl_3 contains a shoulder on the low energy side of the L_3 edge, at 575 eV. This feature is also present in the Cr_2O_3 spectrum. The L_3 e_g peak at 576.5 eV is reproduced by the calculation as well as the L_3 t_{2g} peak at 577.5 eV. In the experimental spectrum there are two shoulders on the high energy side of the L_3 edge at 578 eV and 580 eV. The peak at 578 eV appears as a small shoulder in the calculation however, the feature at 580 eV is not present. The L_2 edge shows the same overall shape as the calculation, with the first main, e_g , peak at 585 eV and the second, less intense t_{2g} feature at 587 eV.

The experimental spectra for $\text{Cr}(\text{acac})_3$ shows similar peak patterns to that of Cr_2O_3 , this is expected as they are both Cr(III). The $\text{Cr}(\text{acac})_3$ shows the appearance of an additional feature on the low energy side of the L_3 edge at 575 eV, this is also present for the Cr_2O_3 and CrCl_3 samples and does not appear to be due to any Cr(VI) impurity. Again the expected 2:1 ratio between the edges is slightly off in the case of the experimental spectrum. The L_2 edge looks as expected for Cr(III) with the less intense t_{2g} feature on the high energy side of the e_g peak which occurs at 585 eV.

The spectra for Na_2CrO_4 shows the two main features for the L_3 edge at 577.5 eV (e peak) and 581 eV (t_2 peak), there is an additional feature at the L_3 edge occurring between the

two main peaks at 579 eV. This feature is present as a small shoulder in the calculation. The L_2 edge consists of peaks at 587 eV (e peak) and 588.5 eV (t_2 peak). The absolute peak positions of the L_2 edge are shifted by approximately 1 eV towards lower energy in the calculation. In this case the ratio of the L_3 to L_2 edges is 2:1 as predicted by the degeneracy of the states, but the relative intensities of the splitting at the L_2 edge is different to that of Cr(III) with the low energy peak being less intense in the experimental spectrum in this case. The spectra for the d^0 compound appear much less complicated due to the fact that the number of final states available is small. This is because in the final states ($2pd^1$), with only a single 3d electron, the 3d-3d Slater integrals are absent¹⁵. The large reduction of the Slater integrals (see chapter 3) for the chromate shows the strong covalent character for the 6+ oxidation state as compared to Cr_2O_3 .

The experimental spectrum for CrO_3 shows the general shape of a Cr(VI) $L_{3,2}$ edge with some additional peaks that are not predicted by theory. There are two small features on the low energy side of the L_3 edge at 575 eV and 576.5 eV. The first of the two main peaks forming the edge appears at 577.5 eV in the experiment and 577 eV in the calculation. There is a small shoulder in the experimental data at 578.5 eV that is also reproduced as a small shoulder in the theoretical spectrum, with the main edge peak at 580 eV for both experiment and theory. The experimental L_2 edge consists of three features; a small shoulder on the low energy side at 585 eV, a shoulder on the low energy side of the main peak at 587 eV and the main edge peak at 588.5 eV. The theoretical spectrum only reproduces two of these features; the main edge peak at 588 eV and the feature on the low energy side at 586 eV. The peaks forming the L_2 edge of the calculated spectrum also experience a slight low energy shift compared to the experimental spectrum.

Although the spectra are affected by lifetime broadening and experimental resolution effects, it is well known that the L_2 part of the spectrum (i.e. the last two peaks) contains an additional Auger decay that accounts for a significant broadening with respect to the L_3 part (electrons can decay from the L_2 to the L_3 making it broader)³³. We can see this from the published lifetimes of the L_2 and L_3 edges (1.2 eV and 0.8 eV respectively)³³. This effect has been found to apply an additional broadening of around 0.5 eV half-width of half-maximum (HWHM). Also an additional broadening has been found between the t_{2g} and e_g states for Ligand Field Multiplet (LFM) calculations. This could be due to the differences in the vibrational effects on the different states or perhaps due to a difference in hybridisation effects and charge transfer multiplet calculations¹⁷. When performing these CTM calculations the spin-orbit coupling is treated as 'on' or 'off', in this case the spin orbit coupling is usually switched on. The program is designed for an ionic case; this

means that the energy shift is usually too large ¹⁸; again this is manually shifted at the end as the absolute energy positions are not reproduced.

It is evident when comparing the L-edges of Cr(III) and Cr(VI) that the multiplets do change with the differing number of d-electrons, we can see this in the experimental spectra shown in figure 7. There is a shift to higher energy as well as a visible change in the pattern and appearance of the peaks forming the L_{3,2} edge. This makes the determination of the valency, and its cubic crystal field, fairly straightforward ^{9b}. Any distortions from perfect O_h and T_d symmetry for the references are not big enough to show a significant disagreement between the experiment and theory, as shown by the fact that for all the references the experiments are well reproduced (even in the distorted O_h examples) and all calculations are performed assuming pure O_h or T_d symmetry. With Cr₂O₃, in particular, the distortions in the symmetry are not big enough to affect the ground state and so the absorption spectrum is only slightly dependent on the distortion ¹⁵.

Although the experimental spectra have been simulated to a high degree of accuracy there are still some limitations to this approach. The character of the ground state is not considered in detail and also the broadenings arising from hybridisation, vibrations, lifetime and experimental resolution are treated very roughly and are included as general Lorentzian and Gaussian broadenings ¹⁵. The calculated branching ratio of the L₃ and L₂ edges can be improved by including the 3d spin-orbit coupling, the simulated spectra for the references show the expected 2:1 ratio. When comparing Cr³⁺ and Cr⁶⁺ spectra there is an observed shift in edge position of approximately 2-3 eV. The observed shifts are towards higher absorption energies, these have also been observed in the literature ¹⁵ and are thought to increase by 0.7 eV for one removed ground state 3d electron ¹⁵.

In the case of 2p XAS spectra, the spectral shape is mainly determined by the intra-atomic multiplet coupling effects ¹⁹. The physical reason for the weaker charge-transfer effects in XAS is the screening of the core hole potential by the excited electron. In the 2p XAS of transition metal compounds the excited electron stays in the 3d states and participates directly with the screening of the core hole potential, thus suppressing a further screening by the charge-transfer effect in going from initial to final states ¹⁹.

Table 1 UV-vis data collected experimentally for a series of Cr reference compounds.

Sample	v^I	v^{II}	v^{III}	v^{IV}	Simulated 10Dq
Cr₂O₃	300 nm 4.1 eV	460 nm 2.7 eV	600 nm 2.1 eV		2 eV
CrCl₃	360 nm 3.4 eV	530 nm 2.3 eV	740 nm 1.7 eV		1 eV
Cr(acac)₃	228 nm 5.4 eV	256 nm 4.8 eV	272 nm 4.6 eV	335 nm 3.7 eV	2 eV
CrO₃	256 nm 4.8 eV	349 nm 3.6 eV			3.0 eV
K₂CrO₄	290 nm 4.3 eV	370 nm 3.4 eV			1.6 eV
K₂Cr₂O₇	300 nm 4.1 eV	355 nm 3.5 eV	435 nm 2.9 eV		
Na₂CrO₄	274 nm 4.5 eV	372 nm 3.3 eV			1.6 eV

The table above shows the UV-vis data collected for the Cr references along with the Δ value determined in the CTM calculations. It is necessary to be careful when comparing the crystal field parameters obtained experimentally to the 10Dq values determined in the experiment as the calculations are performed in a standard way and do not always give the 10Dq value accurately. An additional factor is that the 10Dq values can be different for the initial and final states. It is the final state 10Dq that is measured in the XAS experiments and the initial state 10Dq that is measured by optical spectroscopy^{9b}. The calculated and experimental values differ greatly with the calculated values being much lower than those obtained by UV-visible spectroscopy. The e_g orbitals are bonded to the ligand so they are much higher in energy than the t_{2g} orbitals; this causes changes in the crystal field from the initial to the final state^{9b}. In the case of the core hole in the final state, the d-electrons are more localised due to the increased attraction from the core hole, there is now less overlap of e_g electrons with neighbours. This means they are not as high in energy and so the energy separation is less. This is why the Δ value is 0.8 x Initial State value. This is adjusted at the end of the calculation¹⁹.

Looking at the purely O_h and purely T_d samples we can see the decrease in the splitting value when moving from O_h to T_d symmetry, O_h Cr(acac)₃ has a crystal field splitting value of 3.7 eV compared to 2.9 eV in the case of the T_d K₂CrO₄. We see a decrease in the

splittings going from $\text{Cr}(\text{acac})_3$ to K_2CrO_4 in the CTM simulated values but the absolute values are not the same as explained above.

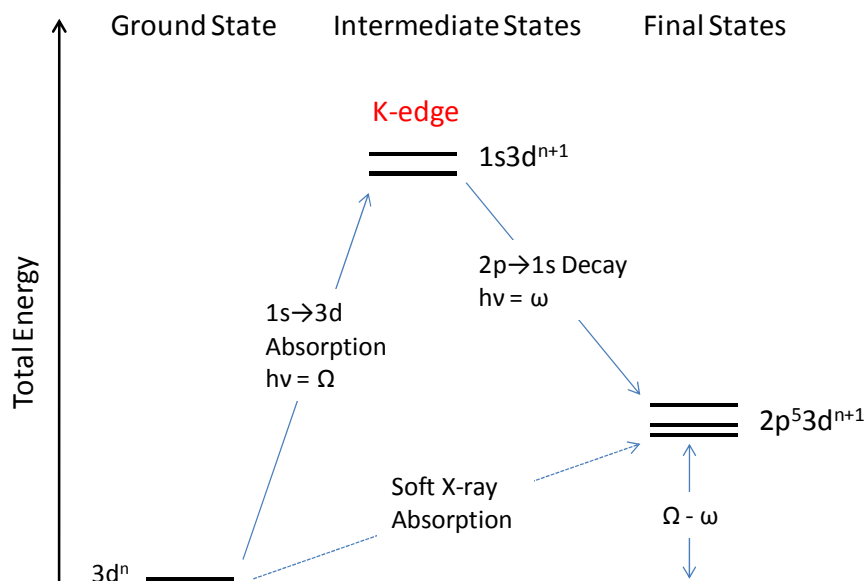


Figure 8 A schematic representation of the $1s2p$ RIXS process showing the same final state as in the direct L-edge XAS experiment ^{1d}.

Figure 8 shows the transitions involved in the hard X-ray RIXS technique, the $2p^5 3d^{n+1}$ final state in this process is the same final state as that reached in the direct $2p \rightarrow 3d$ absorption process occurring in the soft X-ray L-edge experiments. The fact that the same final states are reached, albeit via different transitions, means that the information obtained from both sets of experiments is complementary ^{1d}. Although the shape of the L-edge in both cases is affected by similar properties the fact that the transitions involved are different with different symmetry operations can result in different shapes and features being observed. This is why it is of interest to have both sets of data to compare. Figure 9 (shown below) shows a comparison of the soft X-ray L-edge absorption experiments and indirect L-edge that has been extracted from the hard X-ray RIXS experiments.

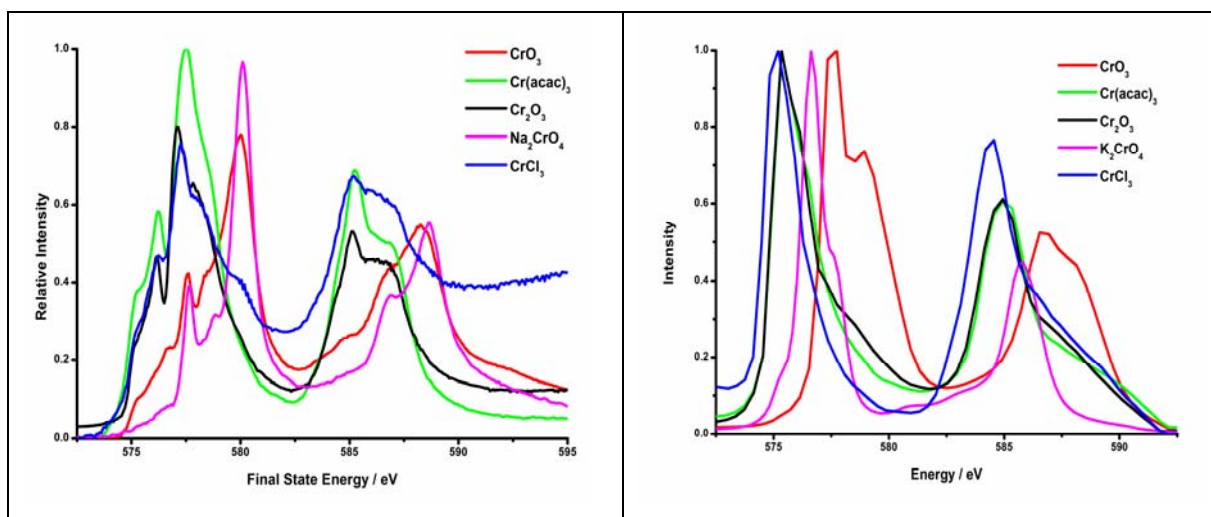


Figure 9 A comparison of the direct and indirect L-edge spectra for a series of Cr reference samples.

It is visible from figure 9 that there are clear differences between the direct and in-direct experiments, the most obvious being the amount of structure present at the edge. There is a difference in resolution between the experimental techniques, this may account for the apparent broadening of the indirect L-edge spectra. For the soft X-ray experiments the resolution is better than 0.1 eV^{1a} compared to 0.6 eV for that of the hard X-ray spectra. A higher resolution for the direct experiments reveals a greater degree of structure at the edge. Although the two techniques are probing the same final states, this does not necessarily mean that the features produced will be the same as they result from different transitions. Figure 9 shows that the indirect L-edges only reproduce the L₃ and L₂ main peaks and most of the multiplet structure present in the hard X-ray experiments is lost. For CrO₃ the L₃ edge consists of two main features at 577.5 eV and 579 eV compared to the five features visible at the L₃ edge in figure 7. The L₂ edge for CrO₃ appears as a broad peak at 587 eV with a shoulder on the high energy side at 588 eV. This is not the same as the peak pattern we see at the L₂ edge in the direct experiments, which consists of the three features; a small shoulder on the low energy side at 585 eV, a shoulder on the low energy side of the main peak at 587 eV and the main edge peak at 588.5 eV. The spectra for Cr(acac)₃ and Cr₂O₃ show the main L₃ edge peak at 575.5 eV, with a small shoulder on the high energy side at 577 eV and 576.5 eV respectively. The L₂ edges for both samples appear as a broad peak at 585 eV. The spectrum for K₂CrO₄ shows three features forming the L₃ edge; a small shoulder on the low energy side of the main peak at 575.5 eV, the main peak appears at 577 eV and a shoulder on the high energy side at approximately 577.5 eV. The L₂ edge again appears as one broad feature at 586 eV. The L₃ edge for CrCl₃ appears as a single peak at 575 eV and the L₂ edge as a single peak at 584.5 eV. The peak positions of the different oxidation states are reproduced in both the soft and hard X-ray methods,

with Cr(VI) compounds lying towards higher energy in both (compared to Cr(III)). In the direct experiments (soft X-ray) all Cr(III) lie on top of each other and all Cr(VI) are also at the same energy position. In the indirect method (hard X-ray) the Cr(VI) samples are slightly skewed with CrO₃ lying towards higher energy than K₂CrO₄.

The relative line intensities in the RIXS spectra are different for the L-edges but the overall shift to higher energies for higher oxidation states is also observed for both techniques (see later). The branching ratio of the L₃ and L₂ edges is not the statistically predicted 2:1, however, this is also observed in the direct cases. In some cases the position of the peaks changes in the different experiments. For example the L₃ edges of K₂CrO₄ and CrO₃ appear at 580 eV but when we compare this to the direct 2p XAS we see that the peaks are shifted to 577 eV and 577.5 eV respectively, this implies that different final states are being probed^{1a}. The lack of fine structure in the indirect L-edges (CIE plot from RIXS plane) means that it is not possible to derive the crystal field and other parameters with the same accuracy as that for 2p XAS spectra. This clearly demonstrates that if the 1s2p RIXS is to be used for electronic structure determinations similar to 2p XAS, then an overall resolution of the order of 0.3 eV is required. This will provide a method of characterisation that is more powerful than 2p XAS because a number of different resonant 1s2p XES spectra can be obtained which will allow a more reliable multiplet fit. Moreover the RIXS can be done at higher energies, probing the bulk system rather than the surface and not requiring UHV conditions, allowing *in-situ* experiments to be done, which is especially useful in dynamic systems to be investigated like catalysts here.

4.3.3 Cr 1s2p RIXS emission studies

X-Ray Absorption Spectroscopy is a useful tool for investigating the nature of the partial density of excited states. The K-edge XANES spectra of chromium mainly reflect the Cr p-orbital contribution to the unoccupied density of states due to the nature of the dipole selection rules governing this transition. It is already accepted that the features in the XANES region provide useful information on the electronic structure of the metal as well as its site symmetry^{25, 38}. However, the pre-edge features in the K-edge XANES region are weak compared to the main edge and for the early transition metals the energy separation between the pre-edge and main edge is low. The 1s broadening of more than 1 eV²⁷ means that the calculations of the metal K-edge only need to be accurate to this resolution. This also means that often a detailed analysis of the K pre-edge spectral features in XAS is limited and contains a certain degree of uncertainty due to a strong background from dipole allowed transitions at higher energies^{1b}. In such cases Resonant Inelastic X-ray

Scattering spectroscopy (RIXS) can be used to provide information on the low-energy unoccupied electronic states. In the RIXS process both the absorption and emission energies are measured, making it a second order process. The X-ray emission is measured as the incident X-ray energy is tuned through an absorption edge, the intermediate state probed is determined by the incident energy ³⁹. The energy transfer dimension present in this process enhances the separation of the pre-edge features from the main edge. RIXS uses hard X-rays to probe the $2p \rightarrow 1s$ fluorescence lines that are emitted after the $1s$ core hole creation, in doing so we are looking at the $3d$ shell indirectly. RIXS is a powerful tool for the study of the electronic excitations and can provide site, element, and orbital selective information once the features are understood and the experiment is tuned properly ³⁹. We will show in this work that the RIXS data provides detailed electronic information on organometallic complexes including charge transfer within the systems making it a useful technique for the study of these catalysts (chapter 5). Another major advantage is the use of hard X-rays; this means that experiments under essentially any condition and on any system are feasible.

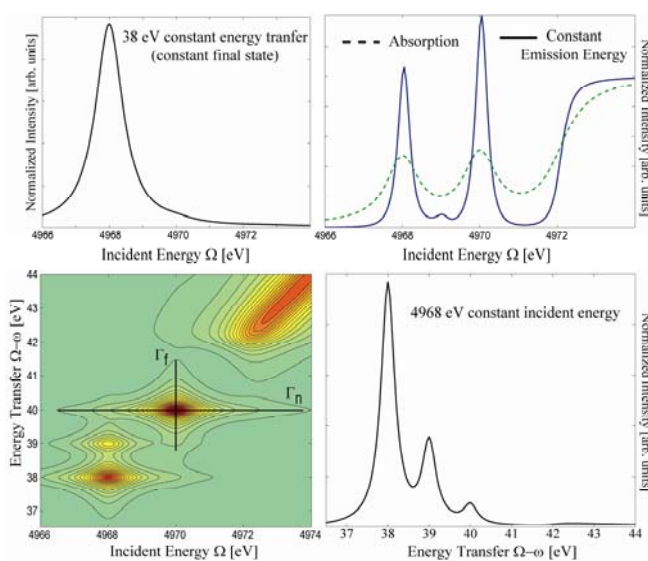
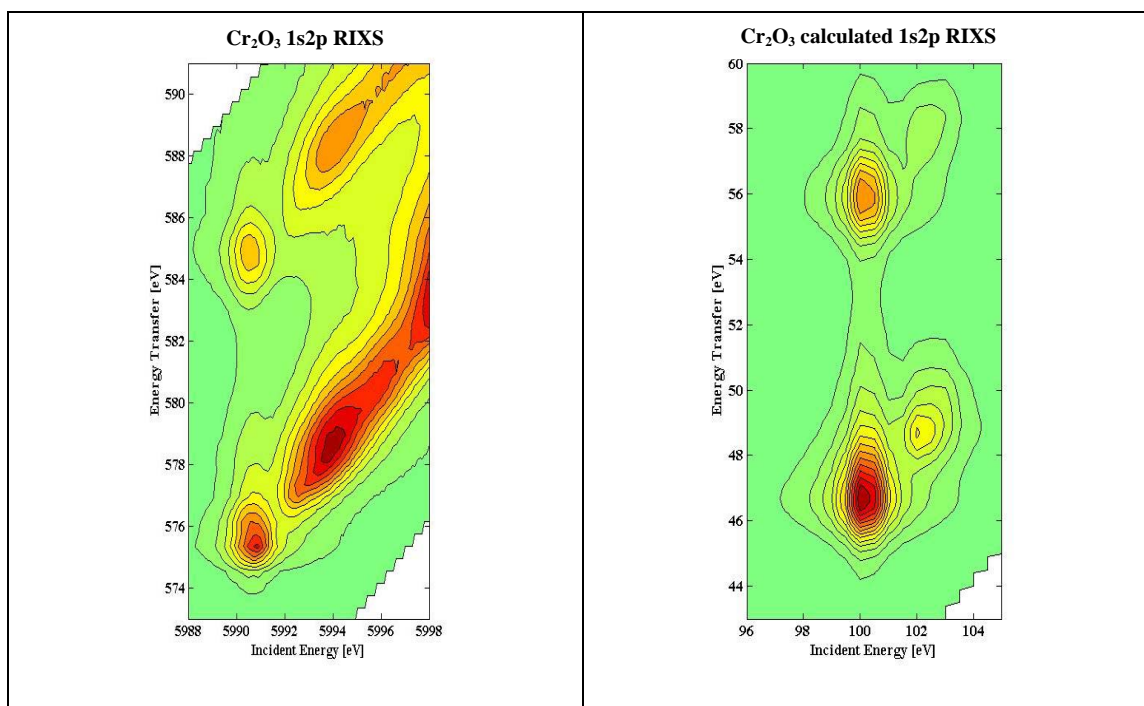


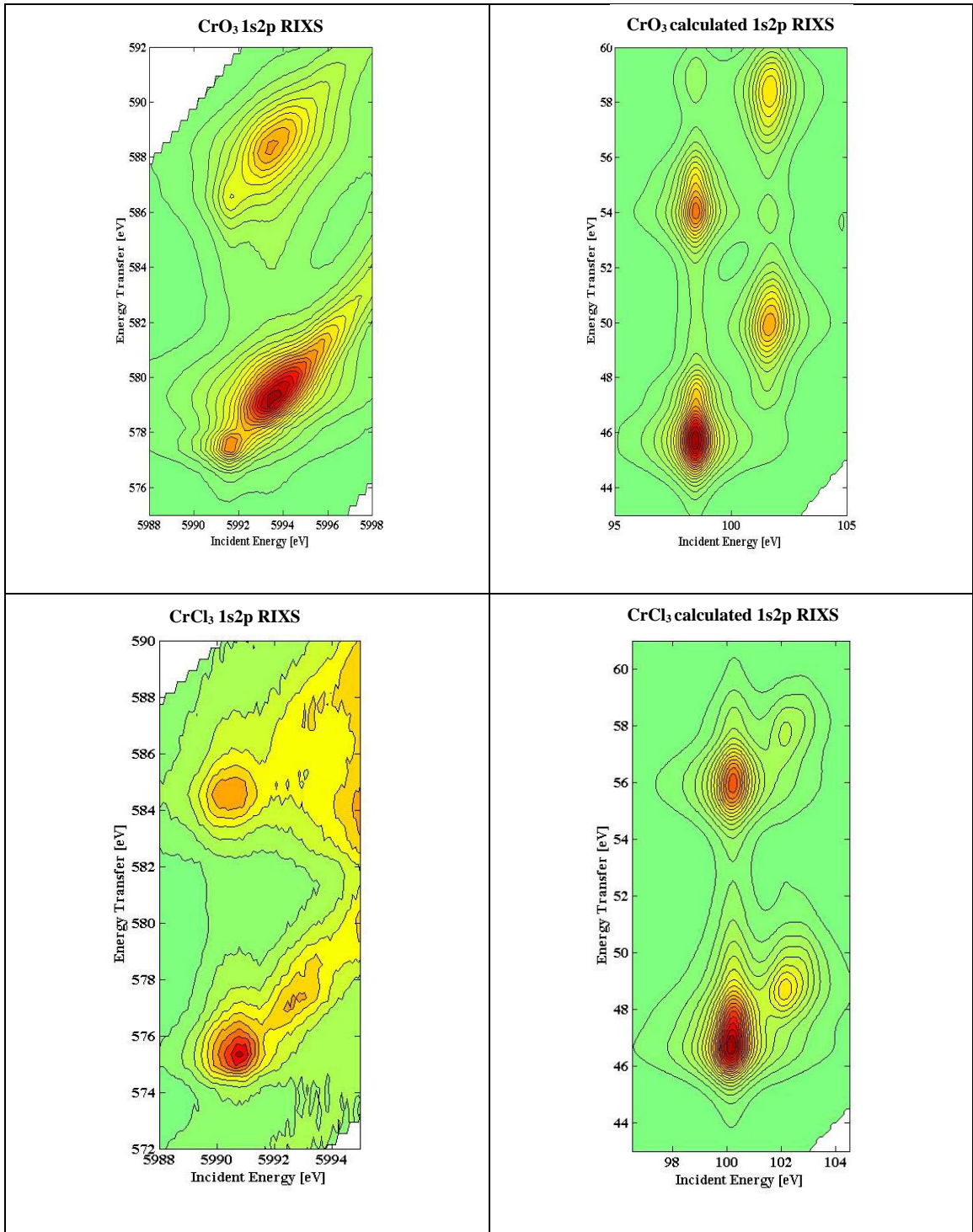
Figure 10 Illustrates the 2D RIXS plot obtained from measuring both XAS and XES along with the corresponding line plots that can be extracted ^{1d}.

The $1s2p$ RIXS planes involve the measurement of the $2p \rightarrow 1s$ X-ray emission spectra at the excitation energies related to the $1s$ pre-edge energies ⁴⁰. These $1s2p$ RIXS planes can be viewed as the transition from the $3d^n$ ground state to the $2p^53d^{n+1}$ final states via the $1s^13d^{n+1}$ intermediate states (a schematic of these transitions is shown in figure 8). The matrices involved in this process are the $3d^n \rightarrow 1s^13d^{n+1}$ quadrupole transition coupled to the $1s^13d^{n+1} \rightarrow 2p^53d^{n+1}$ dipole decay. From the final 2D RIXS contour plot we can obtain both K pre-edge and L-edge like information from a single experiment. The pre-edge

structure is observed by looking at the incident energy and integrating over the emission energy and the L-edge can be obtained by looking at the energy transfer and integrating over the incident energy.

The RIXS spectra can be discussed as a 2D plane or as individual cross sections. The vertical cross section of the RIXS plane is a scan of constant intermediate state (Constant Incident Energy - CIE) over a range of final states; it shows us the possible final states reached by one particular 1s resonance (same final states as in direct L-edge absorption). In the horizontal direction (Constant Energy Transfer – CET) we keep a constant final state while the intermediate states are varied, these intermediate states correspond to the individual K pre-edge features. This scan shows all the 1s resonances that decay to this particular $2p^53d^{n+1}$ final state. In these experimental spectra it is not possible to separate these individual electronic states due to the fact that the splittings between them are smaller than the lifetime broadenings of the experiment. The experimental RIXS planes therefore combine several intermediate states in the constant incident energy direction and several final states in the constant energy transfer direction ^{1d}. In the diagonal direction we are measuring the intensity at constant emission energy while scanning the incident energy (CEE scan). This line plot indirectly measures the HERFD XANES.





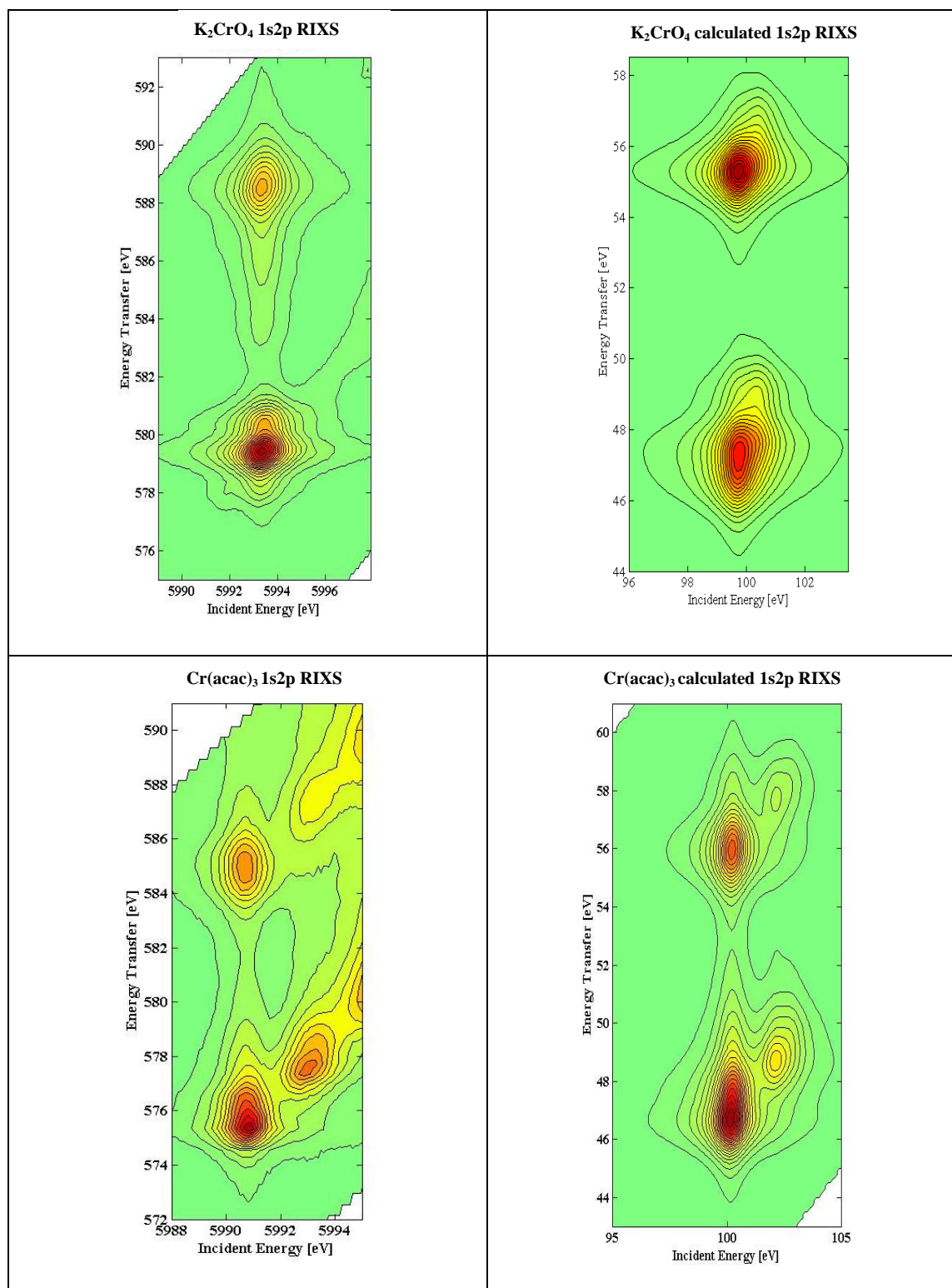


Figure 11 Comparison of $K\alpha$ RIXS experiments with calculated pre-edge spectra for Cr^{3+} and Cr^{6+} compounds.

The $K\alpha$ RIXS for Cr_2O_3 (figure 11) shows the presence of two pre-edge features before the main K -absorption edge along the $K\alpha_1$ emission line; these appear at 5991 eV and 5994 eV incident energy. The main edge rise starts at 5999 eV. The first pre-edge feature at 5991 eV (575.5 eV energy transfer) is spread over a 2 eV range, implying that this peak arises

from two electronic transitions ^{1b}. The second pre-edge peak at 5994 eV (578.5 eV energy transfer) is stretched over 4 eV and is relatively more intense in comparison to the first feature. At the $K\alpha_{II}$ emission line there are also 2 pre-edge features at 5991 eV and 5994 eV incident energy, these two emission energy maxima occur at 585 eV and 588 eV energy transfer. Both of these features appear less intense in comparison to the respective pre-edge features at the $K\alpha_I$ emission line. There also appears to be an absorption tail leading to the main edge, starting at 5996 eV. The broadening observed in the diagonal direction of the experimental spectrum is caused by the experimental broadening and core hole lifetime effects and can be included in the calculation ^{1b}. In the calculation the 2 pre-edge features are nicely reproduced with the first pre-edge feature at 5991 eV (100 eV in theoretical case) being the most intense. When comparing the experimental and theoretical spectra a difference in intensity of the pre-edge features is observed, this may be due to orbital hybridisation and as it is not included in the calculations ^{1b}. The experimental spectrum also shows a splitting of 10 eV in the energy transfer direction; this splitting is also evident in the calculation. This splitting value relates to the energy difference between the L_3 and L_2 edges in the soft X-ray XAS experiments, as the same final states are probed. In this case the energy difference in the soft X-ray experiments is also approximately 10 eV. These RIXS simulations only cover the pre-edge region meaning that the main edge is not reproduced, this is because the calculations to produce the main edge are very complicated and, in the case of chromium, leaving out the main edge does not affect the quality of the pre-edge.

If we compare the 1s2p RIXS plot shown in figure 11 with the normal K-edge absorption XANES spectrum we can see the increased level of separation of the two pre-edge features from the main edge. In the normal XANES spectrum there is a small peak at 5991 eV and a second more intense feature at 5994 eV, when we look at the RIXS spectrum these two features become completely separated out with two distinct peaks at 5991 eV and 5994 eV and the contours returning to base line in-between. When looking at the pre-edges in a XANES experiment the intensity is much weaker in comparison to that of the main edge and so by using RIXS we are able to achieve a greater separation of these features from the main edge along with greater resolution. We can then compare this to the DOS obtained from the FEFF calculation and assign the two resonances forming the peak, which we have done above for the direct HERFD experiments. In this case we can see that the first pre-edge feature at 5991 eV shows DOS intensity from the Cr s, O p and Cr d-orbitals overlapping with the Cr p-orbital probe.

As we move towards CrO_3 the T_d geometry becomes more distorted due to the varying Cr-O and Cr-Cr inter-atomic distances. This will affect the molecular orbital energy levels and therefore the features we see in the X-ray spectra. The $K\alpha$ RIXS spectrum shows the presence of two pre-edge features along the $K\alpha_I$ emission line. The first less intense feature occurs at 5991 eV incident energy and the second more intense feature at 5994 eV incident energy, having energy transfer values of 577.5 eV and 579 eV. The second feature is spread out over approximately 4 eV which implies that four resonances form this feature. The $K\alpha$ RIXS spectra show differences in the appearance of features at the $K\alpha_I$ and $K\alpha_{II}$ emission lines. At the $K\alpha_{II}$ there are two clear pre-edge features compared to the $K\alpha_I$ where we observe an area of spectral intensity at 5991.5 eV and a second more intense feature at 5993 eV incident energy. The simulation shows two features at both the $K\alpha_I$ and $K\alpha_{II}$ emission lines with the separation of the features at the $K\alpha_{II}$ emission line being approximately 2 eV for both experiment and theory. The splitting between $K\alpha_I$ and $K\alpha_{II}$ is 9 eV in both the experimental and theoretical spectra. The difference between the L_3 and L_2 edges in the direct L-edge XAS experiment is also 9 eV, this direct L-edge experiment is comparable to the vertical cross section in the RIXS contour plot.

The CrCl_3 RIXS spectrum shows two areas of intensity along the $K\alpha_I$ emission line, the first feature appears at 5991 eV and the second at 5993 eV incident energy (575.5 eV and 577 eV energy transfer respectively), the main edge rise begins at 5996 eV. Along the $K\alpha_{II}$ emission line the first pre-edge feature appears at 5991 eV (584.5 eV energy transfer) as in the $K\alpha_I$ part. In this case the spectral intensity is weaker but there is also the appearance of a second area of intensity at 5993 eV (586 eV energy transfer). The main edge appears at 5995 eV for the $K\alpha_I$. The calculation of the pre-edge shows two features, the first being of greater intensity both for the $K\alpha_I$ and $K\alpha_{II}$ emission lines. In the experimental spectrum the splitting value between the $K\alpha_I$ and $K\alpha_{II}$ pre-edge features appears to be 9 eV compared to 10 eV in the theoretical spectrum. This value can be compared to that obtained in the direct L-edge experiments, which appears to be closer to 9 eV.

The $K\alpha$ RIXS spectrum of K_2CrO_4 shows one intense pre-edge feature at about 5994 eV incident energy in both the $K\alpha_I$ and $K\alpha_{II}$ emission lines, 577.5 eV and 588.5 eV energy transfer. The splitting value in the vertical cross section for the pre-edges is approximately 9 eV in both the experimental and theoretical spectra. When comparing this to the energy difference between the L_3 and L_2 edges in the direct L-edge experiments we can see that these are in agreement with the difference between the L-edges also being 9 eV. The spectrum for K_2CrO_4 is very different to that of the other Cr(VI) species, CrO_3 . These two complexes possess different geometries, which affects the electronic properties observed.

In the T_d K_2CrO_4 case there is one intense pre-edge feature, also clearly visible in the K-edge XANES spectrum, even in the normal XANES. This feature is caused by hybridisation of O p-orbitals with Cr p-orbitals, as shown in the FEFF9 empty density of states calculations shown above. In the case of CrO_3 the compound possesses distorted T_d geometry; the pre-edge region in the RIXS plot shows two pre-edge features. The feature at lower energy is not present in the K_2CrO_4 spectra due to the fact that although there is O p-orbital contribution there is no Cr p-orbital contribution. For CrO_3 there is Cr p and O p-orbital contributions for both of these pre-edges and so both are visible in both the XANES and the RIXS spectra. When comparing to the XANES we can see that in the low energy resolution case there is only one broad pre-edge with a shoulder on the low energy side, the HERFD shows a better resolved peak, but the RIXS shows a clear separation into two features. This demonstrates the benefits of the RIXS technique when analysing the pre-edge of these metal complexes. The fact that the two Cr^{6+} RIXS calculations show two features for CrO_3 and one feature for K_2CrO_4 suggests that the additional peak is caused by the structural differences between the compounds and the hybridisation of the Cr p and O p-orbitals. The broadening of the peak appears to be symmetric in the incident energy direction but more asymmetric in the energy transfer direction. This can be an indication that the final state is not a single state and that there are additional shoulder states at the high energy transfer site of the main peak ^{1a}.

$Cr(acac)_3$ displays two pre-edge features in the 1s2p RIXS spectrum at 5991 eV and 5993 eV incident energy at both the $K\alpha_I$ and $K\alpha_{II}$ emission lines. The first pre-edge feature at 575.5 eV energy transfer is the most intense and is spread over 2 eV, suggesting there are two resonances forming the peak, it is difficult to explain this using the DOS from FEFF9 as the XANES spectra could not be accurately reproduced using this method. The second pre-edge feature at 577.5 eV is less intense than the first and shows an energy splitting of 2 eV from the first peak. The $K\alpha_{II}$ emission line shows a weaker first pre-edge at 585 eV energy transfer compared to the $K\alpha_I$ but this is also spread over 2 eV and shows an energy splitting of 2 eV from the second (less intense) feature at 587 eV energy transfer. The calculation also shows two pre-edge features with the same energy splitting between the $K\alpha_I$ and $K\alpha_{II}$ lines of 10 eV, and the first peak is also more intense in this case. From the L-edge spectrum we can see the energy difference between the L_3 and L_2 edges is approximately 8 eV and does not seem to agree with that obtained in the RIXS experiment. When comparing to the normal XANES for $Cr(acac)_3$ we see a lot more detail, in the XANES spectra the second feature is not resolved and appears as a small hump, the HERFD shows it more clearly but does still not provide the degree of separation as offered in the RIXS plot.

For both Cr(III) and Cr(VI) compounds the number and relative intensities of the pre-edge features are well reproduced. The Cr(III) spectra show similar peak patterns with two pre-edge features separated by 3 eV. The K_2CrO_4 Cr(VI) case shows the presence of only one pre-edge feature. All of the spectra show asymmetric line shapes with a tail towards higher final state energies in the CIE direction, this may be caused by electron-electron interactions in the $2p^53d^{n+1}$ final states^{1b}. If we compare the spectra of Cr_2O_3 and CrO_3 , it is clear that in moving from Cr^{3+} to Cr^{6+} we see a shift in incident energy of the pre-edge features to higher energies, by approximately 2 eV (and 2 eV in energy transfer). This is also true for the Cr compounds containing non-oxidic ligands. The appearance of the pre-edges for the Cr^{3+} and Cr^{6+} also differ in that for Cr^{6+} the features appear more symmetric than for Cr^{3+} .

Table 2 Crystal field values for Cr reference samples calculated in both soft and hard X-ray simulations

Sample	Simulated crystal field splitting from RIXS	Simulated $10Dq$ from L-edge
Cr_2O_3	2 eV	2 eV
CrCl_3	2 eV	1 eV
$\text{Cr}(\text{acac})_3$	2 eV	2 eV
CrO_3	3 eV	3 eV
K_2CrO_4	0.7 eV	1.6 eV
Na_2CrO_4	0.7 eV	1.6 eV

Table 2 shows the respective crystal field splitting values calculated for both the direct soft X-ray L-edge experiments and those calculated from the hard X-ray RIXS analysis. The two methods produce the same values for each of the samples studied in most cases, however CrCl_3 shows a value of half in the soft X-ray simulations and the chromates show a value that is doubled in the soft X-ray experiments. As discussed previously the L-edge calculations did not produce the same crystal field values as that obtained from UV-vis experiments due to the fact that the two processes are determining the crystal field of different states. In the case of XAS it is the final state crystal field value that is calculated rather than the initial state in the case of optical absorption experiments. For this reason

we would expect to see greater agreement with the values obtained from the XAS and RIXS analysis rather than with the values obtained from optical absorption spectroscopy. From this we can deduce that the RIXS calculations are also governed mainly by the crystal field splitting value of the final state, rather than that of the initial state.

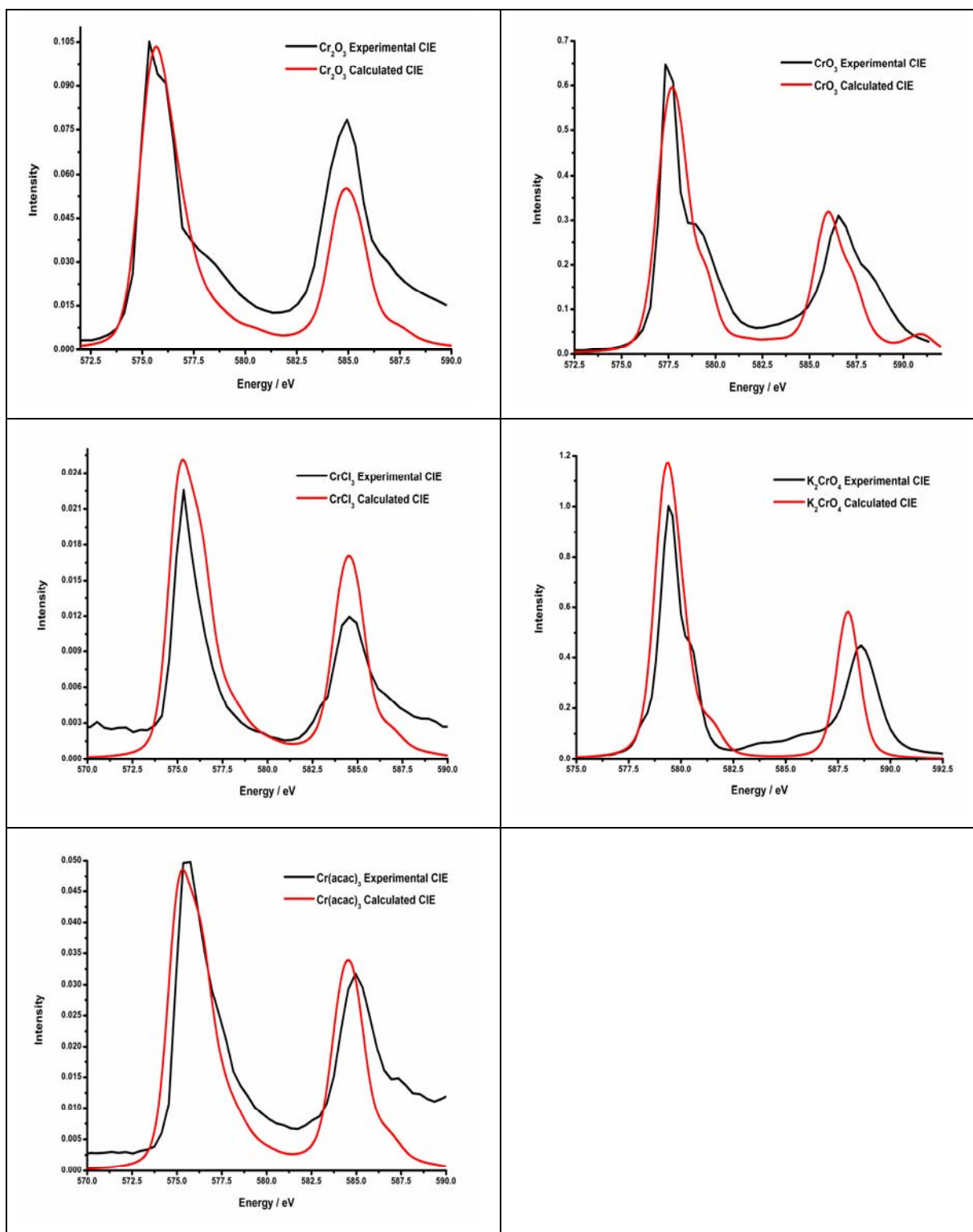


Figure 12 A comparison of experimental and theoretical constant incident energy plots (indirect L-edges taken from the RIXS plot).

Studies have shown that with an increase in the experimental resolution of the monochromator and detector from around 1 eV to 0.3 eV, closer to that obtained with 2p XAS, a great deal more information is revealed. The level of information obtained from calculations of 1s2p RIXS spectra with this increase in resolution is much better than that from the corresponding 2p XAS experimental data ^{1a}. This shows how powerful the RIXS technique could be.

4.3.4 Cr K β Emission Studies

The valence-to-core region of transition metal X-ray spectra contains a wealth of information about the electronic and molecular structure of the system in question. Such valence-to-core X-ray emission spectra have previously been measured for Cr compounds such as oxides, carbides, borides, nitrides, phosphides etc. These results already show good agreement with calculated spectra ^{3b}. Looking at the valence-to-core emission lines gives us detailed information on the first coordination shell of Cr; hopefully by exploring this we can identify the effects of substitution around the central Cr atom, this is an extremely useful property as we are now able to distinguish nearest neighbours that are in the same row of the periodic table, which we are unable to do in EXAFS ⁴¹. It has been known for a while that the K β emission spectra of 3d metals show a pronounced chemical sensitivity. Such chemical effects have been used as a probe of chemical bonding ⁴², the largest of these affecting the valence-to-core X-ray transitions. These transitions carry information on the occupancy and symmetry of the orbitals involved in chemical bonding. Similarly to XAS studies, XES does not require long range order in the system being studied. This is one of the main advantages of XES; it is sensitive to the composition of the bulk of the material rather than just the surface, as in the case of other inner-shell spectroscopies like XPS. Other advantages include the fact that high vacuum conditions are not required and the sample environment is flexible. As with XAS it is also possible to carry out this technique under controlled atmospheric conditions, at cryogenic or high temperatures and for *in-situ* catalysis studies.

In 3d transition metal compounds, the 1s core state can be excited and the 1s core hole can then be filled by 2p, 3p or 4p valence electrons. For a 1s core hole, this yields 1s2p (K α), 1s3p (K β) and 1s4p (K $\beta_{2,5}$) XES. The 1s2p emission spectrum is split into two peaks due to the 2p spin-orbit coupling; these two peaks are the K α_{I} and K α_{II} , where K α_{I} relates to a 2p_{3/2} core hole in the final state and K α_{II} to a 2p_{1/2} core hole. The two regions visible in the K β emission spectrum are the K β main line and K β satellite lines. The K β main line corresponds to the core-to-core 3p \rightarrow 1s transition and consists of a K $\beta_{1,3}$ peak and a low

energy tail $K\beta'$ that is due to (3p,3d) exchange interactions⁴³. The 1s4p valence band XES is split into the cross over peak ($K\beta''$) and the valence band XES ($K\beta_{2,5}$). The $K\beta_{2,5}$ lie immediately below the Fermi level and are used to describe the valence band, $K\beta''$ is the cross-over peak, which appears at higher binding energies (lower fluorescence)^{3b}.

The $K\beta_{2,5}$ is caused by metal 4p character that has hybridised with the valence states of the ligands. There could also be $K\beta_{2,5}$ intensity from quadrupole XES from occupied 3d states. The $K\beta''$ peak is called the cross-over peak because it can be considered as the XES channel from a ligand 2s 'core' state to a metal 1s state, which is a cross-over transition ³². It is better to view this transition as one from metal 4p to 1s, where the metal 4p has hybridised with the ligand 2s core state ³². Due to the nature of the ligand 2s \rightarrow metal 1s transition these features reflect the binding energies of the ligand 2s orbitals (5965-5980 eV in this case). The intensity of the cross-over peak is inversely proportional to the metal-ligand distance; this is caused by the fact that shorter distances imply stronger hybridisation ³².

The $K\beta$ satellite lines are very sensitive to the local environment of 3d transition metal atoms because it is the nature of the ligand in the first coordination sphere around the metal atom that determines the character of the valence orbitals ^{3b}. This technique is also able to discriminate between ligands of similar atomic number such as O, N, C, etc in the first coordination sphere of the metal atom ^{3c}, which is difficult to distinguish by other XAS experiments ^{3a}.

The paper by Sofanov *et al* ^{3a} uses FEFF8.2 successfully to reproduce the experiment. From the experimental data obtained in this study at the ESRF some interesting trends in the $K\beta$ main line spectra were observed, the plots agree with those published for the same compounds ^{3a, b}. All the compounds in the 3+ oxidation state show the additional feature at about 5935 eV, this feature is thought to be due to spin flip transitions ⁴⁴. This part of the spectrum gives us information on the spin state of the compound, the higher the spin the higher the energy of the $K\beta$ main line ⁴⁵.

The figures below (figures 14 and 15) show the $K\beta$ main lines for a series of chromium compounds with different ligands, oxidation states and geometries as well as associated calculations using FEFF9. Both the $K\beta''$ and $K\beta_{2,5}$ valence-to-core lines are also shown (in figures 15 and 16) the $K\beta_{2,5}$ lines involve the highest energy molecular orbitals with Cr 3d, 4s and 4p character as well as ligand 2s and 2p character, providing information on the nature of the bonding in the sample ^{3a, b, 45}. The $K\beta''$ lines come at slightly lower energies

and the structure contained in both of these valence-to-core lines makes up what is called the 'satellite region'.

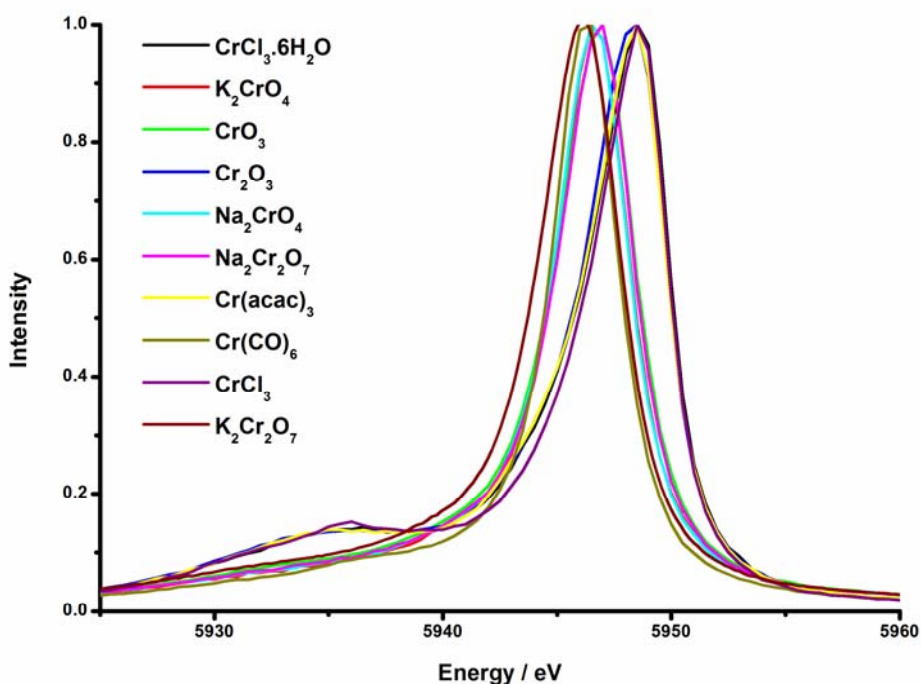


Figure 13 K β main lines for a series of Cr reference materials.

Figure 13 shows the core-to-core K β emission lines for all samples; this figure highlights the additional feature present in the T_d spectra as well as the shift in the position of the K β main line maxima from T_d to O_h materials.

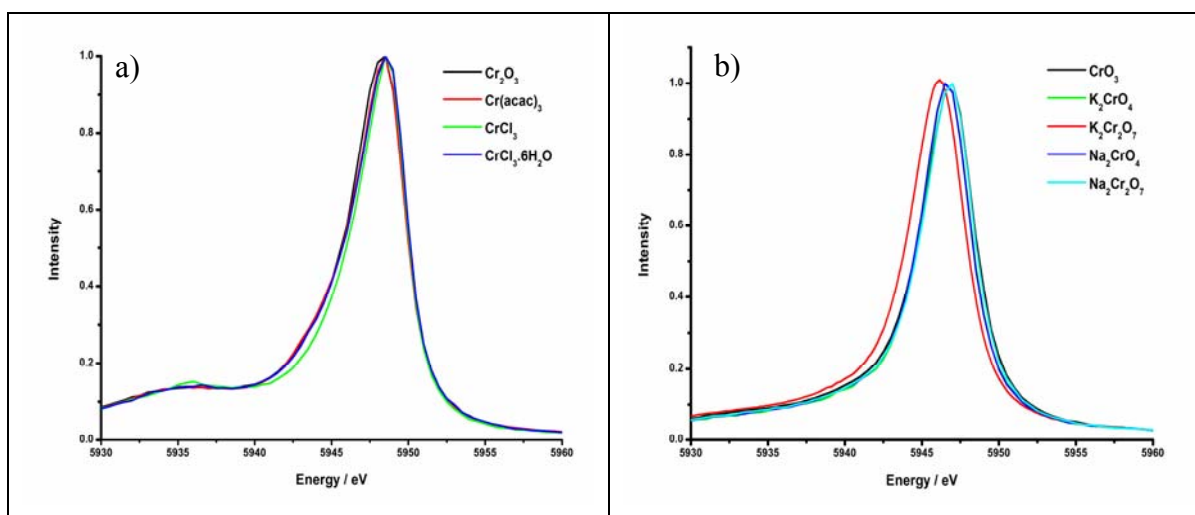


Figure 14 K β main lines for Cr(III) (a) and Cr(VI) (b) reference materials.

The core-to-core spectra for the Cr(III) samples shown in figure 14a show a small, broad feature at 5932.5 to 5940 eV and the main peak at 5949 eV. The Cr(VI) samples only show the presence of the main peak at 5947 eV. There is a shift of 2 eV in the position of the main peak between Cr(III) and Cr(VI). The Cr(CO)₆ (Cr⁰) main line looks similar to that of the Cr(VI) samples with the appearance of one main peak at 5946.5 eV. The work by Sofanov *et al*^{3a} claims to demonstrate the first example of the practical application of the XES method for studying real objects. However, the structures of the Kβ satellite lines and more specifically the Kβ'' cross-over peaks have been mainly used as an index for the local chemical coordination of the chromium, looking at one geometry with one single ligand. The work by Serena de Beer *et al.* investigates the factors influencing the valence-to-core and core-to-core lines (spin state, oxidation state, and coordination environment) in iron based systems⁴⁶. They found that the valence-to-core region was more sensitive to the chemical environment⁴⁶. For catalysis the interest in using this technique is in looking at the replacement of ligands during catalysis which might tell us something about the mechanism involved. Figure 15, below, shows the Kβ satellite region (cross-over and Kβ_{2,5} peaks) for all the chromium reference compounds. A comparison of O_h and T_d geometries is then shown in figure 16.

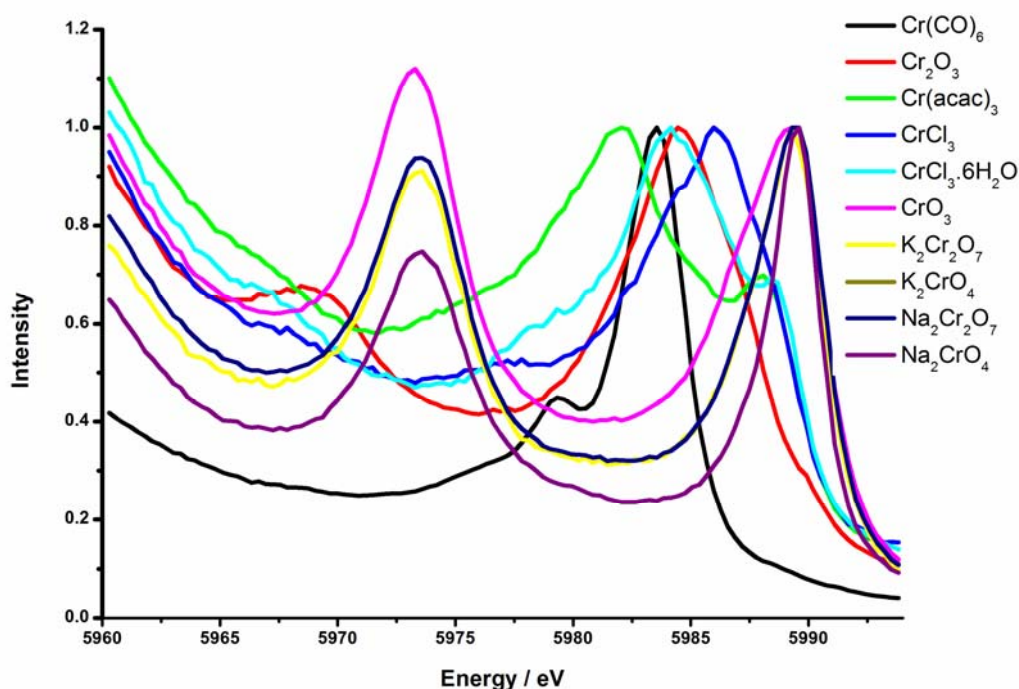


Figure 15 Kβ satellite and cross-over peaks for a series of Cr reference materials

The figure above, figure 15, shows how the position and appearance of the Kβ'' changes depending on the nature of the environment around the central Cr. The T_d compounds all

show a very pronounced $K\beta''$ (cross-over) peak at the same energy position, the splitting between the $K\beta_{2,5}$ peaks and the $K\beta''$ peaks in these samples is around 15-17 eV, this is much larger than that of the O_h samples (8-10 eV) and is similar to that found for oxygen ligands (20 eV) in previous studies ^{3a}.

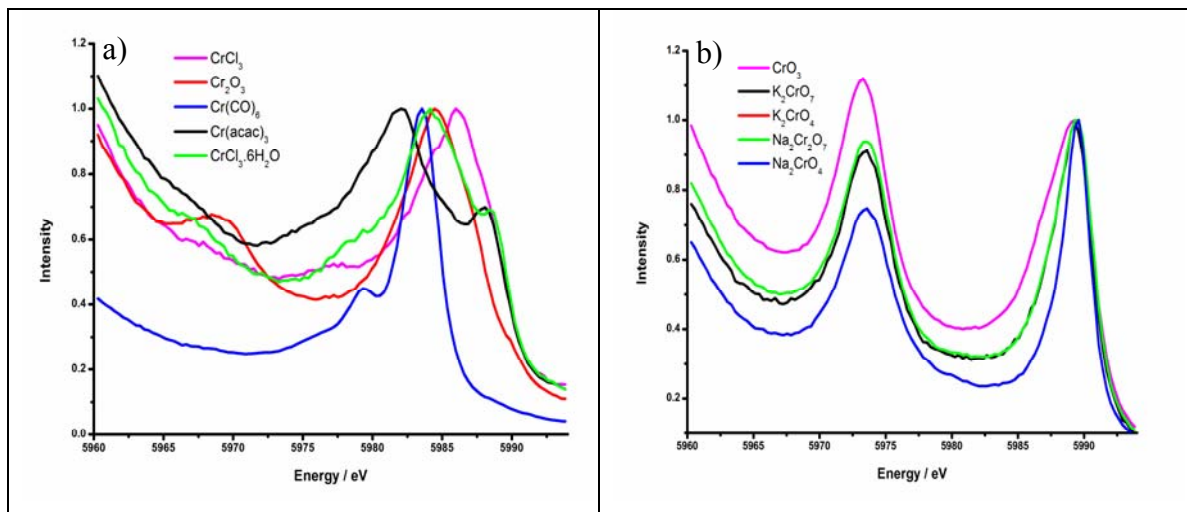


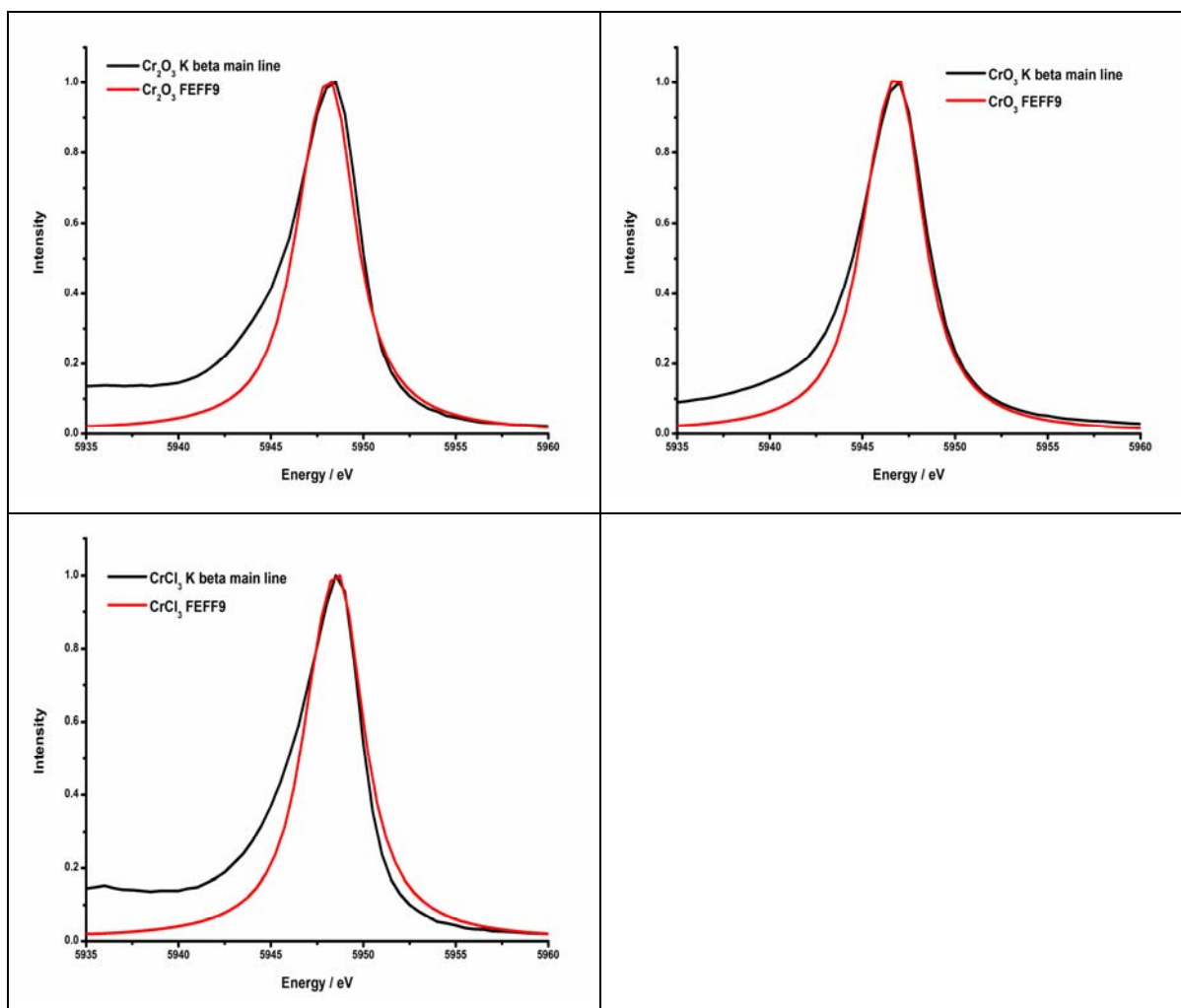
Figure 16 $K\beta$ satellite and crossover peaks for a series of Cr powders in Octahedral (a) and Tetrahedral (b) geometry.

From the experimental data (figure 16) we can see that the position and shape of the satellite and cross-over peaks are changing with the local environment around the central chromium. Previous studies have shown that the crossover peak can be used as a fingerprint of the presence of Cr-O, C-N, or Cr-C bonds in the sample ^{3a}. Although the same trend can be seen from our results it can also be said that the position and shape also appear to be sensitive to the oxidation state and geometry of Cr, so one has to be very careful with this approach. Figure 16 shows the experimental $K\beta$ valence-to-core spectra for a series of Cr reference compounds. The $Cr(CO)_6$ spectrum shows the appearance of a small feature at 5979 eV ($K\beta''$) and a larger peak at 5984 eV ($K\beta_{2,5}$). $Cr(acac)_3$ has two much smaller peaks, one at 5982 eV ($K\beta''$) and 5988 eV ($K\beta_{2,5}$), this is a similar shape to the spectrum of $CrCl_3 \cdot 6H_2O$. There is also a peak at 5988 eV in the $CrCl_3 \cdot 6H_2O$ spectrum; however the first peak is slightly shifted and appears at 5984 eV. In the case of $Cr(acac)_3$ and $CrCl_3 \cdot 6H_2O$ there are direct Cr-O and Cr-C neighbours, this complicates the results and therefore the interpretation of these spectra by producing multiple or broad peaks. In the case of $CrCl_3$ there is a small broad feature from 5982.5 to 5990 eV similar in position to the $CrCl_3 \cdot 6H_2O$ spectrum with only one broad feature rather than two individual peaks. The spectrum for Cr_2O_3 shows some similarities to the shape of the T_d spectra, this maybe due to the fact that Cr_2O_3 is distorted O_h . The distortion from perfect O_h geometry means that certain transitions now become allowed, this may account for the T_d like appearance. The spectrum for Cr_2O_3 contains two peaks at 5969 eV ($K\beta''$) and 5984 eV ($K\beta_{2,5}$) with a

splitting of 15 eV, the same as that visible in the T_d spectra, however the absolute energies are not the same as in the T_d case. The $\text{Cr}(\text{CO})_6$, $\text{Cr}(\text{acac})_3$ and the $\text{CrCl}_3 \cdot 6\text{H}_2\text{O}$ $K\beta$ spectra show either a shift of the $K\beta''$ (cross-over) peak toward the $K\beta_{2,5}$ peak or a strange distortion of the satellite peak region, again this may be a result of having both Cr-O and Cr-C bonds.

All of the spectra for the T_d compounds; K_2CrO_4 , Na_2CrO_4 , $\text{K}_2\text{Cr}_2\text{O}_7$, $\text{Na}_2\text{Cr}_2\text{O}_7$ and CrO_3 show the same features, there are two peaks appearing at 5974 eV and 5989 eV split by 15 eV (Figure 16b), all the T_d samples also contain Cr-O bonds and so we would expect to see this peak in all. In each case the second, higher energy peak, is more intense. The peak at 5974 eV is the $K\beta''$ (cross-over) peak and the peak at 5989 eV is the $K\beta_{2,5}$ peak.

The following spectra show the experimental $K\beta$ main lines along with the FEFF9 calculations; a fairly good agreement between experiment and theory is observed.



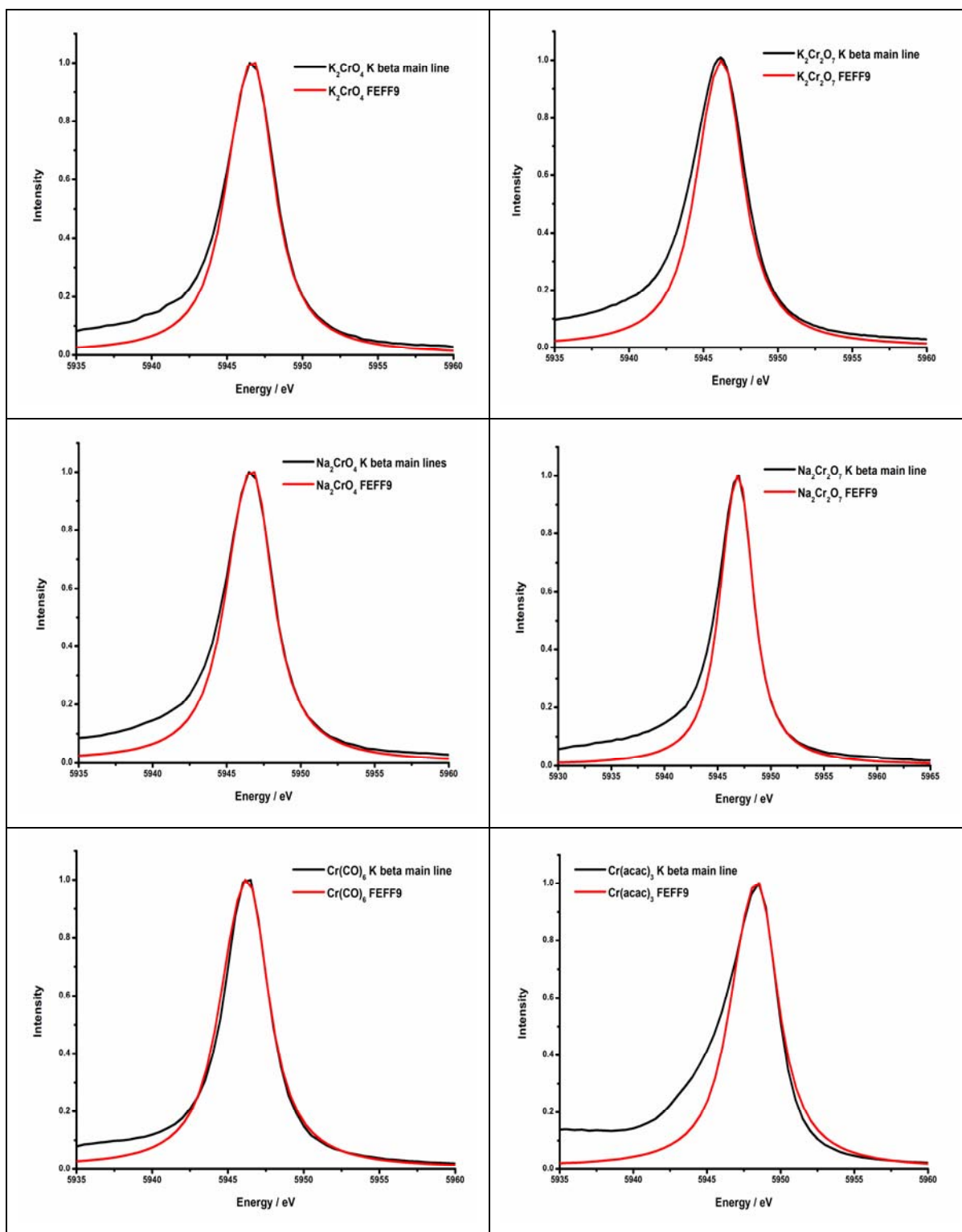
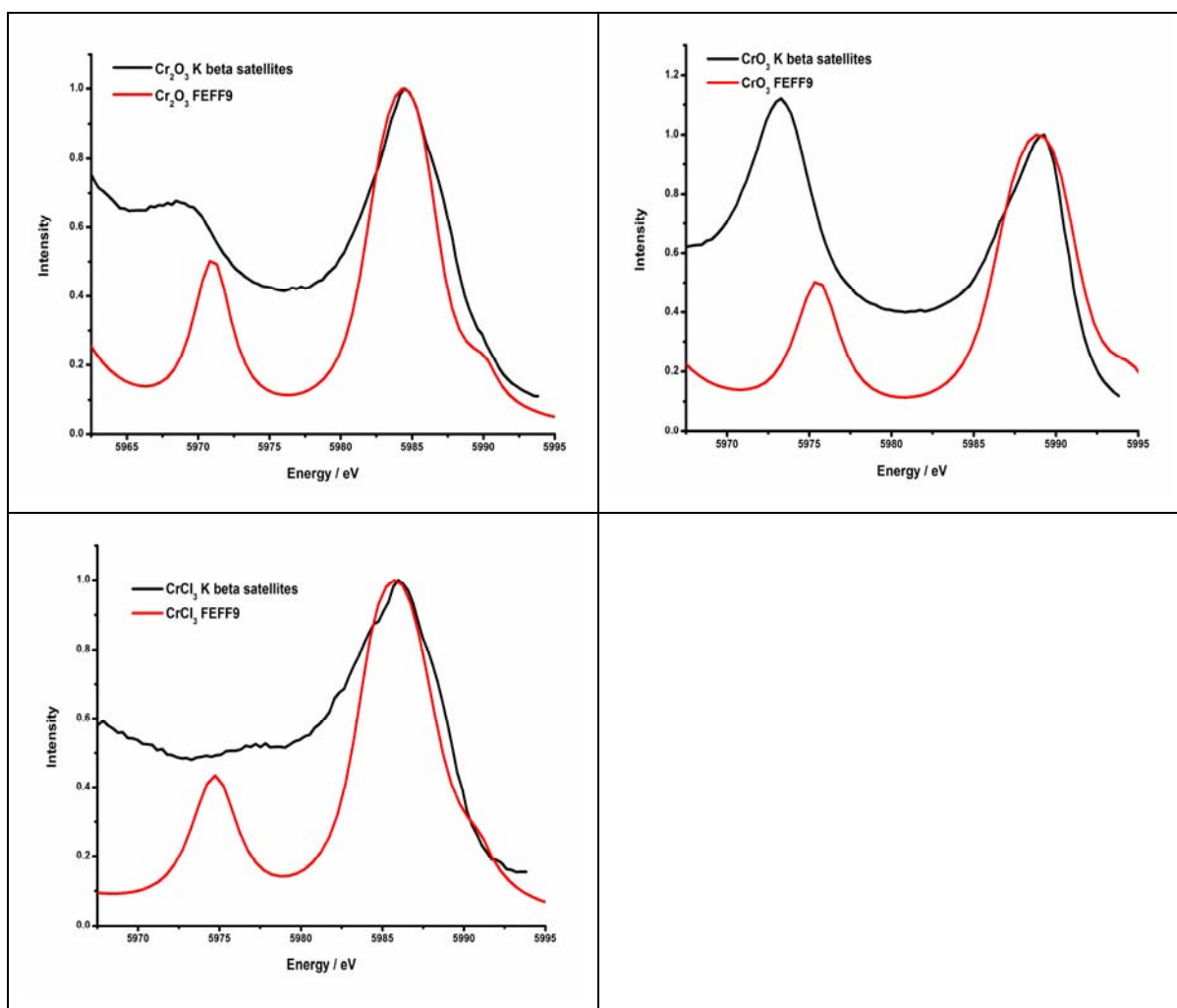


Figure 17 K β main lines and FEFf9 simulations for a series of Cr compounds.

Figure 17 shows the experimental K β main lines with associated FEFf9 simulated mainlines for a series of Cr compounds. For 3d transition metals the K β main lines correspond to the $3p \rightarrow 1s$ transition. The FEFf9 calculated spectra show good agreement with the experimentally obtained main lines. The general shape of the peak is well

reproduced however there is a slight broadening visible experimentally on the low energy side of the main lines for all samples.

FEFF9 has also been used to reproduce the $K\beta$ satellite region for the chromium samples, the experimentally obtained $K\beta$ satellites along with the FEFF9 simulation are shown in figure 18, below.



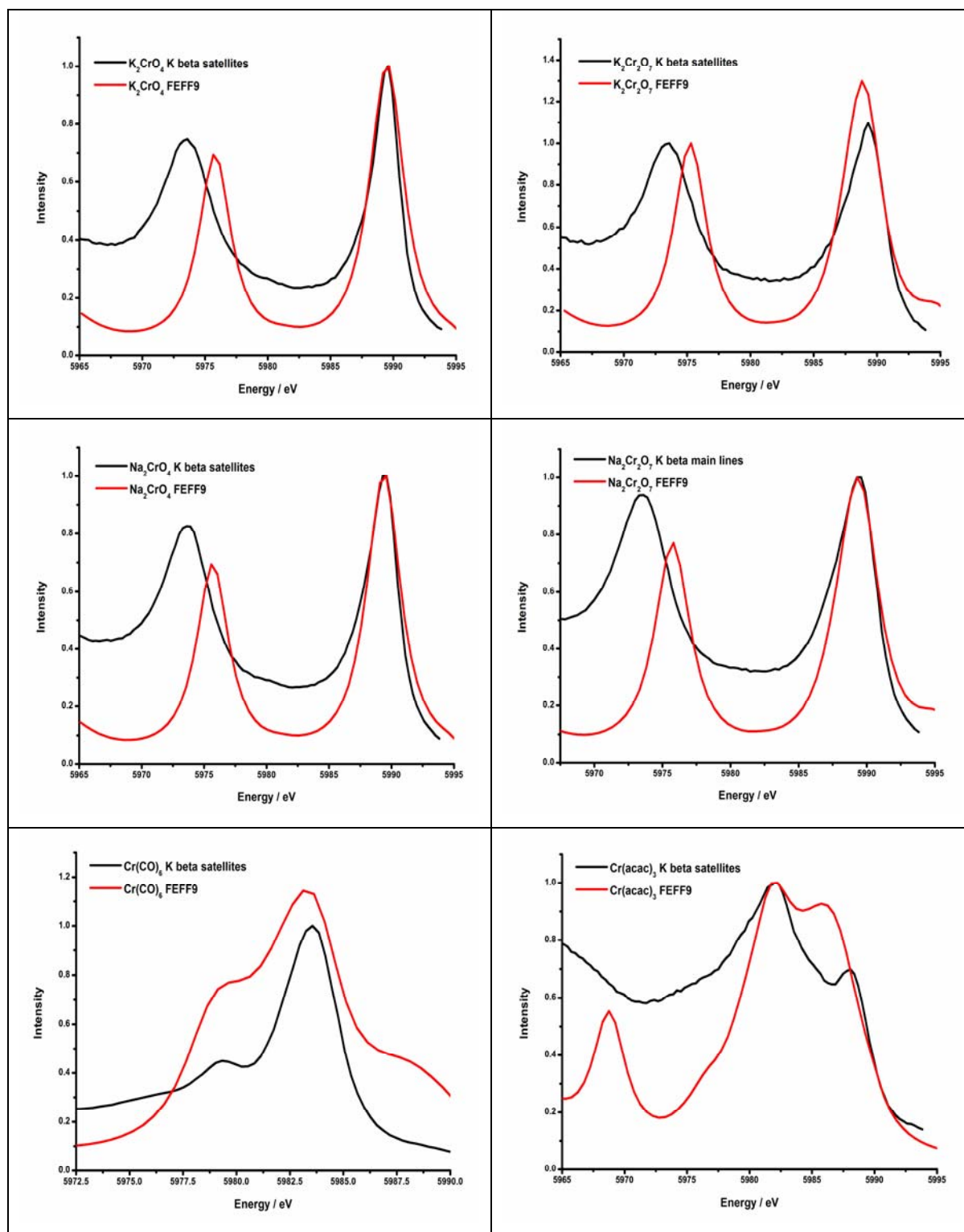


Figure 18 K β satellite lines and FEFF9 simulations for a series of Cr compounds.

Overall good agreement between experimental and theoretical K β satellite lines is observed. The spectra for Cr_2O_3 contains two peaks at 5968 eV and 5984.5 eV. The peak at 5968 eV is the K β cross-over peak (or K β'') and appears slightly shifted in the calculation at 5970.5 eV, this also means the splitting between the K β'' and K $\beta_{2,5}$ peaks is

not the same in the experimental and theoretical spectra (16.5 eV vs. 14 eV respectively). The $K\beta_{2,5}$ peak, at 5984.5 eV, is well reproduced by the calculation and the small shoulder on the high energy side at 5990 eV is also present in the simulation.

The spectra for CrO_3 also shows two peaks, the $K\beta''$ (cross-over) peak appears at 5973 eV and the $K\beta_{2,5}$ peak at 5989 eV. The cross-over peak again appears shifted and appears at 5975.5 eV in the calculation with a splitting between the two peaks of 16 eV experimentally compared to 13.5 eV theoretically. The intensity ratio between the two peaks also appears different in the two spectra; this is difficult to say for sure due to the fact that there is a strong background in the experimental spectrum caused by the tail of the $K\beta$ main line.

The $CrCl_3$ cross-over peak is much weaker in comparison to those of the oxides, there is a small shoulder in the experimental spectrum at 5977.5 eV and the $K\beta_{2,5}$ peak appears at 5986 eV. The calculation shows a much more intense cross-over peak at 5975 eV and the $K\beta_{2,5}$ peak again at 5986 eV. The experimental splitting in this case is smaller than the theoretical case and is 8.5 eV compared to 11 eV in the calculation.

The experimental K_2CrO_4 $K\beta$ satellite spectrum contains two peaks at 5973 eV (cross-over peak) and 5990 eV ($K\beta_{2,5}$ peak). The energy splitting in the experimental spectrum is 17 eV compared to 14 eV in the calculated spectrum. FEFF9 calculates the cross-over peak at 5976 eV and the $K\beta_{2,5}$ peak also at 5990 eV.

The $K_2Cr_2O_7$ spectrum appears similar to that of K_2CrO_4 with the cross-over peak occurring at 5973 eV and the $K\beta_{2,5}$ peak at 5989 eV. The calculated cross-over peak occurs at 5975.5 eV, with a splitting of 13.5 eV in the calculated spectrum and 16 eV in the experimental spectrum.

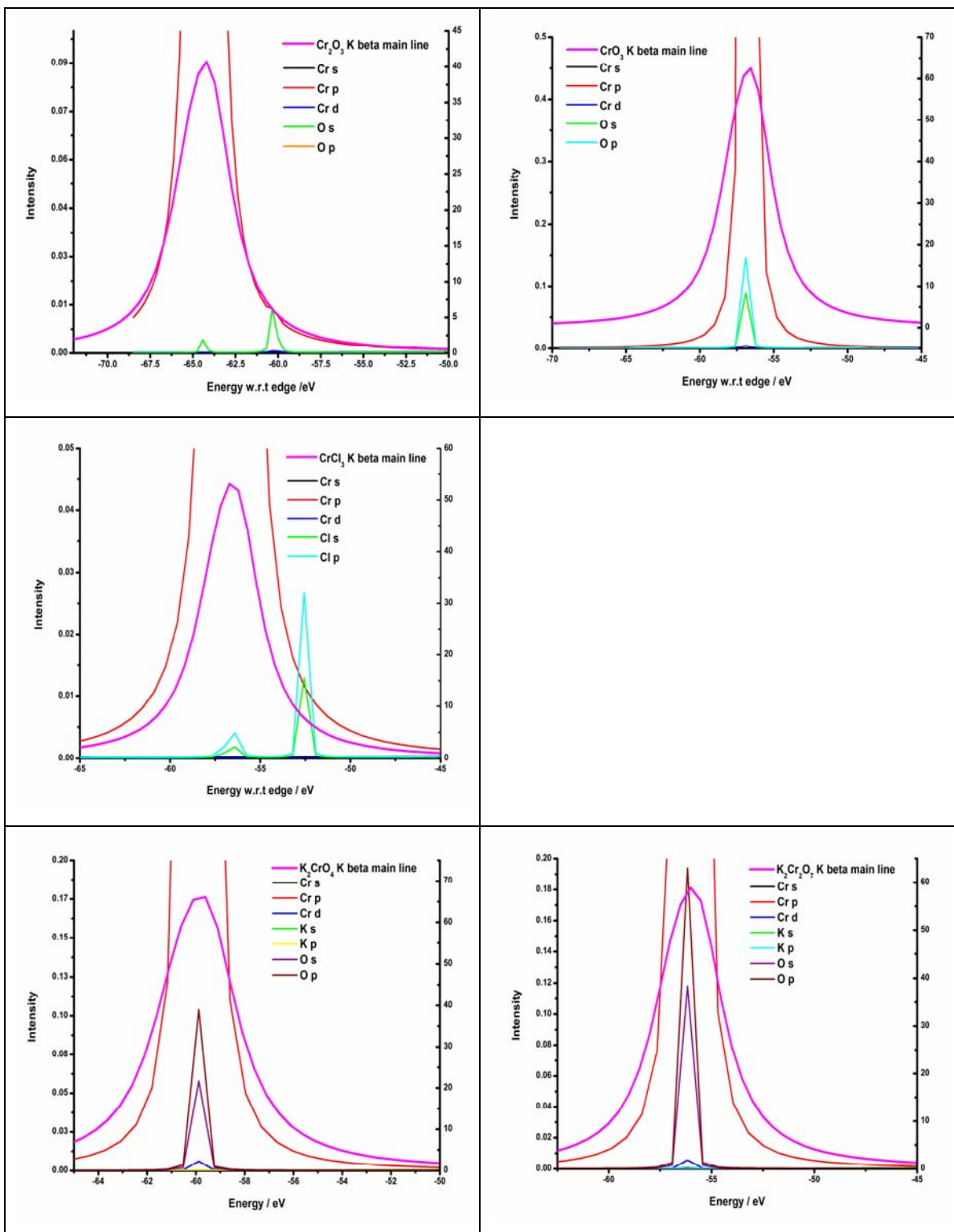
The experimental $K\beta$ satellite spectrum for Na_2CrO_4 contains two peaks; one at 5974 eV (cross-over peak) and the other at 5989 eV ($K\beta_{2,5}$ peak). The energy splitting in the experimental spectrum is 15 eV compared to 13 eV in the calculated spectrum. The calculated cross-over peak appears at 5976 eV and the $K\beta_{2,5}$ peak also at 5990 eV.

The $Na_2Cr_2O_7$ spectrum appears similar to that of Na_2CrO_4 with the cross-over peak occurring at 5974 eV and the $K\beta_{2,5}$ peak at 5989.5 eV. The calculated cross-over peak occurs at 5976 eV, with a splitting of 13.5 eV in the calculated spectrum and 15.5 eV in the experimental spectrum.

The $\text{Cr}(\text{CO})_6$ experimental $\text{K}\beta$ satellite spectrum shows two features at 5979.5 eV and 5983 eV. These features are also reproduced in the simulated spectra, also at 5979.5 eV and 5983 eV. In both cases the first peak is less intense, appearing as a small shoulder. The energy splitting in this case is 3.5 eV for both. The splitting between the satellite peaks, 5 eV, is fairly low compared to that of previously published Cr-C bonds (11 eV), this may be due to the presence of Cr-C-O bond in the sample.

The experimental satellite lines for $\text{Cr}(\text{acac})_3$ show a very small broad feature at 5976 eV, a more intense feature at 5982.5 eV and another feature at 5988.5 eV. The calculation reproduces the first small, broad peak at 5976 eV and also the next peak at 5982.5 eV. The third feature is shifted compared to that in the experiment and appears at 5986.5. In the calculation this feature is almost the same intensity as the peak at 5982.5 eV; whereas in the experiment it appears less intense. The calculation also shows an additional feature at 5969 eV that is not visible in the experiment; however it is unclear whether there is a broad feature hidden by the tail of the $\text{K}\beta$ main line in the experiment.

Most of the $\text{K}\beta$ satellite spectra appear to have been well reproduced from theory in the FEFF9 calculations, the only ones that appear less so are the chromates. As yet it is not quite obvious as to why this is the case.



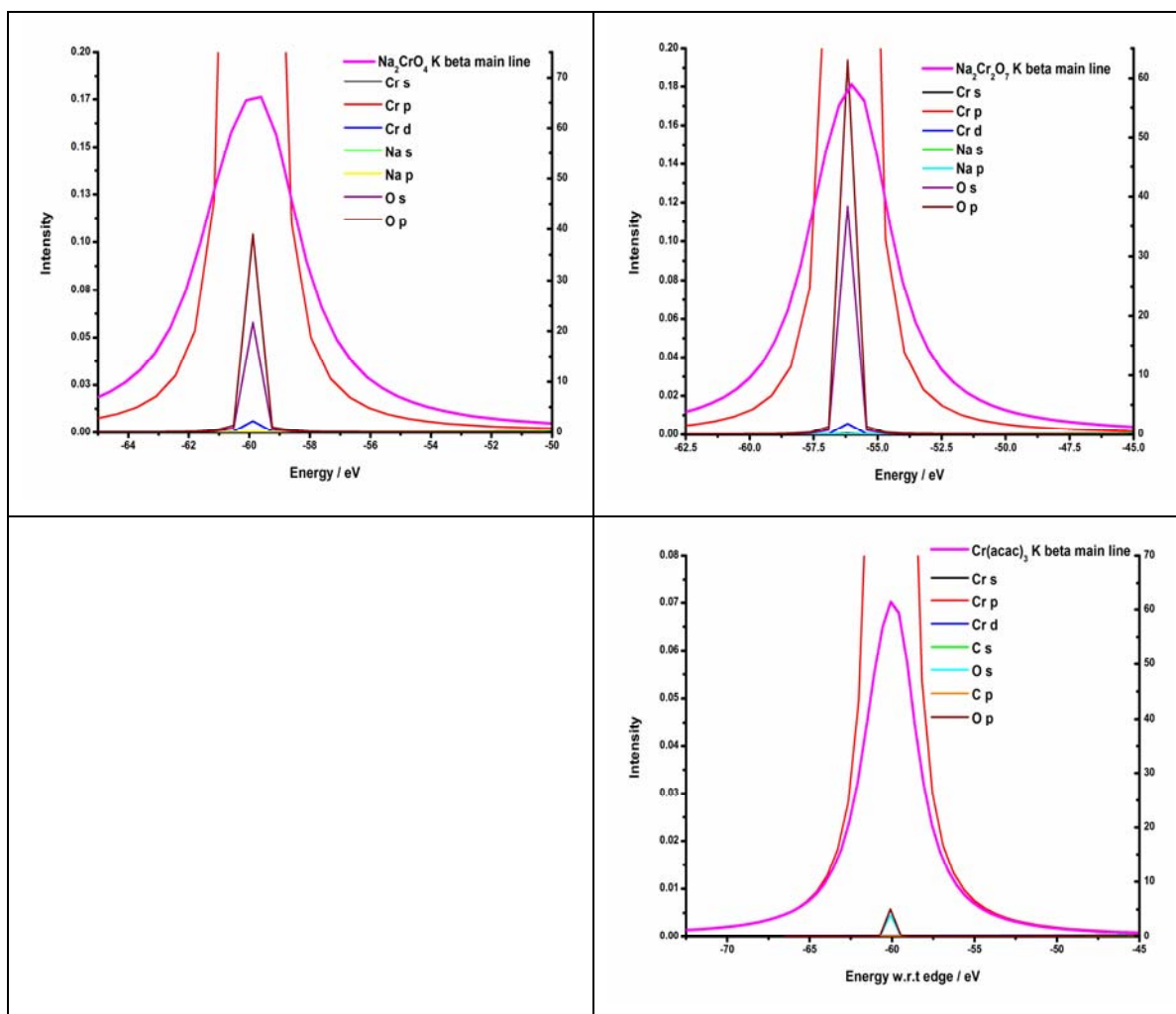
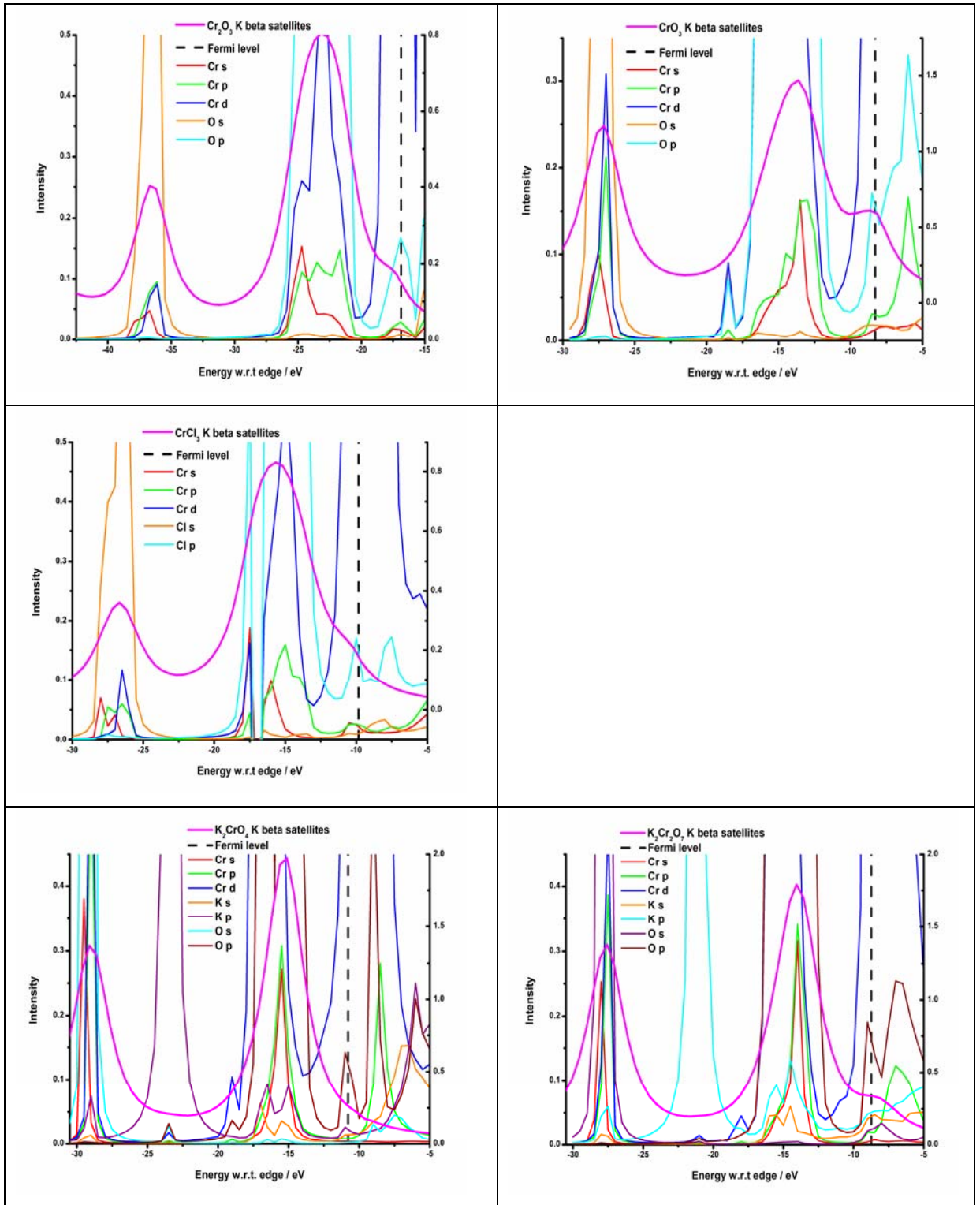


Figure 19 Calculated $K\beta$ main lines and occupied density of states contributions for a series of Cr reference compounds.

Using the FEFF9 code to perform density of states analysis provides insights into the nature of the chemical bond in the sample. The above FEFF9 calculations appear to work very well showing the Cr 1s and 3p contribution that is expected from the $3p \rightarrow 1s$ transition that causes the $K\beta$ main line. The plots show the occupied density of states contributions to the main line (also calculated), we can see that O s, O p and Cr d DOS all contribute to the XES spectrum.

The calculated valence-to-core X-ray emission spectra along with the calculated density of states for the Cr references are shown below; all calculations were performed with FEFF9.



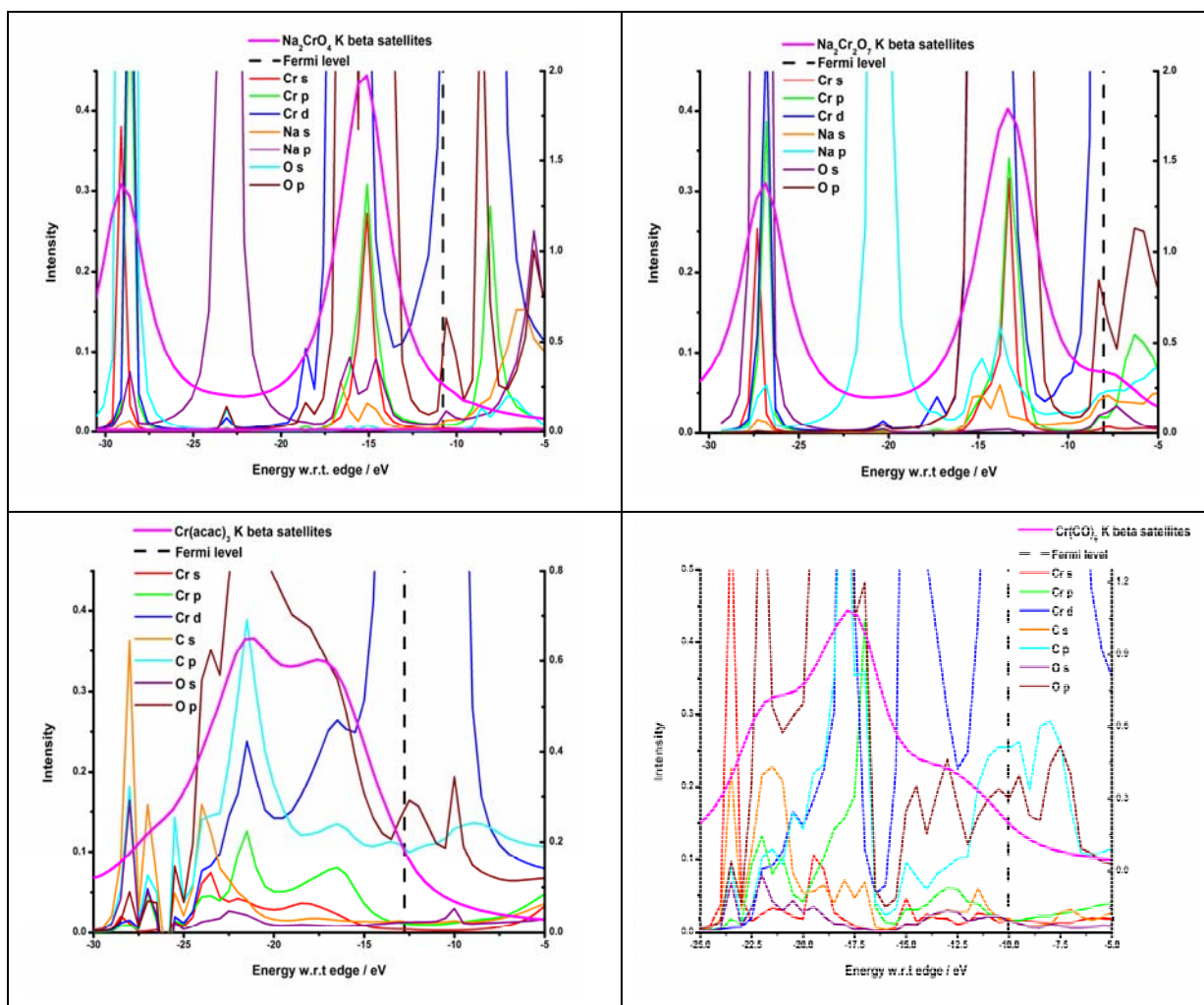


Figure 20 Calculated $K\beta$ satellite lines and occupied density of states contributions for a series of Cr reference compounds.

In figure 20 the calculated $K\beta$ satellites and density of states plot for Cr_2O_3 shows two features in the XES, one at -37 eV (with respect to the main edge) and the other at -23 eV. The feature at -37 eV is the $K\beta''$ peak and shows a contribution in the density of states plots from O s-orbitals, Cr p and Cr d-orbitals. The $K\beta_{2,5}$ peak at -23 eV shows a large degree of intensity in the density of states from O p-orbitals and Cr d-orbitals, and smaller peaks from Cr s and Cr p-orbitals. Previous studies show⁴⁷ that in the case of Cr_2O_3 the $K\beta''$ (cross-over) line corresponds to transitions from the O 2s states, while the $K\beta_{2,5}$ line is due to the band formed of mainly O 2p-orbitals. It has also been said that due to the geometry of Cr_2O_3 there is relatively little mixing of the O p states, the Cr p, and the Cr d states. The Cr d states therefore contribute very weakly to the XES spectrum⁴⁷. However, from the calculated density of states in figure 20 we can see that the Cr d states do contribute to the XES and are in fact quite prominent in the $K\beta_{2,5}$ structure.

The occupied density of states plots for CrO_3 shows contributions to the cross-over peak ($\text{K}\beta''$) at -27 eV from Cr s, Cr p, Cr d and O s-orbitals. The $\text{K}\beta_{2,5}$ line at -13.5 eV, shows large contributions from the O p and Cr d-orbitals and smaller contributions from the Cr s and Cr p states. There is also a feature on the high energy side of the $\text{K}\beta_{2,5}$ line (at the Fermi level) showing intensity from the Cr d states.

The spectrum for CrCl_3 shows intensity from the Cl s, Cr s, Cr p and Cr d-orbitals forming the cross-over peak at -27 eV. The $\text{K}\beta_{2,5}$ line, at -15.5 eV, shows large contributions from the Cl p and Cr d-orbitals and smaller contributions from the Cr s and Cr p density of states.

The density of states plot for K_2CrO_4 shows large O s, Cr p and Cr d-orbital contribution at -29 eV forming the cross-over peak. At -15 eV the $\text{K}\beta_{2,5}$ peak is formed by mainly O p and Cr d character and small amounts of Cr p and Cr s character.

The T_d Cr(VI) sample $\text{K}_2\text{Cr}_2\text{O}_7$ shows that the cross-over peak occurs at -27.5 eV and is formed due to transitions involving O s, Cr p, Cr d and a smaller proportion of Cr s character. The $\text{K}\beta_{2,5}$ peak consists of contributions from Cr d and O p-orbitals and a small amount of Cr p and Cr s-orbitals and is found at -14 eV.

The cross-over peak for the Na_2CrO_4 sample occurs at -29 eV and contains intense O s, Cr d, Cr p and Cr s character. At -15 eV the $\text{K}\beta_{2,5}$ peak is made up of Cr d, O p and a small amount of Cr p and Cr s character.

The spectrum for $\text{Na}_2\text{Cr}_2\text{O}_7$, similar to the other dichromate sample, shows that the cross-over peak, -27 eV, is formed by contributions from O s, Cr d, Cr p, and a small amount of the Cr s density of states. The $\text{K}\beta_{2,5}$ peak, at -13 eV, shows a large amount of O p and Cr d character and a smaller amount of Cr p and Cr s character.

The $\text{K}\beta$ satellites of $\text{Cr}(\text{acac})_3$ consist of one broad double peaked feature from about -30 to -15 eV. The peak at -22 eV shows contributions from O p, C p and Cr d density of states. The second peak at -17 eV arises due to transitions involving Cr d and O p-orbitals and a small amount of C p and Cr p character.

The $d^6 \text{Cr}(\text{CO})_6$ species also shows a broad feature from -22.5 to -10 eV containing three peaks at -22 eV, -17.5 eV and -12.5 eV. The first feature at -22 eV is caused by C s and O p

orbital contributions, the second at -17.5 eV by O p, Cr d and C p contributions and the third peak at -12.5 eV shows O p and Cr d character.

All the orbitals that give rise to the $K\beta_{2,5}$ line lie within a few eV below the Fermi level and take part in the chemical bond. Due to the strong orbital hybridisation, the difference in binding energy in the compounds is not as much as expected for atomic orbitals^{3b}. The calculations show that the ligand 2s-orbitals are the main contributors to the $K\beta''$ lines and the energy position of the $K\beta''$ line is therefore proportional to the atomic value and thus provides a clear indication of the ligand nature^{3b}.

4.4 Conclusions

This chapter focuses on 3d transition metal systems, namely chromium reference compounds such as oxides, chromates and chlorides. Previous studies have demonstrated the sensitivity of X-ray absorption edges and pre-edge features to their chemical environment. The position of the absorption edge is shown to be highly sensitive to its ligand surroundings and geometry; however, the exact origins of the features are unassigned. The aim of this study is to bring together a collection of complementary and some novel X-ray techniques to assign these features.

We hope that with this work we have added to the development of these novel methods of measuring and analysing the pre-edge structures of transition metal compounds. There are many effects hidden in the pre-edge region that have been proven to be extremely valuable in characterising the electronic and molecular structure of the 3d transition metal systems. Whilst the measurement of the K-edge XANES of transition metals is not a novel procedure, we were able to obtain high energy resolution data and simulate the pre-edge with the FEFF9 code. With the HERFD XANES and the possibility to measure concentrated samples we have been able to achieve pre-edge regions with greater intensity than would be possible in other techniques (EXAFS). This increase in structure allows for a more detailed analysis of the features and therefore the electronic structure of the materials under investigation. There is arguably less work on transition metal 2p XAS, in this study we have again managed to measure the 2p XAS of a series of Cr samples using soft X-rays. Although these spectra require a complex theoretical analysis we have been able to reproduce the edges to a high degree of accuracy. This enabled us to determine theoretical values for the crystal field that we can compare with other X-ray techniques (RIXS) as well as optical absorption techniques. As discussed these values do not always

coincide due to differences in the different states. There is the next step in the analysis of the L-edges which has not been attempted in this study, this would be to deduce all possible final states for every ground state and therefore produce a more detailed description of the features observed. This would be a potential area for further work based on this study. The experimental data and calculations in this study do highlight the value of this technique and a good basis for development.

The novel RIXS experiments provide the opportunity to achieve L and K-edge spectra unaffected by lifetime broadening effects and the large background from the main absorption edge. Moreover, 2D images of emission as a function of absorption are obtained, providing information on the relation between absorption and emission features thereby providing detailed information on the presence and position of specific molecular orbitals or bands. Another important aspect is the fact that these 1s2p RIXS experiments, unlike conventional 2p XAS; make use of hard X-ray probes. This means that in theory experiments can be performed under essentially any (extreme) conditions, including experiments in reactors, or *in-situ* situations⁴⁹. In future it would be of interest to use the CTM program to simulate the RIXS in this study rather than the RGAss approach, the CTM theory is based on more recent developments and has the potential to include more parameters and effects. This would allow a more accurate and varied analytical approach to these spectra.

The K β studies have allowed us to take a look at the first coordination shell around the central chromium. This technique enables us to differentiate between different ligands, including those that are neighbours in the periodic table. This is an important step forward in the area of X-ray spectroscopy as it is not possible with all techniques. A detailed analysis of the valence-to-core emission lines has shown their sensitivity to the chemical environment around the central metal. This is an important development opportunity in the field of catalysis as it could be used as a tool to monitor the changing ligands during the catalytic process. In the case of the K β XES studies the calculations have been quite successful at predicting the relative energy positions of the different transitions. We have also been able to perform a density of states analysis on the K β emission spectra thus identifying the orbitals involved in the transitions.

One point that is true for both the K-edge XAS and the K β studies is that the calculation and analysis of these spectra would not be possible without knowing the structure of the compound. This means that performing a structural and electronic analysis of unknowns is not possible using these theoretical methods (FEFF).

4.5 References

- (a) de Groot, F. M. F.; Glatzel, P.; Bergmann, U.; van Aken, P. A.; Barrea, R. A.; Klemme, S.; Havecker, M.; Knop-Gericke, A.; Heijboer, W. M.; Weckhuysen, B. M., *Phys. Rev. B: Condens. Matter* **2005**, *109*, 20751; (b) Glatzel, P.; Yano, J.; Bergmann, U.; Visser, H.; Robblee, J. H.; Gu, W.; de Groot, F. M. F.; Cramer, S. P.; Yachandra, V. K., *J. Phys. Chem. Solids* **2005**, *66*, 2163; (c) Glatzel, P.; Bergmann, U.; Yano, J.; Visser, H.; Robblee, J. H.; Gu, W.; de Groot, F. M. F.; Christou, G.; Pecoraro, V. L.; Cramer, S. P.; Yachandra, V. K., *J. Am. Chem. Soc.* **2004**, *126*, 9946; (d) Glatzel, P.; Bergmann, U., *Coord. Chem. Rev.* **2005**, *249*, 65.
- (a) Hayashi, H.; Takeda, R.; Udagawa, Y.; Nakamura, T.; Miyagawa, H.; Shoji, H.; Nanao, S.; Kawamura, N., *Phys. Scr.* **2005**, 1094; (b) Hayashi, H.; Takeda, R.; Udagawa, Y.; Nakamura, T.; Miyagawa, H.; Shoji, H.; Nanao, S.; Kawamura, N., *Phys. Rev. B: Condens. Matter* **2003**, *68*, 045122.
- (a) Safonov, V. A.; Vykhodtseva, L. N.; Polukarov, Y. M.; Safonova, O. V.; Smolentsev, G.; Sikora, M.; Eeckhout, S. G.; Glatzel, P., *J. Phys. Chem. B* **2006**, *110*, 23192; (b) Eeckhout, S. G.; Safonova, O. V.; Smolentsev, G.; Biasioli, M.; Safonov, V. A.; Vykhodtseva, L. N.; Sikora, M.; Glatzel, P., *J. Anal. At. Spectrom.* **2009**, *24*, 215; (c) Bergmann, U.; Bendix, J.; Glatzel, P.; Gray, H. B.; Cramer, S. P., *J. Chem. Phys.* **2002**, *116*, 2011.
- Grosso, E.; Prestipino, C.; Cesano, F.; Bonino, F.; Bordiga, S.; Lamberti, C.; Thüne, P. C.; Niemantsverdriet, J. W.; Zecchina, A., *J. Catal.* **2005**, *230*, 98.
- Santhosh Kumar, M.; Hammer, N.; Rønning, M.; Holmen, A.; Chen, D.; Walmsley, J. C.; Øye, G., *J. Catal.* **2009**, *261*, 116.
- Requejo, F. G.; Ramallo-López, J. M.; Rosas-Salas, R.; Domínguez, J. M.; Rodriguez, J. A.; Kim, J. Y.; Quijada, R., *Catal. Today* **2005**, *107-108*, 750.
- Wilke, M.; Farges, F.; Petit, P.-E.; Brown Jr, G. E.; Martin, F., *Am. Mineral.* **2001**, *86*, 714.
- (a) Rehr, J. J.; Albers, R. C., *Rev. Mod. Phys.* **2000**, *72*, 621; (b) Kas, J. J.; Rehr, J. J.; Soininen, J. A.; Glatzel, P., *Phys. Rev. B: Condens. Matter* **2011**, *83*, 235114.
- (a) Briois, V.; Cartier dit Moulin, C.; Sainctavit, P.; Brouder, C.; Flank, A. M., *J. Am. Chem. Soc.* **1995**, *117*, 1019; (b) de Groot, F. M. F.; Fuggle, J. C.; Thole, B. T.; Sawatzky, G. A., *Phys. Rev. B: Condens. Matter* **1990**, *42*, 5459.
- Juhin, A.; Brouder, C.; Arrio, M.-A.; Cabaret, D.; Sainctavit, P.; Balan, E.; Bordage, A.; Seitsonen, A. P.; Calas, G.; Eeckhout, S. G.; Glatzel, P., *Phys. Rev. B: Condens. Matter* **2008**, *78*, 195103.
- (a) Igarashi, J.-i.; Nomura, T.; Takahashi, M., *Phys. Rev. B: Condens. Matter* **2006**, *74*, 245122; (b) Takahashi, M.; Igarashi, J.-I.; Nomura, T., *Phys. Rev. B: Condens. Matter* **2007**, *75*, 235113.
- Rehr, J. J.; Kas, J. J.; Vila, F. D.; Prange, M. P.; Jorissen, K., *PCCP* **2010**, *12*, 5503.
- Ankudinov, A. L.; Ravel, B.; Rehr, J. J.; Conradson, S. D., *Phys. Rev. B: Condens. Matter* **1998**, *58*, 7565.
- Rehr, J. J.; Kas, J. J.; Prange, M. P.; Sorini, A. P.; Takimoto, Y.; Vila, F., *Comptes Rendus Physique* **2009**, *10*, 548.
- Theil, C.; van Elp, J.; Folkmann, F., *Phys. Rev. B: Condens. Matter* **1999**, *59*, 7931.
- de Groot, F. M. F.; Fuggle, J. C.; Thole, B. T.; Sawatzky, G. A., *Phys. Rev. B: Condens. Matter* **1990**, *41*, 928.
- de Groot, F. M. F.; Kotani, A., In *Core Level Spectroscopy of Solids*, CRC Press: 2008; pp 93.
- Ikeno, H.; de Groot, F. M. F.; Stavitski, E.; Tanaka, I., *J. Phys.: Condens. Matter* **2009**, *21*, 104208.
- de Groot, F. M. F.; Kotani, A., In *Core Level Spectroscopy of Solids*, CRC Press: 2008; pp 1.

20. Fuggle, J. C.; Inglesfield, J. E., *Topics in Applied Physics*. Springer-Verlag Berlin and Heidelberg GmbH & Co. K: 1992.
21. (a) Cabaret, D.; Bordage, A.; Juhin, A.; Arfaoui, M.; Gaudry, E., *PCCP* **2010**, *12*, 5619; (b) Nakanishi, K.; Ohta, T., *J. Phys.: Condens. Matter* **2009**, *21*, 104214.
22. de Vries, A. H.; Hozoi, L.; Broer, R., *Int. J. Quantum Chem* **2003**, *91*, 57.
23. Ankudinov, A. L.; Conradson, S. D.; Mustre de Leon, J.; Rehr, J. J., *Phys. Rev. B: Condens. Matter* **1998**, *57*, 7518.
24. J.J. Rehr, A. A., B. Ravel, and K. Jorissen.
http://leonardo.phys.washington.edu/feff/Docs/feff9/feff90/feff90_users_guide.pdf.
25. (a) Pantelouris, A.; Modrow, H.; Pantelouris, M.; Hormes, J.; Reinen, D., *Chem. Phys.* **2004**, *300*, 13; (b) Tromp, M.; van Bokhoven, J. A.; van Strijdonck, G. P. F.; van Leeuwen, P. W. N. M.; Koningsberger, D. C.; Ramaker, D. E., *J. Am. Chem. Soc.* **2004**, *127*, 777.
26. (a) Westre, T. E.; Kennepohl, P.; DeWitt, J. G.; Hedman, B.; Hodgson, K. O.; Solomon, E. I., *J. Am. Chem. Soc.* **1997**, *119*, 6297; (b) DeBeer George, S.; Brant, P.; Solomon, E. I., *J. Am. Chem. Soc.* **2004**, *127*, 667.
27. de Groot, F. M. F.; Vanko, G.; Glatzel, P., *J. Phys.: Condens. Matter* **2009**, *21*, 104207.
28. de Groot, F. X-ray Absorption Fine Structure-XAFS13, 2007; pp 37.
29. de Groot, F., *Chem. Rev.* **2001**, *101*, 1779.
30. Atkins, P.; Overton, T.; Rourke, J.; Weller, M.; Armstrong, F., *Inorganic Chemistry*. Oxford University Press: New York, 2006; p 459.
31. van der Laan, G.; Kirkman, I. W., *J. Phys.: Condens. Matter* **1992**, *4*, 4189.
32. de Groot, F. M. F.; Kotani, A., In *Core Level Spectroscopy of Solids*, CRC Press: 2008; pp 11.
33. Fuggle, J. C.; Alvarado, S. F., *Physical Review A* **1980**, *22*, 1615.
34. Pease, D. M., *Phys. Rev. B: Condens. Matter* **1992**, *46*, 8790.
35. Thole, B. T.; van der Laan, G., *Phys. Rev. B: Condens. Matter* **1988**, *38*, 3158.
36. Onodera, Y.; Toyozawa, Y., *J. Phys. Soc. Jpn.* **1967**, *22*, 833.
37. (a) Manoubi, T.; Tencé, M.; Colliex, C., *Ultramicroscopy* **1989**, *28*, 49; (b) Zaanen, J.; Sawatzky, G. A.; Fink, J.; Speier, W.; Fuggle, J. C., *Phys. Rev. B: Condens. Matter* **1985**, *32*, 4905.
38. (a) Solomon, D.; Lehmann, J.; Martínez, C. E., *Soil Sci. Soc. Am. J.* **2003**, *67*, 1721; (b) Tromp, M.; Moulin, J.; Reid, G.; Evans, J., In *X-Ray Absorption Fine Structure-XAFS13*, Hedman, B.; Painetta, P., Eds. 2007; Vol. 882, pp 699.
39. Shukla, A.; Calandra, M.; Taguchi, M.; Kotani, A.; Vanko, G.; Cheong, S. W., *Phys. Rev. Lett.* **2006**, *96*, 077006.
40. de Groot, F., *Coord. Chem. Rev.* **2005**, *249*, 31.
41. (a) Ortega, R., *Metallomics* **2009**, *1*, 137; (b) Yano, J.; Kern, J.; Sauer, K.; Latimer, M. J.; Pushkar, Y.; Biesiadka, J.; Loll, B.; Saenger, W.; Messinger, J.; Zouni, A.; Yashandra, V., *Science* **2006**, 821; (c) Penner-Hahn, J. E., *Coord. Chem. Rev.* **2005**, *249*, 161.
42. Meisel, A.; Leonhardt, G.; Szargan, R., *X-Ray Spectra and Chemical Binding*. Springer-Verlag: Berlin; New York, 1989.
43. Hajji, C.; Roller, S.; Beigi, M.; Liese, A.; Haag, R., *Adv. Synth. Catal.* **2006**, *348*, 1760.
44. Glatzel, P.; Sikora, M.; Smolentsev, G.; Fernández-García, M., *Catal. Today* **2009**, *145*, 294.
45. Bergmann, U.; Glatzel, P., *Photosynth. Res.* **2009**, *102*, 255.
46. Lee, N.; Petrenko, T.; Bergmann, U.; Neese, F.; DeBeer George, S., *J. Am. Chem. Soc.* **2010**, *132*, 9715.
47. Eeckhout, S. G.; Safonova, O. V.; Smolentsev, G.; Biasiolo, M.; Safonov, v. A. A.; Vykholdtseva, L. N.; Sikora, M.; Glatzel, P., *J. Anal. At. Spectrom.* **2008**, *24*, 215.

Chapter Five: Systematic spectroscopic study of Cr(salen) materials

5.1 Introduction

X-ray absorption spectroscopy (XAS) has become a well recognised characterisation tool in many areas of the chemical sciences. The wide usage of XAS for materials characterisation is largely due to the fact that it allows us to determine the geometric and local electronic structures of materials in an element specific manner. X-ray Absorption techniques also allow us to perform these experiments in a bulk sensitive manner. The work into bulk sensitive XAS characterisation of light elements by Uwe Bergmann, Pieter Glatzel and Stephen Cramer shows the versatility of the technique and how experiments that demonstrate the advantages of both soft and hard X-ray measurements can be performed¹. Detailed XANES studies have been described in the literature previously for transition-metal complexes, showing that the X-ray absorption edges are very sensitive to the chemical environment². The reach of these kinds of studies stretches beyond chemistry and physics into many areas of materials research; L-edge XAS has been used to characterise multiple valence states of 3d transition metals in areas of mineralogical and geochemical research³. The pre-edge region in XAS is also indicative of different oxidation states and geometries of the samples being studied²; we saw this in the Cr reference study in chapter 4. The work by Kau, Spira-Soloman, Penner-Hahn *et al* shows how the X-ray Absorption edge of copper was used in the determination of the oxidation state and coordination geometry of copper compounds⁴.

XAS methods are well utilised in catalytic studies; from characterisation of catalysts⁵ to studying reaction intermediates and the determination of mechanistic pathways. Despite the fact that techniques such as X-ray absorption spectroscopy are well established and understood there are also aspects that are currently being developed and new discoveries are being made. One of the main advantages of these types of experiments (especially for catalysis) is the possibility to carry them out under *in-situ* or even extreme conditions; such as at cryogenic temperatures or under ultra high vacuum conditions. M. Bron *et al*⁶ employed *in-situ* X-ray absorption spectroscopy to study heterogeneous silica supported silver catalysts for the gas phase hydrogenation of acrolein. For homogeneous catalysis the application of XAS is very limited whereas for heterogeneous it is more or less standard⁶, at least the EXAFS part of it⁷. It is also now possible to perform *in-situ* measurements in combination with complementary techniques such as infrared, Raman

and UV-vis spectroscopy⁸. This facilitates catalytic studies and therefore allows the determination of structure and its relation to the function of materials. The ever improving understanding of the pre-edge and near-edge regions will lead to a more in-depth knowledge of these types of spectra. However, currently the understanding of the information obtained from these X-ray studies is still in its initial stages. The underlying theory is not straightforward, with different core-holes at different stages of the experimental process interacting with all the other molecular orbitals, and is still very much under development using different approaches to tackle the inclusion of charge transfer and multiplet effects. All the X-ray techniques used, as far as we are able to go for these salen materials, will be demonstrated in a step-by-step manner in this chapter.

In order to develop the Resonant Inelastic X-ray Scattering (RIXS) technique we first began our study with a systematic investigation of chromium reference materials with well defined structures (chapter 4). This study provided insights into the nature of the XANES pre-edges of a variety of different compounds of Cr(III) and Cr(VI). From this basis we then moved on to look at a series of Cr(salen) catalysts using the same experimental techniques, with the information obtained in chapter 4 forming the starting point for the analysis of the pre-edge of the Cr catalysts. The Cr catalysts were subjected to the same range of X-ray techniques; Cr K-edge XANES, Cr L-edge XANES, $K\beta$ emission studies and $1s2p$ RIXS. It is hoped that using what we have found for the reference materials we are able to get a clearer picture of the electronic structure of the central Cr atom within these salen materials and apply this to tailor their future catalytic applications.

This chapter now looks at the Cr K-edge experiments of the Cr(salen) materials along with associated FEFF9 calculations of the pre-edge region. Next the Cr L-edge absorption spectra were investigated; in this case the Charge Transfer Multiplet code was used to simulate the experimental spectra. We then move on to emission studies, first looking at $K\beta$ emission lines (which are also simulated with FEFF9) and then $1s2p$ RIXS, for which the RGAss program is used to calculate theoretical spectra.

By performing these experiments we are able to obtain information relating to both p ($1s \rightarrow 4p$ transition at the K-edge) and d-orbitals ($2p \rightarrow 3d$ transition at the L-edge). The calculations with FEFF9 also provide a detailed analysis of the unoccupied density of states, showing the orbital contributions to the features in the XANES. The d-orbital information obtained from L-edge absorption is a key factor in understanding transition metal chemistry. By understanding the electronic structure at the Cr centre it may be possible in the future to control the positions of the d-orbitals and their relative occupancy.

This is important for metal catalysis since adsorption or activation of reactants, and hence the overall reactivity, are largely a result of the interactions of metal d-orbitals with the ligand valence orbitals.

5.2 Salen Catalysts

Studies have shown that the Cr(III) complexes are very effective catalysts with regard to both reactivity and enantioselectivity⁹. The work by *E.M. McGarrigle, D.M. Murphy, D.G. Gilheany* aimed to decipher the relationship between the electronic character of the salen substituents and the selectivity of the catalyst, this proved to be more complicated than first thought and it was proposed that multiple oxidation pathways existed⁹. The analogous Mn catalysts (Jacobsen's catalyst) show the opposite trend to Cr with higher asymmetric induction in the case of a *cis*-alkene over its *trans*- counterpart, calling into question the proposed side-on approach model.

Salen type materials are widely employed in the catalysis industry¹⁰, the study by *Katsuki and co-workers*^{10a} describes the parallels between enzymes that play an important role in oxidative biochemical pathways, and metal salen materials. As well as work into metal porphyrin materials, the use of metal salen complexes as oxo-transfer catalysts has been investigated since they have similarities with metalloporphyrins. Although various metal ions form complexes with salen ligands, only some (chromium¹¹, manganese¹², nickel¹³ and ruthenium^{10a}) have been used as catalysts for epoxidation. Various salen materials have been found to be efficient catalysts. Being able to tailor the design of these catalysts for a specific function is of great importance. In order to do this we first need to understand the electronic structure within the molecule, around the Cr centre. The electronic structure of the salen materials can be tuned by varying the substituent on the salicylaldehyde precursor; in this way it is also possible to tune the steric effects of the ligand.

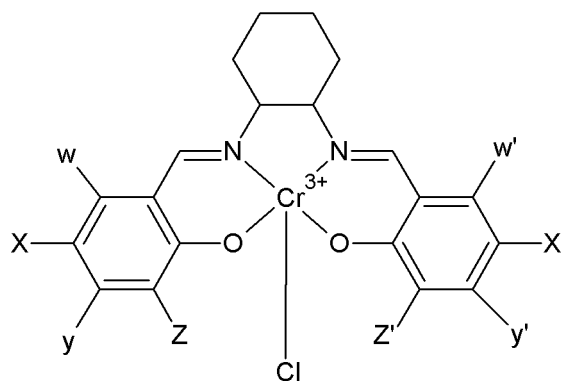


Figure 1 The general structure of the salen ligand showing the various places for substitution around the benzene ring of the salicylaldehyde fragment

Figure 1 shows the Cr(salen) catalyst structure under investigation, the salen complex is made up of two constituent parts; these are the salicylaldehyde component and the -1,2-diammoniumcyclohexane bridge. The different positions at which we can change the salicylaldehyde substitution are denoted by W, X, Y and Z in figure 1. Typically, in this study, substitution was carried out at the X and Z positions (and X' and Z'). Substituting different groups can have varying effects depending on which position in the ring undergoes substitution. A clear dependence in enantioselectivity is found upon subtle changes in the ligand systems around the metal^{10c} (while the direct Cr coordination remains identical). If a sterically bulky and electron-rich group is placed into the space over the C8' carbon, it causes strong steric and electronic repulsion against the larger and more electron-rich group on the oncoming olefin with the undesired orientation that leads to the minor enantiomer of epoxides, thus resulting in the increase of enantioselectivity^{10c}. Other analogues e.g. titanium and aluminium, catalyse the ring opening with similarly good reactivity, but less than 5% enantioselectivity. This suggests a unique mechanism of catalysis for chromium given that the ligand environments in the Cr, Ti and Al complexes are very similar¹⁴.

It has been found that substitution at the Z/Z' position is generally favourable for inducing high enantiomeric excess, ee (the enantiomeric excess of a substance is a measure of how pure it is, in this case the impurity is the undesired enantiomer), while the presence of electron withdrawing groups seems necessary for reasonable reaction rates¹⁵. Asymmetric ligands display a lower ee compared to symmetric ones, which is thought to be due to the Cr structure¹⁶ (bent¹⁵ or C₂ symmetry) which will in turn affect the approach mechanism¹⁷, or due to the formation of different diastereomers forming two different oxygen transfer species (one with high and one with low ee)¹⁵. A number of different oxidation pathways have been proposed to explain the different effects observed in enantioselectivity when

varying the substituents on the salen ring¹⁸. It has been reported that in the case of the Mn(salen) catalysts the presence of a bulky R group in the Z position is crucial to the selectivity and stability of the catalysts¹⁹. In this case specifically if a hydrogen atom was substituted in the Z position the epoxidation reaction was catalyzed with only 0-3% ee. More generally it has been observed that any substituents smaller than a tert-butyl group lead to poor results.

More exploitation and examination of structurally interesting Schiff base complexes in catalysis are warranted, in order to find more effective catalysts to be employed in organic reactions and to gain more insight into the behaviour of the catalyst. In chapter 6 we extend the study to look at the intermediate species that exist during the epoxidation reaction using XAS and XES techniques to try and characterise the active species. It is hoped that this will help us to gain insights into the correct mechanistic pathway. This chapter first starts by looking at the Cr K-edges of the salen catalysts with varying substituents on the salen framework. The next step is to look at the 2p absorption spectra (the Cr L-edge) and lastly the X-ray emission spectra; K β emission lines and Resonant Inelastic X-ray Scattering spectra. The data obtained from the reference materials in chapter 4 will help with the analysis of the pre-edges along with detailed XANES calculations.

5.3 Results and Discussion

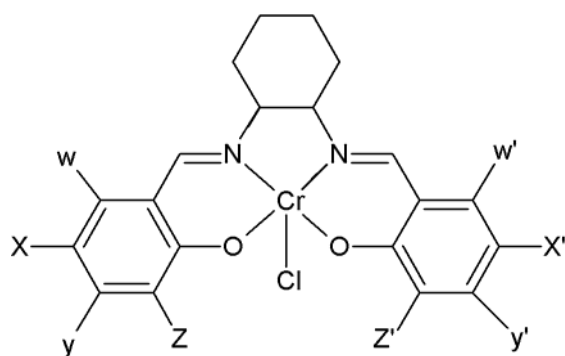
5.3.1 Cr K-edge

Detailed X-ray Absorption Near Edge Structure studies have demonstrated the sensitivity of the transition metal edges and pre-edge structures to their chemical environment. We hope to explore this with the salen series to see the effects of variations in the ligand substitution in different positions in the salicylaldehyde portion of the complex. There can be difficulties in the interpretation of XANES spectra; self-absorption effects in the XAS measurements (as seen in chapter 4) can cause uncertainties in the spectral intensity, making a detailed analysis difficult. In addition the XANES spectral shape reflects a complex relationship between charge screening and orbital hybridisation effects²⁰, making it difficult to assign all the features as was also demonstrated in chapter 4.

We begin this chapter by looking at the Cr K-edge XANES of the Cr(III)(salen) complexes. The experimental Cr K-edge XANES, HERFD and associated FEFF9 calculations for the salen materials are shown below in figure 3. We can see, as with the references, that there

is an increase in spectral resolution going from the normal XANES (shown in black) to the High Energy Resolution Fluorescence Detection XAS spectra. This increase in resolution allows us, in some cases, to see previously unobserved features. Here, we are able to see an increase in separation of the two pre-edge features along with increased resolution and sharpening of the peaks.

The HERFD has proved to be an important development in the determination of spectral details for the K pre-edge region. The FEFF multiple scattering approach has greatly improved and is able to reproduce many of the pre-edge features, even multiple features as seen in the high resolution experiments. Adding the calculated empty density of states (DOS) plots with the XANES allows us to identify the different orbital contributions to the XANES features, thus revealing the orbitals/transitions probed during the experiment and therefore gaining insights into the electronic structure of the central Cr atom. The only drawback is that the theory requires a detailed (3 dimensional) model of the complex under investigation, which is not always present.



Salen 1: X,Z = ^tBu

Salen3: X,Z = CH₂N(CH₂)₄O

Salen4: X,Z = CH₂N(CH₂)₅

Figure 2 A typical salen template is shown on the left, and the substitutions for the samples studied on the right.

The electronic structure of Salen 3 and 4 are very similar, however the structure around salen 1 is different but again the substituents used are bulky. These differences may not be enough to produce large differences in the XANES.

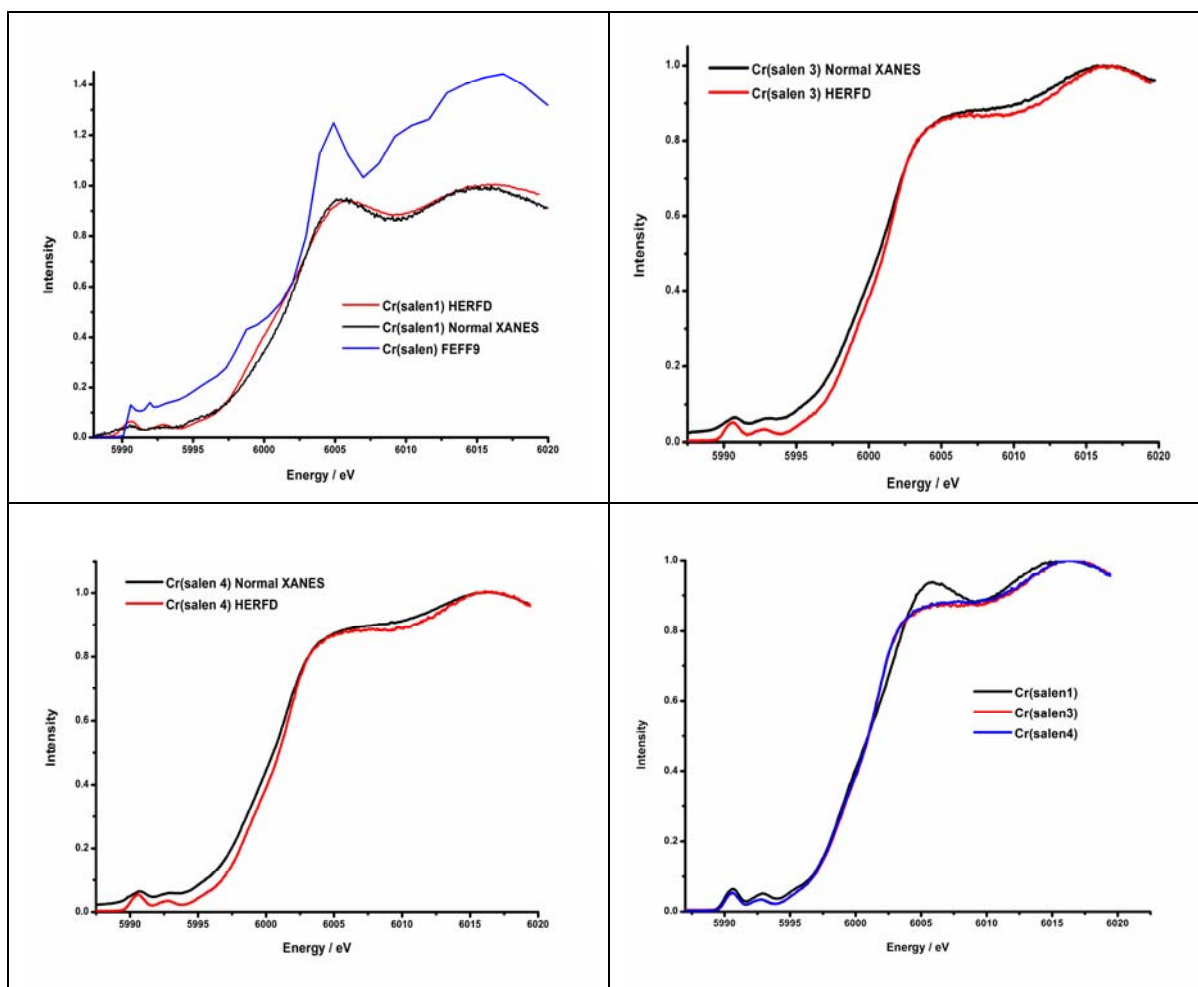


Figure 3 Normal and HERFD Cr K-edge XANES spectra for Cr(salen) materials with the associated FEFF9 calculation.

Figure 3 shows the Cr K-edge XANES with the HERFD XANES and the XANES simulations carried out with FEFF9 for a series of Cr(salen) complexes. The structures of the different complexes are shown again in figure 2. In the FEFF9 calculations a negative broadening was used to reproduce the high resolution data. The crystal structure for ((N,N'-3,5-di-*t*-butylsalicylidene)-1,2-cyclohexanediaminato)-chloro-chromium(iii) dichloromethane solvate was obtained from literature ²¹. For each of the salen materials the additional information available in the high energy resolution spectra is clear, with increased intensity of features in the pre-edge XANES region. In the HERFD process we select a specific emission line over which to measure the XANES of the sample (in this case the $K\alpha_1$ emission line). A secondary fluorescence detector with an energy resolution that is similar to the core-hole lifetime broadening is used, the advantage of this is that only one emission line is probed; so the XAS spectrum is only broadened by the 2p core-hole lifetime rather than of the 1s core-hole lifetime (the 2p being larger than the 1s and therefore the broadening is reduced). This allows previously unobserved features to become visible in the spectra.

The general appearance of the pre-edge region for all the salen materials is the same; this is due to the fact that they all possess the same geometry around the Cr. As shown in chapter 4, the appearance of the pre-edge region in the K-edge is mostly dependent on the structure of the complex under investigation. For complexes of lower symmetry there is a greater degree of hybridisation between p and d or s-orbitals; this mixing of orbitals means that dipole allowed transitions to the p-orbitals contains d character and results in intensity in the pre-edge due to this dipole-quadrupole mixing²². When inversion symmetry is broken the 3d and 4p states to mix and form a combined 3d + 4p symmetry states²³. This means the dipole and quadrupole transitions reach the same final states, and so their peaks are visible at the same energy. Although this rule is relaxed in the solid state and compounds that show inversion symmetry (octahedral symmetry) show small mixtures of p states in the 3d band. Even for perfect octahedral systems, this results in the appearance of small features in the pre-edge. We can see this affect in the K-edge XANES of the salen materials, although they are not octahedral they are most similar in appearance to the octahedral reference materials. The salen complexes have C₂ symmetry²⁴, they do not have inversion symmetry but still have a relatively clear pre-edge.

These spectra are interpreted in terms of a final-state local *l*-projected density of states (LDOS)(bound-bound) transitions²⁵ using FEFF9. The theoretical framework behind the FEFF code is based on the real-space Green's function approach for which explicit calculation of final states is avoided by expressing the Fermi Golden rule in terms of a single particle Green's function in the presence of an appropriately screened core-hole ('final state rule')²⁶. A XANES calculation typically starts with the computation of the scattering potentials. In FEFF, the self-consistent field (SCF) loop computes the coulomb potentials, the electron density, the Fermi energy, occupation numbers as well as the charge transfer between atoms²⁵. The charge transfer accounts for properties of different elements such as oxidation state and electron affinity and is therefore important in coordination compounds for which metal-ligand bonding takes place through appreciable charge transfer²⁵. Recent advances in theory, which are incorporated into the FEFF code, now offer the chance to calculate many-body intrinsic and extrinsic inelastic losses from first principles²⁵. In the XANES spectrum the peak positions are directly related to the scattering path lengths and therefore with the structure of the material^{l25}. The scattering path relates to the distance between atoms, obtaining information about the scattering paths gives an idea of the number, type and distance of nearest neighbours in the material.

The spectra for the Cr (salen1) complex in figure 3 shows two features in the pre-edge region in the normal XANES spectrum, these occur at 5991 eV and 5993 eV and the main edge is visible at 6000 eV. The HERFD spectrum also shows two pre-edge features at 5991 eV and 5993 eV however, they now appear better resolved compared to the normal spectrum. The main edge appears at 6000 eV, consistent with the normal XANES spectra. The FEFF9 calculation does not reproduce the pre-edge region of the salen materials to the same level of accuracy as for the reference materials in chapter 4. The difficulty with these salen materials is the absence of an accurate crystal structure, these calculations need to be run with accurate 3D representations of the atoms in space and don't work so well for unknowns. The calculation does show two pre-edge features at 5991 eV and 5992 eV, although these features show a larger splitting value in the experimentally obtained spectrum. The calculated intensity then starts to rise at the edge; there is an additional feature on the edge at 5999 eV, this appears as a small hump on the edge. The main edge appears less steep in the calculation but there does appear to be the two features after the edge that are also present in the experimental spectra.

The spectrum for Cr(salen3) and Cr(salen4) show two pre-edge features in the normal XANES, these appear at 5991 eV and 5993 eV. In the normal XANES there appears to be some level of background radiation as the spectra do not start at zero intensity. The HERFD XANES spectra also shows two pre-edge features at 5991 eV and 5993 eV; however these appear much better resolved with the two features becoming much more distinct. The two pre-edge features are split by approximately 2 eV, the same as with the salen 1 complex. It is by comparing the normal and HERFD spectra that we can really identify the merits of the high energy resolution XANES technique.

Figure 3 also shows an overlay of the three salen complexes studied; this shows the differences between the experimental spectra. It is evident that the XANES spectra for salens 3 and 4 are identical. We do not expect to see huge differences as the ligand structure is very similar, the change (an extra O atom) is obviously too far away from the central Cr atom to have any influence on the XAS spectrum. The spectrum for salen 1 is very similar but some differences are observed. The similarities arise due to the fact that the direct coordination around chromium is the same. The second pre-edge feature is slightly more intense for salen 1; this may be due to slight differences in the conformation of the molecule, meaning that quadrupole features are more likely.

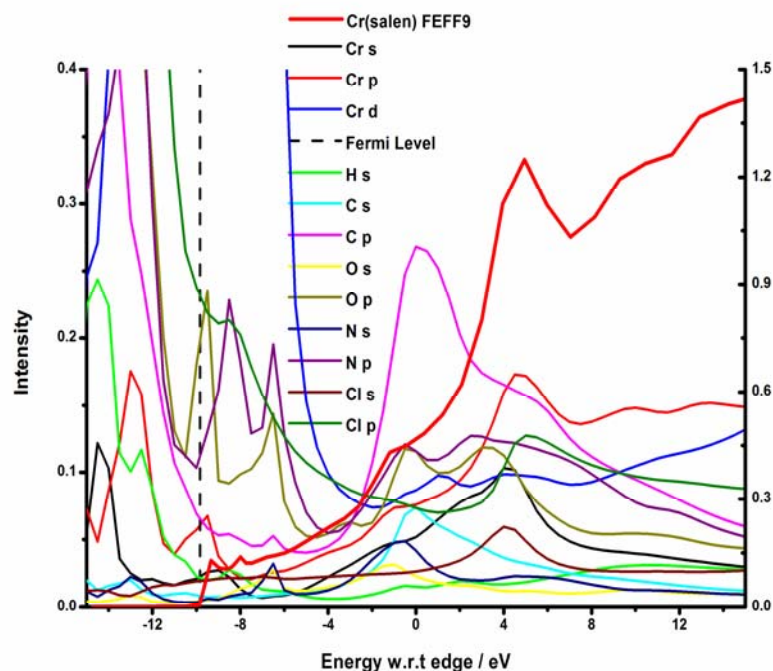


Figure 4 Density of states and associated XANES calculations performed with FEFF9 for Cr(salen).

Figure 4 shows the calculated orbital contributions to the pre-edge XANES features, the Fermi level is marked with the dashed line and we will examine the region above the Fermi level. Starting at the low energy side of the region we can see that there is Cr p orbital overlap with the Cr s and O p-orbitals at the first pre-edge feature at -9.5 eV. We expect to see Cr p and O p-orbital overlap forming the bond between the Cr and O atoms. The features in the pre-edge region are generally formed from $s \rightarrow p$ transitions so we would expect to see Cr p character, any orbitals that overlap with Cr p will also be observed. The second pre-edge feature at -8 eV also shows Cr p overlap with the N p-orbital as well as Cl p-orbitals and a small amount of C p. Again, in this complex Cr bonds to N, O and Cl atoms, so all of these are expected as the p-orbitals are the same size and shape, and when in the same location in space they will form a bond. As we move closer to the main edge there is a small feature at -1 eV on the edge rise; this feature shows Cr p overlap with C s, N s, O s, N p, O p and C p-orbitals. At the main edge there is evidence of Cr p mixing with Cl s, Cr s, O p and N p character. The whole XANES spectrum reflects the Cr p density of states; other orbitals mix with the Cr p forming the pre-edge features, the shoulder at the edge and the main edge.

From the Cr K-edge XANES there are no visible differences in the spectra for the different salen complexes studied, this may be due to the fact that the structural changes around the central Cr atom are more than four bonds away and any electronic effects, which might be

large even over 4 bonds, are not reflected in the Cr K-edge features. It seems that the nature of the K-edge XAS technique is not sensitive enough to detect such subtle differences in the ligand structure and electronics between the difference catalysts. A good agreement between the experimental and theoretical spectra is required in order to obtain quantitative structural information; in this case the current calculations are unable to accurately reproduce the experimental spectra of the salen complexes, this may be due to the model chosen. From figure 3 it is obvious that theoretical calculations are not optimised or the structure used is not correct, this has resulted in appreciable discrepancies between the calculated and experimental spectra. When comparing the salen spectra with the experimental spectra obtained from the references, we can see that the salen XANES spectra appear similar in shape to the octahedral CrCl_3 XANES spectra. Both of these complexes show a relatively clear pre-edge (in comparison with tetrahedral chromates and oxides) and a featureless edge. The FEFF9 calculation of CrCl_3 did also not accurately reproduce the edge and pre-edge features. It may be that there are charge-transfer effects in complexes with Cr-Cl bonds that are not accounted for in the calculation.

5.3.2 Cr L-edge absorption studies

The K-edge XANES region arises mainly from the metal p density of states, and in certain geometries from metal d density of states (although indirectly). For this reason the K-edge is useful in providing information on the metal oxidation state and geometry. In 2p X-ray Absorption Spectroscopy we are directly probing the metal 3d shell (at the L-edge) in doing this we get a more detailed view of the electronic structure at the metal site. As the 4s-orbitals are considerably lower in energy than the 3d-orbitals, the near edge structure of the $L_{2,3}$ edge is more closely related to the empty 3d states. The next section in this chapter is looking at the 2p X-ray Absorption Spectra (2p XAS) with both soft and hard X-rays, these experiments become more complicated to analyse due to the presence of multiplet effects, which were not present in the K-edge absorption studies.

The L-edge has been measured using both soft and hard X-ray techniques (directly and indirectly). In the soft X-ray technique we look at the direct $2p \rightarrow 3d$ absorption (L-edge) to dipole allowed final states, probing the 3d shell directly. The dipole-allowed transitions in 2p XAS are $2p \rightarrow 3d$ and $2p \rightarrow 4s$, but as the transitions to the 3d states dominate the transitions to 4s-orbitals are not included. The L-edges for the salen materials are shown below (figure 5). Information on the local ligand coordination is contained within the $L_{2,3}$ edges in the energy splittings of the 3d orbitals involved, this corresponds to the crystal field splitting value (Δ or $10Dq$). This value is determined by the type and nature of ligand attached to the metal ²⁷. This technique may be able to provide information about the

ligand substitutions on the salen framework that is not visible at the K-edge. The $L_{3,2}$ edge XANES essentially probes the empty density of d-states via dipole allowed 2p-3d transitions, making it an ideal tool to gain an insight into d-electron density, ligand field splitting and orbital hybridisation ²⁵.

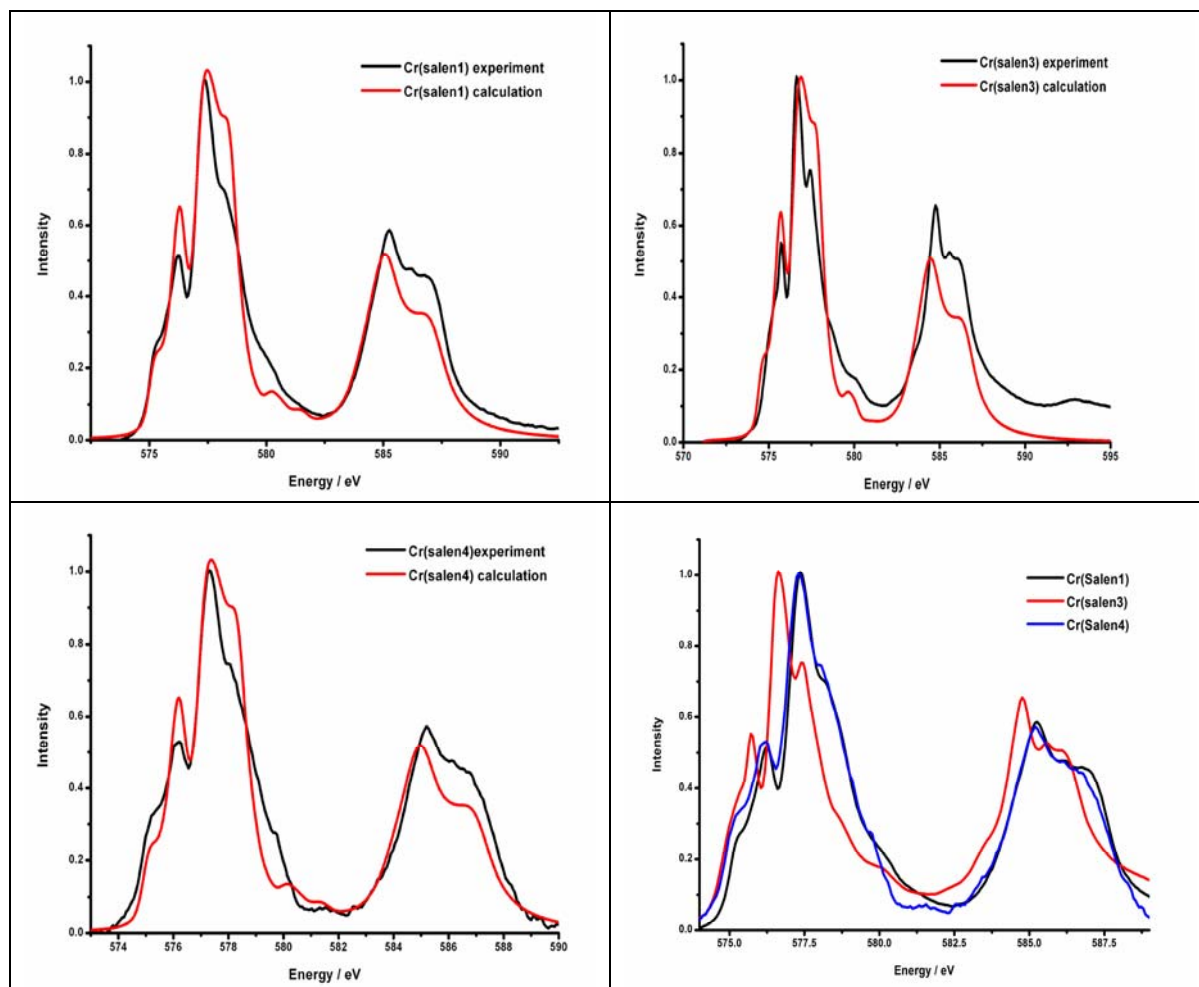


Figure 5 Cr L-edge spectra with associated theoretical calculations using CTM4XAS, the bottom right plot shows all salen experimental $L_{3,2}$ edges.

As with the K-edge absorption studies, only the effects that are larger than the lifetime broadening are observed in the L-edge absorption spectra. The lifetime of the 2p core-hole results in an experimental resolution of 0.2 eV in the soft X-ray spectrum, compared with 1.08 eV at the K-edge ^{2a}. However, as previously mentioned, the lifetime broadening of the L-edge spectra is less than that in the K-edge spectra, for this reason we expect to see additional features in the Cr L-edges compared to the K-edge experiments. From figure 5 we can see that the L-edges are split into the L_3 ($2p_{3/2}$) and L_2 ($2p_{1/2}$) edges, this is caused by the spin-orbit coupling of the 2p core hole ²⁸ and for Cr(salen1) they are split by 8 eV. This is the case for both the experimentally obtained data and the theoretical

calculation. Cr(salen3) and Cr(salen4) also show splitting of 8 eV between the L₃ and L₂ edges.

The L₂ peak arises from the 2p_{1/2} state and the L₃ peak arises from the 2p_{3/2} state, the relative intensities of the L₂ and L₃ are determined by the degeneracy of the states. A 2p_{1/2} configuration consists of two states and the 2p_{3/2} configuration consists of four states. Therefore the intensity ratio of the 2p_{3/2} (L₃) to the 2p_{1/2} (L₂) peak is expected to be 2:1. The experimental spectra for all three salen complexes show a greater intensity for the L₃ edge than the L₂; however it is not the 2:1 ratio that is expected. This observation was also found for the Cr reference materials in chapter 4, it has been shown in previous studies that the branching ratio can vary in transition metal compounds across the series²⁹. The electrostatic interactions between the core-hole and valence electrons also has an effect on the branching ratio³⁰ so the complex nature of the heteroatoms surrounding the central Cr may have an effect in these cases. Existing studies have specifically shown that the experimental intensity ratio of the L₃ to L₂ edge is often much lower for the early transition metals^{29, 31}.

The spectrum for Cr(salen1) shows a small hump on the low energy side of the L₃ peak at 575 eV, this feature is also reproduced by the theoretical simulation with the intensities also being well reproduced. The first main feature making up the L₃ peak appears at 576.5 eV, this is also present in the calculation however it appears slightly more intense in the calculation. The most intense feature at the L₃ edge occurs at 577.5 eV, with a feature on the high energy side at 578.5 eV, both of which are reproduced by theory in position and intensity. There are two smaller features between the L₃ and L₂ edges at 580 eV and 582 eV in the theoretical spectrum however in the experimental spectrum these are visible as slight humps but not as well defined. The L₂ edge is split into a main feature at 585.5 eV in both the experimental and theoretical spectra and in the experimental spectrum there are then two features of similar intensity at 586.5 eV and 587 eV. In the theoretical spectrum these appear as one broad feature. Both of the features at the L₂ edge appear to be more intense in the experiment than in the theoretical spectrum, this may be due to background signal.

The L_{3,2} spectra for Cr(salen3) shows a small feature on the low energy side of the L₃ edge at 575 eV, this is present in the calculation although slightly shifted in energy, this feature is better resolved in the calculation. The first peak of the L₃ edge appears at 575.5 eV, with the main peak at 577 eV, both of these peaks are also reproduced in the simulated spectrum. The peak at 575.5 eV appears less intense in the experiment in comparison to

the main peaks (at 577 eV) to which both spectra are normalised. As in the case of Cr(salen₁) there is also a feature on the high energy side of the main peak, however in this case it is a well resolved peak rather than a hump and appears at 578 eV, this peak shows greater intensity in the calculated spectrum. There are again two small features between the main L₃ and L₂ edges at 579 eV and 580 eV in the experimental spectrum, but only one is reproduced in the calculation. The feature at 580 eV in the calculation only appears as a small hump in the experiment. At the L₂ edge the main peak occurs at 584.5 eV, the second peak is split into two peaks at 585.5 eV and 586 eV. The calculation nicely reproduces the first peak at 584.5 eV but the second peak that consists of two features in the experiment is one broad peak in the calculation. Again for Cr(salen₃) the calculation appears less intense than the experiment and in this case the background does not return to zero intensity. The intensity ratio of the L₃ and L₂ edges is close to the 2:1 ratio expected, more so than in the case of the reference materials in chapter 4.

Cr(salen₄) shows a feature on the low energy side of the L₃ edge at 575 eV, this is observed both experimentally and theoretically but appears more intense in the experimental spectrum. The first main peak of the L₃ edge appears at 576.5 eV; this is also reproduced by theory and appears more intense in the calculation. The next peak occurs at 578 eV and both experimental and theoretical spectra are normalised to this peak. There is a small hump on the high energy side of the main peak, this is at 578.5 eV, and this again appears less intense in the experimental spectrum. There is a small feature in the experimental spectrum at 580 eV; this is not reproduced in the calculation. However there are two features in the calculation at 580.5 eV and 581.5 eV. At 581.5 eV there is a small hump in the experiment but this is of low intensity and could be noise. The L₂ edge consists of a peak at 585 eV in both spectra and a second less intense broad feature from 586-587 eV that is reproduced by the calculation as well. The L₂ edge, as with the other salen compounds, appears more intense experimentally however the intensities are not far off and are a fairly good match. The intensity ratio between the L₃ and L₂ edges for the salen 4 catalyst is close to the 2:1 ratio expected.

The last plot in figure 5 shows a comparison of all L-edges for the salen materials, the spectra for salens 1 and 4 show the same peak positions but the salen 3 L₃ and L₂ edges are shifted towards lower energy. The values used in the calculation for the three simulations are the same; the 10Dq value is expected to be the same as the Cr is in the same geometry for all. The same broadening factors were also needed for all three. We can see from these spectra that the structures are perhaps too similar to see differences in the absorption spectra.

As explained in chapter 4, the L_2 part of the spectrum (i.e. the last two peaks) contains an additional Auger decay that accounts for a significant broadening with respect to the L_3 part (electrons can decay from the L_2 to the L_3 making it broader)³². This is evident in the published lifetimes of the L_2 and L_3 edges (1.2 eV and 0.8 eV respectively)³². Also an additional broadening has been found between the t_{2g} and e_g states for Ligand Field Multiplet (LFM) calculations. This could be due to the differences in the vibrational effects on the different states or perhaps due to a difference in hybridisation effects and charge transfer multiplet calculations³³.

From chapter 4 it is evident when comparing the L-edges of Cr(III) and Cr(VI) that the multiplets do change with the differing number of d-electrons. There is a shift to higher energy as well as a visible change in the pattern and appearance of the peaks forming the $L_{3,2}$ edge. This makes the determination of the valency, and its cubic crystal field, fairly straightforward²⁸. All calculations are performed assuming pure O_h or T_d symmetry, with this in mind we are able to deduce that the deviation from pure O_h or T_d symmetry in the salen complexes are not significant enough to cause large discrepancies in the calculation. Although the experimental spectra have been simulated to a high degree of accuracy there are still some limitations to this approach. The character of the ground state is not considered in detail and also the broadenings arising from hybridisation, vibrations, lifetime and experimental resolution are treated very roughly and are included as general Lorentzian and Gaussian broadenings^{27b}. One of the major limitations when trying to study real systems is that we are unable to look at differences in ligand systems; the only effect that is included is the geometry and crystal field value rather than the ligands themselves. In this case it appears that the complexes studied are not structurally different enough to test the full power of the technique.

5.3.3 Cr K β emission studies

There can be difficulties in the interpretation of XANES spectra due to self-absorption effects in the XAS measurements and the complex relationship between charge screening and orbital hybridisation effects²⁰, however X-ray Emission Spectroscopy is largely free of experimental issues like these. This means that the chemical dependence is considerably simpler than in XANES. While XAS probes the density of unoccupied electronic states, XES reflects the occupied electron levels and provides more direct information on the charge density. We can therefore use XES to provide important complementary information. The valence-to-core region of transition metal X-ray spectra contains a wealth of information about the electronic and molecular structure of the system in

question. The $K\beta$ emission spectra of 3d metals show a pronounced chemical sensitivity, such chemical effects have previously been used as a probe of chemical bonding³⁴, the largest of these affecting the valence-to-core X-ray transitions. These transitions carry information on the occupancy and symmetry of the orbitals involved in chemical bonding; we hope to use this technique to detect the ligand changes around the central Cr atom. Similarly to XAS studies, XES does not require long range order in the system being studied. This is one of the main advantages of these X-ray technique; they are also sensitive to the composition of the bulk of the material rather than just the surface. Other advantages include the fact that high vacuum conditions are not required and the sample environment is flexible. As with XAS it is also possible to carry out this technique under controlled atmospheric conditions, at cryogenic or high temperatures and for *in-situ* catalysis studies (chapter 6).

The 1s4p valence band XES is split into the cross over peak ($K\beta''$) and the valence band XES ($K\beta_{2,5}$). The $K\beta_{2,5}$ lie immediately below the Fermi level and are used to describe the valence band. $K\beta''$ is the cross-over peak, which appears at higher binding energies (lower fluorescence)³⁵. The $K\beta_{2,5}$ is caused by metal 4p character that has hybridised with the valence states of the ligands. The $K\beta''$ peak is called the cross-over peak because it can be considered as the XES channel from a ligand 2s 'core' state to a metal 1s state, which is a cross-over transition³⁶. It is better to view this transition as one from metal 4p to 1s, where the metal 4p has hybridised with the ligand 2s core state³⁶. Due to the nature of the ligand 2s \rightarrow metal 1s transition these features reflect the binding energies of the ligand 2s orbitals. The intensity of the cross-over peak is inversely proportional to the metal-ligand distance; this is caused by the fact that shorter distances imply stronger hybridisation³⁷.

$K\beta$ emission experiments were performed on the salen catalysts in the hope that looking at the valence-to-core lines in particular, more subtle ligand effects may be observed and their effect on the electronic structure of chromium explained. In the case of the salen series any change in chemical activity brought about by the ligands would most probably be due to the subtle changes in the substitution in the extended ligand structure, which would be observed spectroscopically and can explain any differences in chemical activity³⁸. As mentioned above, the differences in the complexes are very small and in the case of the first coordination sphere around chromium they are the same (Cr is bonded to N and O atoms in all three).

It is hard to assign the direct origin of features observed in some of the more complex samples. The work by Sofanov et al³⁹ claims to demonstrate the first example of the

practical application of the XES method for studying real objects, but is in fact only studying single ligand reference materials (i.e. pure chloride, carbides etc). Therefore if we are able to understand the XES spectra for the more complicated coordination compounds and the origin of the features observed, we would be making great advances in this area.

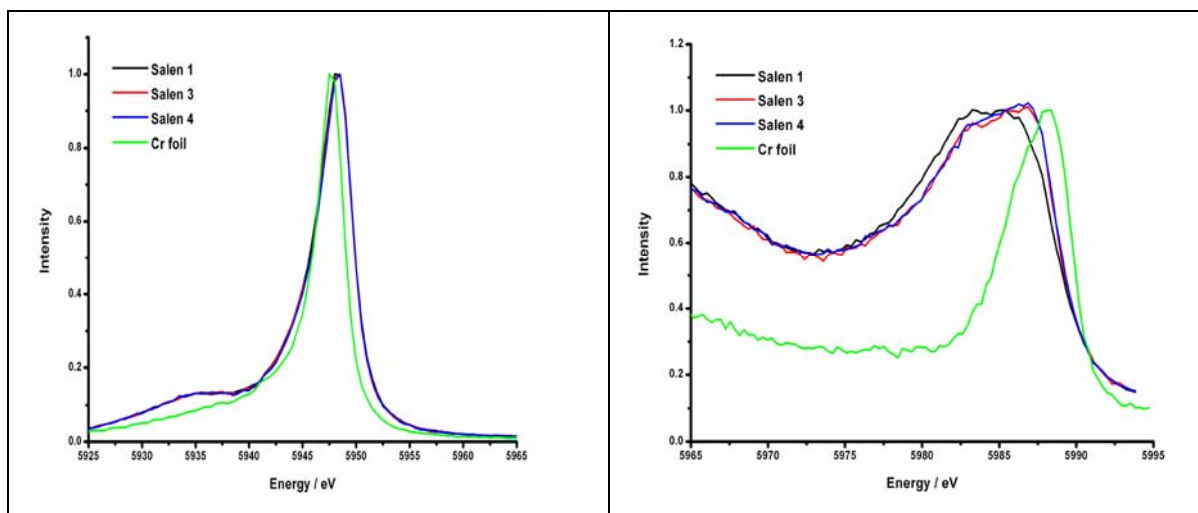


Figure 6 **K β satellite lines for a series of Cr(salen) complexes.**

The experimental K β main and K β satellite lines for the Cr(salen) complexes are shown above in figure 6. The K β main lines (left hand side) for all three salen complexes shows the same general trend, there is a small feature at 5935 eV and the main emission line occurs at 5948 eV. The core-to-core spectrum for Cr foil is also displayed on the same axis; here we see the absence of the first feature at 5935 eV and the main emission line appears slightly shifted towards lower energy at 5947.5 eV.

Figure 6 also shows the experimental K β satellite lines for the salen complexes as well as Cr foil (on the right hand side). The K $\beta_{2,5}$ lines involve the highest energy molecular orbitals with Cr 3d, 4s and 4p character as well as ligand 2s and 2p character, providing information on the nature of the bonding in the sample⁴⁰. The K β'' lines come at slightly lower energies and the structure contained in both of these valence-to-core lines makes up what is called the ‘satellite region’. Again the satellite lines show the same trends for the salen complexes 3 and 4, a broad peak from 5977.5 eV to 5990 eV with a tail towards lower energy from the K β main line. The spectrum for salen 1 is slightly shifted towards lower energy and appears at 5982 to 5987.05 eV. The spectrum for Cr foil shows a much sharper peak at 5988 eV, all the experimental spectra appear noisy but this is due to the low intensity of the K β satellite lines.

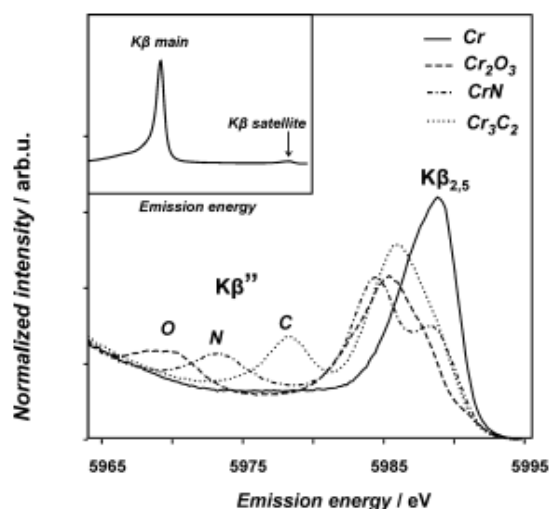


Figure 7 $K\beta$ satellite regions of Cr compounds showing the shape and position of the cross-over peaks for C, N and O ligands ³⁹.

The spectral shape of the satellite lines for the salen complexes does not appear to show the expected features in the cross-over region for samples containing Cr-O, Cr-N or Cr-C bonds (as shown for samples in reference 51, reprinted here in figure 7). It is difficult to tell whether the effects seen are due to the more complex bonding to Cr or partly because of the environment around the Cr, for example geometry and oxidation state.

In the case of the salen complexes we expect to see both the Cr-N and Cr-O peaks as the chromium is directly bonded to N and O in these complexes. In fact, we do not see either of these. It might be that there is a complicated mix of orbitals and they are not as nicely split and thus visible. Another factor could be the temperature during the experiment, in literature these experiments are carried out at cryogenic temperatures. In our case the samples were not cooled during the experiment, this can have the effect of broadening all the features in the spectrum. Another difference is that in these systems we have a mixture of ligands, this may cause an additional broadening to those that are pure ligand systems.

The valence-to-core transitions ($K\beta_{2,5}$ and $K\beta''$) directly reflect the configurations of electron orbitals that participate in the chemical bond and therefore provide valuable information. None of the K emission lines directly reflect the 3d electron configuration due to symmetry selection rules⁴¹.

5.3.4 Cr 1s2p RIXS emission studies

This section looks at the 1s2p Resonant Inelastic X-ray Scattering spectroscopy of the salen materials. This second order process looks at both the X-ray absorption and X-ray emission of the sample under investigation. The RIXS experimental set-up (see chapter 2) results in the removal of the 1s core-hole lifetime broadening and therefore allows the measurement of the K-edge with greater resolution ⁴², with the removal of the 1s core-hole lifetime the spectrum is now broadened only by the 2p core-hole lifetime (which is longer than the 1s core-hole lifetime) and the experimental broadening. The pre-edge features in the K-edge XANES region are weak compared to the main edge and for the early transition metals the energy separation between the pre-edge and main edge is low. The 1s lifetime broadening of more than 1 eV ²³ means that the calculations of the metal K-edge only need to be accurate to this resolution. This means that often a detailed analysis of the K pre-edge spectral features in XAS is limited and contains a certain degree of uncertainty due to a strong background from dipole allowed transitions at higher energies ⁴³. In such cases Resonant Inelastic X-ray Scattering spectroscopy (RIXS) can be used to provide information on the low-energy unoccupied electronic states.

The electronic states that produce the edge of an absorption spectrum are resonantly excited states that subsequently decay. In the case of Cr the decay process with the highest probability after the initial excitation is the 2p to 1s transition or the K α fluorescence line ⁴⁴. The figure below (figure 8) shows the initial excitation and subsequent radiative decay processes that make up this second order process.

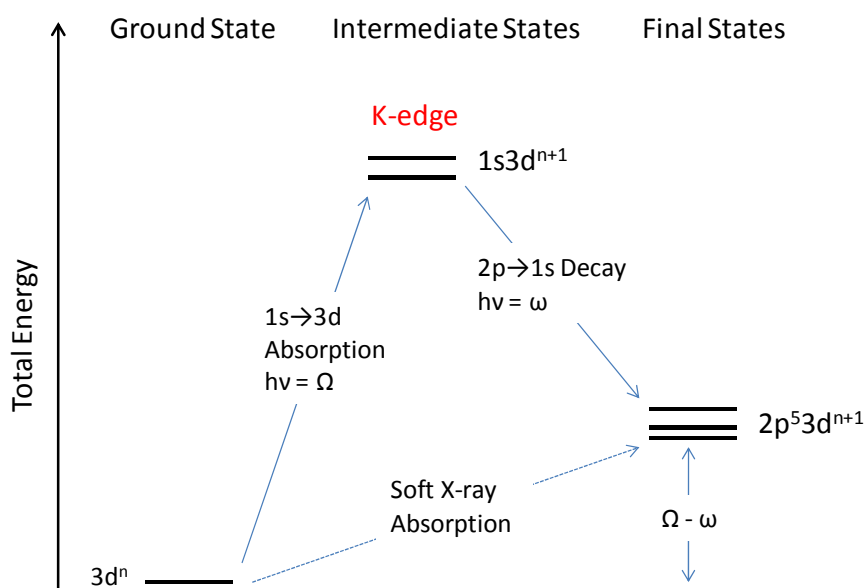


Figure 8 Energy schematic of the 1s2p RIXS process ⁴⁰.

The 1s2p RIXS shown in figure 8 involve the measurement of the 1s2p X-ray emission spectra at the excitation energies related to the 1s pre-edge energies ^{31b}. These 1s2p RIXS planes can be viewed as the transition from the 3dⁿ ground state to the 2p⁵3dⁿ⁺¹ final states via the 1s¹3dⁿ⁺¹ intermediate states, these transitions are shown in figure 8. In the RIXS experiment, along the additional energy transfer axis, the same final state is reached as in L-edge absorption (figure 8), this allows the L-edge to be probed indirectly combined with the advantages of using bulk sensitive hard X-rays (allowing *in-situ* experiments).

Although the plots may not exactly coincide they will still contain information on the metal ion electronic structure that is complementary to K-edge absorption. RIXS uses hard X-rays to probe the 2p→1s fluorescence lines that are emitted after the 1s core hole creation, in doing so we are looking at the 3d shell indirectly by analysing the multiplet interactions between the 2p core-hole and the 3d valence electrons, in the case of Cr these interactions are large. RIXS is a powerful tool for the study of the electronic excitations in solids and provides site, element, and orbital selective information. The RIXS data provides detailed electronic information on organometallic complexes including charge transfer within the systems making it a useful technique for the study of catalysts.

The second energy axis, energy transfer, allows the removal of the strong background that is present at the main K-edge in the range of the pre-edge structure. This enables the separation of the pre-edge features from the main K-edge along the incident energy axis ⁴⁰. These effects can be seen when looking at the 1s2p RIXS spectra of the Cr salen compounds shown below. By measuring both the absorption and emission processes we obtain a 2D contour plot from the RIXS experiment.

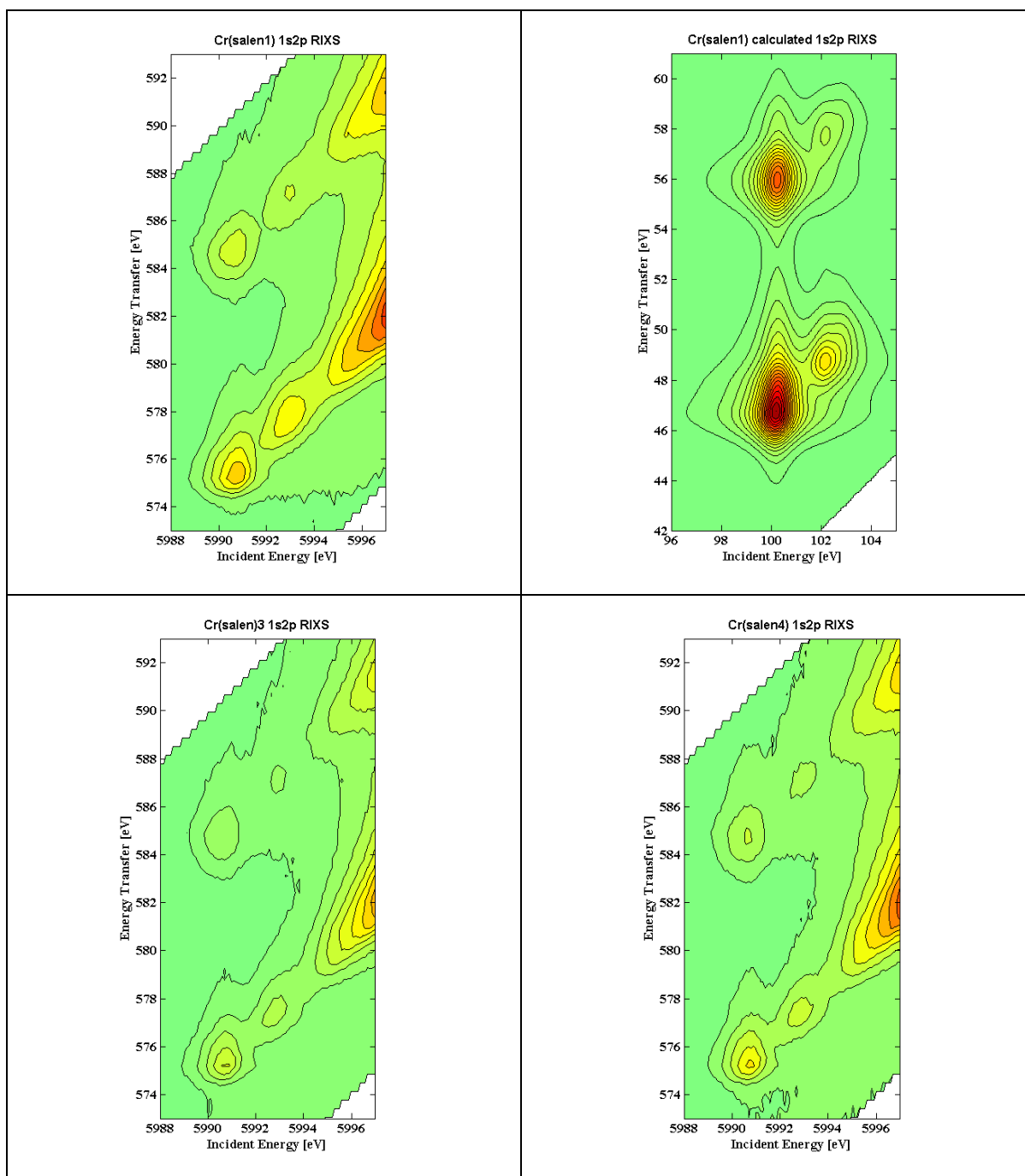


Figure 9 Experimental and theoretical Cr 1s2p RIXS spectra for Cr(salen1), Cr(salen3) and Cr(salen4) complexes.

The Cr 1s2p RIXS experiments were performed by selecting the incident energy whilst scanning a range of possible emission energies. This gives rise to the 2D contour plots shown in Figure 9. These experiments allow a separation of the pre-edge features through a reduced life-time broadening affecting the spectra. The spectrum for Cr(salen1) complex shows two pre-edge features occurring at about 5991 eV and 5993 eV incident energy (575 eV and 577 eV energy transfer) along the $K\alpha_1$ emission line. The main edge starts at 5996 eV incident energy. There are also two pre-edge features along the $K\alpha_{II}$ emission line;

however these appear less intense than the pre-edge features along the $K\alpha_1$ emission line, and appear at 5991 eV and 5993 eV incident energy, these two emission energy maxima occur at 585 eV and 587 eV energy transfer. The main edge appears at 5997 eV incident energy. The first pre-edge feature along the $K\alpha_1$ emission line at 5991 eV incident energy (575 eV energy transfer) is spread over 2 eV, this implies that two electronic resonances make up the feature ⁴³. The second pre-edge feature at 5993 eV incident energy (577 eV energy transfer) is also spread over 2 eV but appears less intense in comparison to the first pre-edge feature. There appears to be an absorption tail leading to the main edge at both $K\alpha$ emission lines, the broadening in the diagonal direction is caused by the experimental broadening and core-hole lifetime effects. The broadening of the pre-edge peak is essentially symmetric in the incident energy axis but appears asymmetric in the energy transfer direction. This indicates that the final state is not a single state and that there are additional states at the higher energy transfer side of the main peak ⁴⁴.

In the calculated 1s2p RIXS spectra the two pre-edge features are reproduced, with the first pre-edge feature at 5991 eV incident energy (100 eV in the theoretical case) being the most intense. When comparing the experimental and theoretical spectra a difference in intensity of the pre-edge features is observed, this may be due to orbital hybridisation and as it is not included in the calculations ⁴³. Both pre-edge features are also spread over 2 eV in the calculated spectrum. The experimental spectrum shows a splitting of 10 eV in the energy transfer direction; this splitting is slightly lower in the calculation at around 9 eV. This splitting value can be compared to the energy difference between the L_3 and L_2 edges in the soft X-ray absorption experiments, as the same final states are probed. In this case the energy difference in the soft X-ray experiments is also approximately 10 eV. The L_3 and L_2 lines are generally split by the 2p spin-orbit interaction ⁴⁵. Again for the calculation we observe the asymmetry in broadening of the pre-edge peak in the energy transfer direction. This follows from the existence of more than one final state ⁴⁴. These RIXS simulations only cover the pre-edge region meaning that the main edge is not reproduced, this is because the calculations to produce the main edge are very complicated and, in the case of chromium, leaving out the main edge does not affect the quality of the pre-edge region.

The 1s2p RIXS spectrum for Cr(salen)₃ also shows two features in the pre-edge region of the experimental spectrum. These two features appear at 5991 eV and 5993 eV incident energy along the $K\alpha_1$ emission line. The main edge rise appears at 5995 eV incident energy. There are also two pre-edge features in the $K\alpha_1$ emission line, these appear at 5991 eV and 5993 eV incident energy however they appear less intense than for the $K\alpha_{II}$ emission line.

Again, for the $K\alpha_I$ emission line the main edge starts at 5995 eV incident energy, but appears less steep than in the $K\alpha_I$ emission line, as seen in the contour spacing. The two emission energy maxima for the two pre-edges occur at 575 eV and 577 eV energy transfer along the $K\alpha_I$ emission line and at 585 eV and 587 eV energy transfer along the $K\alpha_{II}$ emission line. The first pre-edge feature along the $K\alpha_I$ emission line at 5991 eV incident energy is spread over 2 eV, this is an indication of how many electronic transitions make up the feature, in this case two. The second pre-edge feature at 5993 eV incident energy is spread over 1 eV, and appears less intense than the first pre-edge feature. The first pre-edge feature along the $K\alpha_{II}$ emission line is also spread over 2 eV, the second is spread over what appears to be 2 eV but is very broad. The exact position of the pre-edge features as quoted above is determined by the peak maxima. As with the other experimental spectra for the 1s2p RIXS experiments, there is a diagonal absorption tail in the direction of the emitted energy. This absorption tail could be a consequence of the experimental broadening and the core-hole lifetime effects as mentioned above. As in the case of Cr(salen1), the broadening in the energy transfer direction can be explained by the existence of multiple final states ⁴⁴.

The calculation for the 1s2p RIXS spectra of the Cr(salen) materials is only shown once as the resulting spectrum is the same for all three of these catalyst materials. Only one calculation was performed as this nicely reproduces the features present in the Cr(salen3) spectra as well. This is shown by the two pre-edge features at 5991 eV and 5993 eV incident energy in the experimental spectrum also being present in the calculated spectrum. The absolute energy is not reproduced, as with most of the techniques in this study, the calculations do not accurately reproduce these. We can compare the relative energy positions; in this case we can look at the energy splitting of the pre-edge features along both the $K\alpha_I$ and $K\alpha_{II}$ emission lines. Along the $K\alpha_{II}$ line the separation of the pre-edge features is approximately 2 eV in the experimental spectrum, in the calculation the separation is also 2 eV. The same observation is true along the $K\alpha_I$ line, the splitting in both spectra is 2 eV. The calculation shows the same relative intensity between the two pre-edge features, with the first being more intense. The broadening in the vertical direction is present in the calculated spectrum as well as in the experiment, but the broadening in the diagonal direction is no longer visible going from the experiment to the calculation. This could be due to the fact that the main edge is not calculated so the absorption tail is not present. The experimental broadening may not be fully corrected for in the calculation.

In general, all of the experimental spectra for the salen materials appear to show the same peaks and patterns. With the Cr(salen₄) complex also showing two pre-edge features in the 1s2p RIXS appearing at 5991 eV and 5993 eV incident energy and the main edge at 5996 eV incident energy. Again the two pre-edge features along the K α_{II} appear more intense than the two features along the K α_I emission line. Both of the pre-edge features in each case are spread over 2 eV and separated by 2 eV. The energy maxima for the pre-edge features along the K α_{II} line occur at 575 eV and 577 eV energy transfer and 585 eV and 587 eV energy transfer for the K α_I emission line. As for the other Cr(III) complexes, the calculation reproduces the two pre-edge features and the splitting of the two peaks. It also reproduces the relative intensities of the two peaks.

If we compare the 1s2p RIXS plot shown in figure 9 with the normal K-edge absorption XANES spectrum we can see the increased level of separation of the two pre-edge features from the main edge, especially when compared to the normal XANES spectrum. In the normal XANES spectrum there is a small peak at 5991 eV and a second more intense feature at 5993 eV, when we look at the RIXS spectrum these two features become completely separated out with two distinct peaks at 5991 eV and 5993 eV and the contours returning to base line in-between.

5.4 Conclusions

In this project one of the main aims was to analyse the difference in electronic structure between the different catalysts structures. With all of the X-ray techniques used in this chapter we do not observe any significant differences in the features observed for the salen structures. The Cr K-edge XAS can instantly provide a certain level of information about the geometry of the catalyst, this is evident in the shape of the pre-edge. The interesting observation with the salen materials is that they show a relatively clear pre-edge, which would normally be indicative of a higher symmetry order when in fact they have a lower order of symmetry (C₂).

The Cr L-edges provide us with direct d-orbital information about the central metal, the L-edge spectra for the salens show a similar peak pattern to the Cr(III) reference samples in chapter 4. They are also well reproduced by the CTM theory, but we are not able to extract the different electronic information between the salens. In future studies it may be of interest to use multiple scattering methods (FEFF) to simulate the L-edge spectra, in this case the full crystal structure information would be taken into consideration.

The $K\beta$ emission studies focus on the filled density of states rather than the empty density of states (as in XAS), this means that we can obtain information about the first coordination shell of the central Cr. For the salens this turns out not to be hugely useful as the direct bonds to Cr are the same in all complexes. We do however see small differences in going from salen 1 to salens 3 and 4; this suggests that the extended ligand structure does affect the emission spectra to some degree. The broad satellite region visible in the salen spectra may also be a result of experimental conditions in that the temperatures were too high.

The intensity of the pre-edges in a XANES experiment is much weaker in comparison to that of the main edge and so by using RIXS we are able to achieve a greater separation of these features from the main edge along with greater resolution. We cannot accurately calculate the electronic differences in the RIXS experiments based on the charge transfer theory used in this study as it reduces all systems to the same point group symmetry. It is not possible to include different ligand systems and thus look at this effect as such as RGAss does not include a detailed 3D structure. There are theoretical advances that would lead to an improved electronic analysis; the first is that new developments in FEFF9 now allow RIXS calculations and since FEFF9 uses full structural information (from crystal structures) it may now be possible obtain more detailed and structure specific information. Performing different calculations with different broadenings may also provide insights into what resolution is needed to see the differences in the electronics as expected. That would give an indication in how the experiment will need to be improved to obtain this level of information.

Although with further calculations, and the inclusion of more structural information, we may see more detail in the spectra than we currently do, it is likely that there will always be a limit to the level of differences between the spectra for these complexes. This is because the immediate structure around the central Cr atom will always be the same for the salen complexes; this has the largest effect on the spectra as most techniques consider the first coordination shell. The techniques are sensitive up to four bonds away from the central absorber and so this would be an important consideration when planning further work, making sure that the substitutions were within this range.

5.5 References

1. Bergmann, U.; Glatzel, P.; Cramer, S. P., *Microchem. J.* **2002**, *71*, 221.
2. (a) Fuggle, J. C.; Inglesfield, J. E., *Topics in Applied Physics*. Springer-Verlag Berlin and Heidelberg GmbH & Co. K: 1992; (b) Hämäläinen, K.; Siddons, D. P.; Hastings, J. B.; Berman, L. E., *Phys. Rev. Lett.* **1991**, *67*, 2850.
3. Cressey, G.; Henderson, C. M. B.; Laan, G., *Phys. Chem. Miner.* **1993**, *20*, 111.
4. Kau, L. S.; Spira-Solomon, D. J.; Penner-Hahn, J. E.; Hodgson, K. O.; Solomon, E. I., *J. Am. Chem. Soc.* **1987**, *109*, 6433.
5. Chaturvedi, S.; Rodriguez, J.; Brito, J., *Catal. Lett.* **1998**, *51*, 85.
6. Bron, M.; Teschner, D.; Knop-Gericke, A.; Scheybal, A.; Steinhauer, B.; Hävecker, M.; Födisch, R.; Hönicke, D.; Schlögl, R.; Claus, P., *Catal. Commun.* **2005**, *6*, 371.
7. (a) Ressler, T.; Timpe, O.; Neisius, T.; Find, J.; Mestl, G.; Dieterle, M.; Schlögl, R., *J. Catal.* **2000**, *191*, 75; (b) Hashmi, A. S. K.; Lothschütz, C.; Ackermann, M.; Doepp, R.; Anantharaman, S.; Marchetti, B.; Bertagnolli, H.; Rominger, F., *Chem. Eur. J.* **2010**, *16*, 8012; (c) Liu, S. H.; Wang, H. P.; Wang, H. C.; Yang, Y. W., *J. Electron. Spectrosc. Relat. Phenom.* **2005**, *144–147*, 373.
8. Briois, V.; Belin, S.; Villain, F.; Bouamrane, F.; Lucas, H.; Lescouëzec, R.; Julve, M.; Verdager, M.; Tokumoto, M. S.; Santilli, C. V.; Pulcinelli, S. H.; Carrier, X.; Krafft, J. M.; Jubin, C.; Che, M., *Phys. Scr.* **2005**, 38.
9. McGarrigle, E. M.; Murphy, D. M.; Gilheany, D. G., *Tetrahedron: Asymmetry* **2004**, *15*, 1343.
10. (a) Katsuki, T., *Coord. Chem. Rev.* **1995**, *140*, 189; (b) Katsuki, T., *J. Mol. Catal. A: Chem.* **1996**, *113*, 87; (c) Sasaki, H.; Irie, R.; Hamada, T.; Suzuki, K.; Katsuki, T., *Tetrahedron* **1994**, *50*, 11827; (d) DiMauro, E. F.; Kozlowski, M. C., *J. Am. Chem. Soc.* **2002**, *124*, 12668.
11. Samsel, E. G.; Srinivasan, K.; Kochi, J. K., *J. Am. Chem. Soc.* **1985**, *107*, 7606.
12. Srinivasan, K.; Michaud, P.; Kochi, J. K., *J. Am. Chem. Soc.* **1986**, *108*, 2309.
13. Yoon, H.; Burrows, C. J., *J. Am. Chem. Soc.* **1988**, *110*, 4087.
14. Jacobsen, E. N., *Acc. Chem. Res.* **2000**, *33*, 421.
15. Daly, A. M.; Cormac, D. T.; Renehan, M. F.; Gilheany, D. G., *Tetrahedron Lett.* **1999**, *40*, 3617.
16. Zhang, W.; Loebach, J. L.; Wilson, S. R.; Jacobsen, E. N., *J. Am. Chem. Soc.* **1990**, *112*, 2801.
17. Jacobsen, E. N.; Zhang, W.; Muci, A. R.; Ecker, J. R.; Deng, L., *J. Am. Chem. Soc.* **1991**, *113*, 7063.
18. (a) Brandt, P.; Norrby, P.-O.; Daly, A. M.; Gilheany, D. G., *Chem. Eur. J.* **2002**, *8*, 4299; (b) O'Mahony, C. P.; McGarrigle, E. M.; Renehan, M. F.; Ryan, K. M.; Kerrigan, N. J.; Bousquet, C.; Gilheany, D. G., *Org. Lett.* **2001**, *3*, 3435.
19. Zhang, W.; Jacobsen, E. N., *J. Org. Chem.* **1991**, *56*, 2296.
20. Solomon, E. I.; Hedman, B.; Hodgson, K. O.; Dey, A.; Szilagy, R. K., *Coord. Chem. Rev.* **2005**, *249*, 97.
21. Darensbourg, D. J.; Yarbrough, J. C., *J. Am. Chem. Soc.* **2002**, *124*, 6335.
22. (a) Westre, T. E.; Kennepohl, P.; DeWitt, J. G.; Hedman, B.; Hodgson, K. O.; Solomon, E. I., *J. Am. Chem. Soc.* **1997**, *119*, 6297; (b) DeBeer George, S.; Brant, P.; Solomon, E. I., *J. Am. Chem. Soc.* **2004**, *127*, 667.
23. de Groot, F. M. F.; Vanko, G.; Glatzel, P., *J. Phys.: Condens. Matter* **2009**, *21*, 104207.
24. Xia, Q. H.; Ge, H. Q.; Ye, C. P.; Liu, Z. M.; Su, K. X., *Chem. Rev.* **2005**, *105*, 1603.
25. van der Veen, R. M.; Kas, J. J.; Milne, C. J.; Pham, V.-T.; Nahhas, A. E.; Lima, F. A.; Vithanage, D. A.; Rehr, J. J.; Abela, R.; Chergui, M., *PCCP* **2010**, *12*, 5551.
26. Rehr, J. J., *Radiat. Phys. Chem.* **2006**, *75*, 1547.
27. (a) de Groot, F., *Chem. Rev.* **2001**, *101*, 1779; (b) Theil, C.; van Elp, J.; Folkmann, F., *Phys. Rev. B: Condens. Matter* **1999**, *59*, 7931.

28. de Groot, F. M. F.; Fuggle, J. C.; Thole, B. T.; Sawatzky, G. A., *Phys. Rev. B: Condens. Matter* **1990**, *42*, 5459.
29. Thole, B. T.; van der Laan, G., *Phys. Rev. B: Condens. Matter* **1988**, *38*, 3158.
30. Onodera, Y.; Toyozawa, Y., *J. Phys. Soc. Jpn.* **1967**, *22*, 833.
31. (a) de Groot, F. M. F.; Fuggle, J. C.; Thole, B. T.; Sawatzky, G. A., *Phys. Rev. B: Condens. Matter* **1990**, *41*, 928; (b) de Groot, F., *Coord. Chem. Rev.* **2005**, *249*, 31; (c) de Groot, F. M. F.; Arrio, M. A.; Sainctavit, P.; Cartier, C.; Chen, C. T., *Solid State Commun.* **1994**, *92*, 991; (d) Zaanen, J.; Sawatzky, G. A.; Fink, J.; Speier, W.; Fuggle, J. C., *Phys. Rev. B: Condens. Matter* **1985**, *32*, 4905.
32. Fuggle, J. C.; Alvarado, S. F., *Physical Review A* **1980**, *22*, 1615.
33. de Groot, F. M. F.; Kotani, A., In *Core Level Spectroscopy of Solids*, CRC Press: 2008; pp 93.
34. Meisel, A.; Leonhardt, G.; Szargan, R., *X-Ray Spectra and Chemical Binding*. Springer-Verlag: Berlin; New York, 1989.
35. Eeckhout, S. G.; Safonova, O. V.; Smolentsev, G.; Biasioli, M.; Safonov, V. A.; Vykhodtseva, L. N.; Sikora, M.; Glatzel, P., *J. Anal. At. Spectrom.* **2009**, *24*, 215.
36. de Groot, F. M. F.; Kotani, A., In *Core Level Spectroscopy of Solids*, CRC Press: 2008; pp 11.
37. Bergmann, U.; Horne, C. R.; Collins, T. J.; Workman, J. M.; Cramer, S. P., *Chem. Phys. Lett.* **1999**, *302*, 119.
38. Jacobsen, E. N.; Zhang, W.; Guler, M. L., *J. Am. Chem. Soc.* **1991**, *113*, 6703.
39. Safonov, V. A.; Vykhodtseva, L. N.; Polukarov, Y. M.; Safonova, O. V.; Smolentsev, G.; Sikora, M.; Eeckhout, S. G.; Glatzel, P., *J. Phys. Chem. B* **2006**, *110*, 23192.
40. Glatzel, P.; Bergmann, U., *Coord. Chem. Rev.* **2005**, *249*, 65.
41. Bergmann, U.; Glatzel, P., *Photosynth. Res.* **2009**, *102*, 255.
42. Hamalainen, K.; Kao, C. C.; Hastings, J. B.; Siddons, D. P.; Berman, L. E.; Stojanoff, V.; Cramer, S. P., *Phys. Rev. B: Condens. Matter* **1992**, *46*, 14274.
43. Glatzel, P.; Yano, J.; Bergmann, U.; Visser, H.; Robblee, J. H.; Gu, W.; de Groot, F. M. F.; Cramer, S. P.; Yachandra, V. K., *J. Phys. Chem. Solids* **2005**, *66*, 2163.
44. de Groot, F. M. F.; Glatzel, P.; Bergmann, U.; van Aken, P. A.; Barrea, R. A.; Klemme, S.; Havecker, M.; Knop-Gericke, A.; Heijboer, W. M.; Weckhuysen, B. M., *Phys. Rev. B: Condens. Matter* **2005**, *109*, 20751.
45. Glatzel, P.; Bergmann, U.; Yano, J.; Visser, H.; Robblee, J. H.; Gu, W.; de Groot, F. M. F.; Christou, G.; Pecoraro, V. L.; Cramer, S. P.; Yachandra, V. K., *J. Am. Chem. Soc.* **2004**, *126*, 9946.

Chapter Six: Catalysis

6.1 Introduction

Due to the advances in synchrotron radiation and third-generation beam lines providing such high fluxes we are able to make the most of the advantages that X-ray Absorption and secondary X-ray Emission Spectroscopy (XES) offers. Technical developments enable the production of smaller and smaller beam sizes, this along with the ability to carry out experiments under extreme conditions as well as *in-situ*, time resolved studies make this a perfect technique with which to study catalytic systems. In the field of catalysis it is often the aim to use such *in-situ* characterisation techniques to determine the structure of the active site. There is now also the possibility of time-resolved spectroscopy being used to undertake kinetic studies on catalytic systems.

In this current research project it is the Cr(salen) mediated alkene epoxidation reaction that is of particular interest. Over the last two decades there have been a number of important advances in the development of general methods for catalytic asymmetric alkene epoxidation¹. One of the difficulties when looking at the chromium series is that rates are slow with the unsubstituted salen complexes and essentially only alkenes which are electron rich can be epoxidised. This is due to the fact that the reaction mechanism consists of an electrophilic attack of chromium on the alkene². One of the major limitations of Jacobsen's catalyst is that low selectivity is observed in the epoxidation of *E*-1,2-disubstituted alkenes^{1c,3}. Work was then undertaken to develop epoxidation catalysts based on a chromium salen template⁴ to overcome some this problem. These systems have shown a contrasting selectivity pattern to their manganese analogues in that they allow the asymmetric epoxidation of *E*-1,2-disubstituted alkene, with iodosylbenzene as a stoichiometric oxidant. This is the reaction that we have chosen for this study.

The work by Gilheany *et al* reported the use of an optically active (salen)chromium(III) complex bearing a chloro-substituent at C3, C3', C5 and C5' that showed high asymmetric induction of 83% enantiomeric excess (ee) in the epoxidation of *trans*- β -methylstyrene, when triphenylphosphine oxide was added to the reaction medium^{4b}. A reduction in ee of about 10% was observed when going from a chloro substituent to a hydrogen. An asymmetric mix of one chloro substituent and one hydrogen atom showed the same selectivity as two hydrogen atoms.

6.2 Mechanistic studies

Due to the interesting observations made as a result of ligand effects and reaction conditions there are a few mechanistic pathways often considered for the epoxidation of alkenes; one of the more popular ones being the side-on approach model ⁵, this results in a less hindered approach pathway for the *cis*-alkene. This idea was originally proposed by Groves ^{5a,6} and became a useful working model in the design of transition-metal based epoxidation catalysts ^{5b}. If we are to find that this side-on approach mechanism is the only one taking place then we can assume that the epoxidation of *trans*-alkenes with high ees will always provide a challenging problem.

To complicate matters however, the work by O'Mahony *et al* has called into question the side-on approach model for chromium system because for chromium, higher asymmetric induction was observed with the *trans*-alkene ⁷. They did also however, propose an explanation that the Cr complex was non-planar, this gained some support by other research groups ⁸.

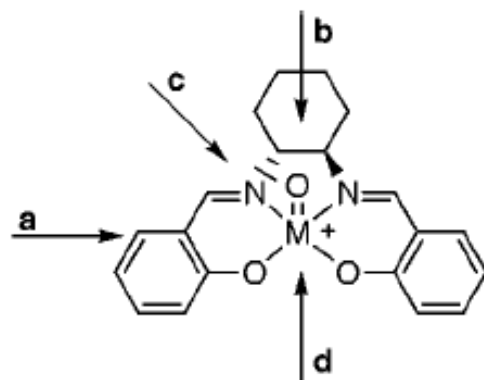


Figure 1 Approach trajectories towards the Cr=O bond ⁷.

Figure 1 shows the different approach pathways that have been put forward to describe the mechanism of epoxidation for Mn and Cr(salen) catalysts in the epoxidation of alkenes. Jacobsen ^{1c}, assuming a flat geometry, considers alkene approach to the metal-oxo bond along either pathway 'a' or 'b' (see figure 1). Which one occurs depends on the nature of the imine bridge and on the presence or absence of large groups at the X-position. Pathway 'b' would therefore apply to the tetra-*tert*-butyl catalyst (Jacobsen's catalyst) as this is the most sterically hindered complex ⁷. In this case for the chromium system, approach mechanism 'd' is currently favoured for the stepped conformation of the complex ^{4a}. It is also thought that approach along 'c', similar to that suggested by Katsuki

^{5c, 9} may also be in operation. This is because of the slightly beneficial effect of W-substituents, which is not additive to the beneficial effect of the Z-substituent ⁷. This would suggest that changes at the two different positions might independently affect the two different approaches. Approach along 'c' might be favoured by Z-substitution while that along 'd' is favoured (to a lesser extent) by W-substitution, substitution at X and Y would then have little effect as observed in studies by O'Mahony *et al* ⁷. Another consideration is that substitution at Z, especially by large groups, will have an effect on the degree of non-planarity of the complex, which will in turn influence selection ⁷. The stepped conformation is shown in figure 2. In this research project we hope to obtain detailed electronic information on the active species in order to assign one of these pathways to the reaction.

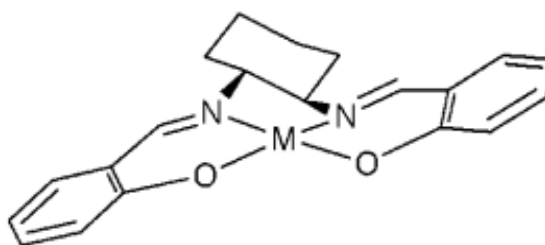


Figure 2 Stepped conformation of metal-salen complexes ⁷

Figure 2 shows the structure of the stepped metal-salen structure as proposed to explain some of the selectivities observed with varying substitution. Houk ¹⁰ proposed a non-planar complex approach along pathway 'd'. An attractive aspect of his analysis was that it unified the explanations of the selectivities given by complexes with different imine bridges.

The study of these metal(salen) mediated epoxidation reactions is becoming increasingly popular^{1b, c, 11} both in terms of determining the mechanistic pathways¹² as well as the practical improvements ¹³. There are a lot of ideas about what is happening at the mechanistic level; multiple pathways have been proposed, the concept of more than one active species taking part and also more than one oxidation process ¹⁴. There is currently no definitive proof either way and different theoretical explanations have been used to explain different data sets and relationships. Hopefully throughout the course of the catalytic study we will reveal information about the active Cr species that will enable us to draw some conclusions about the mechanistic pathway for the Cr system.

6.3 Catalytic studies on Cr(salen) systems (activity and (enantio)selectivity as a function of ligand)

In this study we will investigate Cr(salen) complexes in the asymmetric epoxidation of alkenes. Salen ligands can be easily modified and significant effects of different substituents on the catalytic activity and (enantio) selectivity have been observed ^{4c, 7, 14-15}. The wide range of applications of such an area of the enantioselective catalytic redox processes is obvious because the properties of the metallo-salen complexes make the preparation of a large variety of chiral organometallic reagents possible ¹⁶. The series of salens that have been prepared for this particular study are shown below in figure 3.

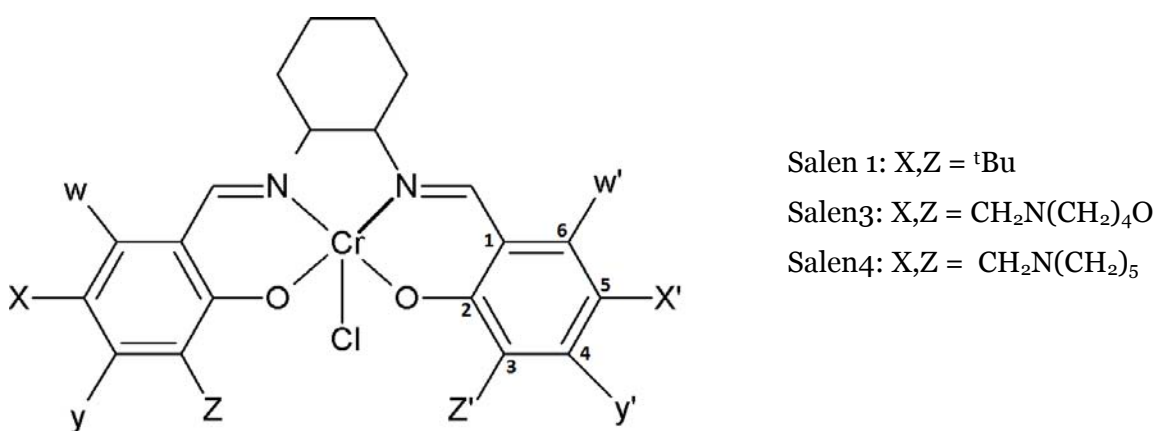


Figure 3 A typical salen template is shown on the left, and the substitutions for the samples studied on the right.

The exact reasons for the different enantioselectivity and activity are not proven, but we hope to provide insights into this with the use of X-ray Absorption and X-ray Emission studies. Catalytic studies have shown that the Cr(III) complexes are very effective catalysts with regard to both reactivity and enantioselectivity. A clear dependence in enantioselectivity is found upon subtle changes in the ligand systems of the chromium complexes (while the direct Cr coordination remains identical). These Cr(salen) systems have shown a contrasting selectivity pattern to their manganese analogues in that they allow the asymmetric epoxidation of *E*-1,2-disubstituted alkene, with iodosylbenzene as a stoichiometric oxidant.

The work by O'Mahony *et al* found that in the stoichiometric asymmetric epoxidation of *E*- β -methylstyrene with chromium-salen oxo complexes, enantioselectivity is increased by halo-substitution at the 3,3'- and 6,6'- positions and decreased at the 4,4'- and 5,5'- positions on the salen rings ⁷. Substituting different groups can have varying effects

depending on which position undergoes substitution. It is thought that the origin of the enantioselectivity is mainly due to $\pi - \pi$ interactions between the ligand and the substrate, causing so-called asymmetric induction ¹⁷.

The work by O'Mahony *et al* ⁷, McGarrigle *et al* ¹⁴ and Venkataramanan *et al* ¹⁸ are other examples of evidence showing that it is necessary to have a substituent in the 3,3'-positions in order to obtain high enantioselectivities. McGarrigle *et al* ¹⁴ observed that the addition of more halo substituents to a 3,3'-halo complex results in a decrease in ee. This is in contrast to the work by Gilheany *et al* ^{4b}. However, after the addition of electron donating groups such as methyl or ethyl the ee also decreases ¹⁴, contrary to what might have been predicted from work on O=Cr(V)(salen) by Rajagopal *et al* ¹⁹. It was also found in this study that the addition of ^tBu groups at the 5,5'-positions on the salen ring leads to ees of up to 90% ¹⁴. The presence of electron withdrawing groups (halogens) is required for reasonable rates in the Cr series.

The optimum substituent for the 3,3'-position and the 5,5'-position is quite different. The effect of the bulky *tert*-butyl group would appear to be (at least partly) of a steric nature ¹⁴. This may take the form of more effective blocking of the alkene trajectory of approach over the 5,5'-positions of the arene ring which otherwise would allow the formation of the disfavoured enantiomer of the epoxide ¹⁴. A similar role has been proposed for the *tert*-butyl group in the 5,5'-positions in Jacobsen's Mn(salen) catalyst, while the effects of methyl groups in the same positions could be fully rationalised in terms of electronic considerations ^{3a, 20}. It is interesting to look at cases where the 3,3'-substituents are different to those at the 5,5'-positions. There was a decrease in ee observed on going from 3,3'-dichloro-substituted complex to 3,3', 5,5'-tetrachloro substituted complex in the work by E. M. McGarrigle *et al* ¹⁴. This decrease could be due to an increase in the reactivity of the complex and an earlier transition state and therefore less selectivity ¹⁴.

There has also been some investigation into the effect of the diamine backbone on the enantioselectivity in the chromium-salen catalysed asymmetric epoxidation ²¹. It was thought that the Cr analogues would show better results than the Mn series due to the fact that the stereoselection obtained using Cr and Mn has been suggested to be related to the non-planarity of the N₂O₂ ligand core of the complex ²². This non-planarity is a result of the sp³ centres on the dimethylene bridge of the ligand. Thus the N-C-C-N dihedral angle is a measure of the resultant twist or step in the complex ²². Chromium salen complexes are thought to facilitate selective epoxidation of *E*-alkenes by their more stepped nature ^{4a, 23}. In this case the methyl groups on the cyclohexane ring, in the place of hydrogens, were

supposed to cause a conformational change (more twist) in the catalyst resulting in a positive effect on the selectivity of the system ²².

There are also associated effects with changing reaction conditions and additives. It has been noted in previous work that the effect of adding Ph₃PO also changes depending on the position of the substituent on the salen ring ⁷. This is in addition to studies that show the change in performance of adding Ph₃PO over other ligands ⁷. The addition of Ph₃PO seems to be most beneficial to stereoselection when X or Z (5,3 position), or both, are substituted.

The effects of L also impact on the degree of non-planarity as well as on the rate of reaction. It was previously thought that the effects of both L and the salen substituents are to cause an increase in non-planarity, with the latter being more effective – hence the ‘ceiling effect’ ⁷. This means that the more enantioselective a system is without the additive ligand, L, the less benefit gained by the addition of L. It is important to note that the preparation of the catalytic complex is also a key issue. In fact (a) using Jacobsen’s methodology *i.e.* starting from CrCl₂, lower levels of enantiomeric excess have been obtained in the catalytic procedure ²⁴; (b) using stoichiometric conditions starting from anhydrous CrCl₂, no reaction between allyl chloride and benzaldehyde was recorded at all and (c) small traces of water completely stop the reaction ¹⁶. Point (a) can be easily explained considering that commercially available CrCl₂ contains water, therefore it is not surprising that (in the light of point (c)) some of the published results collected using the catalyst prepared with the Jacobsen’s protocol were poor.

Although it is difficult to see how variations in conformation can lead to an almost complete loss of selectivity, this means an alternative explanation is required. It could be that there are in fact multiple species present, the work by Kerrigan *et al* have found that the mass spectrometry data of their complexes showed the presence of a substantial amount of species, the masses of which would correspond to dimeric and higher oligomeric complexes. There could be the possibility of dimeric or polymeric contaminants resulting from different metal atoms co-ordinating to the salicylaldiamine moieties ²⁵. In turn these complexes could act as alternative oxidising species in the reaction, potentially lowering the selectivity obtained ²².

Studies using Cr(III) salen complexes derived from *trans*-1,2-dimethyl-1,2-cyclohexanediamine have also shown disappointing results in the stoichiometric asymmetric epoxidation of *E*- and *Z*- β -methylstyrene ²². This was explained by the

presence of multiple oxidants in the system. This hypothesis is supported by recent experimental and theoretical evidence^{12e, 26} which suggests that there are other oxidising species in the reaction in addition to (salen)M(V)=O. It is entirely possible that the addition of electron donating groups to the ligand causes a different oxidation pathway to come in to play; or a different alkene approach trajectory may become competitive since electron donating groups are expected to reduce the reaction rate¹⁴. The observation made with enantioselectivity and solvent also supports multiple pathways being in place²⁷. Evidence has also been found that there may be multiple oxidation pathways in the catalytic mode of Cr(salen) mediated alkene epoxidation^{4c}. Bryliakov *et al* reported evidence that there were two semi-stable oxygen-bearing Cr(salen) species present in solution under catalytic conditions, although they proposed that only one of these species was involved in oxygen transfer to the alkene^{12g}, the presence of two species could make it difficult to analyse the X-ray spectra obtained. Interestingly, Linde *et al* and Adam *et al* have published evidence to support the existence of multiple oxidation pathways in Mn(salen) alkene epoxidation reactions as well^{26a, 26d}. Recently in the manganese series both theoretical and experimental evidence has been reported which suggests that there are other oxidising species in the reaction^{26a-c}. Further theoretical and experimental data is needed on the chromium systems to see if this is indeed the case in the system under investigation in this study.

From this we can see that there is now an increasing amount of evidence for the presence of multiple oxidation pathways for the epoxidation reaction using Cr(salen) complexes. The work by McGarrigle *et al* also uses the theory of multiple oxidation pathways to explain the observation that there was no simple correlation found between the electronic character of the salen substituents and the enantioselectivity¹⁴. Daly *et al*^{4c} also observed a reduced ee and a higher yield in the catalytic mode of Cr(salen) mediated epoxidation of alkenes. They explained this by the possible presence of a second oxidation cycle in which the major oxidant reacts with its reduced form^{4c}.

The key issues that studies of the catalytic reaction cycle need to address are: a) the nature of the oxygen-transfer species; b) the mechanism of oxygen transfer to the organic substrate; c) the highly efficient stereochemical communication between catalyst and substrate; and d) tuning the catalytic activity of the metal-ligand system¹⁸. In summary, it appears that the enantioselectivity in epoxidation using oxo-chromium salen complexes depends on the identity of substituents at all positions on the salen rings. This complex set of relationships must be accommodated by any theory of stereoselection for these types of system⁷.

6.4 *In-situ* characterisation XAS and RIXS

In this part of the project we decided to monitor the stoichiometric epoxidation of *trans*- β -methylstyrene with cationic chromium-salen oxo complexes, as described in the literature ^{7, 14, 22}. For this investigation we mainly focused on salen ligands substituted in the 3,3'- and 5,5'- positions (see figure 1). As we have the opportunity to monitor the stoichiometric variant with the Cr system it is possible to study the stereoselection in the absence of factors related to the catalytic cycle. In this study we have decided to use iodobenzene as the oxidant to form the active Cr(V)=O species. This is because it has been shown to be the most effective oxidant in previous studies ^{4c}, use of bleach as the oxidant (which would be desirable) produced only low selectivity and favoured the opposite enantiomer than with iodobenzene. This along with the fact that the characteristic deep green colour of the iodobenzene derived (salen)Cr(V)=O species is not observed when using bleach, suggests that the bleach and iodobenzene systems follow different pathways ^{4c}. The salen ligands and associated Cr(salen) complexes were synthesised according to literature procedures (see chapter 3). To carry out the *in-situ* studies the catalyst was first pre-formed and filtered to remove excess oxidant, this was then added to an EXAFS cell and the alkene was injected on the beamline. The setup of the cell on the beamline is shown below. These experiments were carried out at room temperature.

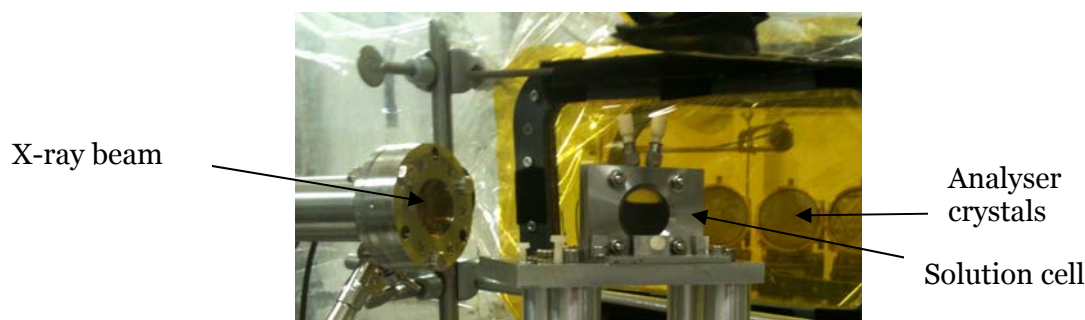
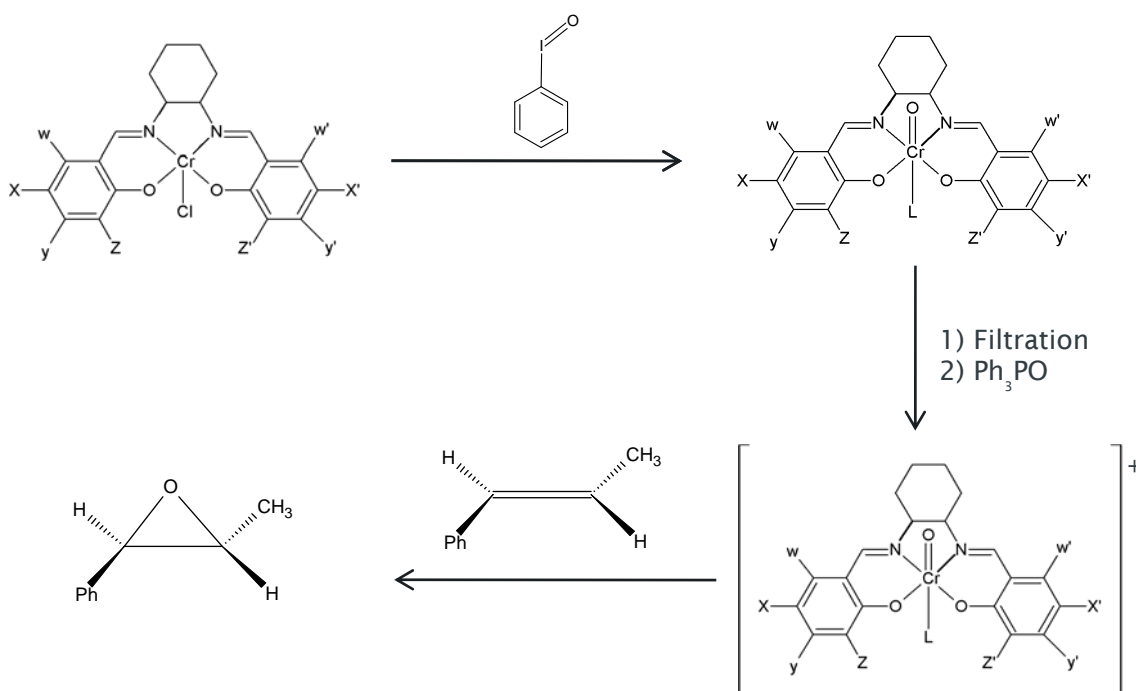


Figure 4 Setup of the cell for the *in-situ* catalysis studies.

Figure 4 shows the cell in the path of the beam, 45° to both the incident beam and the analyser crystals. The position of the sample and the detectors are determined by Rowland geometry ²⁸. The common Rowland geometry uses spherically bent crystals with a suitable Bragg reflection at a specific X-ray emission energy and the X-rays are focussed onto a detector ²⁸.

Table 1 Rates of reaction and substitution for salen 1 with the Ph₃PO additive.

	X,Z Substituents	End of reaction (with Ph ₃ PO)
Salen 1	^t Bu	2hr 56min

**Figure 5** Reaction scheme showing Cr(salen) mediated alkene epoxidation (L=Ph₃PO).

The reaction scheme in figure 5 describes the Cr(salen) mediated alkene epoxidation. The first step of the process is to form the Cr(V)=O species, this is done using iodobenzene as the oxidant. In the mechanism of oxygen transfer, the oxygen-re-bound mechanism suggested by Kochi *et al*²⁹, the metal complex first picks up an oxygen atom from the oxidant (PhIO in our case) and is converted to the oxo-chromium(V) species. This is the catalytically active species that transfers the oxygen to the double bond. This process is repeated with chromium going from the Cr(III) and O=Cr(V) state. For the stoichiometric variant, once we have formed the active Cr(V) species we now need to filter the solution to remove excess iodobenzene (the active species is soluble) to prevent further oxidation. The Ph₃PO ligand is added and then the alkene, resulting in the formation of the epoxide. The epoxide product is soluble and is obtained by removing the solvent *in vacuo* and treating the residue with diethyl ether. The salen complex under study in this chapter is the Cr analogue of Jacobsen's catalyst, the X, Z -di-*tert*-butyl substituted salen ligand.

Both High Energy Resolution Fluorescence Detection X-ray Absorption Near Edge Structure (HERFD XANES) and Resonant Inelastic X-ray Scattering Spectroscopy (RIXS) experiments were carried out on the salen complex in solution, this enabled direct comparison with previously obtained powder HERFD XANES and RIXS. The HERFD XANES of the solutions appeared to be the same as that of powders. At this stage X-ray beam damage tests were performed on the solutions, like the powders they showed no sign of beam damage.

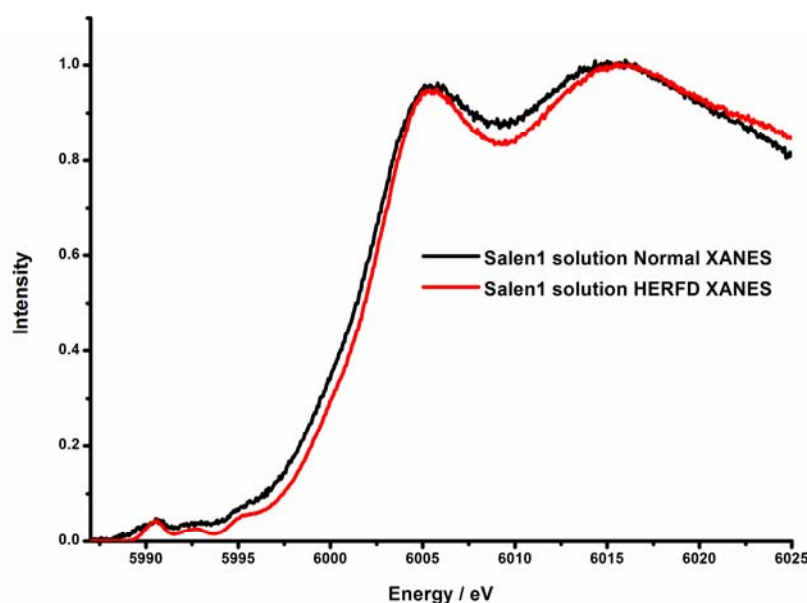


Figure 6 HERFD and normal XANES spectra of salen complex 1 in solution.

Figure 6 shows the normal and HERFD XANES spectra of the Cr(salen1) complex in solution, from this we can clearly see the increase in resolution going from the normal XANES to the high energy resolution fluorescence detection experiment. Although three broad features are visible in the normal XANES at 5991 eV, 5992.5 eV and 5995.5 eV these become much better resolved into distinct peaks in the HERFD spectrum. The normal XANES also displays a higher level of background noise than the HERFD. The main edge for the salen 1 complex is at 6001 eV.

The pre-edge region and the features contained within it, tell us a great deal of information; including an idea about the geometry of the complex. For complexes of lower symmetry there is a greater degree of hybridisation between the p and d or s-orbitals; this mixing of orbitals means that dipole allowed transitions to the p-orbitals contains d-character and this results in intensity in the pre-edge due to this dipole-quadrupole mixing

30. This is demonstrated in chapter 4, where we can clearly see that the tetrahedral complexes contain a great deal more intensity in the pre-edge. The spectra in figure 6 more closely resemble a complex with higher degree of symmetry as there is only a small amount of detail in the pre-edge.

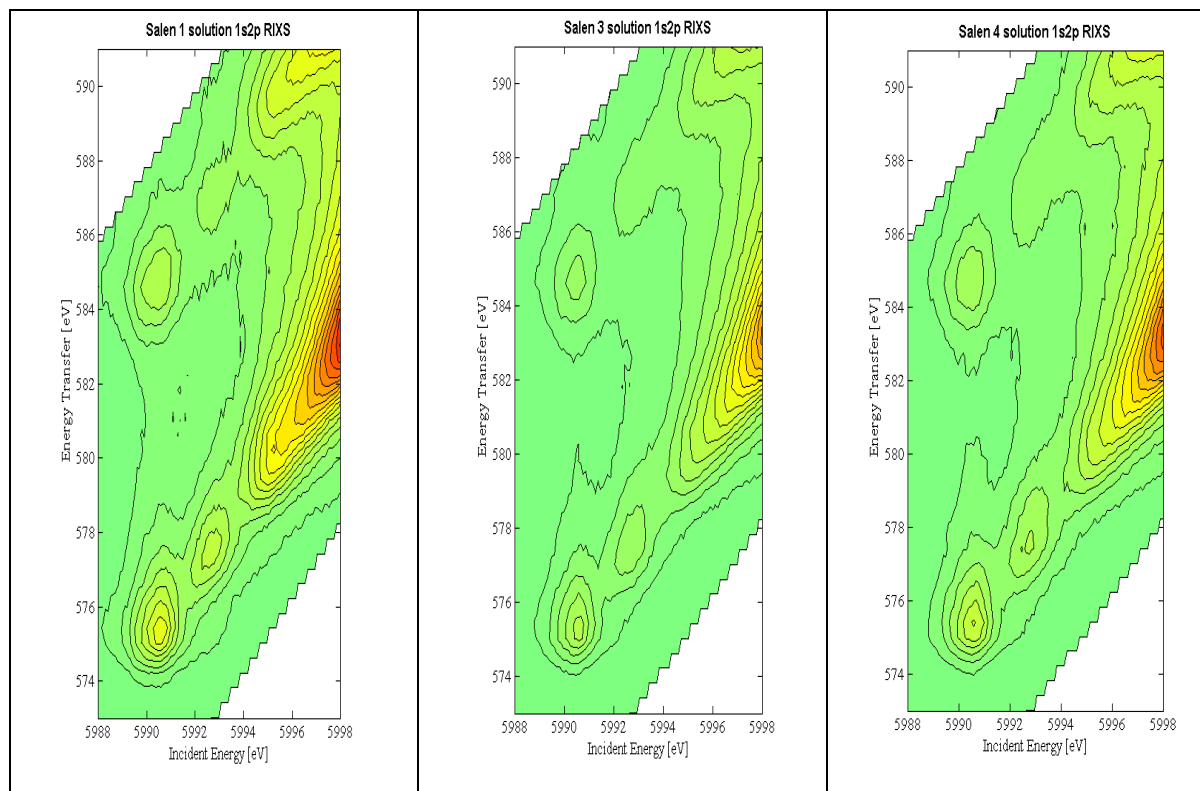


Figure 7 The figure shows a comparison of the 1s2p RIXS spectra of different salen complexes in solution. Cr(salen)1, 3 and 4 from left to right.

Cr(salen) complexes 1, 3 and 4 show very similar features in the pre-edge region of the 2D 1s2p RIXS planes (figure 7). The 1s2p RIXS of the powder samples (chapter 4) and the solutions (figure 7) are the same; this tells us that there are no solvent effects that we have to consider in terms of interpreting the X-ray data. Both of the salen complexes shown above have two pre-edge features along both the $K\alpha_I$ and $K\alpha_{II}$ emission lines; these appear at 5991 eV and 5993 eV Incident Energy (IE) for both complexes. Along the $K\alpha_I$ the first pre-edge feature at 5991 eV appears to be more intense than the second (5993 eV), this can also be seen in the HERFD XANES for the salen complexes in solution. The first feature is spread out over 2 eV; this implies that the peak results from two transitions. The second feature at 5993 eV is less intense and is only spread over 1 eV. The $K\alpha_{II}$ emission line also contains two pre-edge features; these appear at the same IE; 5991 eV and 5993 eV. Both of these pre-edge features are less intense than their $K\alpha_I$ equivalents. Along the $K\alpha_I$ the main edge intensity begins at 5997 eV with the absorption tail stretching towards lower energy. The broadening observed in the diagonal direction of the

experimental spectrum is caused by the experimental broadening. In the Energy Transfer direction (indirect L-edge - see schematic in chapter 2) the splitting between the two features at 575 eV and 585 eV ET relates to the energy difference between the L_3 and L_2 edges in the soft X-ray XAS experiments, as the same final states are probed. In this case the energy difference in the soft X-ray experiments is also approximately 10 eV.

The next stage was to look at the isolated Cr(V)=O species in solution, it was possible to take XANES for all variations of the $(\text{salen})\text{Cr(V)=O}$ complexes, but obtaining full RIXS planes was not possible as we observed changes in the XANES spectra upon beam exposure, i.e. meaning the Cr(V) sample is fairly beam sensitive. The RIXS planes take a lot longer than the HERFD XANES to acquire (For XANES we are able to run quick scans in 30 seconds, a full RIXS plane requires 1.5 hours) and so if the complex is not stable in the beam for long periods of time the species will decompose, this is visible in the shape of the pre-edge region in the XANES as well as the position of the main edge. Figure 8 shows a comparison of the HERFD XANES of the $\text{Cr}(\text{salen})$ complex and the active Cr(V)=O species, where we can clearly see the difference in shape at the pre-edge and the shift in the edge position which is indicative of a change in metal oxidation state.

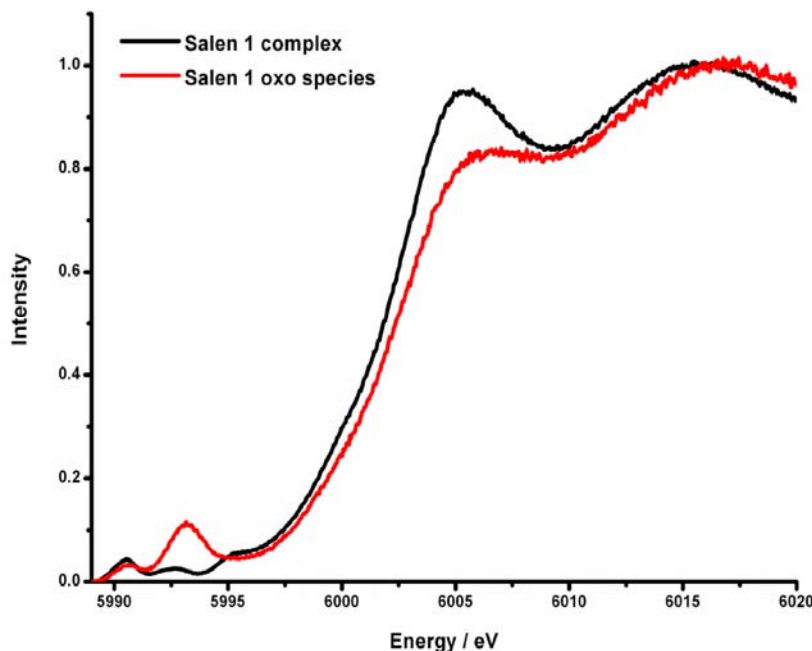


Figure 8 HERFD XANES of $\text{Cr}(\text{salen1})$ complex (black) and the oxidised active species (red) in solution.

The HERFD XANES of the salen complex and the associated active species are shown in figure 8. The XANES spectra clearly show two different Cr species, the change in the pre-

edge and the shift in the edge position are both indicative of a change in oxidation state. This is in agreement with the proposed active species of Cr(V)=O from the Cr(III)(Salen) complex. The HERFD XANES of the starting Cr(III) complex contains three features in the pre-edge region, these occur at 5991 eV, 5992.5 eV and 5995 eV respectively. The main edge appears at 6002 eV. The Cr(V)=O species has two pre-edge features; one at 5991 eV as in the starting complex, and the second at 5993 eV. The main edge in the oxo species is shifted towards higher energy and appears at 5993 eV. In the pre-edge region of the active species the second pre-edge feature at 5993 eV is the most intense meaning that there are a larger proportion of transitions to that particular final state. The density of states plot for Cr(salen1) in chapter 5 shows orbital contributions from N p, O p, O s, C p and Cr s density of states in that region. There is no Cr p contribution in this region (in the calculated spectra) and so no feature in the calculated XANES, there is however a small feature in the experimental Cr(salen1) and the larger peak in the oxo-complex that is slightly shifted from the calculation. It could be that the structure used in the FEFF calculation is not accurate enough to reproduce the relative peak positions or all of the density of states and that the second peak is a result of the bonding interaction between Cr, N and O atoms. This then means that a conformational change on forming the active species leads to Cr p-orbitals being in a different orientation and so allowing mixing with the orbitals seen in the density of states. Without a full and accurate structure determination of the salen 1 complex and the oxo-species it is difficult to fully assign the origin of these peaks. Although the Cr(V)=O species was stable in the beam long enough to obtain XANES spectra we were unable to obtain the full RIXS planes.

The observed shift of the edge towards higher energy would could be explained by the change in oxidation state going from a Cr(III) complex to a Cr(V) complex. The absolute position of the X-ray absorption edge is dependent on the energy difference between the initial state and the final state. The trend of an increase in edge shift with an increase in oxidation trend is followed by most transition metal systems, when the final state is localised on the ligand. Normally the increase in the coulomb potential with an increase in oxidation state is felt mainly by the metal valence orbitals ³¹. With the final state focused on the ligand this is no longer the case. The interesting observation with the shape of the pre-edge is that normally in a spectrum with a relatively clear pre-edge we would expect a complex of higher symmetry, as the degree of orbital mixing in a higher order complex would lead to less intensity in the pre-edge compared to a complex with lower symmetry. Although the symmetry will have changed going from a five coordinate to a six coordinate species, it will not be as high as octahedral.

In the next part of the investigation the catalysis was monitored *in-situ* by running quick 60 second HERFD scans over the first 20 minutes of the reaction and then longer 120 second HERFD at intervals of 5 minutes for the remainder of the reaction cycle. The first XANES scan of the reaction looked comparable to the isolated Cr(V) oxo species; from this we made the assumption that the six minute delay from adding the alkene in the lab to recording the X-ray spectra did not cause us to miss any significant changes in the complex structure.

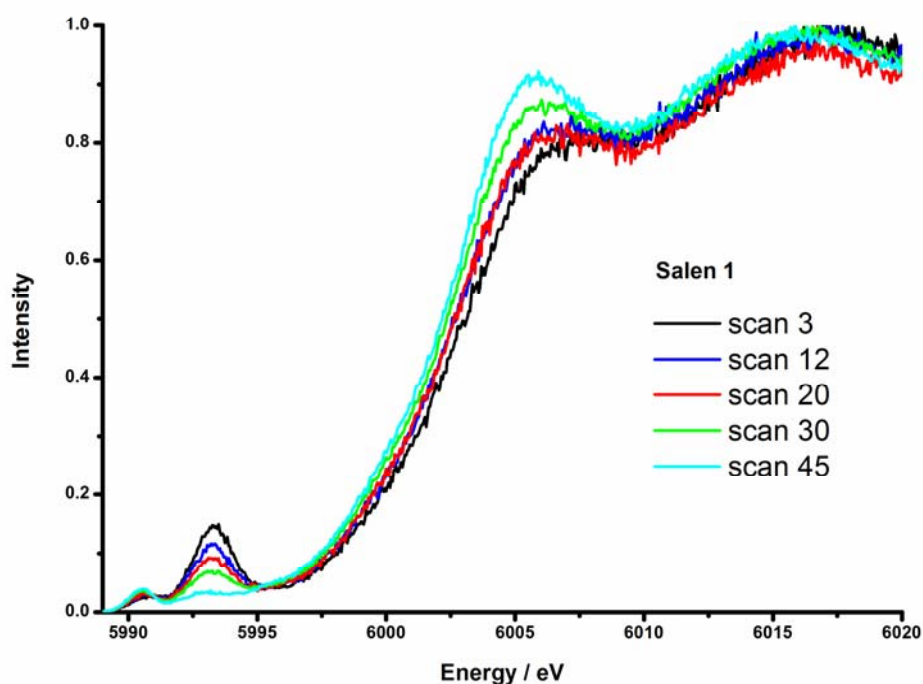


Figure 9 Continuous *in-situ* HERFD XANES during the Cr(salen) mediated alkene epoxidation with *trans*- β -methyl styrene.

Figure 9 shows the progress of the alkene epoxidation monitored *in-situ* with HERFD XANES scans. The initial XANES scan (with the most intense second pre-edge feature) looks the same as the XANES of the active species; this means that we did not miss the start of the reaction. As the reaction progresses we can see that the intensity of the second pre-edge feature (at 5993 eV) decreases. This would tie in with the active species being consumed in the reaction producing a Cr species with a different oxidation state. On first observation it may appear that the final XANES spectra resembles that of the starting complex, but when we directly compare the XANES we can see that we end up with a slightly different species to that which we started with, so we can deduce that the catalyst is possibly not completely re-generated in the reaction.

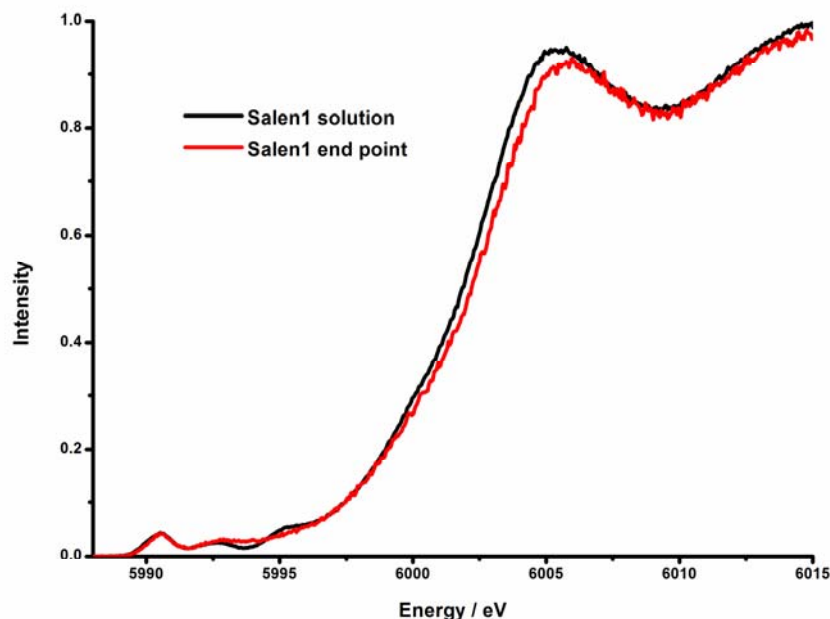


Figure 10 HERFD XANES spectra of salen complex 1 in solution and the end species after the epoxidation reaction.

The figure above shows the HERFD XANES spectra of the starting Cr(III)(salen1) complex in solution compared to the resulting end species after the alkene epoxidation reaction has taken place. As we can see from the spectra the two species appear similar. The first pre-edge feature at 5991 eV is present in both the Cr species, as well as the second pre-edge feature at 5993 eV, although in the end point this feature trails off rather than returning towards the base line. The rest of the pre-edge for the end point is clear and the main edge occurs at 6002 eV. For the starting complex in solution, the second feature at 5993 eV is a more defined peak and then there is also a third peak at 5995 eV. The edge position for the end point is slightly shifted towards higher energy; this is normally associated with an increase in oxidation state (see chapter 4). As the shift is only very small, this could be a mix of species (Cr(III) and Cr(V)) or just a distorted geometry of the original Cr(III). It would be helpful to compare with a Cr(IV) spectrum to see if there is a mixture of states present, unfortunately we did not measure a Cr(IV) sample.

The same pattern was observed for all complexes, with an edge shift and change in the pre-edge features showing the decline of the peak characteristic of the Cr(V)=O species. The reactions were also carried out *ex-situ* (out of the beam) so that any beam damage occurring in the *in-situ* reactions would be highlighted. Both HERFD XANES and RIXS were carried out on the resulting end species (figures 11 and 12).

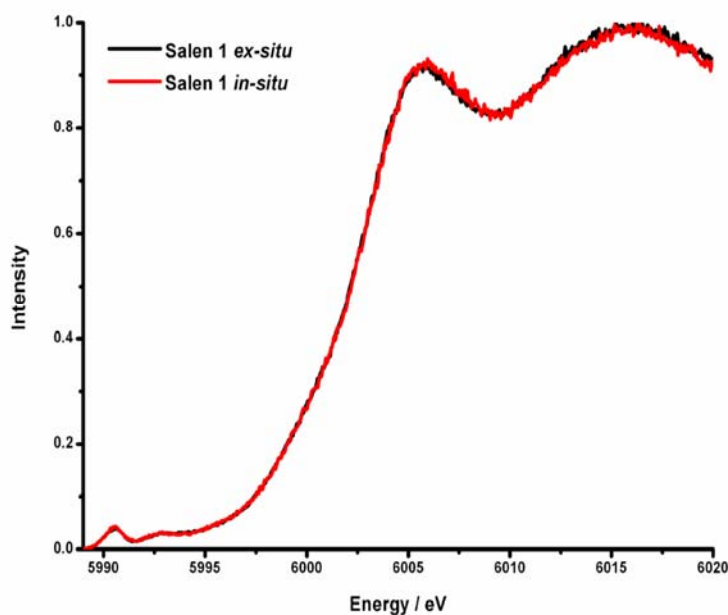


Figure 11 HERFD XANES of the Cr end species after epoxidation *in-situ* (red) and *ex-situ* (black).

As we can see from figure 11 the end species is the same after both the *in-situ* (in the X-ray beam) and the *ex-situ* reactions, meaning that the reaction pathway and intermediates were not affected by the beam. Compared to the starting Cr(V) complex, the second pre-edge feature has almost completely disappeared, however the first peak at 5991 eV remains unchanged by the reaction. This means that the transitions forming this peak are still allowed by the geometry of the end species. There are references to say that the geometry of these complexes is C_2 ³² and others that say square pyramidal³³ or square planar for the starting and oxo species¹⁶, these geometries are lower in symmetry octahedral and do not contain inversion symmetry, however we still see a relatively clear pre-edge. A detailed structural determination of the oxo species is required.

We also performed 1s2p RIXS experiments on both the end species from the *in-situ* and *ex-situ* catalytic runs, these were compared with the initial starting Cr(III)(salen) complex. The resulting RIXS spectra are shown below in figure 12.

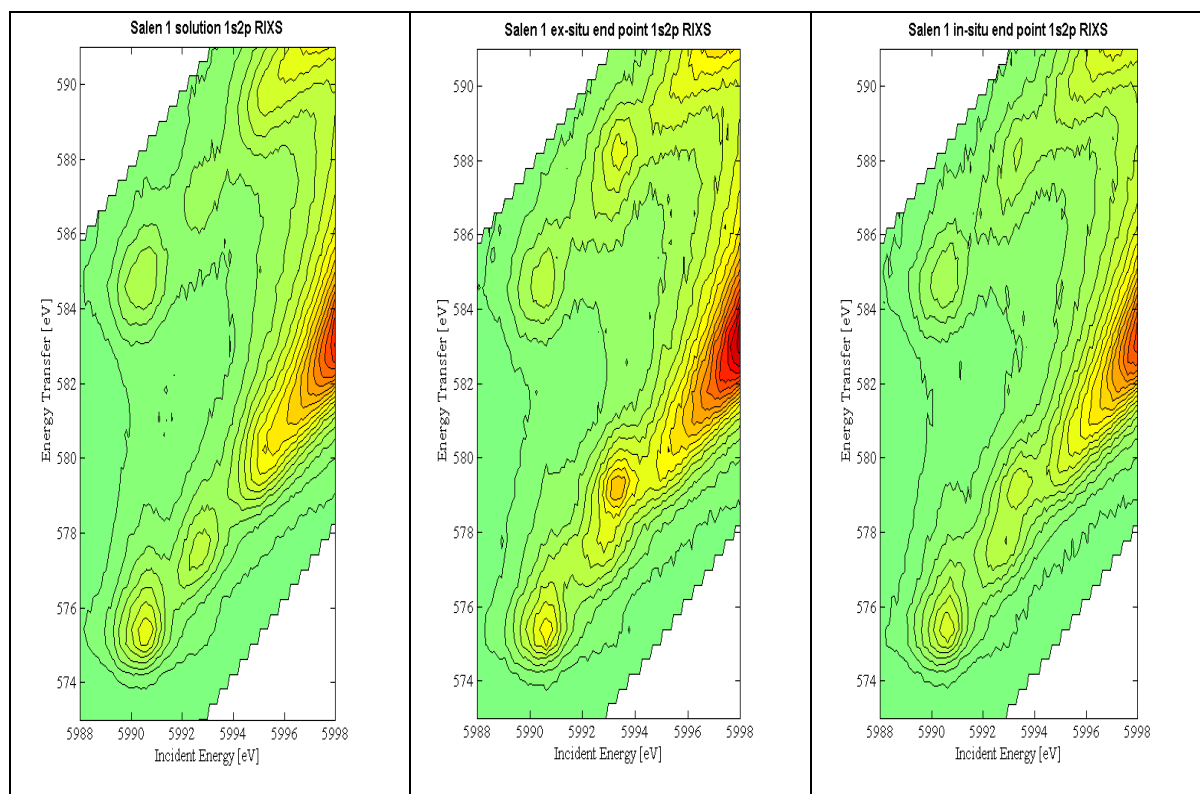


Figure 12 **1s2p RIXS of the starting complex and the *in-situ* and *ex-situ* end species.**

The 2D RIXS planes in figure 12 show the pre-edge regions of the complex in solution compared to the end points. All of the spectra above are very similar to the RIXS spectra of the Cr(III) salen samples, in the case of the end-species we see the appearance of one additional feature. The two spectra for the end points (*in-situ* and *ex-situ*) show the same pattern of features. The pre-edge region for the end points contain three features; one at 5991 eV (575 eV ET), 5993 eV (577.5 eV ET) and 5993.5 eV (579 eV ET). As with the other 1s2p RIXS there is an absorption tail leading back from the main edge, caused by the experimental broadening. The intensity of the additional feature does appear to be slightly reduced in the *in-situ* reaction, this could be an experimental factor though or a result of delay in measuring the *ex-situ* reaction. The feature at 5993.5 eV (579 eV ET) is an additional peak, compared to the complex in solution, that appears off the diagonal line in the RIXS plot for the end species. This off-diagonal peak appears at 5993.5 eV Incident Energy and 579 eV Energy Transfer, the feature stretches over 1 eV, suggesting that it is caused by only one transition. There are no additional features that line up with this additional peak in the vertical direction, which makes this an interesting feature. This is because we would normally expect to see two peaks in the vertical direction split by the core hole spin orbit coupling ³⁴.

We were unable to obtain RIXS spectra for the Cr(V) species as it was not stable in the beam for long enough to run the experiment, as of yet no spectra for Cr(IV) or Cr(V) RIXS have been found in literature to compare with this experiment to identify whether the spectra is formed from mixed oxidation states. The peak is not present in the starting Cr(III) complex and comparing to the RIXS of the references we can see that a peak from Cr(III) in Cr₂O₃ appears at 5994 eV incident energy and 578.5 eV energy transfer. For Cr(VI) in CrO₃ a peak appears at 5994 eV incident energy and 579 eV energy transfer. These both show peaks in a similar position to the additional peak but we still have the problem that there is no extra peak in the vertical direction of the RIXS plane. We also wouldn't necessarily be expecting to see a Cr⁶⁺ species in the reaction mixture. As there have been studies suggesting a Cr(IV) species at the end of the reaction it would be extremely helpful to compare to the RIXS of Cr(IV) to see whether there is Cr(IV) character present in the final species. Having Cr(III) present is also expected, the change in features compared to the starting complex could be due to some distortions in the geometry of the complex but we would expect to see another feature in the vertical direction (L-edge).

One possibility is that this peak could be a non-local peak formed due to the presence of a neighbouring Cr atom bonded through an oxygen atom ((IV)Cr-O-Cr(IV)). This has been suggested to be the catalyst sink in the manganese series³⁵. The pre-edge region is a mixture of dipole and quadrupole transitions that is difficult to unravel. Transitions to a valence orbital, that is formed between neighbouring metal atoms, have been referred to as non-local excitations³⁶. In oxides this non-local effect arises from weak 1s→3d transitions to off-site metal 3d states^{36b}, this transition is made possible by the presence of O 2p states (this could be possible with a bridged dimer). The O 2p states of the oxygen atom hybridise with 3d-orbitals of neighbouring Cr atoms, allowing off-site dipolar 1s→3d transitions^{36a} through 4p-O-3d intersite hybridisation³⁷. These local and non-local 1s3d transitions are separated in XAS due to the fact that the core hole screening will be different in both cases³⁷. The absorption spectrum is relatively clear for our end species but this is also observed for non-local peaks in literature^{36a}. The understanding of the interactions between p and d-orbitals of neighbouring metal atoms is not completely understood. This hybridisation is expected by symmetry and band structure theories^{36b} and can be predicted by density of states calculations³⁷⁻³⁸. With an accurate model of the salen species FEFF 9 should be able to reveal overlap of neighbouring Cr orbitals. Applying these methods to our systems may show whether the additional peak is predicted and indeed due to neighbouring metal atoms.

Table 2 Rates of reaction for salen 1 with and without the Ph₃PO additive.

	End of reaction (with Ph ₃ PO)	End of reaction (without Ph ₃ PO)
Salen 1	2hr 56min	2hr 10min

We only have data from *in-situ* stoichiometric XAS/XES studies of alkene epoxidation for one type of salen structure. At this stage therefore, we are unable to compare the effects of different ligand substitution on the structure of the active species, other intermediates that may or may not be present or the reaction pathway. As different reaction pathways and/or oxidised species have been proposed for different substitutions, this would be something that would need to be examined in more detail to ascertain whether, or not, multiple species and pathways are in play. This data was obtained on the last synchrotron trip of the project, this leaves an area open for development in subsequent studies. We see interesting features in the spectra for the di-tert-butyl substituted ligand; further studies are needed to see how this changes on substitution and how that explains the different catalytic effects in literature.

6.4 Conclusions

It has been observed in literature that the catalytic system with Cr results in a lower ee, this could be indicative of the presence of more than one oxidising species in solution ^{4c}, this is mentioned above in the introduction and has gained support from other authors. An alternative proposal is that a dimer is formed between two metal species to form a μ -oxo Cr(IV) dimer ^{35, 39}. This was also a reason for the assumption that the additional peak in the X-ray spectra was from a non-local Cr atom. A similar μ -oxo Mn(IV) dimer has been postulated to be in equilibrium with (salen)Mn(V)=O in the catalytic manganese system²⁹. The formation of the μ -oxo Cr(IV) dimer does not result in the production of the epoxide, or regeneration of the active species ^{4c} and therefore is a sink for the (salen)Cr(V)=O rather than as a reservoir as in the manganese based system ^{4c}; for this reason low yields are not unexpected in the stoichiometric mode ^{4c, 12g}. The work by Bryliakov *et al* has shown evidence of the presence of two discrete (salen)Cr-oxo species starting from Cr(salen)Cl complexes and iodosylbenzene, these are the monomeric (salen)Cr(V)=O species and a dimeric mixed valent Cr(III)Cr(V)-oxo species. They proposed that only the former species was acting as an oxidant under their conditions, while the latter species acted as a reservoir for the catalyst ^{12g}.

The structural relationship between the Cr(V) complex and its chromium(III) precursor has been noted in literature. There are conflicting references to the point group of the complex; some studies show that in each complex the metal shows a square planar coordination geometry, but the presence of the oxygen in the Cr(V) system displaces the metal by 0.5 Å above the salen ligand ¹⁶. From the X-ray absorption and emission data we can see that the structure of the pre-edge implies a complex with relatively high symmetry (higher than tetrahedral), with just a few small pre-edge features present. Comparing the starting complex and the active species we can see that there is not a huge difference in the XANES, not enough to imply significant changes to the geometry. The increase in the peak at 5993 eV can be explained by distortion effects causing more overlap with Cr p density of states. The XANES spectrum of the end species is also very similar in shape to that of the complex in solution, this implies no change in oxidation state or geometry and that a Cr(III) complex is reformed at the end of the reaction. It is only when we look at the 2D RIXS planes that we see the appearance of the additional peak.

Currently the most promising explanation for this peak is that it is a non-local peak formed from intersite transitions of neighbouring Cr p-orbitals through hybridisation with O 2p-orbitals. This supports the theory that an oxygen bridged dimer is formed at the end of the reaction, or exists as a reservoir in the reaction, but without comparing to the HERFD XANES of a Cr(IV) species it is difficult to draw firm conclusions on the oxidation state. The fact that the spectrum looks a lot like the Cr(III) complex and the active species supports the suggestion that there could be a dimer formed from mixed oxidation states as proposed by Bryliakov *et al* ^{12g}.

In order to conclusively reveal the structure of the active species and the oxidation pathway in operation in this reaction we would need to further optimise the theoretical modelling of the data obtained. For accurate FEFF calculations a crystal structure of the end species is necessary to calculate the density of states and to identify any neighbouring Cr d density of states that mix with O p (and Cr p). Alternatively it has been observed that band structure calculations are also successful in reproducing the non-local peak, these methods could be applied to the data obtained in this study. This would provide further insights into the structure of the species present and the electronic transitions occurring. At present the capabilities are there to perform these kinds of studies but unfortunately this did not fall within this period of research.

6.5 References

- (a) Johnson, R. A.; Sharpless, K. B., 2nd Edition ed.; Wiley-VCH: New York, 2000; (b) Katsuki, T., In *Catalytic Asymmetric Synthesis*, 2nd ed.; Ojima, I., Ed. Wiley-VCH: New York, 2000; pp 287; (c) Jacobsen, E. N.; Pfaltz, A.; Yamamoto, H., In *Comprehensive Asymmetric Catalysis*, Springer-Verlag: Berlin, 1999; pp 649.
- Samsel, E. G.; Srinivasan, K.; Kochi, J. K., *J. Am. Chem. Soc.* **1985**, *107*, 7606.
- (a) Jacobsen, E. N.; Zhang, W.; Muci, A. R.; Ecker, J. R.; Deng, L., *J. Am. Chem. Soc.* **1991**, *113*, 7063; (b) Takeda, T.; Irie, R.; Shinoda, Y.; Katsuki, T., *Synlett* **1999**, 1999, 1157.
- (a) Dalton, C.; Ryan, K.; Wall, V.; Bousquet, C.; Gilheany, D., *Top. Catal.* **1998**, *5*, 75; (b) Bousquet, C.; Gilheany, D. G., *Tetrahedron Lett.* **1995**, *36*, 7739; (c) Daly, A. M.; Renehan, M. F.; Gilheany, D. G., *Org. Lett.* **2001**, *3*, 663.
- (a) Collman, J.; Zhang, X.; Lee, V.; Uffelman, E.; Brauman, J., *Science* **1993**, *261*, 1404; (b) Jacobsen, E. N., In *Catalytic Asymmetric synthesis*, Ojima, I., Ed. Wiley: New York, 1993; pp 159; (c) Hamada, T.; Irie, R.; Katsuki, T., *Synlett* **1994**, 479; (d) Chang, S.; Galvin, J. M.; Jacobsen, E. N., *J. Am. Chem. Soc.* **1994**, *116*, 6937.
- (a) Groves, J. T.; Nemo, T. E.; Myers, R. S., *J. Am. Chem. Soc.* **1979**, *101*, 1032; (b) Groves, J. T.; Myers, R. S., *J. Am. Chem. Soc.* **1983**, *105*, 5791; (c) Groves, J. T.; Han, Y.; Van Engen, D., *J. Chem. Soc., Chem. Commun.* **1990**, 436.
- O'Mahony, C. P.; McGarrigle, E. M.; Renehan, M. F.; Ryan, K. M.; Kerrigan, N. J.; Bousquet, C.; Gilheany, D. G., *Org. Lett.* **2001**, *3*, 3435.
- (a) Norrby, P.-O.; Linde, C.; Aakermark, B., *J. Am. Chem. Soc.* **1995**, *117*, 11035; (b) Hamada, T.; Fukuda, T.; Imanishi, H.; Katsuki, T., *Tetrahedron* **1996**, *52*, 515; (c) Hashihayata, T.; Ito, Y.; Katsuki, T., *Synlett* **1996**, 1079; (d) Miura, K.; Katsuki, T., *Synlett* **1999**, *6*, 783; (e) Hashihayata, T.; Ito, Y.; Katsuki, T., *Tetrahedron* **1997**, *53*, 9541.
- Hosoya, N.; Hatayama, A.; Yanai, K.; Fujii, H.; Irie, R.; Katsuki, T., *Synlett* **1993**, 641.
- Houk, K. N.; DeMello, N. C.; Condroski, K.; Fennen, J.; Kasuga, T. Electronic Conference on Heterocyclic Chemistry '96, ECHET96, Rzepa, H. S., Snyder, J., and Leach, C. (Eds), Ed. Royal Society of Chemistry: 1996.
- Katsuki, T., *Synlett* **2003**, 281.
- (a) Abashkin, Y. G.; Burt, S. K., *Org. Lett.* **2003**, *6*, 59; (b) Cavallo, L.; Jacobsen, H., *J. Org. Chem.* **2003**, *68*, 6202; (c) Cavallo, L.; Jacobsen, H., *Eur. J. Inorg. Chem.* **2003**, 892; (d) Ivanic, J., *J. Chem. Phys.* **2003**, *119*, 9377; (e) Khavrutskii, I. V.; Musaev, D. G.; Morokuma, K., *Inorg. Chem.* **2003**, *42*, 2606; (f) Feth, M. P.; Bolm, C.; Hildebrand, J. P.; Köhler, M.; Beckmann, O.; Bauer, M.; Ramamonjisoa, R.; Bertagnolli, H., *Chem. Eur. J.* **2003**, *9*, 1348; (g) Bryliakov, K. P.; Talsi, E. P., *Inorg. Chem.* **2003**, *42*, 7258.
- (a) Kureshy, R. I.; Khan, N. H.; Abdi, S. H. R.; Ahmad, I.; Singh, S.; Jasra, R. V., *J. Catal.* **2004**, *221*, 234; (b) Kureshy, R. I.; Khan, N. H.; Abdi, S. H. R.; Ahmed, I.; Singh, S.; Jasra, R. V., *J. Mol. Catal. A: Chem.* **2003**, *203*, 69; (c) Kureshy, R. I.; Khan, N. H.; Abdi, S. H. R.; Singh, S.; Ahmed, I.; Shukla, R. S.; Jasra, R. V., *J. Catal.* **2003**, *219*, 1; (d) Sellner, H.; Karjalainen, J. K.; Seebach, D., *Chem. Eur. J.* **2001**, *7*, 2873; (e) Leadbeater, N. E.; Marco, M., *Chem. Rev.* **2002**, *102*, 3217; (f) McNamara, C. A.; Dixon, M. J.; Bradley, M., *Chem. Rev.* **2002**, *102*, 3275; (g) Prasad, J. S.; Vu, T.; Tottleben, M. J.; Crispino, G. A.; Kacsur, D. J.; Swaminathan, S.; Thornton, J. E.; Fritz, A.; Singh, A. K., *Org. Process. Res. Dev.* **2003**, *7*, 821; (h) Lane, B. S.; Burgess, K., *Chem. Rev.* **2003**, *103*, 2457; (i) Bräse, S.; Lauterwasser, F.; Ziegert, R. E., *Adv. Synth. Catal.* **2003**, *345*, 869.
- McGarrigle, E. M.; Murphy, D. M.; Gilheany, D. G., *Tetrahedron: Asymmetry* **2004**, *15*, 1343.

15. (a) Daly, A. M.; Cormac, D. T.; Renehan, M. F.; Gilheany, D. G., *Tetrahedron Lett.* **1999**, *40*, 3617; (b) Dalton, C. T.; Ryan, K. M.; Langan, I. J.; Coyne, E. J.; Gilheany, D. G., *J. Mol. Catal. A: Chem.* **2002**, *187*, 179.
16. Bandini, M.; Cozzi, P. G.; Umani-Ronchi, A., *Chem. Commun.* **2002**, 919.
17. Arends, I. W. C. E., *Angew. Chem. Int. Ed.* **2006**, *45*, 6250.
18. Venkataramanan, N. S.; Kuppuraj, G.; Rajagopal, S., *Coord. Chem. Rev.* **2005**, *249*, 1249.
19. Venkataramanan, N. S.; Prem Singh, S.; Rajagopal, S.; Pitchumani, K., *J. Org. Chem.* **2003**, *68*, 7460.
20. Palucki, M.; Finney, N. S.; Pospisil, P. J.; Güler, M. L.; Ishida, T.; Jacobsen, E. N., *J. Am. Chem. Soc.* **1998**, *120*, 948.
21. Daly, A. M.; Gilheany, D. G., *Tetrahedron: Asymmetry* **2003**, *14*, 127.
22. Kerrigan, N. J.; Müller-Bunz, H.; Gilheany, D. G., *J. Mol. Catal. A: Chem.* **2005**, *227*, 163.
23. Brandt, P.; Norrby, P.-O.; Daly, A. M.; Gilheany, D. G., *Chem. Eur. J.* **2002**, *8*, 4299.
24. Jacobsen, E. N.; Schaus, S. E.; Dossetter, A. G.; Jamison, T. F. US 6,211,370 2001.
25. (a) Kerr, J. M.; Suckling, C. J.; Bamfield, P., *J. Chem. Soc., Perkin Trans. 1* **1990**, 887; (b) Larson, E. J.; Pecoraro, V. L., *J. Am. Chem. Soc.* **1991**, *113*, 3810.
26. (a) Adam, W.; Roschmann, K. J.; Saha-Möller, C. R.; Seebach, D., *J. Am. Chem. Soc.* **2002**, *124*, 5068; (b) Collman, J. P.; Zeng, L.; Brauman, J. I., *Inorg. Chem.* **2004**, *43*, 2672; (c) Bryliakov, K. P.; Kholdeeva, O. A.; Vanina, M. P.; Talsi, E. P., *J. Mol. Catal. A: Chem.* **2002**, *178*, 47; (d) Linde, C.; Koliaï, N.; Norrby, P.-O.; Åkermark, B., *Chem. Eur. J.* **2002**, *8*, 2568; (e) Cavallo, L.; Jacobsen, H., *Inorg. Chem.* **2004**, *43*, 2175; (f) Khavrutskii, I. V.; Musaev, D. G.; Morokuma, K., *J. Am. Chem. Soc.* **2003**, *125*, 13879.
27. Imanishi, H.; Katsuki, T., *Tetrahedron Lett.* **1997**, *38*, 251.
28. Glatzel, P.; Sikora, M.; Smolentsev, G.; Fernández-García, M., *Catal. Today* **2009**, *145*, 294.
29. Srinivasan, K.; Michaud, P.; Kochi, J. K., *J. Am. Chem. Soc.* **1986**, *108*, 2309.
30. (a) Westre, T. E.; Kennepohl, P.; DeWitt, J. G.; Hedman, B.; Hodgson, K. O.; Solomon, E. I., *J. Am. Chem. Soc.* **1997**, *119*, 6297; (b) DeBeer George, S.; Brant, P.; Solomon, E. I., *J. Am. Chem. Soc.* **2004**, *127*, 667.
31. Tromp, M.; van Bokhoven, J. A.; van Strijdonck, G. P. F.; van Leeuwen, P. W. N. M.; Koningsberger, D. C.; Ramaker, D. E., *J. Am. Chem. Soc.* **2004**, *127*, 777.
32. Xia, Q. H.; Ge, H. Q.; Ye, C. P.; Liu, Z. M.; Su, K. X., *Chem. Rev.* **2005**, *105*, 1603.
33. Cozzi, P. G., *Chem. Soc. Rev.* **2004**, *33*, 410.
34. de Groot, F. M. F.; Kotani, A., In *Core Level Spectroscopy of Solids*, CRC Press: 2008; pp 11.
35. Woo, L. K., *Chem. Rev.* **1993**, *93*, 1125.
36. (a) Shukla, A.; Calandra, M.; Taguchi, M.; Kotani, A.; Vanko, G.; Cheong, S. W., *Phys. Rev. Lett.* **2006**, *96*, 077006; (b) Vankó, G.; de Groot, F.; Huotari, S.; Cava, R. J.; Lorenz, T.; Reuther, M., *arXiv:0802.2744v1* **2008**.
37. Joly, Y.; Cabaret, D.; Renevier, H.; Natoli, C. R., *Phys. Rev. Lett.* **1999**, *82*, 2398.
38. Elfimov, I. S.; Anisimov, V. I.; Sawatzky, G. A., *Phys. Rev. Lett.* **1999**, *82*, 4264.
39. Kerrigan, N. J.; Langan, I. J.; Dalton, C. T.; Daly, A. M.; Bousquet, C.; Gilheany, D. G., *Tetrahedron Lett.* **2002**, *43*, 2107.

Chapter Seven: Conclusions and Future Recommendations

7.1 Introduction

Throughout the course of this project the aim was to develop the relatively new X-ray technique, Resonant Inelastic X-ray Scattering spectroscopy (RIXS), as a tool in catalysis providing more insights into electronic properties and related performance. This started with the testing of a series of well known chromium reference materials (oxides and chlorides) with a range of X-ray absorption and emission experiments. The next step of the project was to apply these X-ray techniques, and the data obtained from the reference study, to a more complicated family of chromium materials; the Cr(salen) catalysts. A combination of the observations from the references and detailed theoretical calculations subsequently allowed the in-depth analysis of the electronic structure of the salen complexes as a function of ligand substitution, as well as providing preliminary insights in reaction intermediates in the Cr catalysed epoxidation reaction.

7.2 Experiment versus Theory

7.2.1 K-edge XAS

The Cr K-edge XANES experimental spectra for the reference materials studied in chapter 4 are well reproduced using the FEFF9 package. The FEFF package is an automated program for *ab initio* multiple scattering calculations of X-ray Absorption Fine Structure, X-ray Absorption Near-Edge Structure (XANES), X-ray Emission spectroscopy and various other spectra for clusters of atoms. The FEFF calculations rely on the use of basic and established principles without the inclusion of extra assumptions, a 3D input structure is necessary so a proposed structure of the material is required. It also involves the simultaneous calculation of excitation spectra and electronic structure (density of states).

In most cases the calculations shown in chapter 4 accurately reproduce the structure of the pre-edge as well as the position and shape of the main absorption edge. In other cases it has been more difficult to exactly replicate the position and intensity of all the features but the number and shape are correct. For example the simulation of Cr₂O₃ in figure 3 (chapter 4) does show the correct number of pre-edge features; however these are slightly distorted from the experimental spectra. The pre-edge features in the calculation appear

sharper than in the experiment. Obviously experimental broadening can be included in the calculation but it is hard to optimise this without losing all of the structure underneath for the calculation. Materials, such as $\text{Cr}(\text{CO})_6$ are more complicated as FEFF does not always reproduce charge redistributions and π -systems in materials well, FEFF does not include multiplets either. Oxides and chlorides are normally easier to simulate but when organometallic systems are considered it becomes more difficult. The spectrum for $\text{Cr}(\text{CO})_6$ shows a large number of features in a narrow energy region of the pre-edge. Again the optimised calculation does show higher resolution of some of the features but the complicated topography remains in the calculation.

By looking at the XANES and empty density of states calculations it is possible to determine the orbitals involved in the transitions forming the pre-edge features. Figure 6 (chapter 4) shows the Cr p density of states that form the K pre-edge, any orbitals that mix with Cr p-orbitals will also appear in the XANES. The other orbital contributions are Cr 1s, Cr d and ligand 2p-orbitals that form a bonding interaction with Cr p-orbitals. In the case of the dichromates the additional feature on the low energy side of the first pre-edge peak shows contributions from Os, K s and O p-orbitals. The presence of features in the pre-edge region is due to hybridisation with Cr p density of states. In complexes of lower symmetry quadrupole transitions become dipole allowed due to Cr p and d-orbitals hybridisation. This degree of orbital hybridisation is more pronounced in structures without inversion symmetry. This means the dipole and quadrupole transitions reach the same final states, and so their peaks are visible at the same energy, as shown in the empty density of states. In the case of the references we already know their structure and geometry so this is a case of finding out which electronic information can be obtained from the technique. These observations mean that we can gain a fairly detailed understanding of the electronic structure and geometry of an unknown. This is more useful when studying increasingly complex catalysts systems.

Chapter 5 contains the study of the Cr(salen) materials with the same X-ray techniques. The salen materials are all the same oxidation state and geometry so there are not many differences in the XANES to observe and compare. Any electronic effects should be visible in the XANES region but only if they coincide with the Cr p density of states. We can however compare these spectra to those of the other Cr(III) samples and see how the spectra differ. The pre-edge region of the salen materials is relatively clear when comparing to the tetrahedral Cr reference compounds. For complexes of lower symmetry there is a greater degree of hybridisation between p and d-orbitals. This mixing of d-orbitals with p-orbitals means that dipole allowed transitions to the p-orbitals contains d

character and so are also visible in the pre-edge. In this way we can gain insights into the geometry when visibly inspecting the XANES spectra. The more structure in the pre-edge the lower the symmetry. Any electronic effects that are not visible in the XANES (do not overlap with Cr p-orbitals) may become apparent in the 2p XAS due to influence on the charge redistribution between states.

The salen materials may in fact be more complicated to analyse by K-edge XANES at this stage due to the distance of the substituents on the salen framework from the central Cr. Although the substitutions happen on the salen framework rather than at the Cr itself, any charge transfer through the system will affect the chromium, as charge transfer effects don't affect the K-edge then we will need to look to L-edge and RIXS experiments to see any effects.

7.2.2 The Benefits of High Energy Resolution (HERFD)

We can see the benefits of the High Energy Resolution Fluorescence Detection XANES method by comparing the HERFD experimental data with the normal XANES data. This is true for the reference materials in chapter 4 (figure 3) and the salen materials in chapter 5 (figure 2). The HERFD spectra allow a much better resolution of the peaks, making them appear sharper than in the normal XANES experiments. In some of the samples studied this makes a huge difference. In Cr₂O₃ an extra feature appears as a broad hump in the HERFD but was not visible at all in the normal XANES, instead it was masked by the underlying peak. Again in the spectrum for CrO₃ one of the peaks is resolved from a small hump to a sharp peak on the low energy side of the first pre-edge feature. This quality is essential when carrying out a detailed analysis of the pre-edge. The dichromate samples figure 3 (chapter 4) also show this to be true with an additional feature visible on the low energy side of the first pre-edge feature, at around 5992 eV. This provides additional information about the orientation of orbitals in space, and therefore their overlap, by showing the allowed transitions in the density of states. The more detail that is obtained in the experiment, the more detailed the resulting analysis can be. Identifying the orbitals that take part in the bonding between the Cr and the ligand and the space that they occupy could be a useful property when looking at future applications.

7.2.3 L-edge XAS

The L-edge XAS spectra were simulated using a different theoretical approach, the Charge Transfer Multiplet program (CTM4XAS). The Charge transfer multiplet (CTM) theory includes both the charge transfer and multiplet effects, which makes it a very effective

theoretical approach that is especially useful in the calculation of most 2p XAS spectra in transition metal systems ¹. The reason that CTM theory is important at the L-edge and not the K-edge is that the K-edge is not affected by charge transfer multiplets. These multiplet coupling effects are caused by interactions between the core hole and the 3d valence electrons. The 1s core hole has essentially no effect (other than its charge) on the multiplet states ². In 2p XAS, in the final state of the X-ray absorption process there is a partly filled core state (2p⁵). When looking at a system with a partly filled 3d shell the final state will have an incompletely filled 3d band. The 2p hole and the 3d hole have radial wave functions that overlap significantly in 2p XAS ³ and so these cannot be reproduced with single particle methods.

In the CTM approach the symmetry of the complex is reduced to the symmetry of the central atom, treating all ligands as point charges. This reflects the point group of the central metal, and no further ligand effects are taken into consideration. In FEFF however a full crystal structure is present in the input file. When calculating the L-edges we also assume either octahedral or tetrahedral geometry, this means that any distortions from perfect geometry are not accounted for in the calculation. This is again, in contrast to the FEFF simulations where distortions can be accounted for in the central atom coordinates.

The calculations of the L-edges of the reference materials have worked very well, in all cases the L_{3,2} peak patterns are well reproduced. Figure 7 (chapter 4) shows the CTM4XAS calculations for the Cr reference materials. Generally the L₃:L₂ ratio is theoretically calculated at being 2:1 based on the degeneracy of the states, however in practice the experimental value has been shown to deviate from 2:1. It was found that the electrostatic interactions between the core hole and valence electrons also has an affect on the branching ratio ⁴. The fact that the multiplet effects, as well as the metal spin state, can influence the branching ratio leads to a variation in the branching ratio across the transition metals ³. Other than the intensity ratio being different the peak shapes and splittings match up nicely. The spectrum for Na₂CrO₄, in particular, is very nicely reproduced with the small feature in the centre of the L₃ edge being picked out in the calculation as well. The main issue across the simulations appears to be that the calculations are broader than the experiment; this could be due to the presence of an increased level of noise in the experimental spectra.

It is evident when comparing the L-edges of Cr(III) and Cr(VI) that the multiplets do change with the differing number of d-electrons, we can see this in the experimental spectra shown in figure 7 (chapter 4). There is a shift to higher energy as well as a visible

change in the pattern and appearance of the peaks forming the $L_{3,2}$ edge. In this way we are able to obtain information on the d-electrons and apparent oxidation state of the compound and the charge transfer effects, this is again useful when looking at compounds about which less is known. Straight away when looking at the L-edge spectra of the salen materials we can deduce information about the oxidation state, in a similar way to how we can predict the geometry at the K-edge XANES. The salen materials all show the same edge shape as the Cr(III) reference materials, which is what we would expect. The Cr(III) samples tend to have a more intense first peak at the L_2 edge whereas the Cr(VI) show the opposite with a more intense second peak. The salen L-edge spectra look very similar except for a shift in the edge positions, the salen 3 complex is shifted to slightly lower energy. Although the substitutions at the salen framework are small any charge transfer effects caused should be visible in the L-edges.

Any distortions from perfect O_h and T_d symmetry for the references are not big enough to show a significant disagreement between the experiment and theory, as shown by the fact that for all the references the experiments are well reproduced (even in the distorted O_h examples) and all calculations are performed assuming pure O_h or T_d symmetry. This makes it harder to distinguish between complexes that are not either O_h or T_d . Although the experimental spectra have been simulated to a high degree of accuracy, in this way there are still some limitations to this approach. This and the fact that only the direct Cr environment is considered means that the surrounding ligands are not included, it is therefore not possible to look at neighbour and ligand effects. Only the crystal field splitting is included.

7.2.4 K β XES

The K β emission studies are also simulated with the FEFF9 program, as mentioned above the FEFF package is able to calculate the emission spectra and electronic spectra simultaneously. Non-resonant X-ray emission spectra are treated in the same way as the X-ray absorption process for states below the Fermi level. This means that we are able to use the same input files and parameters as for the optimised K edge XANES, but just change the XANES card to the XES card.

The simulations of the XES of the references in chapter 4 show fairly good agreement with the experimental data. For the K β main lines the experimental spectrum is extremely simple and we are only looking to reproduce one peak. The leading tail of this peak is at slightly higher energy than the experiment which is the case for all samples; this may be

caused by the tail of the transitions at lower energy (main lines). The cross-over peaks contain more structure and so require more optimisation. The calculated spectrum for Cr_2O_3 (chapter 4) does show the $\text{K}\beta''$ (at 5968 eV) and $\text{K}\beta_{2,5}$ (at 5984.5 eV) peaks that are also present in the experiment, the relative intensities of the peaks however is not so well reproduced. For both the oxide and chloride samples the calculated cross-over peak intensity does not correspond to the experiment. However for the chromate and dichromate samples the relative peak intensities are a good match. The cross-over peaks are prone to be affected by background intensity from the tail of the $\text{K}\beta$ main line, as it is much more intense (see figure 10 in chapter 2, this puts the relative peak intensities into perspective). This causes the cross-over features to become buried in noise and appear as broader peaks. This is one reason for the discrepancy in the calculation, further calculations could be attempted to apply additional broadening to the cross-over region of the spectrum to see if a better match can be obtained. It may also be beneficial to look at additional theoretical approaches to calculating the filled density of states, Density Functional Theory for example.

In chapter 5 we look at the XES experiments for the Cr(salen) materials; unfortunately we were unable to perform an accurate simulation of the experimental data from theory. This may be in part due to the lack of an adequate crystal structure, or because of the complex nature of the structure with a number of heteroatoms around the central Cr. The presence of heteroatoms in the sample produces a characteristic cross-over peak position and shape in the XES spectra (chapter 5, figure 6). A combination of multiple heteroatoms in the sample could confuse this region, causing the appearance of one broad peak in this energy range.

7.2.5 1s2p RIXS

The 1s2p RIXS performed throughout this study have been analysed using a program called RGAss. The RGAss program is a PC interface to the Atomic Multiplet Code written by R. D. Cowan (LANL) with extensions by B. T. Thole and others. The program consists of different components used to produce the final simulation. RGAss includes the electronic configurations for the ground states, intermediate states and final states in the excitation and emission processes as well as parameters for the local geometry of the central atom, crystal field splitting value, the type of transition probed, charge transfer effects, p-d / d-d interactions and a Gaussian broadening of full width at full maximum (FWFM).

The theoretical 1s2p RIXS spectra for the references (figure 11, chapter 4) only reproduce the pre-edge region and not the main absorption edge. This does not matter for the calculation as subtracting the main edge from the experiment does not make too much difference in the case of chromium. The calculations of the pre-edge actually match the experiments very closely, as we can see in figure 11 (chapter 4). The Cr₂O₃ spectra, for example, both show two features in the pre-edge of the same shape and size. From the spectra we can deduce how many transitions form the peak by measuring the width of the feature in electron volts. Again with the pre-edge in the RIXS spectra we are also able to deduce the geometry of the complex by looking at the number, position and intensities of the pre-edge features. Complexes of lower symmetry possess a higher degree of orbital hybridisation and therefore more structure in this region. It is also possible to tell the difference between oxidation states due to the appearance of the pre-edge, Cr(III) and Cr(VI) have very different patterns in the pre-edge. The Cr(VI) spectra (K₂Cr₂O₄) contains only one large pre-edge feature with absorption tails in both the horizontal and vertical directions compared to the Cr(III) samples (oxides, and salens) that show two features each with an absorption tail in the vertical direction. The salen materials are also well reproduced, all being Cr(III) they show similar features to that of the Cr(III) references with two features present in the pre-edge. The RIXS spectra do not show many differences for the salen complexes, the differences in the structures do not appear big enough to be measured using these techniques. They do however show the appearance of additional features for the end species in the catalysis, this feature appears to be formed from non-local Cr s→d transitions with neighbouring Cr atoms. The appearance of the XANES spectra and the non-local peak support the theory that there is a Cr(III)Cr(V)-oxo species present at the end of the reaction or as a reservoir⁵. More analysis is needed to prove the presence of this species but this has given us further insights into the structure of the end species in the epoxidation reaction.

The RIXS experiments provide HERFD XANES spectra with reduced lifetime broadening; however the L-edges measured with the RIXS technique showed decreased resolution compared to the soft X-ray experiments, this was highlighted in figure 8 (chapter 5). The soft X-ray experiments typically show a resolution of 0.1 eV⁶ compared to 1 eV in the RIXS process. Although the final states probed are the same the transitions involved are different. In the soft X-ray experiments the final states are probed directly in a 2p→3d transition, whereas in the RIXS experiment the final states are reached in a two step process (s→d excitation followed by p→s decay).

7.3 Catalysis

During this project we also tried to monitor the reaction *in-situ* to study the starting species, intermediates and end-species during the reaction. The same X-ray techniques were used as in the reference and solid salen studies; however there was not time to calculate the spectra as some of the features observed during the reaction and in the end species were not typical to what had previously been observed for ideal geometries and oxidation states. These species are more complicated to analyse due to the fact that a model will have to be made and optimised to represent the different species in the reaction. As mentioned above other theoretical approaches may also be necessary to produce better agreement with experiment. There is a new version of FEFF that is able to calculate the RIXS spectra. The fact that one would then be able to include the full structural detail would make this a promising option for the analysis of these more complicated systems. Employing other characterisation techniques will help to gain a more detailed understanding of the structure of the intermediates and end species. EXAFS and UV-vis are some of the techniques that could be beneficial for this system, this would help in developing an accurate model to use in the FEFF program.

It is in the catalytic study that we perhaps see the benefits of the RIXS plots over the HERFD XANES. When looking at the HERFD XANES spectra of the end species, in particular, it is hard to tell the difference between the positions of the second pre-edge peaks figure 10 (chapter 6). However, when looking at the 2D RIXS planes you can clearly see that in the end-species the second peak is off the diagonal line, figure 12 (chapter 6). This non-local peak may provide evidence of a Cr(III)Cr(V)-oxo dimer in the reaction. Further theoretical development is needed to confirm this, as discussed in chapter 6.

Any effects, decomposition or otherwise, are not caused by the beam. We ran experiments both *in-situ* and *ex-situ* and the resulting product was the same according to the XANES data. However we would obviously need further theoretical study and characterisation to deduce exactly what the structure of the resultant species is. Full catalytic studies with the ligands present, and more are needed in order to assess the affects on catalysis; there was not time for this in the current research, the focus of which initially was the analysis of the features present in the XAS and RIXS data. The associated differences in electronics can be measured *in-situ* with K-edge XANES, the possibility of complementary characterisation techniques could also be investigated.

7.4 Recommendations and Further Work

One of the first areas that I would recommend for further work is in the synthesis of an extended series of catalyst materials. Originally this part of the study was to include investigations of asymmetric salen complexes to observe any electronic effects on changing heteroatoms at the 3,3' or 5,5' positions, due to the reactivity of the half unit in the reaction it was the double substituted symmetric salen product that was formed. By optimising the synthetic procedure this would be an extremely desirable series of salens to investigate. In this series there would be a greater chance of observing more pronounced electronic differences. The changes occurring in the ligand structure are, in some cases more than four bonds away from the central metal across aromatic systems. Although XAS methods have been used in literature to study aromatic systems ⁷, for a development technique like this it may be easier to start with a more simple series of catalyst structures. Using the salen framework we have the added advantage of keeping the structure constant around the central metal and changing only the ligands attached. It may also have been easier to use materials for which one can obtain a crystal structure. The difficulty in obtaining crystals of the salen materials meant that there was only one published structure that we could use to perform the theoretical calculations. Clearly from the references we have learned that small changes in the structure can lead to significant changes in the XANES/XES/RIXS features obtained.

When looking at the L-edge XANES we were able to see good correlation between experiment and theory. However, in future studies it would be beneficial to look at the individual resonances that make up the over all $L_{3,2}$ edges to see exactly which final states correspond to the features at the edge. This would involve detailed theoretical calculations and a deep understanding of multiplet theory to unravel.

The calculation to reproduce the L-edges is based on either pure octahedral or pure tetrahedral geometry; this could be another variable to test with the experiment. So far we have good agreement with O_h and T_d based calculations for our samples but not all samples are perfect O_h or T_d geometry. It could be interesting to test the limits of theory by studying complexes with more extreme distortions from perfect geometry. It would then also be possible to see if there was a degree of O_h and T_d character that was visible in the shape and appearance of the edge, like in K-edge XANES where we can see differing levels of intensity at the pre-edge.

Although the RIXS data obtained from the reference and salen solid samples is reproducible by theory and we are able to make some structural and electronic deductions upon inspection, it would have been extremely beneficial if it had been possible to measure the full range of oxidation states as planned. This would allow us to see if there are noticeable differences in all oxidation states, rather than comparing just Cr(III) and Cr(VI). The problem faced in the current study was that $\text{Cr}(\text{CO})_6$ was not stable enough to run the full RIXS experiment. We were able to measure XANES by moving around in the beam but this was not possible for RIXS and the sample sublimed in vacuum conditions, which is why we were unable to measure an L-edge. A chromium(II) sample (CrCl_2) was also measured but this also damaged too quickly in the beam, it becomes slightly more difficult in the transfer and manipulation of air and/or moisture sensitive samples, even with a cryostat. The chromium (V) sample measured was in the form of the salen active species; this was stable in the beam long enough for XANES but not for full RIXS planes. It is impossible to predict how samples will react in the beam but finding beam stable Cr(IV) and Cr(V) references would also be beneficial when looking at the end species of the catalysis as Cr(IV) dimmers⁸ or mixed Cr(III)Cr(V) have been suggested in literature⁵.

The catalysis section needs extensive further study; in order to fully understand the results we obtain from the X-ray studies we would need to fully characterise the reaction and the species involved outside of the beam. Unfortunately we did not have time to do this properly as the catalysis was started towards the end of this research project, with the developmental X-ray work in chapter 4 being the initial focus. The results obtained have provided some interesting observations and promising spectra; however we cannot draw many firm conclusions about the reaction pathway without being able to fully analyse the intermediate and end species.

The RIXS spectra of the end species would need further analysis to assign the origins of this 'non-local' (Cr-O-Cr) type peak. It may be that band structure calculations are needed to simulate this off-diagonal peak in the spectrum of the end species. Definitely the application of additional theoretical approaches is needed in order to obtain more insights into all the intermediates. With the possibility now to calculate a RIXS spectrum including a detailed structural description, the development of models for the different species could provide significant advances in this area.

This study has allowed us to gain some interesting insights into both RIXS and the Cr(salen) mediated epoxidation reaction. To fully assign features observed I think that a great deal more characterisation on the catalysis itself needs to be performed.

Unfortunately this was not possible in the time available towards the end of the research project. There is also the possibility of carrying out complementary techniques *in-situ*, for example with an appropriate cell it may be possible to measure the UV during the reaction as the reaction times are relatively long (long enough to obtain HERFD XANES spectra). This would also provide additional electronic information on the species.

7.5 References

1. de Groot, F. M. F.; Kotani, A., In *Core Level Spectroscopy of Solids*, CRC Press: 2008; pp 93.
2. de Groot, F. M. F.; Vanko, G.; Glatzel, P., *J. Phys.: Condens. Matter* **2009**, *21*, 104207.
3. de Groot, F., *Coord. Chem. Rev.* **2005**, *249*, 31.
4. Onodera, Y.; Toyozawa, Y., *J. Phys. Soc. Jpn.* **1967**, *22*, 833.
5. Bryliakov, K. P.; Talsi, E. P., *Inorg. Chem.* **2003**, *42*, 7258.
6. de Groot, F. M. F.; Glatzel, P.; Bergmann, U.; van Aken, P. A.; Barrea, R. A.; Klemme, S.; Havecker, M.; Knop-Gericke, A.; Heijboer, W. M.; Weckhuysen, B. M., *Phys. Rev. B: Condens. Matter* **2005**, *109*, 20751.
7. Tromp, M.; Moulin, J.; Reid, G.; Evans, J., In *X-Ray Absorption Fine Structure-XAFS13*, Hedman, B.; Painetta, P., Eds. 2007; Vol. 882, pp 699.
8. Woo, L. K., *Chem. Rev.* **1993**, *93*, 1125.